

This item was submitted to [Loughborough's Research Repository](#) by the author.
Items in Figshare are protected by copyright, with all rights reserved, unless otherwise indicated.

Studying resonant frequency and dissipation shifts in a mechanical resonator using a fixed-frequency drive

PLEASE CITE THE PUBLISHED VERSION

PUBLISHER

Loughborough University

PUBLISHER STATEMENT

This work is made available according to the conditions of the Creative Commons Attribution-NonCommercial-NoDerivatives 4.0 International (CC BY-NC-ND 4.0) licence. Full details of this licence are available at:
<https://creativecommons.org/licenses/by-nc-nd/4.0/>

LICENCE

CC BY-NC-ND 4.0

REPOSITORY RECORD

Guha, Arnab. 2018. "Studying Resonant Frequency and Dissipation Shifts in a Mechanical Resonator Using a Fixed-frequency Drive". Loughborough University. <https://hdl.handle.net/2134/36245>.

Studying resonant frequency and dissipation shifts in a mechanical resonator using a fixed frequency drive

**by
Arnab Guha**

A Doctoral Thesis

Submitted in partial fulfilment of the requirements for the award of Doctor
of Philosophy of Loughborough University

2018

© Arnab Guha 2018

Declaration

I hereby certify that this PhD dissertation depicts the original work carried out by me and does not consist anything which is the result of the work carried out in collaboration with others except as mentioned in main text and acknowledgements. Significant portions of this dissertation have been submitted for publication in peer reviewed journals and are currently under review process. I also certify that neither of the work has been submitted to Loughborough University or any other institutions worldwide for any other degree, diploma or qualification.

Arnab Guha

Copyright © 2018

All rights reserved

Abstract

Measurement of biomolecular interactions are widely used in various sectors including life sciences, pharmaceutical, clinical diagnostics, and industrial, food and environmental monitoring. The shifts in resonant frequency and dissipation of mechanical resonators have been extensively used for biomolecular measurements. Conventional resonant frequency and dissipation measurement techniques are largely limited in terms of simplicity, time resolution and potentials for on-chip integration and multiplexability. This PhD research focused on the development of a simple method for quantification of resonant frequency and dissipation shifts of a mechanical resonator, which could potentially allow system-integrable and multiplexable biomolecular measurements with high time resolution.

A quartz crystal resonator was chosen as a model mechanical resonator due to its wide applicability. Analytical expressions obtained utilising Butterworth Van Dyke model allowed real-time measurements of resonant frequency and dissipation from each acquired impedance data point at a fixed frequency and amplitude. The method is suited over a broad resonance bandwidth. Quantitative validations were performed against frequency sweep method for inertial and viscous loading experiments using a 14.3 MHz quartz crystal resonator.

Resonant frequency shifts related to temporal steps of quick needle touches on a self-assembled-monolayer-functionalised 14.3 MHz quartz crystal resonator surface were estimated with a time resolution of 112 μ s, which is nearly hundred times smaller than the reported time resolution in the quartz crystal microbalance literature. The fixed frequency drive method has been utilised for demonstration of label-free detection of a gram negative bacterial infection biomarker namely N-hexanoyl-L-Homoserine lactone (~199.2 Da), using molecular imprinted polymer nanoparticles as the receptor. The feasibility of the method has also been tested for direct detection of a large immunoprotein such as immunoglobulin E (~190 kDa), using an aptamer as the receptor.

This fixed frequency based method for determination of resonant frequency and dissipation of a mechanical resonator, with no need for averaging, fitting or measurement dead time, potentially allows a simple and low-cost method suitable for integration into online or miniaturised system with significantly improved time resolution and multiplexability.

KEYWORDS: *Mechanical resonator; Quartz crystal resonator; Fixed frequency drive; Resonant frequency shift; Time resolution; Biomolecules; Dissipation*

Acknowledgements

First and foremost, I would like to thank almighty God for giving me a wonderful opportunity to pursue PhD in one of the reputed higher education institutions of UK. It has been a great experience to perform a doctoral research on novel acoustic sensors for biomarker based diagnosis at Loughborough University. I am thankful to Wolfson School of Mechanical, Electrical and Manufacturing Engineering for awarding me with a prestigious Wolfson School Indian International Excellence Doctoral Studentship which covered tuition fees at international rate and living expenses for three years of my PhD. I sincerely acknowledge the EU project Norosensor (FP7-NMP 604244) and the EPSRC Bridging the Gap in Antimicrobial Resistance grant (EP/M027341/1) for covering the cost of consumables needed for my research.

I would like to sincerely thank my principal PhD supervisor, Dr. Sourav Ghosh for his untiring support and consistent guidance during the course of my study. He was always approachable and available either in person or over phone and email apart from the scheduled weekly meetings for quick advices and tips which appeared quite beneficial in terms of planning experiments during the initial stages of my doctoral research. His advice helped me in choosing my future career options. He also gave me the opportunity to explore undergraduate teaching duties within my PhD curriculum. I am really grateful to him for his support and compassion during some of the toughest times of my PhD journey. He never stopped to motivate me during those difficult times. His example of patience, tenacity, meticulousness and curiosity has immensely helped me in growing as an ideal researcher in the field of acoustic sensors during the course of my PhD journey. His extraordinary scientific writing skills have helped me in improving mine over the subsequent years of my PhD.

I would also like to thank my co-supervisor, Professor Alexandra Stolzing for her advice on selection of appropriate biorecognition elements for different biomarkers during different stages of my PhD. I am also thankful to my independent assessor, Professor Stephanos Theodossiades for providing feedback on first, second and third year annual reviews during my PhD. His review comments have helped me in shaping up my dissertation.

A successful multidisciplinary research is always accomplished through collaboration with great minds from varied backgrounds. I would like to express my sincere gratitude to Mr Victor Ostanin of Department of Chemistry, University of Cambridge as a principal collaborator for his unwavering support and indispensable suggestions throughout my PhD in spite of having severe health problems. I am grateful to him for training me in the field of electronics, acoustic sensors and data processing during the initial stages of my research. I

am also thankful to him for his valuable feedback on research results and drafting of journal articles. I sincerely acknowledge Mr. Omar Sheej Ahmad, a Chemistry PhD student of Professor Sergey A Piletsky from University of Leicester for coming down to Loughborough and helping me with his biochemistry skills for immobilising molecular imprinted polymer nano particles on quartz crystal resonator surface for detection of gram negative bacterial infection biomarker. I am really grateful to Professor Sergey for allowing me to borrow necessary reagents needed for detection of bacterial infection biomarker from his research laboratory. I also acknowledge Dr. Niklas Sandström of KTH Royal Institute of Technology, Stockholm, Sweden for sharing his microfluidic skills with me during my PhD. I acknowledge the contribution and effort of Dr Alexander Zhukov of University of Cambridge for development of the graphical user interface of the vector network analyser instrument which has been used for conducting biosensing experiments during my PhD.

I acknowledge the cooperation of Wolfson school staff Mr. Keven Smith, Mr. David Brock, Mrs. Lauren Wragg and Mrs. Jo Mason in the course of my PhD journey. I would like to particularly thank my multidisciplinary research group members Mr. Carlos Da Silva Granja, Mr. Stavros Yika Tuesta, Dr. Shilpa Khobragade, Ms. Sam Swarbrick, Dr. Oluwasesan Adegoke and Dr. Igor Efimov and for their help and support during the course of my PhD. I am thankful to Mr. Carlos Da Silva Granja for training me in preparation of stock solutions of streptavidin, human immunoglobulin E aptamer and human immunoglobulin E, to name a few in buffers. I am grateful to Dr. Shilpa Khobragade for preparing me during my initial stages for the interview with Wolfson School Safety Officer in order to get entry into containment level 2 laboratories in Centre for Biological Engineering (CBE). Discussion of theoretical background of my research with Dr. Igor Efimov appeared to be very fruitful for me. Conversation with Mr. Carlos Da Silva Granja and Ms. Sam Swarbrick about biochemistry related topics was very helpful to me regarding understanding of bioassays. I am thankful to Dr. Oluwasesan Adegoke for sharing his views regarding writing styles for scientific articles and PhD dissertation. The expertise of Mr. Stavros Yika Tuesta in electronics helped me in getting a better overview of my doctoral work. I would also like to acknowledge my past and present CBE colleagues Dr. Sujith Sebastian, Mr. Dimitris Tampakis, Mr. Luis Costa Marques, Mr. Alexandros Englezakis and Dr. Preeti Holland for providing a helping hand to me when it was required. I sincerely acknowledge the cooperation of lab managers Dr. Amit Chandra, Mr. Kulwinder Sikand and Mrs. Carolyn Cavanagh. I would like to specially thank some of my Loughborough friends Mr. Vallabh Kshirsagar, Ms. Nikita Sachdev, Mr. Neville Rebelo, Ms. Winta Tridhatu Satwikasanti, Ms. Begum Zeybek, Ms. Danna Guo, Dr. Ramakrishnan Ambur Shankarnarayanan and Dr.

Saikat Dutta for spending their precious spare time with me over several occasions during my PhD journey.

I am really indebted to different religious communities of Loughborough namely Gurudwara Sahib, Geeta Bhawan, Ramakrishna Centre and Swaminarayan temple for feeding me with sumptuous and hygienic free meals on multiple occasions over lunch and dinners during my entire PhD journey. This has saved a significant amount of my time and allowed me to focus more on my PhD which otherwise would have spent in cooking food for myself. I hope to sponsor the meal for them in jubilation of my upcoming PhD achievement and future endeavours.

Finally, I would like to express my sincere gratitude to my parents for their love, affection and inspiration they have bestowed upon me throughout my life. This PhD thesis wouldn't have been written without their constant support and motivation. I am grateful for the countless sacrifices they have made over the years due to my doctoral study in UK. I am eagerly looking forward for spending some quality and even happier time with them in the near future.

Table of Contents

Abstract	i
Acknowledgements	ii
Chapter 1. The Motivation	1
1.1 Introduction	1
1.2 Existing biomolecular measurement tools	1
1.2.1 Nuclear magnetic resonance.....	2
1.2.2 X-ray crystallography.....	2
1.2.3 UV/Visible spectroscopy	2
1.2.4 Fluorescence resonance energy transfer.....	3
1.2.5 Fluorescence polarization	3
1.2.6 Enzyme linked immunosorbent assay.....	4
1.2.7 Affinity capillary electrophoresis	4
1.2.8 Surface plasmon resonance.....	5
1.2.9 Isothermal titration calorimetry.....	5
1.2.10 Electrochemical Impedance Spectroscopy.....	5
1.2.11 Atomic Force Microscopy.....	6
1.2.12 Mechanical Resonators	7
1.3 Challenges in existing biomolecular measurement tools	12
1.3.1 Simplicity and online measurement	12
1.3.2 Time resolution	13
1.3.3 Multiplexability	14
1.4 Objectives of the PhD project.....	14
1.5 Fixed Frequency Drive Method	15
1.6 Contributions to Knowledge.....	16
1.7 Organization of this doctoral work	17
Chapter 2. Review of current methods for measurement of resonant frequency and dissipation of a quartz crystal resonator	18
2.1 Introduction	18
2.2 Electrical equivalent of a quartz crystal resonator	18
2.3 QCR resonant frequency and dissipation quantification methods.....	19
2.3.1 Oscillator circuits.....	19
2.3.2 Frequency sweep analysis	22
2.3.3 Ring down analysis.....	24
2.4 Summary of challenges of conventional methods	26

2.5 Idea of single frequency measurement of quartz crystal resonator: A path ahead	26
2.5.1 Background	26
2.5.2 Limitations of single frequency measurement method	27
2.6 Prelude to fixed frequency drive method	27
Chapter 3. Fixed Frequency Drive Method– Going beyond the state of the art.....	28
3.1 Introduction	28
3.2 Fixed Frequency Drive Theory	28
3.2.1 Estimation of resonant frequency.....	28
3.2.2 Estimation of characteristic wave impedance and shunt capacitance	30
3.3 Determination of quality factor of quartz crystal resonator in liquid.....	31
3.4 Error in resonant frequency shift estimate when characteristic wave impedance is assumed as constant.....	31
3.5 First and second order series approximation of the resonant frequency offset	33
3.6 Dissipation shifts using fixed frequency drive method.....	35
3.7 Intrinsic advantages of FFD	36
3.8 Limitation.....	37
3.9 Conclusion.....	38
Chapter 4. Experimental validation of Fixed Frequency Drive method.....	39
4.1 Introduction	39
4.2 Experimental hardware	39
4.2.1 Instrumentation	39
4.2.2 Sensor Assembly	40
4.3 Comparative analysis of FFD and frequency sweep for inertial loading experiments.....	43
4.3.1 Reagents.....	43
4.3.2 Protocol for cleaning of QCR	44
4.3.3 Protocol for formation of self-assembled monolayer of thiol on QCR	44
4.3.4 Protocol for baseline preparation	44
4.3.5 Method of Drive	44
4.3.6 Inertial loading results	46
4.3.7 Agreement with Sauerbrey model for resonant frequency shift due to streptavidin-biotin binding	51
4.4 Comparative analysis of FFD and frequency sweep using viscous loading experiments.....	53
4.4.1 Materials and preparation of QCRs.....	53
4.4.2 Method of Drive	53

4.4.3 Viscous loading results	54
4 . 4 . 4 E s t i m a t e s f r o m K a n a z a w a ' s t h e o r y	58
4.5 Noise analysis	59
4.6 Time resolution of resonant frequency shift measurement	63
4.6.1 Theoretical estimate of time resolution	63
4.6.2 Needle touch experiment.....	66
4.7 Conclusion.....	69
Chapter 5. Application of fixed frequency drive for detection of gram negative bacterial infection biomarker	70
5.1 Introduction	70
5.1.1 Definition of biomarker	70
5.1.2 Importance of Acylated Homoserine Lactones.....	71
5.1.3 Conventional AHL detection techniques.....	73
5.1.4 Label-free AHL detection techniques	75
5.1.5 QCM based AHL detection: A way forward	75
5.1.6 Problem statement.....	76
5.1.7 Methodology.....	76
5.2 Experimental Hardware.....	77
5.2.1 Instrumentation	77
5.2.2 Sensor Assembly	77
5.3 Materials and Excitation methods.....	78
5.3.1 Reagents.....	78
5.3.2 Protocol for preparation of glass beads.....	79
5.3.3 Protocol for preparation of anti-C6-HSL glass beads.....	79
5.3.4 Protocol for polymerisation and anti- C6-HSL MIP nanoparticles synthesis	80
5.3.5 Protocol for immobilisation of QCR with anti- C6-HSL MIP nanoparticles	80
5.3.6 Protocol for preparation of baseline	81
5.3.7 Protocol for preparation of C6-HSL stock solution	81
5.3.8 Steps of excitation	81
5.4 Quantification of C6-HSL	82
5.5 Investigation of Specificity	86
5.6 Conclusion.....	92
Chapter 6. Application of fixed frequency drive for Human Immunoglobulin E detection.....	93
6.1 Introduction	93
6.1.1 Importance of Human Immunoglobulin E.....	93

6.1.2 State-of-the art detection methods for human IgE	94
6.1.3 Label-free detection methods for human IgE.....	94
6.1.4 Potential of acoustic sensors for human IgE detection	94
6.1.5 Problem statement of research.....	96
6.1.6 Experimental methodology	97
6.2 Materials and Methods.....	97
6.2.1 Reagents.....	97
6.2.2 Protocol for immobilisation of D17.4 biotinylated anti-IgE aptamer on QCR and baseline preparation.....	97
6.2.3 Steps of excitation	98
6.3 Quantification of Human Immunoglobulin E	99
6.4 Investigation of Specificity	104
6.5 Conclusion.....	107
Chapter 7. Conclusion and Future Work.....	109
7.1 Achievement of Objectives.....	109
7.2 Comparison of FFD with state-of-the art techniques.....	110
7.3 Future Investigations	115
7.3.1 Exploring detection of C6-HSL and hIgE in clinical samples.....	115
7.3.2 Exploring detection of other biomarkers.....	115
7.3.3 Exploring higher frequencies for sensitive detection	115
7.3.4 Modification of calibration procedure	118
7.3.5 Exploring self-oscillating quartz crystal resonator.....	120
7.3.6 Exploring applications apart from biomolecular measurements.....	121
Appendix A. Supplementary Information	122
A.1 Calibration Theory	122
A.2 Explanation of Mathematica code for producing the calibration file (abcd.dat)	125
A.3 Resonant frequency shift calculation using Sauerbrey theory	139
A.4 Quick needle touch experiments in air and PBS using VNWA and custom built network analysers	141
A.5 Continuous mode FFD and FS experiments for streptavidin detection.....	146
A.6 Continuous mode FFD experiments involving hIgE detection	148
A.7 Continuous FFD and FS experiments for C6-HSL detection	150
A.8 Cleaning protocol of mesa QCR	151
A.9 Derivation of quality factor and half resonance bandwidth for liquid loading of a QCR surface	151
A.10 Location of spurious modes for 14.3 MHz QCR under liquid loading.....	154

Appendix B. List of Publications	157
B.1 Journal Papers.....	157
B.2 Conference Proceedings.....	157
References	158

List of Abbreviations

ACE	Affinity Capillary Electrophoresis
AFM	Atomic Force Microscopy
AGC	Automatic Gain Control
BVD	Butterworth-Van Dyke
CNC	Computer Numerical Control
CV	Cyclic Voltammetry
DPV	Differential Pulse Voltammetry
DUT	Device Under Test
EIS	Electrochemical Impedance Spectroscopy
ELISA	Enzyme Linked Immunosorbent Assay
EQCM	Electrochemical Quartz Crystal Microbalance
FBAR	Film Bulk Acoustic Resonator
FET	Field Effect Transistor
FFD	Fixed Frequency Drive
FP	Fluorescence Polarization
FPW	Flexural Plate Wave
FRET	Fluorescence Resonance Energy Transfer
FS	Frequency Sweep
GC-MS	Gas Chromatography coupled with Mass Spectrometry
HPLC	High Performance Liquid Chromatography
HPLC-MS	High Performance Liquid Chromatography coupled with Mass Spectrometry
ITC	Isothermal Titration Calorimetry
LC-MS	Liquid Chromatography coupled with Mass Spectrometry
LC-MS/MS	Liquid Chromatography coupled with tandem Mass Spectrometry
LOD	Limit of Detection
MALDI-MS	Matrix Assisted Laser Desorption Ionisation Mass Spectrometry
MQCM	Multichannel Monolithic Quartz Crystal Microbalance
NAAT	Nucleic Acid Amplification Test
NMR	Nuclear Magnetic Resonance
PCB	Printed Circuit Board
PCR	Polymerase Chain Reaction
PZT	Piezoelectric
QCR	Quartz Crystal Resonator
QCM	Quartz Crystal Microbalance
QCM-D	Quartz Crystal Microbalance with Dissipation monitoring

RAST	Radio Allergo Sorbent Test
SAM	Self-Assembled Monolayer
SAW	Surface Acoustic Wave
SC	Stress Compensated
SNR	Signal-to-Noise Ratio
SPR	Surface Plasmon Resonance
TLC	Thin Layer Chromatography
UV	Ultraviolet
VNWA	Vector Network Analyser

List of Nomenclature

Initial phase angle for an exponentially damped sinusoidal oscillation
Gain of amplifier
Effective area of a quartz crystal resonator
Amplitude of oscillation of a quartz crystal resonator
Feedback factor
Coefficient of damping
Capacitance
Shunt capacitance
Piezoelectric strain coefficient for an AT cut quartz
Penetration depth of a bulk acoustic wave
Dissipation factor
Additional surface mass of a quartz crystal resonator
Absolute viscosity of a liquid medium
Average energy dissipated per oscillation cycle of a mechanical resonator
Average energy stored in a mechanical resonator
Driving frequency
Resonant frequency of a quartz crystal resonator
Force applied to a mechanical resonator
Frequency constant of a quartz crystal resonator
Angular resonance bandwidth
Resonance bandwidth
Quadrature component
Stiffness
Wavelength of a bulk acoustic wave
Inductance
Mass of a mechanical resonator
Shear modulus of quartz
Overtone number
Avogadro number
Angular driving frequency
Angular resonant frequency
Initial phase angle for an underdamped free vibration of a mechanical resonator
Average power dissipated per oscillation cycle of a quartz crystal resonator
Charge

	Quality factor
	Density of a liquid medium
	Density of quartz
	Resistance
	Electrical electrode loss of a quartz crystal resonator
	Time
	Thickness of quartz
	Decay constant
	Velocity of a standing wave through quartz substrate
	Voltage applied across a series RLC circuit
	Amplitude adjusted voltage
	Voltage across an automatic gain control circuit
	Voltage applied across a quartz crystal resonator
	Displacement of a mechanical resonator
	Reactance of a motional arm of a quartz crystal resonator
	Equivalent admittance of a quartz crystal resonator
ζ	Automatic gain control circuit constant
	Equivalent impedance of a quartz crystal resonator
	Impedance of a motional arm of a quartz crystal resonator

Chapter 1

The Motivation

1.1 Introduction

The interactions among different biomolecules take place on microscopic or smaller scales. However, the impact of such interactions in human lives and the surroundings occurs on a macroscopic level. As an example, the ordinary flu appears at the onset of binding of hemagglutinin with sialic acid coated glycoproteins and glycolipids, which are present on the surface of host human cells. Such interactions permit duplication of influenza viruses within the human body [1]. Studying biomolecular interaction analysis is therefore essential for the understanding of disease mechanisms, and the development of suitable diagnostics and drugs. Measurement of biomolecular interactions has been widely explored in various sectors including life sciences [2], pharmaceutical [3], clinical diagnostics [4], industrial process monitoring [5], food [6] and environmental safety [7] and biosecurity [8]. The sizes of the particles such as cells, fungus, bacteria, viruses, proteins and small molecules, to name a few involved in biomolecular interactions ranges from hundreds of microns to few nanometres [9] and there is no single detection technique that suits all interaction analysis. Some of the challenges faced during biomolecular interactions include delivering specificity, sensitivity, robustness, real-time measurements, speed and multi-parameter analysis at low cost and ease of use. The research in this field focuses on addressing these challenges, which is still an unmet need. Hence, the techniques for measuring these interactions are an active field of research due to various requirements and challenges for performing biomolecular interaction analysis.

1.2 Existing biomolecular measurement tools

Conventional tools used for biomolecular interaction analysis include nuclear magnetic resonance (NMR) [10], X-ray crystallography [11], ultraviolet (UV) /visible spectroscopy [12], fluorescence resonance energy transfer (FRET) [13], fluorescence polarization (FP) [14], enzyme-linked immunosorbent assay (ELISA) [15], affinity capillary electrophoresis (ACE) [16], surface plasmon resonance (SPR) [17], isothermal titration calorimetry (ITC) [18], electrochemical impedance spectroscopy (EIS) [19], atomic force microscopy (AFM) [20] and mechanical resonators involving cantilever [21], surface acoustic wave (SAW) devices [22] and quartz crystal microbalance (QCM) [23]. A summary depicting the principle,

advantages and disadvantages of the above-mentioned biomolecular recognition tools have been provided below. Mechanical resonators form the main focus of this dissertation.

1.2.1 Nuclear magnetic resonance

Nuclear magnetic resonance (NMR) takes into account the quantum mechanical properties of atomic nuclei from a given sample [1]. In NMR technique, firstly, application of a strong exterior magnetic field helps in aligning the atomic nuclei, which is subsequently exposed to an electromagnetic field. NMR effective atomic nuclei are represented by a peak at a particular frequency in the spectrum of NMR. Since the resonance frequencies of different atoms are different for an applied magnetic field, each peak in the NMR spectrum can be designated to an individual atom pertaining to a given molecule. Resonant frequency data obtained from NMR research provides information about structure and conformational changes of a molecule during intermolecular interactions. An atomic resolution of approximately 1.5-3 angstroms can be achieved for backbone atoms using NMR. However, NMR can only be applied to a sample having molecular weight less than 40 kDa. Certain NMR also requires use of costly and tagged ligands [1].

1.2.2 X-ray crystallography

X-ray crystallography [1] is another biomolecular measurement tool which provides atomic resolution similar to that of NMR. It comprises the following three steps. Firstly, a large and pure crystal is obtained. Secondly, the crystal is rotated and subjected to X-rays and the intensity of the X-rays diffracted from the electrons of the crystal is measured. Thirdly, the final structure of the crystal is achieved by computationally processing and refining the obtained measurements. In spite of having higher atomic resolution, it possesses certain disadvantages. It is difficult in reality to obtain a pure and sufficient amount of crystal for structural analysis. In case of protein crystal, a large amount of water content can alter the structure of the crystal lattice to a greater extent in comparison to the crystals of minerals and small molecules. X-ray diffraction signals from a fragile crystal are very weak. Further, the crystals should be frozen and devoid of ice formation for crystallographic use in order to avoid expansion or damage of lattice structure [1].

1.2.3 UV/Visible spectroscopy

Monitoring of biomolecular interactions in UV/Visible spectroscopy [1] is performed using a spectrometer, which is easily accessible. A sample cell consisting of different biomolecules is scanned in a spectrometer utilizing an electromagnetic radiation which spans from visible

to ultraviolet range. Absorption spectra are obtained following the scan where the absorbance level is plotted against the incident radiation wavelength. The absorption spectra vary for different molecules due to their diverse bonds and conjugation patterns. Further, a single molecule will produce distinct absorption spectra in comparison to that obtained from a molecule attached to another molecule. However, UV/visible spectroscopy is a low resolution technique and a change in maximum incident radiation wavelength or shape of absorption curve is necessary for differentiation among different biomolecules [1].

1.2.4 Fluorescence resonance energy transfer

The interaction between two molecules which are tagged with different fluorophores is measured using fluorescence resonance energy transfer (FRET) method [1]. The molecule which is labelled with a fluorophore comprising lower excitation wavelength is termed as the donor molecule. The molecule which is tagged with a fluorophore of higher excitation wavelength is termed as the acceptor molecule. Excitation of donor molecule with a light of wavelength equivalent to excitation wavelength of its own fluorophore yields radiation less energy transfer into acceptor molecule where emission of light occurs at a wavelength equivalent to the emission wavelength of its own fluorophore. FRET allows study of biomolecular interactions involving a wide range of donor and acceptor molecules. However, FRET is only capable of analysing biomolecular interactions, provided that the distance between donor and acceptor molecules is within 10 nm. It also involves use of multiple labels which should not have significant impact on the function and interaction of biomolecules such as proteins [1].

1.2.5 Fluorescence polarization

Fluorescence polarization (FP) method [1] utilises fluorescence for comparison of rotational motion of a biomolecular complex comprising a fluorophore labelled molecule and an unlabelled molecule with the rotational motion of the same fluorophore tagged molecule in an unbound state. A plane polarized light is used for linear excitation of fluorophore labelled molecule as its fluorescence lasting time is of the order of nano seconds. Taking into account the size of a biomolecule, rotational correlation time is usually higher for a biomolecular complex in comparison to an unbound biomolecule. Hence, a measure of rotational correlation time is employed in FP for studying the binding affinity between various biomolecules such as receptor-ligand and DNA-protein interactions. FP method permits real-time measurement of biomolecular interactions in addition to high-throughput screening.

However, a considerable change in molecular volume is essential for obtaining a maximal FP signal. The range of FP magnitudes is also limited by the life time of the fluorophore [1].

1.2.6 Enzyme linked immunosorbent assay

Enzyme linked immunosorbent assay (ELISA) [1] is a biochemical method used for detection of antigen in a given sample. Detection of antigen using ELISA comprises the following steps. Firstly, the sample containing the antigen is immobilised on the surface of microwell plates [24]. Secondly, an enzyme conjugated antibody that binds specifically to the antigen is added to the well plate in order to allow amplification of signal. Thirdly, the material bound non-specifically to the well plate surface is removed through a series of detergent washes. Finally, the enzyme tagged to the antibody is activated by addition of colourless substrate. The reaction between the enzyme and the substrate yields a visible signal which is either chromogenic or fluorogenic in nature. Production of the signal confirms the presence of the antigen which can be quantified based on the intensity of the signal. The advantages of ELISA involve fast detection, low cost and simple set up [1]. However it does not provide real-time monitoring of any biomolecular interaction as it is based on an end point readout [24] . The intermediate signal amplification and sample processing steps involved with ELISA are often very complex.

1.2.7 Affinity capillary electrophoresis

Affinity capillary electrophoresis (ACE) is utilized for assessing the migration pattern of a biomolecular species inside an electrophoretic chamber, which are essentially capillaries [1]. Variations in shape, size or charge of a species lead to alterations in mobility pattern within an electrophoretic chamber. In a standard ACE method, a target biomolecule termed as analyte and a standard, which does not interact with the analyte, are injected inside an electrophoretic chamber, which consists of electrophoresis buffer and an interacting biomolecule termed as receptor. A shift in migration time of the analyte is observed in comparison to the standard upon increase in concentration of the receptor molecule in electrophoresis buffer. ACE is fully automated and has the capability to investigate various compounds with diverse ionic strengths, temperatures and pHs. However, non-specific adsorption of proteins inside the capillaries prohibit the general applicability of ACE for biomolecular interaction analysis [1].

1.2.8 Surface plasmon resonance

Surface plasmon resonance (SPR) is a label-free biomolecular interaction tool with minimal sample preparation and washing steps. It is one of the widely used optical transduction mechanism that relies on the interaction of light with the adsorbed molecules on the sensor surface. Sensor surface is essentially a cell chamber consisting of thin metallic film, which is immobilised with a receptor molecule. An analyte solution, which is specific to the receptor, is flowed over the cell chamber surface after immobilisation. SPR relates the interaction between a receptor and an analyte with changes in refractive index near the sensor surface [25]. SPR is generally considered as the gold standard among label-free biosensing techniques for detection of biomolecules due to its sub-nano gram detection limit and real-time measurement capability. However, it involves use of expensive and bulky instrumental setup.

1.2.9 Isothermal titration calorimetry

Isothermal titration calorimetry (ITC) [25] measures the heat absorbed or generated from a biochemical reaction due to titration of a solution of a target biomolecule or analyte into a solution of its receptor or interacting component. A simple ITC set up contains two cells accommodated in an isothermal environment. One cell acts as a reference consisting of water or buffer and the other cell is dedicated for the sample consisting of the target analyte. Each of the cells possesses thermocouple circuits with a feedback control system for temperature regulation as both the cells need to be maintained at the same temperature. Analyte is introduced into the sample cell by means of a syringe. Magnitude of reaction heat obtained from a single ITC measurement for a given concentration of analyte provides information including binding constant and enthalpy and entropy of binding, to name a few. ITC does not involve any surface immobilisation or analyte labelling for monitoring of biomolecular interactions. However, the method is only applicable for biomolecular interactions having a quantifiable change in enthalpy and requires lot of effort in terms of planning and execution of experiments [25].

1.2.10 Electrochemical Impedance Spectroscopy

Electrochemical Impedance Spectroscopy (EIS) is the most commonly used electrochemical transduction technique used for biomolecular recognition. It is based on measurement of changes in electrical impedance due to the interaction between a receptor and an analyte [26]. A very low amplitude sinusoidal voltage ($\sim 5\text{-}10\text{ mV}$) with variable frequencies is

applied to an electrochemical cell and as a result, an electric current is generated [27]. The impedance of the electrochemical cell is obtained by taking the ratio of applied electric voltage to that of generated electrical current and is expressed as a function of excitation frequency. EIS is the most widely used biomolecular interaction tool due to its ease of use, smaller size, good specificity, cost effectiveness, real-time measurement capability and disposable nature. However, EIS needs electrically conducting analytes as a prerequisite for its operation [28].

1.2.11 Atomic Force Microscopy

Atomic force microscopy (AFM) is an important imaging tool for investigation of different biomolecular interactions involving quantifications of unbinding force [20] between bound biomolecules and conformational changes of DNA-protein assemblies [29], to name a few. An AFM experimental setup comprises a micro-cantilever probe with a sharp tip, piezoelectric (PZT) actuator, position delicate photo detector and a laser [30]. The cantilever tip is housed on the PZT actuator. A photo diode receives a laser beam reflected from the cantilever surface in order to supply a cantilever deflection feedback for PZT scanner. In a typical AFM experiment, the tip is scanned over a sample surface with an appropriate feedback system based on AFM operation such as maintaining the tip at a consistent force or consistent height over the sample surface. AFM can be operated in non-contact, contact and tapped modes. In non-contact mode, the micro-cantilever is vibrated at or in the vicinity of its natural resonant frequency and positioned 50-150 angstroms above the sample surface [30]. The measured shift in cantilever resonant frequency, amplitude or phase due to van der Waals attractive forces between the tip and the sample surface facilitates extraction of topographic parameters of the sample surface. In contact mode, the cantilever tip is in contact with the sample surface which enables real-time monitoring of repulsive interaction forces [30] between them. Tapped mode is a combination of non-contact and contact modes where the oscillating cantilever tip is in intermittent contact with the sample surface. Such a mode enables imaging of soft samples with high resolution due to dissipation of energy resulting from minimal intermittent touches [30]. Dissipation of energy is indicated from reduction of cantilever oscillation amplitude. Dynamic images of biomolecules have been taken using AFM with sub 100 ms time resolution [31]. However, use of optics limits its use for miniaturized applications [32].

1.2.12 Mechanical Resonators

Continuous conversion of kinetic and potential energies takes place for a mechanical resonator. A frequency relying response is usually exhibited in a mechanical resonator. The frequencies at which optimum transfer of energy occurs after taking into consideration the system losses are termed as the resonance frequencies of a mechanical resonator [33]. A specific motion pattern known as the resonance mode is associated with each resonant frequency. Different modes of vibration of a mechanical resonator include thickness shear mode [34], transverse mode [35], torsional mode [35], lateral mode [35] and longitudinal mode [35]. Apart from resonant frequency, another important parameter used for performance assessment of mechanical resonators is quality factor. Quality factor can be written as follows [33]:

$$\dots\dots\dots \text{---} \quad (1.1)$$

where is the average energy stored in the resonator and is the average energy dissipated per oscillation cycle from the resonator. The resonant frequency and dissipation factor, which is the inverse of quality factor, are often employed for characterisation of mechanical resonators.

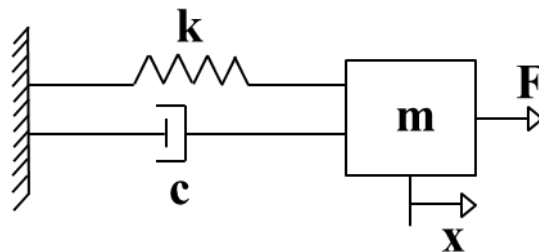


Figure 1.1. Spring-mass-damper model of a resonance mode of a mechanical resonator

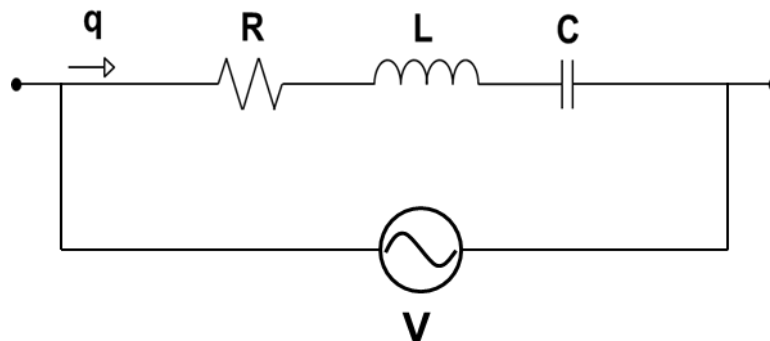


Figure 1.2. An equivalent electrical circuit for a mechanical resonator

A mechanical resonator dynamics encompassing a particular resonance mode can be expressed in the form of a mechanical model (Figure 1.1) consisting of a spring, mass and a damper [36]. The mass and the spring are responsible for storage of kinetic and potential energies respectively. The damper accounts for system losses. Usually, a mechanical resonator is compelled to oscillate through conversion of an electric input signal into force, followed with its application to the resonator. As a result, the resonator picks up the oscillations which are again converted into electrical signals by means of suitable transduction techniques [33]. The dynamic model of a mechanical resonator can be represented by an electrical equivalent RLC circuit (Figure 1.2), where the electrical resistance (R), inductance (L), capacitance (C), voltage (V) and charge (Q) are associated to the coefficient of damping (γ), mass (m), stiffness (k), force (F) and displacement (x) by $\gamma = R/m$, $m = L$, $k = 1/C$, $F = V$ and $x = Q$ respectively [36]. Mechanical resonators have been explored for biomolecular interactions where the receptor immobilised resonator surface has been used to detect the target analyte that binds specifically to the receptor [37]. The most commonly used mechanical resonators have been discussed in the following sections.

Cantilevers

The concept of cantilever sensors has been evolved from the use of an atomic force microscope probe [38]. Cantilevers are usually made of silicon or silicon based substrates [39]. Cantilever sensors can be run in two modes namely static mode and dynamic mode [40]. Generally, the upper surface of the cantilever is immobilized with receptors. In static mode cantilevers, the difference in surface stress between the top and bottom surfaces on account of analyte binding gives rise to deflection. Cantilever deflection is measured by various methods including interferometric, piezoresistive and piezoelectric techniques [41]. In some cases, reference cantilevers are used to improve sensitivity and deduct background noise from the system [41]. In dynamic mode, the cantilever is allowed to oscillate at or near its resonant frequency which varies from several kHz to MHz range [40]. A change in resonant frequency is observed due to binding of analyte with the receptor immobilised cantilever surface. There is a need for external driving mechanism such as optical or piezoelectric for the operation of cantilever in dynamic mode [35]. The quality factor and mass sensitivity of cantilevers reduce significantly in liquid environment due to viscous damping [41]. Depending on varied material, size, geometry, design, actuation mechanism, resonant frequency, resonance mode type and resonance mode order of dynamic

cantilevers, the quality factor in air ranges from 11 to 10,000 for detection of proteins [35]. In case of protein detection in liquid medium, quality factor ranges from 43 to 625 [35] depending on different parameters.

Surface acoustic wave resonators

Surface acoustic wave (SAW) resonators comprise a pair of closely spaced interdigital electrodes which are either patterned on a substrate with piezoelectric properties such as quartz, lithium niobate and lithium tantalate [25] or on piezoelectric thin films accumulated on a substrate based on silicon. SC cut quartz is the most commonly used piezoelectric substrate for surface acoustic wave resonators. Interdigital electrodes act both as a sender and a receiver by converting the input electric signal into acoustic wave and vice versa. Acoustic wave propagates on the surface between the sender and the receiver electrode pair. Such resonators are very ideal for surface adsorption studies. The operating frequency of a SAW device ranges normally from 30-500 MHz [42] and can extend up to certain GHz [43]. Two modes of operation exists for SAW devices namely resonator and delay line modes [39]. In a resonator mode, shift in resonant frequency of the acoustic waves is measured due to interaction of receptor functionalised surface and a rigid analyte. Changes in dissipation factor also occur in addition to resonant frequency for a soft analyte. In delay line configuration, the velocity of the acoustic wave changes due to its interaction with the adsorbed analyte on the sensor surface [41] and therefore the time taken for the acoustic wave to travel between the electrode pair is measured as an output. Liquid damping accounts for energy dissipation from the SAW resonator surface. Hence, the resonator surface is often coated with a guiding layer composed of polymer or silica for confining the acoustic energy close to the sensor surface. A quality factor of ~ 250 has been reported in water for a 185 MHz SAW resonator [44]. SAW devices have been successfully used to detect different proteins and nucleotides [45] in liquid environment. However, SAW resonator measurements such as frequency shift is affected by conductance, dielectric and elastic constants of the adsorbent and liquid conductance [25]. Such influences makes quantitative biomolecular measurements very challenging and therefore building of a robust device involving SAW resonators appears to be problematic.

Quartz crystal microbalance

A typical quartz crystal microbalance (QCM) set up (Figure 1.3) consists of an oscillating AT cut quartz crystal sandwiched between two circular metal electrodes and a quartz driver circuit [46] required for providing an input excitation. Gold is the most commonly used

material for electrodes in QCM. The method of transduction of QCM is piezoelectric [47]. The application of alternating electric field between the electrodes induces alternating expansion and contraction of the quartz crystal lattice on account of inverse piezoelectric effect. As a result, a transverse shear wave (Figure 1.3) is produced which propagates along the direction of crystal thickness. The mode of vibration of a quartz crystal is termed as thickness shear mode [48]. The resonant frequency of the quartz crystal resonator is a function of crystal thickness and shear wave velocity [41]. The fundamental resonant frequency of an AT cut quartz crystal normally varies from 5 to 30 MHz [42]. For a 6 MHz AT cut QCR, quality factors of ~ 74118 and ~ 2790 have been observed in air and water respectively [49]. Shift in resonant frequency of an AT cut quartz crystal resonator (QCR) is usually observed due to relative changes in inertial [50] or viscous loadings [51] and sometimes a combination of both on the surface of the resonator. There is a transfer of acoustic energy from the bulk of a QCR to the rigid mass when there is a formation of rigid films over the resonator surface. Hence, monitoring of resonant frequency shift is enough for detection of a rigid adsorbent as there is hardly any loss of acoustic energy from the resonator. In case of a liquid loading, there is a loss or dissipation of acoustic energy from the bulk of the resonator to the interface between the resonator surface and the liquid. Hence, measurement of motional resistance [52], conductance [53] or dissipation factor [54] is also needed in addition to resonant frequency read out in order to distinguish between inertial loadings and liquid loadings.

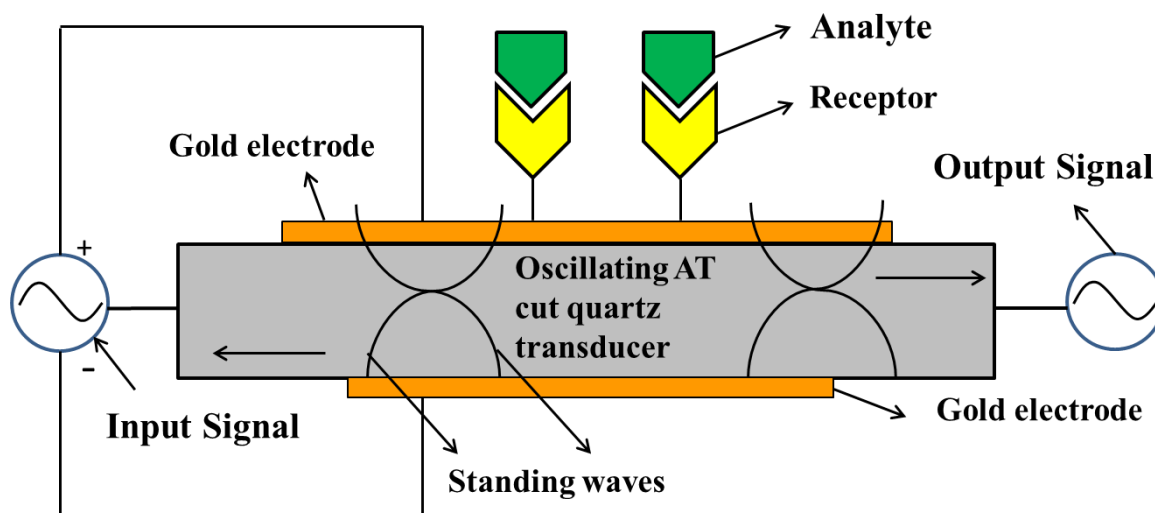


Figure 1.3. Schematic of a receptor immobilised QCM sensor vibrating at its fundamental resonance mode

Quartz crystal microbalance (QCM) is commonly used to study biomolecular binding by measuring shifts in resonant frequency of a quartz-crystal-resonator [55]. In case of biomolecular detection, a receptor specific to the target analyte such as an antibody [56], aptamer [57] or molecular imprinted polymer [58], is immobilised on the surface of the gold electrode and an electrical signal is produced due to the interaction of the analyte with the receptor. QCM transduces the interaction between the receptor and the analyte with changes in resonant frequency of the receptor immobilised QCR surface. Investigations involving cross-linking of protein layers [59] and alterations in viscoelastic properties of polymers [60], to name a few have been performed using QCRs. In spite of the facts that QCM measurements are influenced by interfacial parameters such as surface roughness, free energy and charge and QCM sensitivity is lower than labelled fluorescence techniques, it holds a number of advantages. QCM is a label-free biomolecular measurement tool and is capable of detecting surface bound mass in sub-nanogram level [1]. A wide range of biomolecules can be accommodated as receptors for biomolecular measurements involving QCM. QCM measurements can even be taken in an optically opaque liquid solution. The operation of QCM is relatively simpler in comparison to other techniques. The essential apparatus for production of QCRs is inexpensive and the central element of a QCR, i.e. quartz is cheap [1].

Film Bulk acoustic Resonator

A film bulk acoustic resonator (FBAR) comprises of thin piezoelectric film which is sandwiched between two layers of metal [61]. Materials for thin piezoelectric films include zinc oxide and aluminium nitride [62]. The resonance frequency of a typical FBAR sensor lies in GHz range as the thickness of the thin film ranges between 100 nm to few microns [62]. A quality factor of 883 has been reported in air for a 1.56 GHz bare FBAR [63]. The quality factor for the same FBAR decreased to 798 after protein adsorption [63]. A shear mode FBAR sensor operating in liquid medium achieved a mass sensitivity of $585 \text{ Hz cm}^2 \text{ ng}^{-1}$ and a mass resolution of 2.3 ng/cm^2 [62]. FBAR sensors can be suitably integrated with complementary metal oxide semiconductor technologies which make integration of single sensor or sensor arrays with electronics very easier [62]. Miniaturization and optimisation of fluidic system is also important along with the miniaturization of sensors as there is an increased level of noise for such high frequency sensors [62].

1.3 Challenges in existing biomolecular measurement tools

The key challenges that provided the motivation for this PhD work have been discussed in the following sections.

1.3.1 Simplicity and online measurement

Majority of the biomolecular measurement tools such as NMR, AFM and X-Ray crystallography involve use of complex instruments and require a good laboratory infrastructure. FRET, FP and ELISA involve labelling steps and demand skilled user intervention due to complex sample preparation steps. The use of labels is believed to modify the interactions among different biomolecules [25]. Use of label-free biomolecular measurement tool reduces consumption of resources. ELISA requires different reagents and multiple sample preparation or processing steps for analysing interactions between two biomolecules. It does not provide real-time analysis of biomolecular interactions. Some of the tools such as SPR and UV/Visible spectroscopy are associated with bulky and expensive instrumentation and often involves cumbersome setting up procedures prior to the actual measurements. Implementation of such tools in limited resource settings is therefore extremely difficult. A biomolecular recognition tool with minimal sample preparation or processing steps is therefore needed. Additionally, it should be relatively affordable, easy to use and possess the potential for miniaturization such as QCM. Such a tool favours on-chip integration which is beneficial for hand held point of care (POC) sensor applications [64–68]. A simple, label-free on-chip biomolecular measurement tool with real-time monitoring feature can be utilised in remote and field settings with limited availability of resources. Real-time measurement can favour online monitoring of processes involving biomolecules such as fermentation [69] and distillation [70]. Real-time monitoring of ligand-receptor binding plays a vital role in drug discovery research [71]. Conventional tools such as SPR, AFM and FRET, to name a few can provide online measurements for biomolecular interactions. However, they face severe challenges in various aspects such as set up complexity and maintenance, accessibility, portability and miniaturization. Real-time and label-free monitoring of the interactions between proteins A/G and immunoglobulin G (IgG) have been performed using an on-chip sensor, which combines plasmonic microarrays together with dual wavelength imaging devoid of a lens [72]. However, quantification of the binding event employing the on-chip plasmonic sensor involves use of intricate digital data processing of diffraction images. Use of mechanical resonators such as QCM appears to be a plausible solution as they have been successfully implemented in integrated circuits [73]. Further, miniaturized quartz crystal

resonators have been utilized as contamination sensors for real-time measurement of thin film deposition on delicate surfaces for spacecraft and missile applications [74].

1.3.2 Time resolution

Transient biomolecular processes such as protein-DNA interactions, protein folding reactions and protein-ligand interactions, to name a few [75] usually occur on a millisecond time scale. Protein folding usually occurs within a time scale ranging from milliseconds to minutes [76]. Protein folding studies can be used for better understanding or diagnosis of neurodegenerative diseases like Alzheimer's [77] which is believed to have a strong correlation with protein misfolding. Folding mechanism for some fastest proteins can also be of the order of tens of microseconds [77]. Apart from protein folding phenomenon, activation switch of G protein coupled bioreceptors such as α_{2A} -adrenergic receptor on the surface of the living cells [78], controlling crucial cellular functions including cardiovascular, neural and endocrine, also requires a millisecond time resolution. Monitoring of the transient processes with sub-millisecond time resolution have been performed using techniques like mass spectrometry [79], fluorescence resonance energy transfer (FRET) [78], multi-channel time correlated single photon counting fluorometry [75] and time resolved small-angle X ray scattering apparatus [80]. In spite of offering a high time resolution, the above mentioned techniques are associated with some of the combinations of bulky equipment including CCD cameras, monochromators, polychromators, undulators, lasers, lenses, bandpass filters, microscopes and polarizers which make their operation sometimes cumbersome due to misalignment of the equipment, thereby adding complexities to the measurement system. Mechanical resonators such as the QCM has been widely utilised for monitoring biomolecular interactions [53,55,81,82]. Recently, 10 ms time resolution has been reported to be achieved by quantifying resonant frequency shifts of a 5 MHz AT cut QCR [83] from fixed frequency measurements. However, it is only applicable for studying stable and repetitive electrochemical processes. The Q-Sense QCM instrument [84], which is based on ring down analysis [85], claims to provide a minimum measurement time of 5 ms albeit with no reported data on noise at that time resolution. Although the state-of-the-art QCM methods offers a real-time and label-free platform for studying biomolecular interactions [55,86–88], delivering exhaustive gravimetric (mass, thickness) and non-gravimetric (viscosity, softness) data at multiple overtones, there is no reported evidence of millisecond process measurements with appropriate noise performance.

1.3.3 Multiplexability

Multiplexability plays an important role if there is a necessity of high throughput in an abbreviated time scale. Such a feature can favour biomarker based disease diagnostics [89–91]. Biomarkers are specific indicators of a disease in the human body that can be derived from body fluids, such as cerebrospinal fluid and blood plasma [92]. As an example, T-tau, P-tau and A β_{42} (Amyloid β protein) are the most extensively used cerebrospinal fluid (CSF) biomarkers for Alzheimer's disease [93]. However, multiple biomarkers are required in most cases to conclusively diagnose a disease or monitor its progression. Hence, multiplexing capability is an important feature to have in a biomolecular recognition tool. Conventional labelled biomolecular recognition tools, such as ELISA, have been attempted for multiplexed detection [94]. However, multiplexed ELISA needs simultaneous cumbersome working with multiple reagents, which involves the chances of error and cross contamination. It also involves more consumption of resources with increase in number of analytes in comparison to single analyte detection [95]. Label-free multiplexed detection of biomolecules has also been performed using various techniques such as surface plasmon resonance [96], electrochemical impedance spectroscopy [97] and quartz crystal microbalance [98]. Huge instrument and sensor expenses are associated with multiplexed SPRs which prevents their use for routine clinical diagnosis [99]. Electrochemical transduction technique yields mass production of integrated multiplexed biosensor arrays with low cost and high precision [99]. However, use of reference and auxiliary electrodes for individual sensor probes and an independent multi-channel electrochemical work station induces complexity in instrumentation [100]. QCM sensors are potential candidates for multiplexed detection if acoustic and electrical interferences among each sensors are taken care of [101].

1.4 Objectives of the PhD project

Considering the above-mentioned challenges, mechanical resonators have been chosen for investigation of biomolecular measurements and a novel approach for measurement of resonant frequency and dissipation has been developed in this work. Mechanical resonators are advantageous in different ways [39]. Miniaturisation of mechanical resonators is possible without sacrificing the cost, size and scalability [102]. They can be suitably integrated with electronics [103]. Several mechanical resonators can be embedded on a chip which favours multiplexed detection [101]. A mechanical resonator analyses biomolecular interactions using quantitative estimates of parameters, such as resonant frequency and dissipation. Resonant frequency measurements of resonators, such as quartz crystals and cantilevers,

have been extensively utilised in various sectors including electrochemistry [104–107], surface science [108–110] and biosensors [35,47,68,111] for quantification of surface processes. The main aim of this dissertation is to improve the method for determination of resonant frequency and dissipation of a mechanical resonator, so that these measurements are simplified for better integrability and multiplexability, and have improved time resolution. A quartz crystal resonator has been taken as the exemplar for a mechanical resonator in this dissertation. The objectives of this PhD work can therefore be summarized as follows:

- Development of a novel and simple method for the determination of resonant frequency and dissipation of a quartz crystal resonator
- Investigation of the time resolution and noise performance of a quartz crystal resonator by applying the method
- Validation of the method for real-time biomolecular detection of a range of molecular size using quartz crystal resonators

1.5 Fixed Frequency Drive Method

Resonant frequency of a QCR can be determined using various methods, the most common ones being oscillator circuits, frequency sweep and ring down [85]. The details of the existing techniques have been described in Chapter 2. The initial investigations in this thesis were carried out by looking at some of the challenges of the conventional QCM, which is the most common example of a frequency sweep analyser, such as cost and complexity for real-time or multiplexed analysis and low time resolution. This doctoral work focuses on the development of a novel technique, termed as fixed frequency drive (FFD) technique, which allows the quantification of resonant frequency and dissipation of a QCR by driving it continuously at a fixed frequency. Analytical expressions for resonant frequency and dissipation factor in terms of the drive frequency are derived using the Butterworth-Van Dyke (BVD) model [112] of a quartz crystal resonator (QCR). The expression allows the determination of resonant frequency and dissipation factor directly from each acquired impedance data point without any need for fitting unlike in frequency sweep and ring-down studies. Thus, resonant frequency and dissipation shifts can be read out using a continuous fixed frequency drive (FFD) with a time resolution that is practically limited by the duration of transient processes on the QCR.

1.6 Contributions to Knowledge

The novel method of quantification of resonant frequency and dissipation of a QCR is true over a wide bandwidth. Quantitative estimates of resonant frequency and dissipation factor obtained using the FFD method for different driving frequencies have been compared with the frequency sweep method for streptavidin-biotin binding experiments. The shifts in resonant frequency estimated for streptavidin binding experiments using FFD were validated to be within 1% of those derived using the frequency sweep (FS) method when the QCR driving frequency was set to the resonant frequency of the baseline (i.e. before streptavidin binding) obtained using FS. Experiments involving the subsequent loading of a bare QCR surface with two liquids of different absolute viscosities namely methanol and Deionised (DI) water were performed and similar quantitative estimations were performed using FS and FFD methods. The resonant frequency shift obtained due to changes in viscous loading using FFD was also within 1% of those estimated using FS method when the driving frequency was chosen as the resonant frequency measured using FS in methanol phase at the start of the experiment.

To mimic fast mass loading, quick needle touches were made on self-assembled-monolayer-functionalised surface of a 14.3 MHz AT-cut QCR. Noise and time resolution were investigated for different data acquisition rates ($\mu\text{s}/\text{data point}$) ranging from 32.77 to 524.29 for needle touch experiments. Frequency shifts associated with the transient processes of the touches were monitored with $\sim 112 \mu\text{s}$ resolution from a continuous fixed frequency drive. This measurement exhibited 1 order of magnitude lower baseline noise ($\sim 0.3 \text{ Hz}$) compared with continuous frequency sweep measurements ($\sim 5.4 \text{ Hz}$) from a bench-top commercial network analyser for a data acquisition rate of 66.5 ms.

The FFD technique was also successfully used for label-free detection of two classes of biomolecules in spiked phosphate buffered saline (PBS) solutions: human IgE (MW 190 kDa) and N-hexanoyl-L-Homoserine lactone (MW 199.2 Da) with their molecular weights varying by three orders of magnitude. Analytical formula-based FFD method, therefore, provides simple, low-cost and real-time resonant frequency and dissipation shifts measurements with immensely improved time resolution in comparison to the state-of-the art QCM techniques. The intrinsic simplicity of the method also suits its application to multiplexed detection more than the conventional QCM based on admittance analysis.

1.7 Organization of this doctoral work

- Chapter 2 focuses on conventional QCR resonant frequency and dissipation measurement methods for identification of major challenges. Limitations in time resolution associated with conventional QCM analysers have also been discussed. Insights achieved through studies involving traditional QCR resonant frequency and dissipation quantification techniques and impedance monitoring method at constant frequency lead to the work on resonant frequency and dissipation measurements based on FFD in later chapters of this thesis.
- Chapter 3 presents a novel FFD technique for analytical estimation of resonant frequency and dissipation factor of a QCR. The capabilities of FFD technique including online analysis and high time resolution have been illustrated here.
- Chapter 4 presents the validation of the proposed novel technique through viscous and mass loading experiments. Resonant frequency shift estimated from FFD method due to subsequent viscous loading of 14.3 MHz QCR surface with methanol and DI water were compared with those obtained using conventional FS technique. Experiments involving the interaction of streptavidin protein with biotin functionalized 14.3 MHz QCR surface have been performed for using FFD and FS methods for quantitative validations of the resonant frequency and dissipation shifts. Experiments involving quick needle touches on self-assembled-monolayer immobilised AT-cut QCR surface have been demonstrated using FFD technique. Needle touch experiments on the same QCR were also performed using a commercial bench top network analyser for comparison of results obtained from FFD.
- Chapter 5 focuses on detection of small biomolecules (~199.2 Da) such as acylated Homoserine lactones (AHL), a biomarker for gram negative bacterial infections using FFD method.
- Chapter 6 focuses on detection of large biomolecules (~190 kDa) such as human immunoglobulin E (hIgE), an allergic biomarker using FFD method.
- Chapter 7 presents the conclusion and future work of this doctoral work.

Chapter 2

Review of current methods for measurement of resonant frequency and dissipation of a quartz crystal resonator

2.1 Introduction

The previous chapter reviewed the existing biomolecular recognition tools and highlighted the need for simplicity, online measurements, high time resolution and multiplexability. Depending on the above-mentioned need, a quartz crystal resonator (QCR), which is a commonly used mechanical resonator, has been selected as the potential tool for analysing biomolecular interactions [113]. A QCR is essentially a transduction platform and the method of mass measurement using resonant frequency shift of a QCR is termed as quartz crystal microbalance (QCM). As a label-free sensing method, QCM has attracted attention of the sensing community after surface plasmon resonance and electrochemical impedance spectroscopy in the last few decades. QCM is entirely electronic and can be suitably integrated into portable platforms. It has particular merit in addressing the need for low cost sensors, which require low skills and infrastructure, thereby fulfilling the need for rapid biomolecular detection. An overview of different QCR resonant frequency and dissipation measurement techniques has been presented in this chapter. Limitations in time resolution of different QCM analysers have been reported followed with a brief discussion on single frequency measurements. Such investigations provided the motivation for a novel work on analytical estimation of resonant frequency and dissipation of a QCR utilising a fixed frequency excitation. Such a method of estimation enhances the features of QCM by making it simpler and faster.

2.2 Electrical equivalent of a quartz crystal resonator

The Butterworth-Van Dyke (BVD) model [114] has been used to represent the equivalent electrical circuit for a commonly used thickness shear mode of an AT cut quartz crystal resonator. BVD model consists of two arms. The arm comprising resistance R , inductance L and capacitance C is termed as the motional arm. R , L and C represent the electrical equivalence of coefficient of viscous damping, inertia and shear compliance for an AT cut quartz crystal resonator [115]. Hence, the motional branch models the quartz crystal resonator (QCR) dynamics. The other branch consisting of parallel capacitance (C_0) is termed as the static arm. C_0 , also termed as shunt capacitance [116] models the parasitic electrical capacitance between the QCR electrodes [115]. In a modified BVD electrical circuit

(Figure 2.1), electrode electrical losses represented by resistance R_x is usually added in series with the traditional BVD circuit. However, such losses are negligible ($\sim 1-3 \text{ } \Omega$) [117] and are therefore, not considered in this thesis for modelling a QCR. Typical values of motional resistance, motional inductance, motional capacitance and shunt capacitance for Deionised (DI) water loading of a bare 14.3 MHz QCR were 225.4 Ω , 4.8 mH, 26 fF and 8.4 pF respectively.

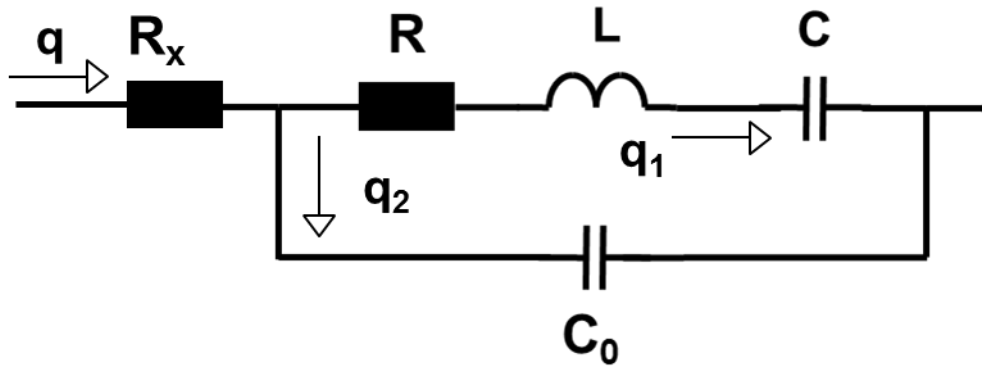


Figure 2.1. Modified Butterworth-Van Dyke model of a quartz crystal resonator (QCR)

2.3 QCR resonant frequency and dissipation quantification methods

Conventional methods based on oscillator circuits [85,118–121], frequency sweep analysis [46,115,122–126] and ring-down operation [81,127–129] have been used for measuring resonant frequency and dissipation of a quartz crystal resonator. Their principle and key relevant features are discussed in the following sections. The details of the interface electronics associated with each of the methods are beyond the scope of this dissertation and have not been included.

2.3.1 Oscillator circuits

Principle

Oscillator circuits are capable of producing alternating electrical waveforms including square or sinusoidal ones in absence of any alternating input electrical signal [130]. In general, an oscillator circuit consists of a resonator such as a quartz crystal and an amplifier [85] such as an operational amplifier [73], where the former forms a part of the feedback circuit (Figure 2.2). A quartz crystal acts as the resonant frequency determining element for an oscillator circuit. Resonant frequency of a QCR is actively interrogated using a frequency

counter or a frequency data acquisition card [131]. Frequency counters do not provide instantaneous estimation of QCR resonant frequency. QCR resonant frequency is estimated from calculation of the mean of the resonance frequencies obtained in a particular time interval.

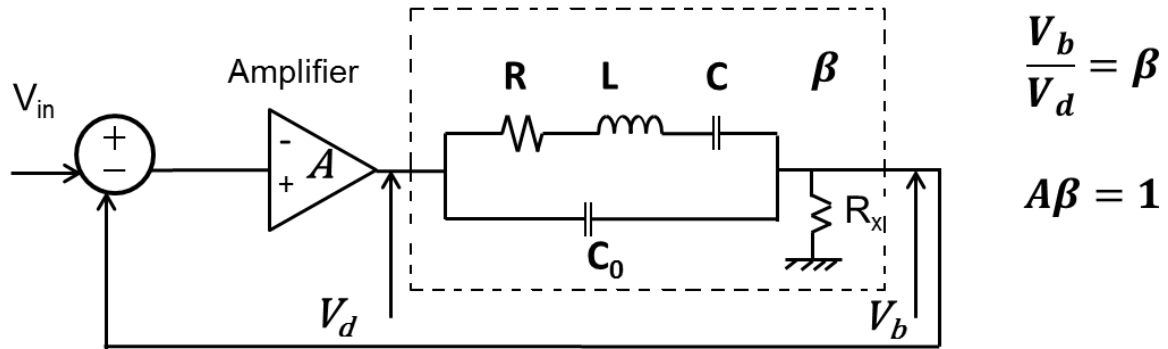


Figure 2.2. A simplified block diagram of a QCM oscillator circuit comprising an amplifier with gain A and a quartz crystal resonator (QCR) with feedback factor β [85].

Simplified oscillator circuits are not capable of measuring the dissipation factor. Hence, automated gain control unit [120] is installed in the oscillator circuit for quantification of QCR dissipation factor in addition to resonant frequency. The amplitude of QCR oscillation is altered due to loss of acoustic energy from damping. A self-sustained oscillation is achieved if the losses in the feedback circuit are compensated by the gain of the amplifier

and the phase shift of the feedback circuit is an integral multiple of 2π [85]. An automatic gain control (AGC) oscillator circuit maintains constant amplitude of oscillation of a QCR without altering its quality factor. Instead it alters the voltage applied by the oscillator circuit across QCR. The expression relating the AGC output voltage and QCR dissipation has been derived below.

Mean amplitude of motion () for an AT cut QCR surface [120] can be expressed as follows:

$$\dots\dots\dots (2.1)$$

where Q is the quality factor, d_{31} is the piezoelectric strain coefficient, which is equal to 1.25 for an AT cut QCR [132] and V_d is the QCR driving voltage. The expression for x can be written as follows [120]:

$$\dots\dots\dots \frac{\zeta}{\dots\dots\dots} \quad (2.2)$$

where ζ is the AGC circuit constant and $\dots\dots\dots$ is the amplitude adjusted voltage level. The ratio $\dots\dots\dots$ is termed as the unitless gain factor for an AGC amplifier. AGC circuit constant converts the gain factor into an equivalent voltage. Using Eq. (2.1) and Eq. (2.2), the expression of dissipation factor $\dots\dots\dots$ is given by:

$$\dots\dots\dots - \frac{\dots\dots\dots}{\zeta} \quad (2.3)$$

Hence, measurements of AGC output voltage $\dots\dots\dots$, amplitude adjusted voltage $\dots\dots\dots$ and unperturbed QCR oscillation amplitude provide the QCR dissipation factor.

Time Resolution

Time resolution for a QCR measurement is defined as the time taken for one measurement. Oscillator circuits usually take 1 second to measure the resonant frequency of a QCR [133,134]. For 1 sec measurement time, resonant frequency readings were obtained in distilled water for anti-corrosion cataphoretic painting coated 5 MHz QCR with a noise of 0.021 Hz [133]. Some oscillator circuits permit monitoring of resonant frequency and dissipation of QCRs every 100 ms with a noise reading of 0.1 Hz [73]. Minimum time per measurement for oscillator circuits can be reduced to 0.8 ms at the expense of complex electronic circuitry by using reciprocal frequency counters [135]. However, there is no experimental evidence of using oscillator circuits at 0.8 ms time resolution.

Advantages

Production of frequency analogue output signal from an oscillator circuit makes digital processing very convenient [115]. Inexpensive electronic circuitry, integration potential, and real-time monitoring are the important attributes associated with oscillator circuits [62].

Limitations

The estimation of dissipation factor from amplifier's gain factor is not very straight forward and needs use of separate instruments such as network analyser. Amplitude of oscillation of a QCR needs to be estimated prior to the start of any oscillator circuit measurements. The

oscillator circuits are optimized for a particular resonance mode or overtone and additional elements are needed for switching to other overtones, thereby making resonant frequency and dissipation measurements at multiple overtones cumbersome for users [85]. Use of oscillator circuits for a time resolution below 100 ms increases the complexity of circuitry.

2.3.2 Frequency sweep analysis

Principle

Evaluation of electrical characteristics of a QCR can be performed, employing electrical admittance, which is given by the ratio of current flow through QCR to the voltage applied across QCR [112]. Admittance analysis [136] is performed using a network analyser, where a QCR is passively interrogated around resonance by means of an oscillating voltage with variable frequencies. A QCR is subjected to a linear sweep frequency mode comprising a certain number of frequency data points and a particular frequency span, which leads to the construction of admittance-frequency curves [137]. Resonance condition is fulfilled at the frequency, where the real part of the admittance termed as conductance attains its maximum value. Such a method of estimation is also termed as frequency sweep (FS) technique. Alternatively, the admittance data is fitted with a known electrical equivalent model of QCR such as Butterworth Van Dyke [138] model in order to obtain the parameters such as resonant frequency and dissipation factor. Obtaining the resonance parameters including resonant frequency, dissipation factor, motional resistance, motional inductance and motional capacitance using fitting procedure is the most widely practised method for analysing biomolecular measurements. The numerical fitting procedure has been described in details in the next chapter of this dissertation.

Time Resolution

The frequency sweep analysis method requires a frequency sweep to have at least 50 frequency steps in order to achieve an acceptable quality of fit [83]. The time per frequency step needs to be inversely proportional to the resonance bandwidth, which is given by the ratio of resonant frequency to the quality factor for avoiding artifacts from transient ringing process [83]. A time resolution or time per measurement below 500 ms is hard to obtain with the conventional network analysers after taking into account these requirements [83]. Gores and co-workers have fabricated a cost effective network analyser for electrochemical applications such as deposition and dissolution of copper, wherein a frequency sweep has been performed in 200 ms for a 6 MHz QCR comprising a bandwidth of 20 kHz [124]. A

noise of 7 Hz has been reported for such a data acquisition rate. However, the information regarding actual measurement time including data acquisition followed with fitting of the obtained data is unknown. Seiko has commercialised a fast electrochemical QCM (EQCM) with a minimum time per measurement of 100 ms [139]. However, there is no experimental evidence of noise at such a speed.

Advantages

Frequency sweep analysis allows direct estimation of resonant frequency and dissipation factor from a numerical fitting of the complex admittance data obtained from a QCR. It is advantageous over methods involving oscillator circuits, when the experimental configuration is complicated. Such configurations include use of long cables or interference of anharmonic side bands with the measurements. The possible problems can be easily identified and diagnosed by the users through viewing the admittance curve in such circumstances. An oscillator circuit stops working under such conditions and users may not have any clue about the problems. A network analyser suffices the requirement of a comprehensive QCM sensor due to its large frequency range and various measurement criteria. Hence, resonant frequency and dissipation factor can be estimated for several resonance modes of a quartz crystal resonator. A network analyser permits QCM sensor characterisation in isolation and as a result, there is no effect of external circuitry on the electrical behaviour of a QCR. In addition, passive interrogation eliminates the parasitic electrical influences by means of calibration [140].

Limitations

Expensive electronic circuitry and large dimensions associated with a conventional network analyser hinder its use for remote and point of care sensing applications [120]. Such a configuration is suitable for analysing biomolecular interactions in laboratory environment. Large dimensions of the QCM instrument also limit the degree of multiplexing. It involves complex data management procedure due to the necessity for numerical fitting. The need for fitting also limits the time resolution of QCR measurements obtained using FS method. Multiple resonator measurements performed using single network analyser becomes challenging sometimes due to perturbation in instrument response [140].

2.3.3 Ring down analysis

Concept

Ring down technique has also been explored for simultaneous measurement of resonant frequency and dissipation factor [129]. It is also known as decay method [140] or impulse excitation method [115]. In ring down technique, the driving voltage of a QCR is periodically switched on and off at a frequency located in the vicinity of an actual resonant frequency. The amplitude of oscillation of a QCR experiences an exponential decay with time after the termination of driving voltage. The output voltage from a freely decaying QCR is recorded using a digital oscilloscope [23]. The frequency of the output voltage denotes the resonant frequency of a QCR. The resonant frequency and the decay time of the output voltage are obtained by numerically fitting the same with an exponentially damped sinusoidal oscillation which is given by [141]:

$$V(t) \approx A e^{-t/\tau} \sin(\omega t + \phi) \quad (2.4)$$

where A is the amplitude of the decaying sinusoidal curve at time $t=0$, ϕ is the phase angle and τ is the decay time. Decay time is defined as the time in which the amplitude of oscillation reduces to $1/e$ times the original value. The equation of motion [142] for an underdamped free vibration of a mechanical resonator can be expressed as follows

$$m \ddot{x} + b \dot{x} + kx = 0 \quad (2.5)$$

where x is the amplitude of motion at time t , ω_d is the damped natural frequency, ϕ is the phase angle and $\Delta\omega$ is the resonance bandwidth. Comparing Eq. (2.4) and Eq. (2.5), the expression of resonance bandwidth ($\Delta\omega$) in terms of decay time τ is given as:

$$\Delta\omega = \frac{1}{\tau} \quad (2.6)$$

The expression relating resonance bandwidth $\Delta\omega$, resonant frequency ω_r and dissipation of a QCR is given by:

$$\Delta\omega = \frac{\omega_r}{Q} \quad (2.7)$$

Using Eq. (2.6) and Eq. (2.7), dissipation factor Q can be written as follows:

Q-sense Company [23,54,86,143] has come up with an advanced QCM analyser based on the decay method and is termed as QCM-D (quartz crystal microbalance with dissipation monitoring) technique.

Time Resolution

Accounting for the averaging time in ring-down method, Petri, Johannsmann and co-workers have stated a time resolution of the order of 1 s [83]. The measurements can be faster but at the expense of increased noise [83]. Q-Sense reports the current capability of minimum time per measurement for ring down analysis as 5 ms. However, there is no available evidence of any reported data that demonstrates the noise at this data acquisition time period [84].

Advantages

Decaying QCR response obtained from ring down method is not affected by interface electronics due to disconnection of QCR from the driving power [144]. The ring down technique followed by the Q-Sense company allows simultaneous and direct measurement of resonant frequency and dissipation factor in succession at different overtones for a quartz crystal resonator with a fundamental frequency of 5 MHz. Measurements up to 13th overtone, i.e. 65 MHz can be performed using a QCM-D instrument.

Limitations

It is difficult to generate an impulse excitation in practice [115] as ideal pulse front slopes are hardly attainable. The necessity of fitting, followed with signal averaging limits the time resolution of measurements for ring down technique. The accuracy of ring down method depends on the accuracy of the measurement of frequency and the envelope of a decaying sinusoidal curve. Measurement of frequency and envelope becomes challenging during strong damping loads due to production of short decay times. It requires significant averaging for strong damping loads in order to achieve accurate estimates. The quality and overall dimensions of the equipment associated with the decay method also need to be high for accurate estimation of frequency from the envelope of an exponentially decaying sinusoidal curve. Use of high quality components make ring down technique quite expensive. Hence, QCM-D device is more suitable for experiments conducted using laboratory infrastructure [140]. Requirement for large dimensions impose restriction on degree of multiplexability.

2.4 Summary of challenges of conventional methods

Conventional methods such as frequency sweep analysis and ring down operation are able to report measurements of resonant frequency and dissipation factor at numerous resonance modes with ease. However, the time resolution of a single resonant frequency or dissipation factor data point is still constrained for the state-of-the art QCM analysers due to the need for fitting or averaging. There is usually a trade-off between the data acquisition time period and noise. The lowest reported time resolution using admittance analysis method is 100 ms [139]. However, it is only applicable for electrochemical applications. There is no reported evidence of using ring down technique at its minimum measurement time of 5 ms for any application [84]. Use of conventional instruments for frequency sweep and ring down methods such as frequency synthesizer and impulse generator add complexity to the measurement setup. Although, QCR quantification method using oscillator circuits is relatively simpler, there is no reported documentation on its use for measuring processes occurring in ms time scale.

2.5 Idea of single frequency measurement of quartz crystal resonator: A path ahead

2.5.1 Background

Petri, Johannsmann and his fellow workers reported a new method of sequentially acquiring quick time traces (10 ms) of electrical admittance for a set of constant frequencies located in the vicinity of QCR resonant frequency. The purpose of the method was to deal with the problems related to speed of measurements [83]. The number of frequencies used for the analysis was ~ 10 . A frequency sweep was performed prior to the fixed frequency traces for estimating the resonant frequency of the quartz crystal resonator. Subsequently, deviations in real and imaginary components of the admittance data namely conductance and susceptance for different fixed frequencies were calculated with respect to a measured reference. Estimated shifts in conductance and susceptance were numerically fitted to a phase shifted Lorentzian function for obtaining resonant frequency and dissipation at multiple resonance modes [83] of a 5 MHz QCR. A minimum time per measurement of 10 ms was reported with noise readings of 0.3 and 0.01 Hz for experiments related to copper and electrically conducting polymer films respectively. The new method provided faster estimation of resonant frequency and dissipation through numerical fitting of the admittance

data obtained from single frequency measurements instead of a conventional frequency sweep, thereby adding robustness to the method.

2.5.2 Limitations of single frequency measurement method

Although, the single frequency measurement method provides 10 ms time resolution, it is applicable only for studying stable and repetitive electrochemical processes, such as square wave amperometry and cyclic voltammetry. There are certain transient processes which could not be repeated in a reasonable time. Biomolecular events, such as protein folding [76] or activation of G-protein-coupled bioreceptors [78], which control important biological functions, are not repetitive processes, and require millisecond time resolution. Studying these processes is critical to the understanding of mechanisms of critical diseases, including cognitive, neurological, cardiovascular or endocrinal. Important studies related to surface science field such as gas to surface adsorption and desorption processes dynamics [145], occurring in sub-millisecond time scale are often transient in nature. State-of-the-art single frequency measurement method for a QCR cannot be utilised to investigate the above-mentioned processes. The single frequency measurement method works in a narrow region around a resonance. Hence, there is a need for a new method utilising single frequency measurement, which will address the above limitations and achieve the need for simplicity and high time resolution.

2.6 Prelude to fixed frequency drive method

A novel analytical method of estimation of resonant frequency and dissipation factor of a QCR based on single frequency measurement has been reported in the next chapter. The novel method is termed as the fixed frequency drive (FFD) method as real-time measurements of resonant frequency and dissipation can be obtained by continuously driving a QCR at a fixed frequency. A time resolution of 112 μ s has been achieved employing the FFD method. The method eliminates the need for any numerical fitting or averaging, thereby aiding in simplicity, low cost and online integration. The method works over a broad resonance bandwidth. The method can be utilised for investigation of any surface binding processes and is not limited for studying stable and repetitive electrochemical processes unlike the single frequency measurement method. The method has an intrinsic ability to multiplex without an increase in complexity or cost.

Chapter 3

Fixed Frequency Drive Method– Going beyond the state of the art

3.1 Introduction

A novel method of quantification of quartz crystal resonator (QCR) resonant frequency and dissipation employing Butterworth Van Dyke model [112] has been introduced here. The new method does not require any frequency sweep or impulse excitation and instead utilises a fixed frequency excitation for estimation of QCR resonant frequency and dissipation factor. The new technique has been validated through experiments, which are reported in Chapter 4.

3.2 Fixed Frequency Drive Theory

3.2.1 Estimation of resonant frequency

According to the BVD model [114], the impedance of the motional arm of a QCR can be written as:

$$Z_m = \frac{j\omega L_m}{1 - \omega^2 L_m C_m} + \frac{R_m}{1 - \omega^2 L_m C_m} \quad (3.1)$$

where ω is the angular drive frequency and $\omega_0 = \frac{1}{\sqrt{L_m C_m}}$. During resonance, the motional impedance becomes entirely resistive. Hence, the motional reactance, given by $\frac{j\omega L_m}{1 - \omega^2 L_m C_m}$, is diminished which expresses the angular resonant frequency (ω_0) of the motional arm as:

$$\omega_0 = \frac{1}{\sqrt{L_m C_m}} \quad (3.2)$$

where $Z_0 = \sqrt{\frac{L_m}{C_m}}$ is the characteristic wave impedance. From Eq. (3.2):

$$\omega_0 = \frac{1}{\sqrt{L_m C_m}} \quad (3.3)$$

$$\text{---} \quad (3.4)$$

Using Eq. (3.3) and Eq. (3.4) for substitution of L and C in Eq. 3.1, then:

$$\text{---} \quad (3.5)$$

$$\text{---} \quad (3.6)$$

From Eq. (3.6) the motional reactance can be written as:

$$\text{---} \quad (3.7)$$

Solving Eq. (3.7) for ω :

$$(3.8)$$

Thus:

$$\text{---} \quad (3.9)$$

Eq. (3.9) depicts the expression for QCR resonant frequency as a function of the drive frequency and electrical equivalent circuit parameters such as the motional reactance and the characteristic wave impedance. If the characteristic wave impedance is measured at the outset and the QCR is driven at a fixed frequency, then the resonant frequency can be determined from Eq. (3.9) using the motional measured reactance. In order to avoid, mathematically unfeasible solution, the expression of ω is chosen as the following:

(3.10)

3.2.2 Estimation of characteristic wave impedance and shunt capacitance

The equivalent electrical impedance measured from an experiment takes into account the impedance contribution arising from the shunt capacitance, which is given by

Eq. (3.10). The shunt capacitance and the characteristic wave impedance are estimated only once at the beginning of an experiment by fitting the impedance measured from a frequency sweep with the equivalent impedance estimated using the BVD model. The shunt capacitance can also be obtained at much lower frequency in comparison to fundamental resonant frequency of a QCR, where the admittance of the motional branch can be neglected. This shunt capacitance (C_0) is then used to determine the motional reactance from the equivalent motional impedance (Z_m) measured in a fixed frequency drive scan as shown in Eq. (3.10) and used in Eq. (3.10) along with the characteristic wave impedance to determine the resonant frequency. The difference of the resonant frequency with respect to the drive frequency (Δf), after eliminating large values inside bracket, is given by:

(3.11)

Inertial or elastic loading on the resonator changes the inductance or capacitance of the equivalent circuit. Thus, it shifts the resonant frequency (f_r) which is indicated by Eq. (3.2). If the resonator is driven at a fixed frequency close to its initial resonant frequency, then the shift in resonant frequency during a process can be determined by calculating the frequency offset from Eq. (3.11), using the measured reactance. Although the characteristic impedance changes with shift in resonant frequency, it can be assumed to be constant in

3.3 Determination of quality factor of quartz crystal resonator in liquid

(3.12)

(3.13)

3.4 Error in resonant frequency shift estimate when characteristic wave impedance is assumed as constant

impedance $\cdot \frac{\rho}{\rho}$ using Eq. (3.2) can be written as:

[illegible]

$$\dots\dots\dots - \quad - \quad (3.15)$$

Using Eq. (3.14) and Eq. (3.15):

$$\begin{array}{c} \text{****} \\ \text{---} \end{array} \quad \text{---} \quad (3.16)$$

A quartz crystal resonator (QCR) with an initial resonant frequency of 14.3 MHz and an initial characteristic wave impedance (Z_0) of 400 k Ω (as depicted in Section 3.3) has been considered. The drive frequency is also chosen as 14.3 MHz, such that the frequency offset indicates the resonant frequency shift along with the progress in mass binding. The values of reactance have been chosen from -2000 to 2000 Ω with a gradual increase of 10 Ω . The 'true' resonant frequency shift is evaluated by first determining the 'approximate' Δf from Eq. (3.11). An assumption of $\Delta f \ll f_0$ has been considered for the chosen values of reactance. Thereafter, the 'true' Δf is estimated from Eq. (3.16) using the approximate Δf , i.e. $\Delta f_{true} \approx \Delta f_{approx}$. Finally using this 'true' Δf in Eq. (3.11), the error between the 'true' and the 'approximate' Δf , and the percentage of error with respect to the approximate Δf , have been calculated (Figure 3.1).

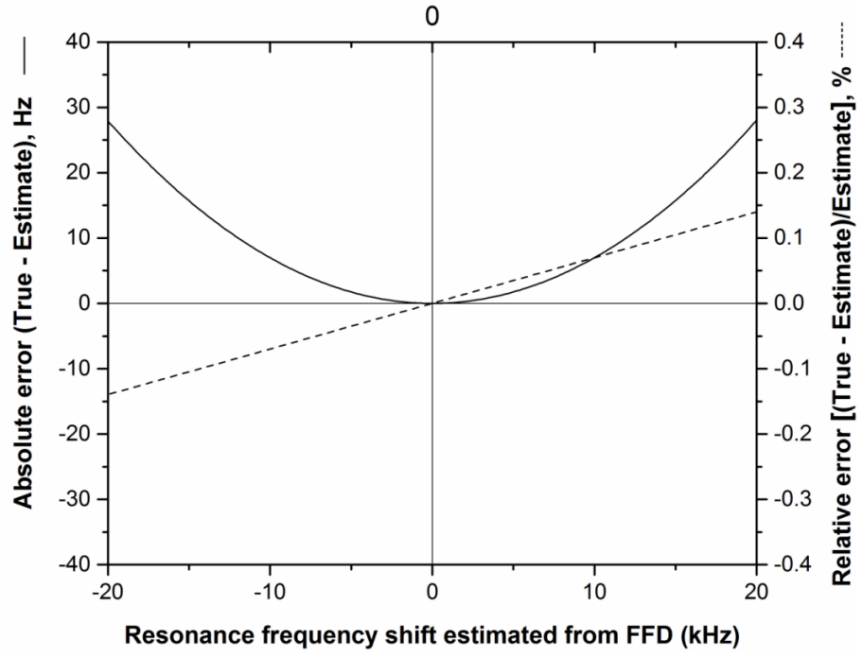


Figure 3.1. Error of the resonant frequency shift estimate (assuming the characteristic impedance is constant) with respect to the ‘true’ estimate (considering change in characteristic impedance).

It can be evidenced from Figure 3.1 that the error and % error are approximately 0.9 Hz and 0.025% for a resonant frequency shift of 3.57 kHz, which is typically one resonance half-bandwidth considering a quality factor of 2000 (— — —). Since the resonant frequency shift in the case of inertial loading is within the resonance half-bandwidth for most of the cases, (e.g. protein binding), the characteristic impedance can be assumed to be constant without affecting the accuracy of estimation of resonant frequency in practice. However, there is a need for accurate calibration to meet the above-mentioned estimated error in practice.

3.5 First and second order series approximation of the resonant frequency offset

The expression of resonant frequency offset in terms of the driving frequency, the characteristic wave impedance and the motional reactance is given by Eq. (3.11). In Eq. (3.11) is obtained from experiments by driving the quartz crystal resonator at a fixed frequency. Considering the drive frequency as an initial resonant frequency, the

resonant frequency shift due to mass or viscous loading can be estimated from Eq. (3.11). However, the expression of resonant frequency offset (i.e. Eq. (3.11)) is a radical expression consisting of square root term which makes data processing less convenient. Hence, the expression is simplified by applying series approximation. The first order Maclaurin series approximation of this offset is expressed as:

$$\Delta f = \frac{1}{2} \frac{\Delta Z}{Z_0} f_0 \quad (3.17)$$

The second order Maclaurin series approximation after discarding the term $\frac{1}{2} \frac{\Delta Z}{Z_0} f_0$ under radical in Eq. (3.11) is given as:

$$\Delta f = \frac{1}{2} \frac{\Delta Z}{Z_0} f_0 + \frac{1}{8} \left(\frac{\Delta Z}{Z_0} \right)^2 \frac{f_0^3}{Z_0} \quad (3.18)$$

The approximate form as in Eq. (3.18) can be used in place of the exact expression of Eq. (3.11) for all practical purposes.

$$\Delta f = \frac{1}{2} \frac{\Delta Z}{Z_0} f_0 + \frac{1}{8} \left(\frac{\Delta Z}{Z_0} \right)^2 \frac{f_0^3}{Z_0} \quad (3.19)$$

The relative errors of the linear () and second order () series approximations have been determined with respect to the exact formula for frequency offset (i.e. Eq. (3.11)) by considering the initial resonant frequency as 14.3 MHz, and the characteristic wave impedance as 400 kΩ (as discussed in Section 3.3). This is presented in Figure 3.2.

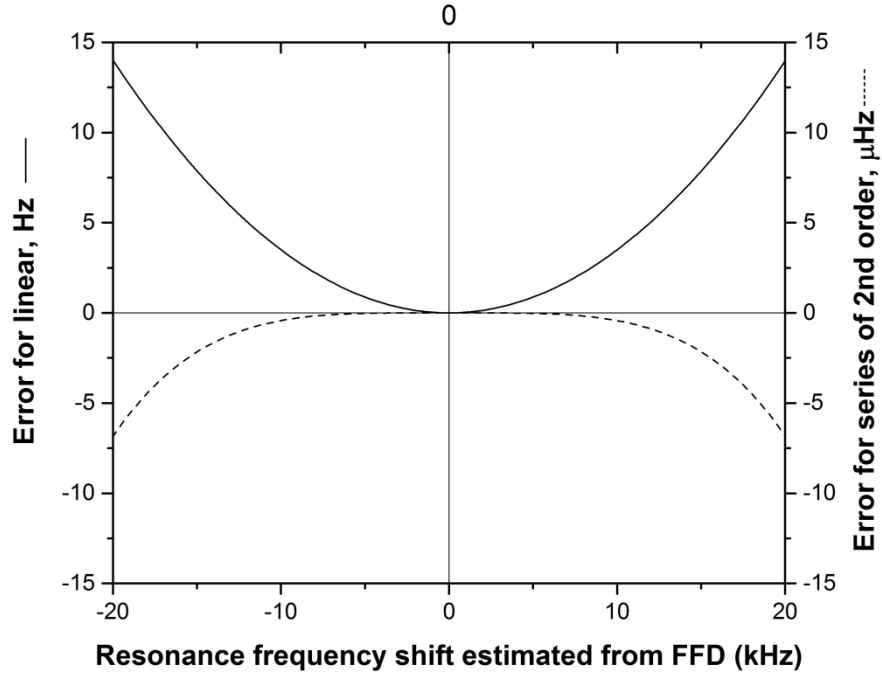


Figure 3.2. Error of the expressions for first and second order approximations of the frequency offset with respect to the exact expression (Eq. 3.11).

Taking into account, the linear expression for frequency offset, an error of 0.5 Hz has been obtained for a resonance frequency shift of 3.57 kHz. Such an error is negligible, considering the fact that the estimated resonant frequency shift (i.e. 3.57 kHz) is within the resonance bandwidth (i.e. 7.14 kHz) for most of the cases. An error of approximately 7 μHz is obtained for a resonant frequency shift of 20 kHz (~ 2.8 times resonant frequency bandwidths) by considering the second order approximation. Hence, use of second order approximation for frequency offset expression eliminates the use of radicals and aids in maintaining a good accuracy at the same time. Such an expression also favours processing of experimental data using a simple and inexpensive microprocessor.

3.6 Dissipation shifts using fixed frequency drive method

The quality factor of an electrical equivalent circuit is given by (Section 3.3). The dissipation factor is, therefore, given by:

$$(3.20)$$

As the characteristic wave impedance can be considered as constant (Section 3.4), the dissipation and its shifts for a process can be estimated from Eq. (3.19) by monitoring the

motional resistance from a fixed frequency drive. Motional resistance is calculated from the real part of motional impedance using Eq. 3.5. Motional impedance is estimated after deduction of the impedance of shunt capacitance from the equivalent impedance of a QCR, obtained using a custom made network analyser.

3.7 Intrinsic advantages of FFD

- The fixed frequency drive (FFD) method allows purely analytical estimation of resonant frequency and dissipation factor from each impedance data point measured using a continuous drive for a particular time interval. The method is applicable for studying any physical processes unlike the single frequency measurement method which is valid only for stable and repetitive electrochemical processes. There is no need for any numerical fitting for estimation of resonance parameters as in frequency sweep or ring down methods. There is not any necessity for averaging of FFD estimates unlike ring down method. The method has high time resolution feature which has been illustrated in the next chapter.
- The driving frequency does not need to be located in the vicinity of the QCR resonant frequency. The driving frequency can be situated several resonance bandwidths apart the resonant frequency without sacrificing the accuracy of estimation. The range of driving frequency for a 14.3 MHz QCR is selected as ± 20 kHz (Figures 3.1 & 3.2), which is approximately 2.8 resonance bandwidths (—) away for application in liquid (for $Q = 2000$) and more than 75 bandwidths for application in air (for $Q > 54000$).

3.8 Limitation

The BVD model accounts for a single mode of resonance. The influence of satellite or spurious modes [146] can affect the accuracy of FFD estimate, if the drive frequency is within the bandwidth of a satellite mode (Section A.10). Hence, it is practically safe to drive at resonance if the location of the satellite mode is unknown. The details of the location of spurious modes under deionised (DI) water loading for five different 14.3 MHz QCRs for fundamental and 3rd overtone modes have been mentioned below in Section A.10. The peak of the fundamental resonance mode is located approximately 79.17 kHz (SD, 1.59 kHz) away from the peak of the nearest satellite mode under DI loading for a 14.3 MHz QCR. Considering a resonance half bandwidth of 3.57 kHz for fundamental mode, it is safer to drive the QCR anywhere within 22 resonance half-bandwidth in order to avoid the influence of spurious mode. In case of a 3rd overtone mode, they are located approximately 45.42 kHz (SD, 1.26 kHz) away from each other under DI water loading. Considering a resonance half bandwidth of 6.18 kHz for 3rd overtone mode (Section A.9), it is safer to drive the QCR anywhere within 7 resonance half bandwidth in order to avoid the influence of spurious modes.

In certain situations, the resonant frequency shift due to binding is larger than the resonance bandwidth at a particular mode of resonance and there can be potential interference by satellite modes. This is not a practical issue for the fundamental mode as the half bandwidth of QCRs typically used for biomolecular measurements (~0.68 kHz for 5 MHz QCR from theory, ~3.57 kHz for 14.3 MHz QCR obtained from experiments) are considerably higher than the shifts observed in most experiments (<2 kHz). But, the fundamental resonant frequency shift due to binding of amyloid precursor protein with monoclonal DE2 antibodies immobilised 19.5 MHz QCR after 450 sec is approximately 2 kHz [147]. The half resonance bandwidth at the fundamental mode of 19.5 MHz QCR under liquid loading is approximately 5.2 kHz (Table A.2), which is less than the resonant frequency shift. However, the seventh overtone resonant frequency shift due to amyloid precursor protein binding will be approximately 14 kHz (Section A.3) which is more than the half resonance bandwidth (~13.76 kHz) (Table A.2) at the same mode. In such cases, there can be significant influence of satellite modes and BVD model cannot be used for estimation of resonant frequency for FFD technique. Hence, resetting the driving frequency to the modified resonant frequency at the time of FFD scan will help in eliminating the effect of spurious modes.

3.9 Conclusion

FFD method utilises a Butterworth-Van Dyke model for analytical estimation of resonant frequency and dissipation factor from experimentally measured values of reactance and resistance respectively at a fixed frequency drive. Such a method potentially favours high time resolution measurements, which have been demonstrated in the next chapter. The estimates of FFD hold well over a wide resonance bandwidth (Section 3.4). Although the physical processes occurring on the surface of a QCR, such as binding, lead to slight variation in the characteristic wave impedance, its effect on resonant frequency and dissipation is negligible (Section 3.4). Hence, characteristic impedance measured at the beginning of the physical process can be used throughout for estimation of resonant frequency and dissipation shifts using FFD technique. The practical range for driving frequency selection does not depend on QCR quality factor, but the accuracy of estimate of the value of shunt capacitance, which relies on an accurate calibration.

Chapter 4

Experimental validation of Fixed Frequency Drive method

4.1 Introduction

The previous chapter focused on the theory behind fixed frequency drive technique. Based on the presented theory, validation of quantitative estimates of resonant frequency and dissipation against frequency sweep method were performed for inertial and viscous loadings. This experimental validation is presented in this chapter. Binding of streptavidin protein to a biotinylated QCR surface was studied for demonstration of inertial loading. Viscous loading was studied by flowing two liquids of different absolute viscosities (methanol and deionised water) one after another over a bare QCR surface. The latter part of this chapter focuses on noise analysis and time resolution of the resonant frequency shift measurements obtained using the FFD method.

4.2 Experimental hardware

4.2.1 Instrumentation

The hardware of the vector network analyser used for all experiments in this thesis was designed and built by Mr. Victor P. Ostanin, a retired Senior Technical Officer from the Department of Chemistry, University of Cambridge. The author contributed towards providing user feedback information for development of the instrument. The instrument is capable of driving with a wide range of amplitude (0 to 26 V) and frequency (RF 100 kHz to 300MHz) and recording complex (in-phase and quadrature) current and voltage at three different frequencies simultaneously. There are three driving modes available in the instrument namely linearly varying frequency mode subjected to constant amplitude (used for frequency sweep method), linearly varying amplitude mode subjected to constant frequency and constant amplitude and frequency mode (used for FFD method). The development of graphical user interface was performed by Dr. Alex Zhukov from the Department of Chemistry, University of Cambridge, followed with an installation on a PC for effective communication with the instrument. Wolfram Mathematica¹⁰ was utilised for data analysis. A controlled and measured delivery of liquid sample over the QCR surface was performed employing a syringe pump (Harvard Apparatus).

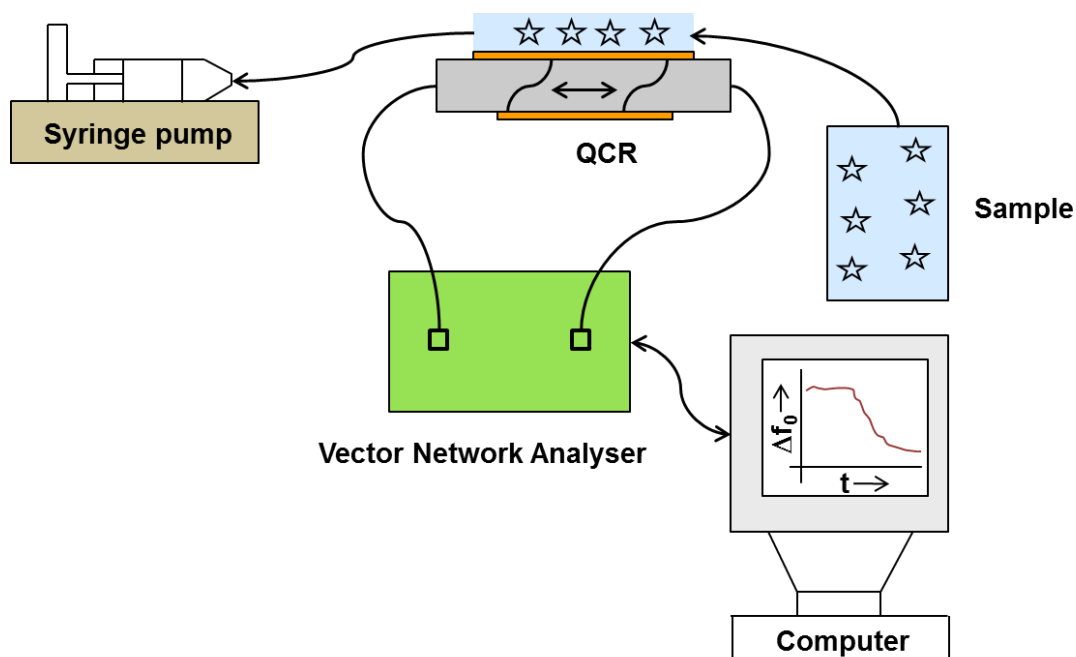


Figure 4.1. Schematic of the experimental set up (Not to scale)

4.2.2 Sensor Assembly

The sensor assembly [148] consisted of three main parts namely a microfluidic cartridge, a quartz crystal resonator (QCR) or the sensor and a printed circuit board (PCB) (Figure 4.2). An exploded cross-sectional view involving all the sub-parts is presented in Figure 4.2-ii. The description of the different parts of the sensor assembly has been provided below.

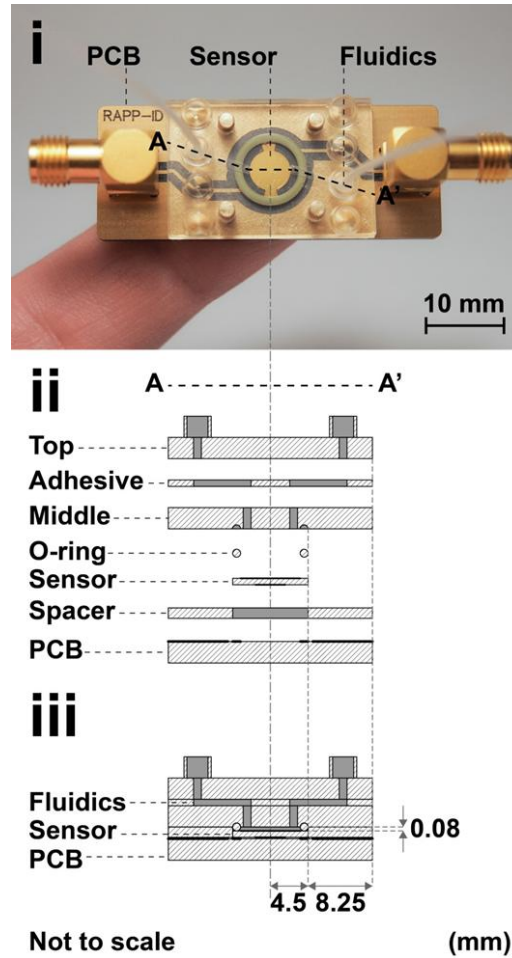


Figure 4.2. i) Top view of an assembly of a sensor between a microfluidic cartridge and a PCB. ii) An exploded cross-sectional (A-A') illustration iii) A cross-sectional illustration of a fully assembled sensor [36]

Microfluidic cartridge

The microfluidic cartridge used in this work was designed by Dr Niklas Sandström of Micro and Nanosystems laboratory of KTH Royal Institute of Technology (Stockholm, Sweden) (PI: Prof Wouter Wijngaart) as part of a EU consortium project, Norosensor, of which Loughborough University was a partner (PI: Dr Sourav Ghosh). The cartridge comprised two injection molded cyclic olefin copolymer (COC) slides (Microfluidic ChipShop GmbH, Germany). The COC slides were bonded together by a medical-grade ARcare® 90106 double-sided pressure-sensitive adhesive (Adhesive Research Inc., Ireland). The top COC slide contained integrated mini-luer connectors which favors fluidic interfacing. The silicone gaskets composed of tube stubs were fitted inside the connectors, which provided tight liquid sealing with use of external tubing. The milling of bottom COC slide provided inclusion of two

vertical fluidic interconnects which served as inlet/outlet to the sample chamber above the QCR, and a circular trench. The trench is centered on the bottom side which allowed insertion of UPS VI classified EPDM O-ring (Trelleborg AB, Sweden). Patterning of microfluidic channels in the adhesive film was performed using CNC cutting. Such channels connected the mini-luer connectors with the two vertical interconnects.

Quartz Crystal Resonator

14.3 MHz AT-cut thickness-shear mode quartz crystal resonators were purchased from Laptech Precision Inc., Bowmanville, Ontario, Canada. The diameter and thickness of QCRs were 8.3 mm and 115 μm respectively. The quartz substrate was sandwiched between two circular gold electrodes. The diameters of top and bottom electrodes were 5 mm and 4 mm respectively. A wrap around top electrode was provided for ensuring electrical connection from the bottom. The operating temperature range of the QCRs varied from 20° to 40°C.

Printed Circuit Board

The printed circuit board (PCB) was designed by Niklas Sandström of Micro and Nanosystems laboratory of KTH Royal Institute of Technology (Stockholm, Sweden) [36] to electrically connect the QCR electrodes. A standard FR4/Cu PCB laminate comprising a 1 μm Au layer and a 0.1 μm TiW adhesion layer was used for experiments. Sputtered of TiW layers provided a non-oxidizing metal surface which is beneficial for repeated electrical contact. Patterning of the PCB with isolated electrical lines and neighboring grounded areas were performed with CNC milling [36]. This provided contact pads for the QCR and conductive lines, leading to two SMA coaxial connectors, which are soldered at each end of the board. The PCB consists of four drilled holes which were utilized for insertion of straight brass pins. The brass pins acted as alignment structures while performing the assembly of the cartridge. Alignment of a polycarbonate spacer above the patterned PCB surface was performed using the brass pins. The spacer contained a central hole which was patterned using CNC milling. Such an operation aids in fitting and aligning the QCR during final assembly.

During assembly, the QCR was placed in the centered hole of the spacer on the PCB for providing contact of the bottom QCR electrode with the electrical contact pads patterned on the PCB. After that, the microfluidic cartridge was fixed on top of the QCR and the PCB by use of clamps, thereby forming a 3 μL sample chamber above the QCR. The spacer acted as a physical stop during clamping of different parts, which limited the maximum pressure

applied on the QCR. A quality factor of ~ 2000 was obtained in liquid during assembled condition. Such a quality factor suggested minimal damping due to the O-ring.

4.3 Comparative analysis of FFD and frequency sweep for inertial loading experiments

The inertial loading experiments were performed for the validation of the theoretical expression of resonant frequency shift (Eq. 3.10) obtained using FFD method with frequency sweep method. Demonstration of the inertial loading was performed by conducting a protein binding experiment. A 14.3 MHz AT-cut thickness-shear-mode QCR was immobilised with a mixture of self-assembled monolayer (SAM) of biotin and methoxy thiols (Figure 4.3). Streptavidin protein solution was flowed over the SAM immobilised QCR surface in order to facilitate binding of streptavidin with biotin [149]. The QCR was actuated and sensed electrically using a dedicated network analyser.

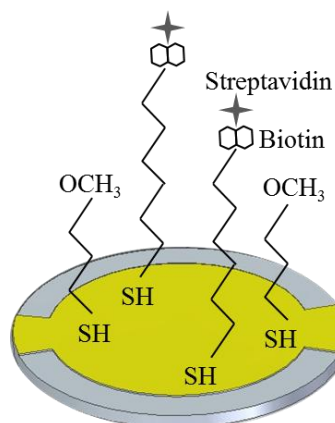


Figure 4.3. Streptavidin binding to biotin-thiol functionalised on a gold electrode surface of a QCR (Not to scale)

4.3.1 Reagents

Acetone, isopropanol, ultra-pure 200-proof ethanol, phosphate buffered saline (PBS) and streptavidin (60 kDa) were procured from Sigma-Aldrich (UK). PBS is composed of 8.1 mM Na_2HPO_4 , 1.1 mM KH_2PO_4 , 1 mM MgCl_2 , 2.7 mM KCl, and 138 mM NaCl with a pH of 7.4. Deionised (DI) water was collected from a Milli-Q Integral system, Millipore, USA. Thiolated alkane solutions, namely $\text{HS}-(\text{CH}_2)_{11}\text{-EG6-Biotin}$ and $\text{HS}-(\text{CH}_2)_{11}\text{-EG3-OCH}_3$, were purchased from ProChimia (Poland).

4.3.2 Protocol for cleaning of QCR

The QCR was placed in a Petri dish and cleaned in acetone for 5 min using ultrasonication technique. Thereafter, the QCR was cleaned in isopropanol in a similar way for 10 min. The QCR was then dried using a flow of nitrogen gas followed with further cleaning using argon plasma for 45 seconds. A Harrick Plasma Cleaner was used for plasma cleaning operation. The power level of the plasma cleaner was 29.6 W.

4.3.3 Protocol for formation of self-assembled monolayer of thiol on QCR

Cleaned QCRs were placed in 24-well plate and suspended in 250 μL of 1 mM ethanolic solution of thiols comprising 10% biotin thiol ($\text{HS}-(\text{CH}_2)_{11}\text{-EG6-Biotin}$) and 90% methoxy thiol ($\text{HS}-(\text{CH}_2)_{11}\text{-EG3-OCH}_3$) by volume for approximately 18 hours. As a result, self-assembled monolayer (SAM) of thiols was formed on the QCR surface.

4.3.4 Protocol for baseline preparation

Baseline refers to the phase before the introduction of measurand or analyte (i.e. streptavidin in this case) to the functionalised sensor surface. Baseline measurements are usually performed by exposing a QCR surface to a buffer medium. Establishment of a stable baseline is necessary for accurate measurements of analyte. The steps needed for baseline preparation have been described below.

Any loosely bound thiol layer on QCR surface after the immobilisation step was removed through a series of ethanol and DI water washes. The SAM immobilised QCR was then dried using nitrogen gas assembled between a microfluidic cartridge made of cyclic olefin copolymer, to ensure controlled delivery of sample, and a printed circuit board to permit electrical connection (Figure 4.2). 1 mL of DI water was flowed over a QCR (at 100 $\mu\text{L}/\text{min}$) using a syringe pump. Subsequently, phosphate-buffer-saline (PBS buffer) was flowed over the functionalised QCR (at 40 $\mu\text{L}/\text{min}$) for 10 min in order to achieve a stable baseline.

4.3.5 Method of Drive

Frequency sweeps (0.1 sec, 0.52 V) and fixed frequency scans (0.1 sec, 0.52 V) were taken at an interval of 2 min in phosphate buffered saline (PBS) for 10 min after establishing a baseline. 2.5 $\mu\text{g}/\text{mL}$ streptavidin solution in PBS was then flowed (at 40 $\mu\text{L}/\text{min}$) into the microfluidic cartridge to facilitate binding for 10 min. Similar frequency sweeps and fixed frequency scans as mentioned above were then taken for 10 min at the end of the binding

phase. In total, there were six measurement points in both baseline and binding phases. The method of estimation of resonant frequency and dissipation factor using frequency sweep and fixed frequency drive techniques have been described in the following sections.

Frequency sweep estimates

A linear frequency sweep mode, comprising a central frequency around 14.3 MHz (14.299491 MHz as an example) and a span of 0.02 MHz was performed for 0.1 s. The amplitude of oscillation was ~ 0.47 V. A 0.1 s frequency sweep consists of 763 data points. For each frequency sweep taken in baseline and binding phases, resonant frequency f_r , motional resistance R_m , quality factor Q and shunt capacitance (C_p) were estimated by numerically fitting the experimentally obtained equivalent electrical impedance data (Z) with a mathematical expression of equivalent QCR impedance based on BVD model (Figure 2.1). The expression takes into account the contribution of shunt capacitance and is derived using Eq. (3.6), which is given by:

$$\frac{1}{Z} = \frac{1}{R_m + j\omega L_m + \frac{1}{j\omega C_p}} \quad (4.1)$$

where ω is the driving frequency and $j = \sqrt{-1}$. The initial guesses for the fitting parameters involving resonant frequency f_r , motional resistance R_m , quality factor Q and shunt capacitance (C_p) were 14.3 MHz, 240 Ω , 1800 and 9 pF respectively. The typical values of resonant frequency, motional resistance, quality factor and shunt capacitance obtained from a frequency sweep comprising driving frequencies ranging from 14.289491 to 14.309491 MHz of a phosphate buffered saline loaded 14.3 MHz SAM functionalised QCR surface were 14.299573 MHz, 232.14 Ω , 1790.15 and 9.12 pF respectively. Dissipation factor for each measurement point was estimated by taking the reciprocal of the obtained quality factor from the fit.

Fixed frequency drive estimates

The resonant frequency ($f_{r, \text{PBS}}$) and the characteristic impedance ($Z_{0, \text{PBS}}$) of a QCR were estimated in PBS medium, employing frequency sweep method. Such estimates were obtained just before the baseline phase by taking the mean of three successive measurements as they were relatively close to each other (SD, 0.65 Hz). At each baseline and binding measurement point, following the frequency sweep, fixed frequency scans were taken successively at 5 different drive frequencies spanning ~84% of

the resonant frequency bandwidth namely ω_{PBS} kHz, ω_{PBS} kHz, ω_{PBS} , ω_{PBS} kHz and ω_{PBS} kHz. FFD scans were taken at five different frequencies in order to test the applicability of the method over a wider bandwidth. The calibrated reactance of the motional branch of a QCR () from each fixed frequency scan and the previously measured characteristic impedance in PBS (ω_{PBS}) were used to determine the resonant frequency at every measurement point (Eq. (3.10)). The calibrated resistance of the motional branch of a QCR () from each fixed frequency drive and characteristic impedance measured just before the baseline phase (ω_{PBS}) were used for the estimation of dissipation factor from each measurement point (Eq. 3.19).

4.3.6 Inertial loading results

Biotin-streptavidin binding experiments were conducted for three different QCRs for validation of FFD estimates such as shifts in the nominal resonant frequency and dissipation with frequency sweep (FS) technique for demonstration of inertial loading. The word nominal has been applied before resonance frequency and dissipation due to use of different QCRs and analyte samples under nominally similar conditions. The nominal resonant frequency shifts for FFD and FS techniques were calculated by deducting the value of resonant frequency obtained in the respective first baseline measurement point from all the subsequent measurement points including the same. The nominal dissipation shifts were calculated in a similar manner and divided by the dissipation value of the first measurement point in respective baseline phases for obtaining a quantitative estimate of relative dissipation shifts for each method. The mean of nominal resonant frequency and relative dissipation shifts for all drive frequencies with respect to the respective reference points (i.e. first baseline point) were calculated to obtain the measurement points for the “Average FFD method”. The quantitative formula of fixed frequency drive method (Eq. 3.9) was also applied to each of the frequency sweep scans as during a frequency sweep; the QCR is excited at multiple driving frequencies subsequently within a short span of time.

There was negligible variation in absolute resonant frequency values estimated using FFD method for those multiple driving frequencies with respect to the absolute resonant frequency value estimated from frequency sweep method for a thiolated QCR surface in PBS (Figure 4.4). Average of all the individual resonance parameters (nominal resonant frequency and dissipation) was taken to obtain the respective final values. Such a method of obtaining QCR resonance parameters is termed as “Average FFD from FS” (Figure 4.5). The resonant frequency shifts estimated from FS and FFD methods at each measurement point

showed satisfactory agreement over the baseline and streptavidin-bound phases for all 5 drive frequencies (Figure 4.5). There were hardly any variations in relative dissipation due to binding of streptavidin (Figure 4.5).

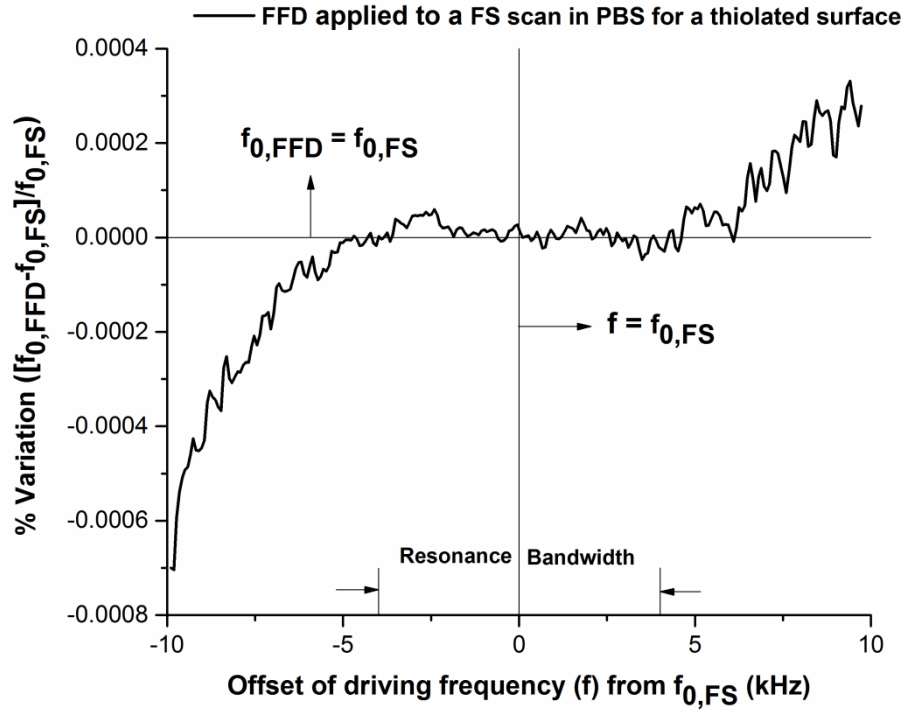


Figure 4.4. Percentage variation in absolute resonant frequency obtained from FFD method at different drive frequencies within a frequency sweep with respect to that obtained using evaluation of a frequency sweep

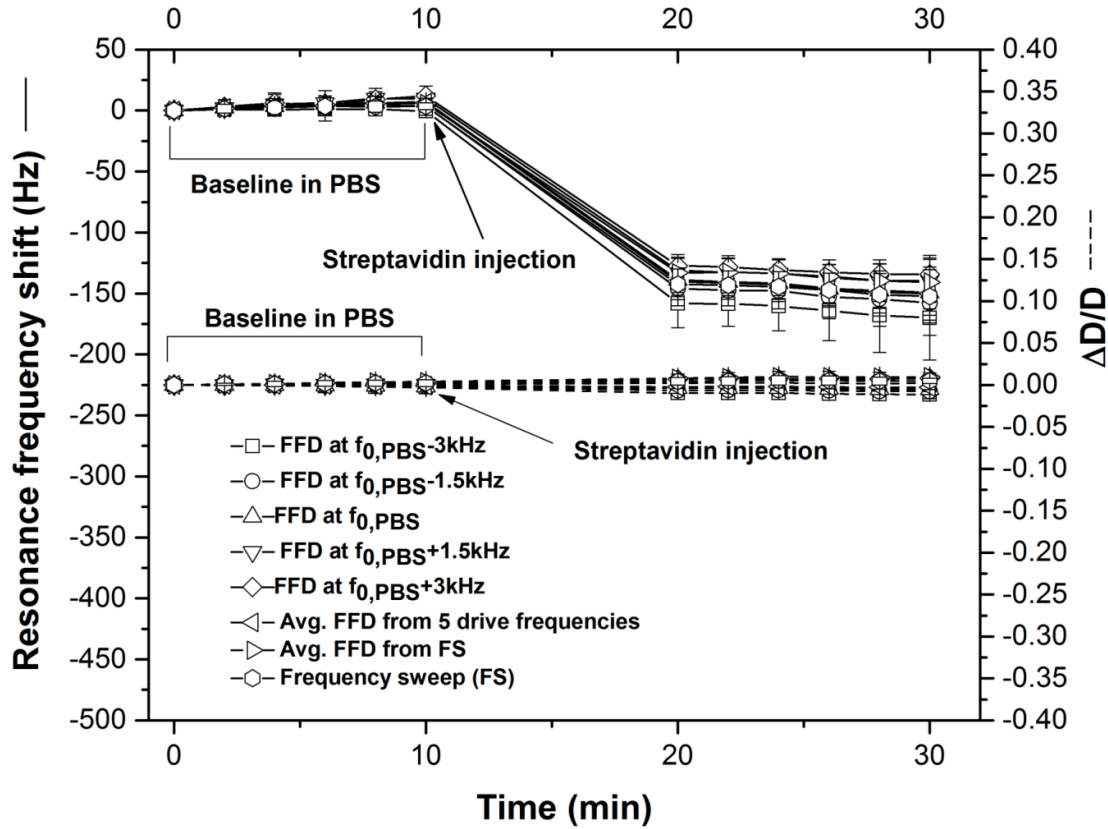


Figure 4.5. Resonant frequency and relative dissipation shifts due to streptavidin binding using frequency sweep and FFD methods (with 5 drive frequencies) with 2 min measurement interval.

The average of the resonant frequencies obtained from baseline measurements were subtracted from the average of the resonant frequencies obtained from binding measurements for each of the techniques including FS and FFD to estimate the average resonant frequency shifts due to streptavidin-biotin binding. They showed satisfactory agreement with each other (Figure 4.6). Percentage variation of the average resonant frequency shift obtained from different FFD methods were estimated with respect to the frequency sweep technique. The agreement varied between +9.54% (SD, 5.44%) and -7.84% (SD, 4.4%) over the range of drive frequencies explored, and was found most satisfactory -0.55% (SD, 2.47%) when the drive frequency for FFD was set to $f_{0,PBS}$ (Figure 4.7). Such variations were due to inaccurate calibration procedure. The accuracy of calibration depends on the definition of terminals of open, short and loaded circuits. The details of the calibration procedure can be found in Section A.1. The device used between the terminals is termed as Device Under Test (DUT). In case of experiments, the measurements were taken between the terminals of a QCR assembled printed circuit board

(PCB). However, the PCB was not taken into account while performing the calibration prior to the experiments, which resulted in slight inaccuracy. If the DUT was just the QCR, then the accuracy of feedthrough capacitance estimation would have improved the FFD estimate nearly as per the prediction of the theory.

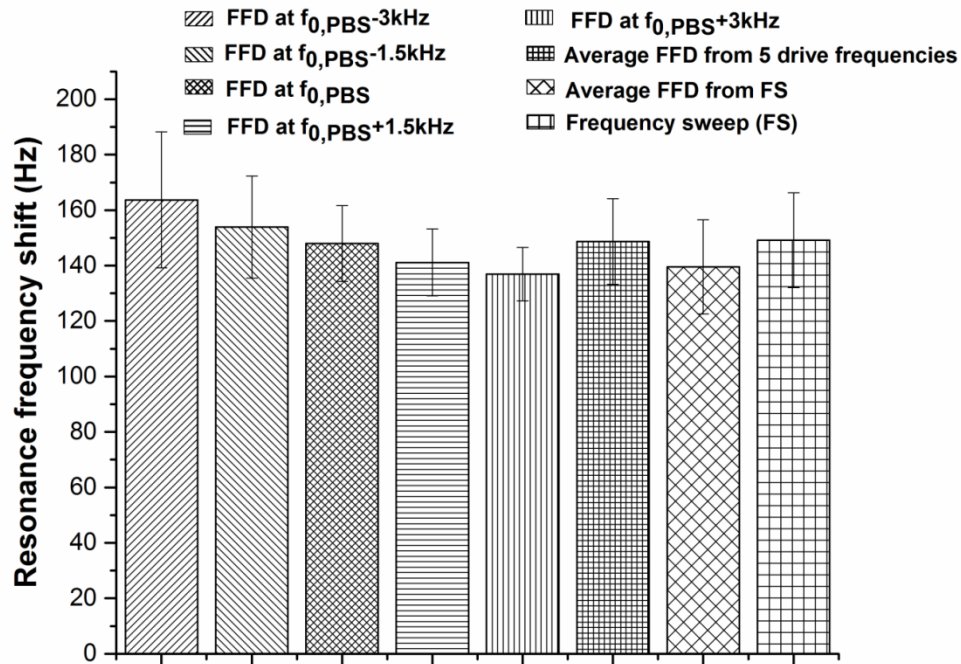


Figure 4.6. Absolute values of average resonant frequency shifts 10 min after streptavidin injection

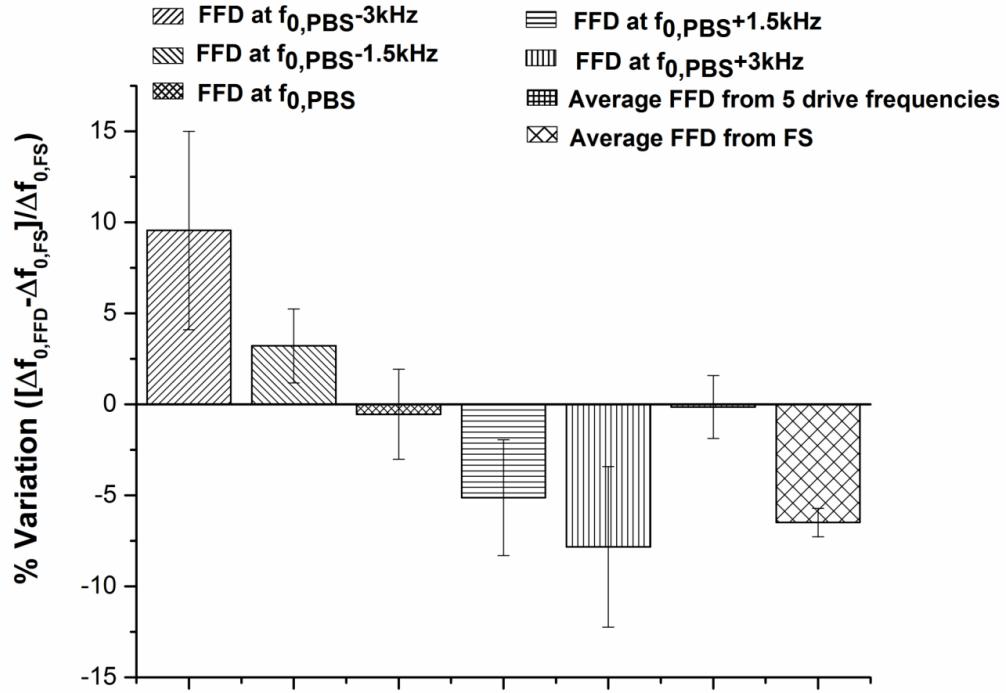


Figure 4.7. Percentage variation in absolute average resonant frequency shifts for FFD (at different drive frequencies) with respect to the frequency sweep method

Average relative dissipation shifts were also estimated in a similar manner as described above. The changes in relative dissipation obtained using FS and FFD methods were negligible. The average relative dissipation shifts in case of FFD method varied nearly from 0.002 to 0.009 for the explored driving frequencies (Figure 4.8). Percentage variation of average relative dissipation shift for each of the FFD techniques with respect to FS technique was not calculated due its negligible variation.

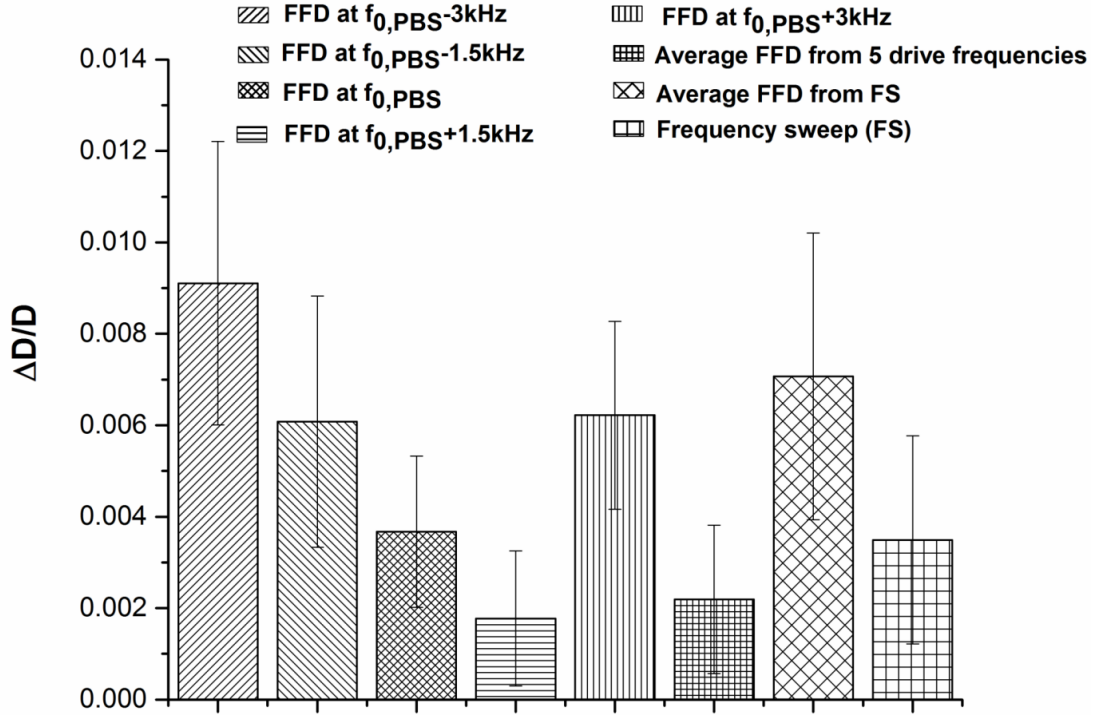


Figure 4.8. Average relative dissipation shift 10 min after streptavidin injection

4.3.7 Agreement with Sauerbrey model for resonant frequency shift due to streptavidin-biotin binding

Sauerbrey observed that there is a linear decrement in resonant frequency of an unperturbed AT cut QCR due to mass adsorption on sensor surface [50]. However, Sauerbrey's hypothesis is valid based on three assumptions. Firstly, the mass of the adsorbate must be smaller compared with the mass of the quartz crystal resonator. Secondly, the mass adsorption on the quartz crystal resonator surface should be rigid. Thirdly, the mass of the adsorbate should be evenly distributed over the active area of the quartz crystal sensor surface [23].

The resonant frequency shift at the n^{th} resonance mode as per Sauerbrey's equation [50] is given by:

$$(4.2)$$

where n is the number of overtone, m is the additional mass bound to the surface, f_0 , ρ , and A represent the unperturbed fundamental resonant frequency, density, frequency constant and effective binding area of the QCR respectively. Frequency constant f_0 is 0.5 times the velocity of the acoustic wave through the quartz substrate. The details of the derivation of Eq. (4.2) can be found in Section A.3 of appendix. The maximum amount of additional mass due to binding of streptavidin on a biotinylated QCR surface can be given by:

$$\Delta f = \frac{2\pi f_0^2 m}{\rho A} \quad (4.3)$$

where M is the molecular weight of streptavidin molecule, N_A is the Avogadro Number and A_m is the cross-sectional area of one streptavidin molecule. Using Eq. (4.1) and Eq. (4.2), the resonant frequency shift due to streptavidin binding is given as:

$$\Delta f = \frac{2\pi f_0^2 M}{\rho A_m N_A} \quad (4.4)$$

Taking $n=1$ (fundamental mode), $M=54$ kDa, $f_0=14.3$ MHz, $\rho=2650$ Kg/m³, $A=0.0001$ kHz-mm, and $A_m=0.0001$ nm² [150], the estimated maximum resonant frequency shift from Eq. (4.3) becomes -230 Hz. This theoretical estimate agrees reasonably with the FFD estimate of -148 Hz (SD, 13.65 Hz), considering a drive frequency equals to f_{PBS} . The resonant frequency shift value of -149 Hz (SD, 17.10 Hz) obtained using FS method was also in agreement with that obtained using theoretical estimate. The measured resonant frequency shift values were found to be within -36% of the theoretical estimate for both FS and FFD methods.

The observed discrepancies in resonant frequency shift values obtained due to streptavidin binding from theoretical estimate and experimental methods involving FS and FFD can be attributed to many factors. Firstly, the resonant frequency shift estimate for biotin-streptavidin interaction depends on the surface coverage of the QCR with biotin thiols. A 14.3 MHz QCR surface has been only immobilised with 10% biotin thiol by volume for

experiments. Such a surface coverage does not indicate uniform loading of streptavidin. Secondly, the loading of biomolecular film such as streptavidin on a QCR surface is non-rigid or viscoelastic in nature [39]. Thirdly, the entire biomolecular film, in particular the outer areas of the film do not couple to the oscillating motion of a QCR, thereby leading to dissipation of acoustic energy in the form of kinetic motion of the biomolecules [39].

4.4 Comparative analysis of FFD and frequency sweep using viscous loading experiments

This section presents the experiments carried out using bare cleaned QCR in two different liquids with varying absolute viscosities. Resonant frequency and dissipation shifts obtained using FFD technique was validated with frequency sweep technique for changes in viscous loading of a QCR surface.

4.4.1 Materials and preparation of QCRs

Methanol and Deionized (DI) water were used as viscous liquids for demonstration of viscous loading experiments using FS and FFD techniques. The quartz crystal resonators were cleaned using the protocol mentioned in Section 4.3.2. A cleaned unfunctionalised QCR was assembled in a similar manner as mentioned in Section 4.3.4 and used to study the resonant frequency and dissipation shifts when methanol (MeOH) in the sample chamber was replaced with DI water over a 14.3 MHz QCR surface.

4.4.2 Method of Drive

Frequency sweeps (0.1 sec, 0.52 V) and fixed frequency scans (0.1 sec, 0.52 V) were taken every 5 min, first in methanol to establish the baseline for 20 min, and then 20 min after DI water injection again for 20 min. There were ten measurement points including the methanol and DI water phases. The calibrated impedance from each frequency sweep scan was fitted with the BVD model (Figure 2.1) to determine the resonant frequency, quality factor, motional resistance and shunt capacitance. The details of estimation using the frequency sweep method have been provided in Section 4.3.5. The resonant frequency (f_{MeOH}) and characteristic impedance (Z_{MeOH}) of a QCR in methanol were estimated from a set of three frequency sweeps. The characteristic wave impedance (Z_{DI}) of a QCR in DI water was also obtained from a set of three frequency sweeps. Fixed frequency scans were taken successively at 5 different drive frequencies spanning ~84% of the frequency bandwidth:

$f_{MeOH} - 10$ kHz, $f_{MeOH} - 5$ kHz, f_{MeOH} , $f_{MeOH} + 5$ kHz and $f_{MeOH} + 10$ Hz in both

methanol and DI water phases following the frequency sweep. The calibrated reactance of the motional branch (X_{MeOH}) from each fixed frequency scan and the previously estimated QCR characteristic wave impedance (Z_0) in methanol were used to quantify the resonant frequency in methanol phase. Calibrated resistance of the motional branch (R_{MeOH}) and (X_{MeOH}) were used for quantification of dissipation from each fixed frequency drive in methanol phase. Resonant frequency and dissipation were obtained in a similar manner for DI water phase. The details of estimation using FFD method have been provided in Section 4.3.5.

4.4.3 Viscous loading results

Experiments involving subsequent flooding of a bare QCR surface with methanol and DI water were performed for demonstration of viscous loading. Viscous loading results obtained using FFD method was validated with frequency sweep method. Measurements taken in the methanol phase constituted the baseline measurements. Resonant frequency and dissipation in methanol and DI water were estimated using Eq. 3.9 and Eq. 3.19 respectively. Resonant frequency and relative dissipation shifts for each method were calculated by subtracting the resonant frequency and relative dissipation of the first measurement point in methanol respectively from all the subsequent measurement points including the same. The explanations for decrease in the resonant frequency and increase in the relative dissipation due to change in phase from methanol to DI water have been provided in the following section. Satisfactory agreement was observed between FFD and FS methods in terms of resonant frequency and relative dissipation shifts (Figure 4.9) due to alterations in viscous loading.

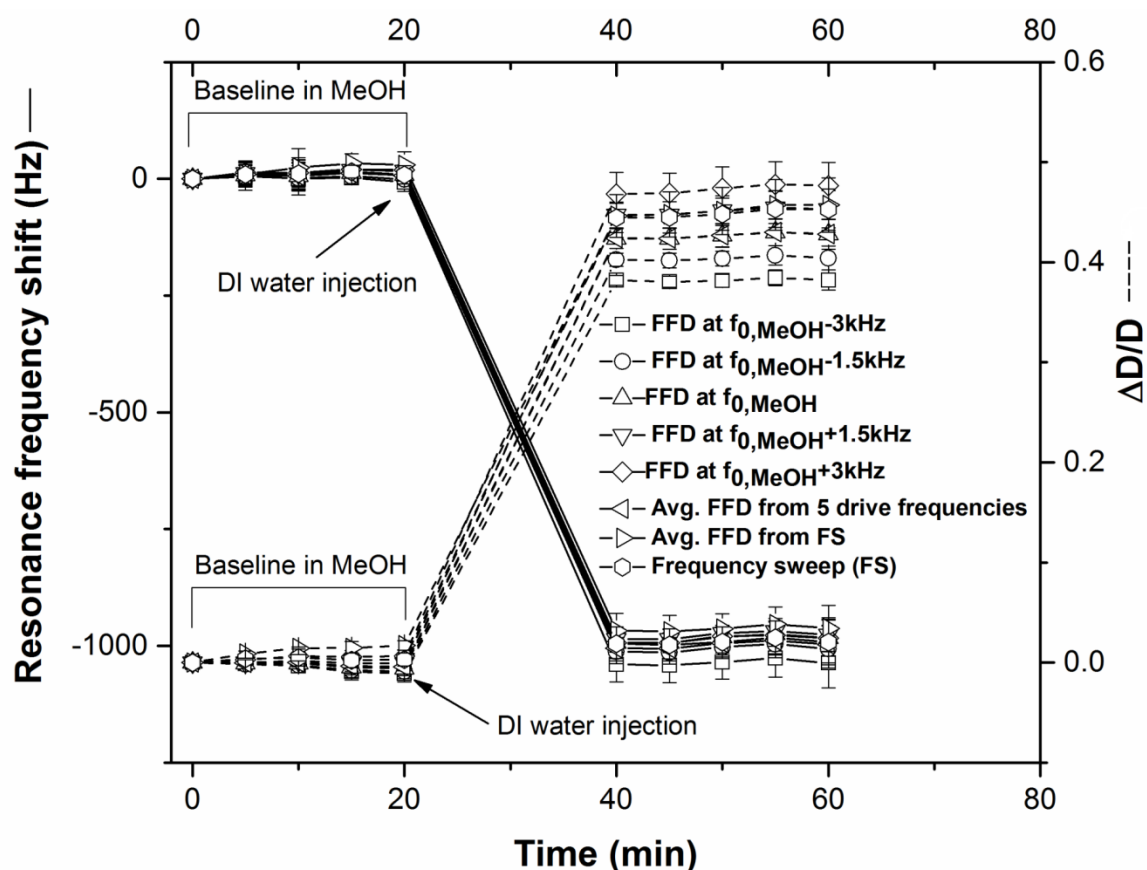


Figure 4.9. Resonant frequency and relative dissipation shifts due to change in liquid phase from methanol to DI water using frequency sweep and FFD methods (with 5 drive frequencies) with 5 min measurement interval

The average resonant frequency shift for each method was estimated by deducting the average of the resonance frequencies obtained in methanol phase from the average of the resonance frequencies obtained in DI water phase. The average resonant frequency shift estimated from FS and FFD methods also showed satisfactory agreement (Figure 4.10). Percentage variation of average resonant frequency shift obtained for different FFD methods were calculated with respect to the frequency sweep method. The agreement between FS and FFD methods in terms of estimated average resonant frequency shift varied between +3.54% (SD, 0.92%) and -1.1% (SD, 0.95%) over the range of drive frequencies explored, and was found most satisfactory 0.77% (SD, 0.64%) when the drive frequency for FFD was set to $f_{0, \text{MeOH}}$ (Figure 4.11).

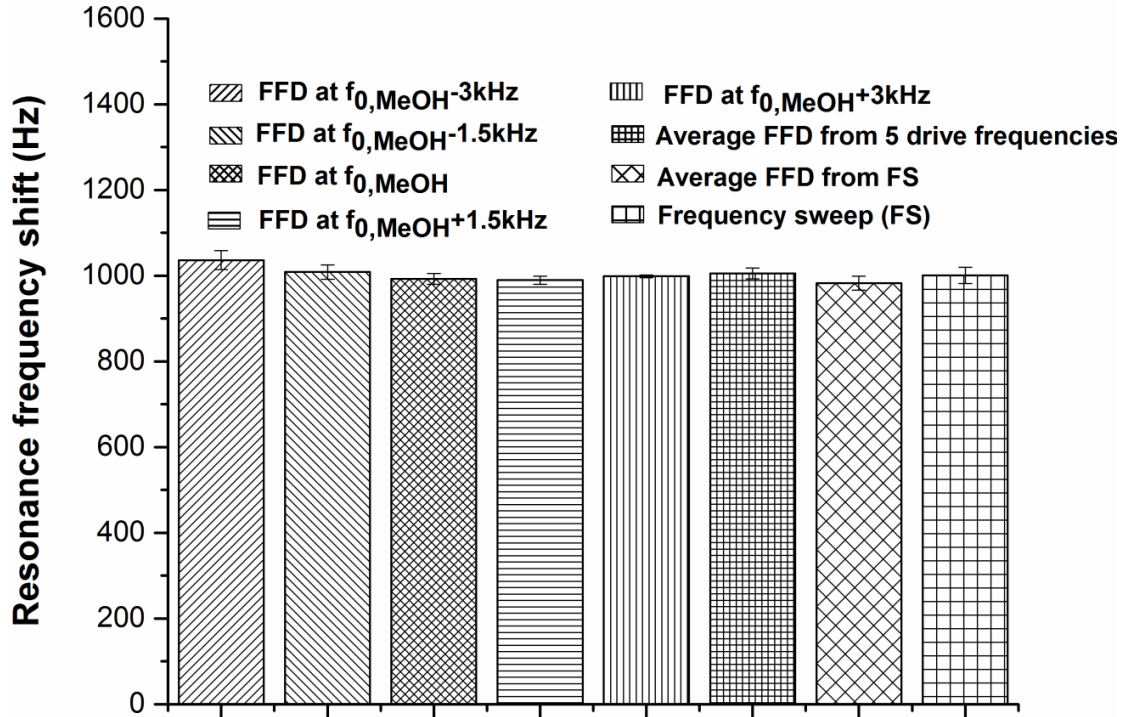


Figure 4.10. Average resonant frequency shift 20 min after flow of DI water.

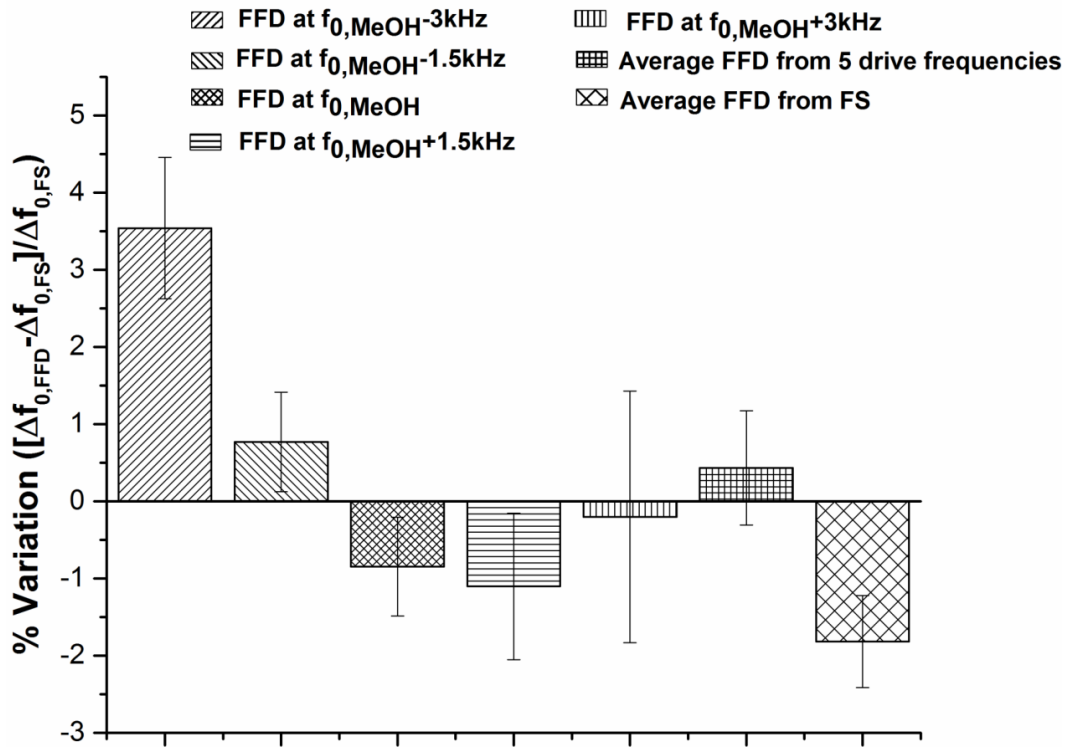


Figure 4.11. Percentage variation in the average resonant frequency shifts for FFD (at different drive frequencies) with respect to frequency sweep method.

The dissipation factor () for FFD method in methanol and DI water phases was estimated from Eq. 3.19 using the calibrated motional resistance (), and the previously measured characteristic wave impedance from the respective phases. The average relative shift in dissipation () were estimated in a similar way as described in the case of average resonant frequency. Average relative dissipation shift quantified using various FFD methods showed good agreement with that estimated from the frequency sweep (Figure 4.12) method. The agreement varied between -13.13% (SD, 1.55%) and +5.14% (SD, 1.83%) over the range of drive frequencies explored, and was found to be most satisfactory 1.11% (SD, 0.63%) when the drive frequency for FFD was set to $f_{0, \text{MeOH}}$ MHz (Figure 4.13). Such high variations were due to inaccuracies in calibration procedure as described in Section 4.3.6.

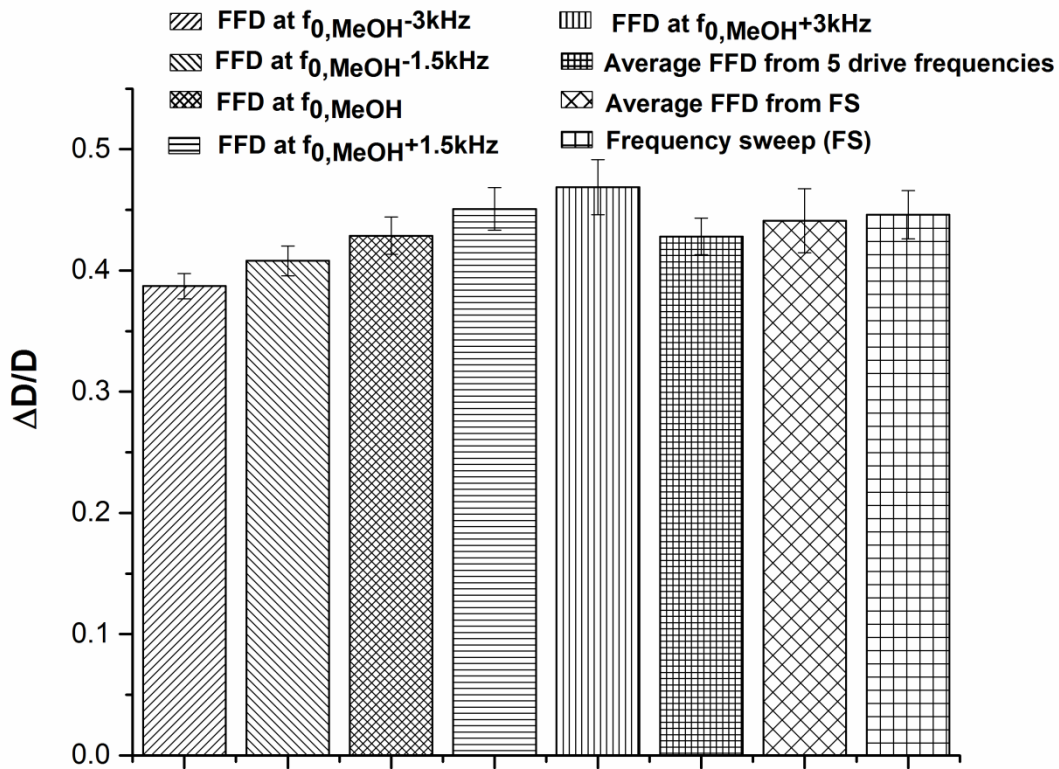


Figure 4.12. Average relative dissipation shift 20 min after flow of DI water.

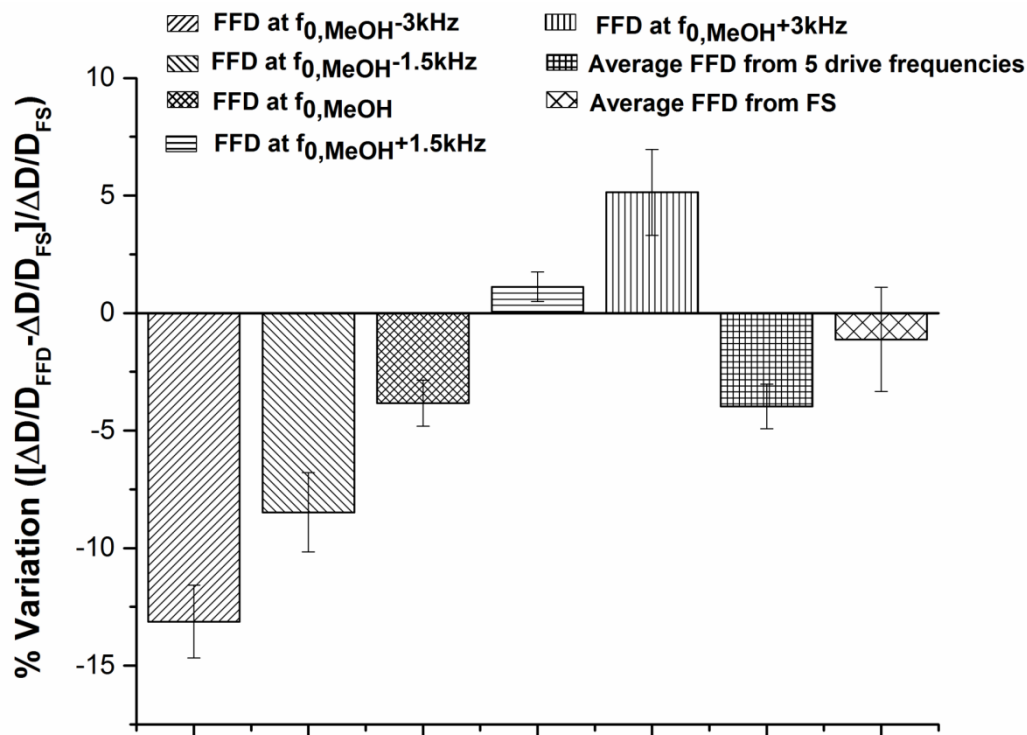


Figure 4.13. Percentage variation in the average relative dissipation shift for FFD (at different drive frequencies) with respect to frequency sweep method.

4 . 4 . 4 E s t i m a t e s f r o m K a n a z a w a ' s t h e o r y

Kanazawa's theory predicts shift in resonant frequency and dissipation of a QCR, represented by the shift in half-bandwidth (also known as "Gamma") $\gamma = \frac{\Delta f}{f_0}$. The shift in resonant frequency on account of change in liquid phase from methanol to DI water can be determined employing Kanazawa and Gordon formula [51], which is expressed as:

$$\Delta f = - \frac{f_0^2}{2} \left(\frac{\eta_l}{G} + \frac{\rho_l}{\rho_q} \right) \quad (4.5)$$

where f_0 is the unperturbed resonant frequency of a bare quartz crystal, η_l and ρ_l are the absolute viscosity and density of liquid respectively, and G and ρ_q are the shear modulus and density of the QCR respectively.

Taking, $f_0 = 10.0$ MHz, $\eta_l = 0.01$ Pa.s, $\rho_l = 1000$ kg/m³, $G = 2.94 \times 10^{11}$ Pa.s, and $\rho_q = 2650$ kg/m³, reads to

Hz and Hz. Hence, the resonant frequency shift due to change in liquid phase from methanol to DI water is estimated as

Hz. Therefore, the experimentally observed frequency shift agreed satisfactorily with the theoretical estimate (within 0.59% for the FS method and -0.27% for the FFD method when driven at MeOH). The expression of quality factor for liquid loading of a QCR surface in terms of , , , and for a fundamental mode of vibration is given by the following expression.

$$\dots\dots\dots - \frac{\dots\dots\dots}{\dots\dots\dots} \quad (4.6)$$

The details of the derivation of can be found in Section A.9 of appendix. The expression of half resonance bandwidth for a liquid loading using Eq. (4.6) can be expressed as follows.

$$\dots\dots\dots - \frac{\dots\dots\dots}{\dots\dots\dots} \quad (4.7)$$

Hence, the shift in resonant frequency of an unperturbed bare QCR due to loading of its surface with a liquid and half resonance bandwidth of a QCR in the same liquid have the identical absolute value if other losses are discarded. Since $\dots\dots\dots$, and the relative change in is negligible, the relative shift in dissipation due to change in phase from methanol to DI water can be theoretically estimated as $\dots\dots\dots$

$\dots\dots\dots$. Hence, experimentally observed relative shift in dissipation agreed satisfactorily with the theoretical estimate (within 1.81% for the FS method and -2.12% for the FFD method when driven at MeOH).

4.5 Noise analysis

Noise analysis was performed for investigation of the quartz crystal resonator noise obtained from FFD and FS measurements at different data acquisition rates. The data involving resonant frequency or dissipation of a quartz crystal resonator are often non-stationary in nature [151]. Allan deviation [152] is used as a standard for measuring the stability of such time dependent data. The allan deviation frequency noise for number of samples and measurement time, is given by the following expression [153]

$$\frac{\sigma}{f_0} = \frac{\sigma}{f_0} \quad (4.8)$$

where f_0 is the unperturbed QCR resonant frequency and σ represents the mean of instantaneous variation in relative frequency estimated for a measurement time from a particular instant.

Allan deviation baseline noise values were measured in PBS from a continuous fixed frequency scan for various data acquisitions rates and compared with those measured from a continuous frequency sweep employing the same QCR, functionalised with a mixed thiol SAM. Intermittent quick needle touches on SAM immobilised QCR surface were monitored during flow of PBS (at 40 $\mu\text{L}/\text{min}$) employing customised and commercial network analysers, which were used for FFD and FS measurements respectively. The QCR was driven close to resonance in FFD technique. For the network analyser used in this thesis, the maximum data acquisition rate is 30518 points per second, i.e. 32.76 μs per acquired data point. Impedance data was recorded from a continuous fixed frequency drive (FFD, 100 s, 0.47 V) at this data acquisition rate. An exponential running (also known as moving) average was then applied on this data in order to obtain data streams with a range of acquisition time per data point from 32.7 to 41888481.2 μs . The same QCR, functionalised with a mixed thiol SAM, was then used to record baseline resonant frequency data from continuous frequency sweeps (FS, 100 s, 0.03 V) employing a commercial bench-top Vector Network Analyzer (VNWA 3E, SDR-Kits, UK) at three data acquisition rates allowed by the instrument: 66.5 ms, 665 ms and 6650 ms per data point.

Allan deviation noise (Eq. 4.8) was estimated for each data stream obtained for both the continuous FFD and continuous FS methods from the two instruments and compared (Figure 4.14, Table 4.1). It may be noted that after the data is acquired by the network analyser VNWA 3E, nonlinear fitting utilising BVD model is applied before the frequency data is written into the file. So the measurement time per data point is much higher for the VNWA 3E network analyzer. Hence, to compare the noise between the two methods, only the equivalent data acquisition times for the two instruments have been considered, and not the total measurement time as the latter would also depend on the processing speed of the instrument.

Figure 4.14 shows the dependence of noise on data acquisition rate. There was no simple linear relation between the noise values obtained from the two methods. However, the noise values obtained from the continuous FFD method were much lower at similar data acquisitions rates for all cases. As an example, noise from FFD was 5.5% of noise of FS at a data acquisition rate of ~66.5 ms (Table 4.1).

Type of drive	Time per measurement (ms) / Data acquisition rate (ms)	Baseline noise (mHz)	Noise ratio (FFD/FS)
Continuous FFD	59.18 / 59.18	298.19	0.055
Continuous FS	800 / 66.5	5436.13	
Continuous FFD	616.73 / 616.73	643.12	0.567
Continuous FS	1250 / 665	1133.57	
Continuous FFD	6425.02 / 6425.02	373.11	0.207
Continuous FS	7690 / 6650	1804.05	

Table 4.1. Allan deviation noise calculated from experimental data for continuous fixed frequency drive and continuous fixed frequency sweep for three comparable data acquisition rates and their comparisons

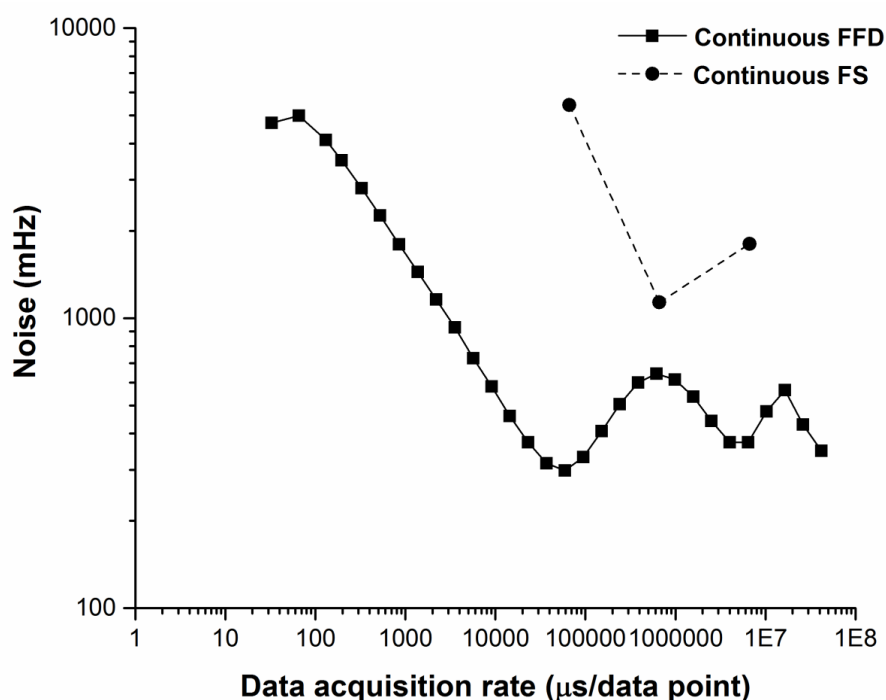


Figure 4.14. Allan deviation noise estimated from continuous fixed frequency drive (FFD) and continuous frequency sweep (FS) methods at various data acquisition time per measurement

The noise in a functionalised QCR is believed to be predominantly from the biomolecular functionalised surface to liquid interface dynamics. However, since the same QCR was used for both the methods and the measurements were taken in succession, we can consider that the comparative noise presented above relied primarily on the method and the instrument. Although different noise performance of the two instruments used (receivers, analog-to-digital converters) can play a role in the difference in noise observed, it is believed that the difference in the methods of resonant frequency measurement have played a crucial role in the striking difference in the noise performance. This may be justified as for frequency sweep method, the impedance data is collected across a range of frequencies. The signal-to-noise is lower for frequencies away from resonance, which impacts the quality of fitting in the FS method. In comparison, for FFD, as the impedance data is collected continuously near the resonant frequency, signal-to-noise is higher and there is no ‘dead time’ unlike in FS.

4.6 Time resolution of resonant frequency shift measurement

4.6.1 Theoretical estimate of time resolution

A sinusoidal response $\propto e^{-j\omega t}$ from a QCR with amplitude A angular drive frequency ω and phase angle ϕ is multiplied with a sine $\sin(\omega_c t + \theta)$ or a cosine $\cos(\omega_c t + \theta)$ signal of frequency synchronous to the drive frequency ω_c along with an offset ω_o . An offset frequency of 30.518 kHz has been adopted in the network analyser used for fixed frequency drive experiments. Resultant signal obtained from analogue down-conversion of QCR signal to an intermediate frequency ω_i due to multiplication with a cosine signal is given by

$$\dots \propto e^{-j\omega t} \cos(\omega_c t + \theta) \quad (4.9)$$

$$\dots - \cos(\omega_c t + \theta) \cos(\omega_c t + \theta) \quad (4.10)$$

The resultant signal obtained from analogue down-conversion of QCR signal to an intermediate frequency ω_i due to multiplication with a sine signal is given by

$$\dots \propto e^{-j\omega t} \sin(\omega_c t + \theta) \quad (4.11)$$

$$\dots - \sin(\omega_c t + \theta) \sin(\omega_c t + \theta) \quad (4.12)$$

The higher frequency component obtained from analogue down-conversion, $\propto e^{-j\omega t} \cos(\omega_c t + \theta)$ or $\propto e^{-j\omega t} \sin(\omega_c t + \theta)$ is filtered out employing a low pass filter. The down-converted analogue signal $\propto e^{-j\omega t} \cos(\omega_c t + \theta)$ or $\propto e^{-j\omega t} \sin(\omega_c t + \theta)$ is first converted to a digital signal comprising 32 points per period and then multiplied by a digital signal consisting of 32 points per period. Considering further digital down-conversion of the digitised and down-converted cosine signal, the following real and imaginary components are obtained as:

$$\dots - \cos(\omega_c t + \theta) \cos(\omega_c t + \theta) - \cos(\omega_c t + \theta) \sin(\omega_c t + \theta) \quad (4.13)$$

$$\dots - \cos(\omega_c t + \theta) \sin(\omega_c t + \theta) - \sin(\omega_c t + \theta) \sin(\omega_c t + \theta) \quad (4.14)$$

The in-phase sinusoidal signal (Eq. 4.13) with step increase in amplitude after double down-conversion with an intermediate frequency ω_{if} is given as:

$$x(t) = A \cos(\omega_{if} t) \text{UnitStep}(t) \quad (4.15)$$

where Unit Step $\text{UnitStep}(t) = 1$, when $t \geq 0$, and Unit Step $\text{UnitStep}(t) = 0$, when $t < 0$. The laplace transform of this signal is given by:

$$X(s) = \frac{A}{s^2 + \omega_{if}^2} \quad (4.16)$$

Application of the running average to Eq. (4.16) for four successive times helps in filtering out the ω_{if} component; thereby achieving the real zero frequency component. Similarly, the imaginary zero frequency component can be obtained from the quadrature-phase sinusoid signal (Eq. 4.14). Such a quadruple moving averaging filter is also known as a type B-spline. The B-spline operation is followed by quadruple exponential moving averaging. Such an operation helps in running the network analyser at different data acquisition rates. Considering the time transient process of the QCR upon stepwise change of attached mass (time constant τ) along with B-spline and quadruple exponential moving averaging operations, yields:

$$Y(s) = \frac{A}{s^2 + \omega_{if}^2} \frac{1}{(s + \frac{1}{\tau})^4} \quad (4.17)$$

where, Unit Step $\text{UnitStep}(t) = 1$, when $t \geq 0$, and Unit Step $\text{UnitStep}(t) = 0$, when $t < 0$ is B-spline Laplace Transform, τ is the time constant of exponential averaging, and ω_{if} is the intermediate frequency used in double down-conversion. For a 14.3 MHz QCR,

Figure 4.15 shows the Laplace transform transient process of Eq. (4.17) for $\tau = 32.7, 65.5$ and $131.1 \mu\text{s}$ per data points respectively.

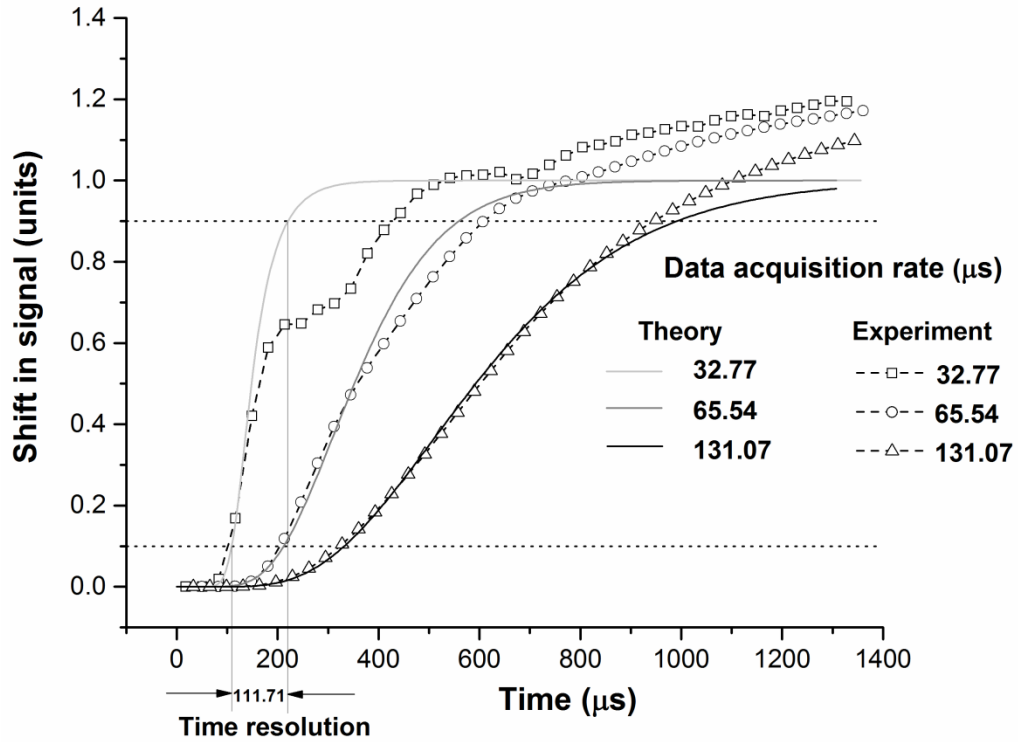


Figure 4.15. Needle touch experimental data of resonant frequency shift over 1.4 ms for three data acquisition rates compared with theoretical estimates

The theoretical front rise time [154], (i.e. time between 10% and 90% of the increase in amplitude of the signal), calculated for a range of data acquisition rates are shown in Table 4.2. The front rise time corresponding to minimum data acquisition rate of the instrument is termed as the time resolution of the measurement, which is 111.71 μs in this case. The deviations of the theoretical predictions from measurements at higher sampling rates have been explained in the following section.

Data acquisition rate (μs / data point)	Theoretical time resolution (μs)	Noise (mHz)
32.77	111.71	4711.01
65.54	202.66	4991.06
131.07	501.4	4109.91
196.61	818.42	3503.57
327.68	1460.98	2804.96
524.29	2429.26	2258.85

Table 4.2. Experimentally evaluated Allan deviation noise against the theoretical rise time for a range of data acquisition rates.

4.6.2 Needle touch experiment

Quick metallic needle touch experiments on a thiolated QCR in PBS were conducted to study the minimum time resolution of the resonant frequency shift measurement. Mechanical contact of needle tip to QCR surface introduces a very quick mass loading event as well as provides additional elastic stiffness. The elastic force is believed to be acting between the QCR surface, which is in contact with the needle tip and the rest of the needle. An overall rise in resonant frequency was observed from the needle touching event. Hence, it can be interpreted that elastic loading was more dominant. The frequency rise and decay features in response to quick needle touches, were clearly distinguished in timescales of 60-90 ms, for a continuous FFD scan (Figure 4.16).

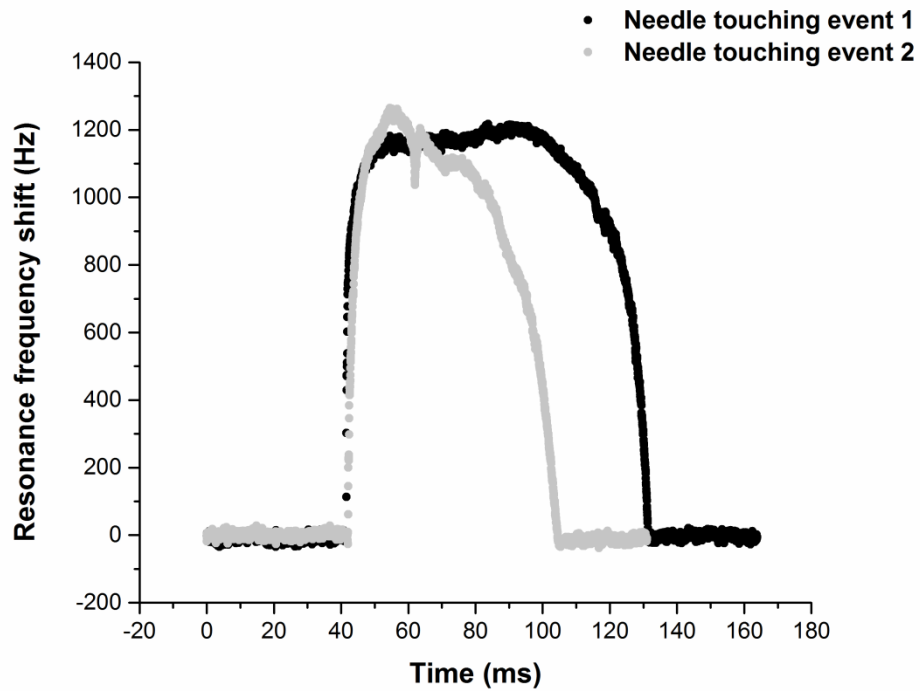


Figure 4.16. Resonant frequency shift measured from two successive needle touches at an acquisition rate of $32.7 \mu\text{s}/\text{data point}$.

However, these quick touches were apparently not detected using the continuous frequency sweep mode of the Vector Network Analyzer from SDR-Kits with data acquisition rates of 66.5, 665 and 6650 ms per data point (Figure 4.17).

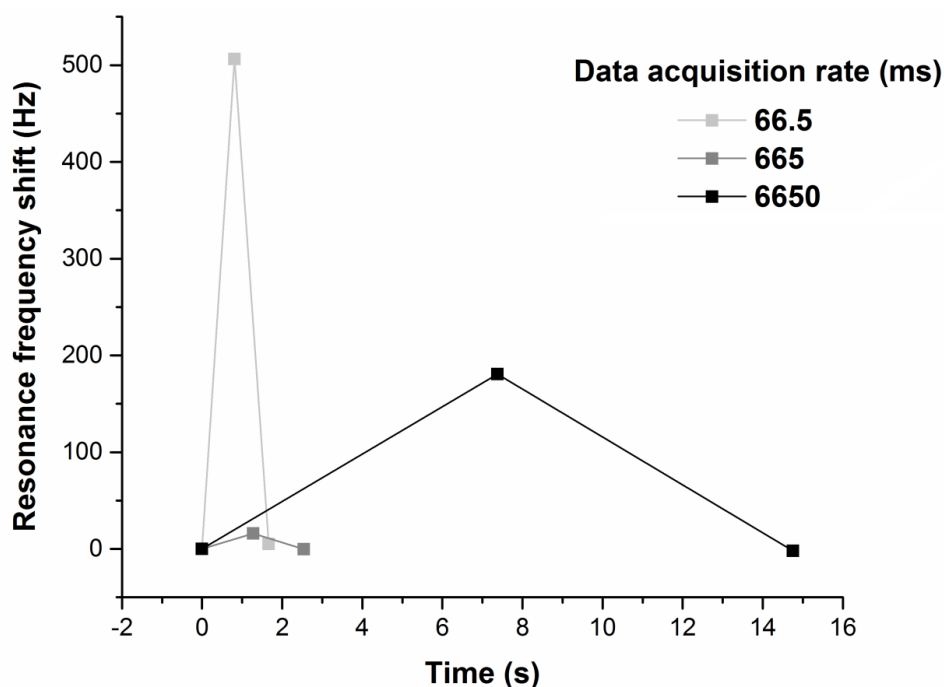


Figure 4.17. Resonant frequency shifts due to instantaneous needle touches using VNWA 3E from SDR-Kits.

The front rise time (time passed between 10% and 90% of step value) was theoretically estimated for a recorded signal due to a stepwise transient process for a QCR with a quality factor of 2000 and a receiver with acquisition rate of 30.518 kHz for a range of data averaging times (Section 4.6.1). The rise time for the quickest data acquisition rate (32.77 μ s/data point) was found to be $\sim 112 \mu$ s, which agreed reasonably well with the first frequency rise feature duration of a typical needle touch experiment (Figure 4.15). Therefore this rise time has been referred as the time resolution of the FFD method for this QCR set up. Deviation of theory from measured data at longer time scales can probably be explained by continuous physical dynamics of the touching process. The needle tip is believed to move into further wider contact along the QCR surface with the force provided by operator's hand after initial abrupt touch. Hence, the area of contact continues to increase during invading and jamming of the self-assembled monolayer immobilised gold surface of a QCR by the metallic needle tip. The restoring elastic force increases as a result of wider contact, thereby causing increase in resonant frequency. Further, the agreement of the theoretical prediction with the experiment at 32.77 μ s data acquisition rate is expected to be true during the rise time period.

The Allan deviation noise for some of the quickest data acquisition rates from the baseline experiment with thiolated QCR in PBS as described in Figure 4.14 was evaluated against

the time resolution at the respective rates as depicted in Table 4.2. The noise values at these high time resolutions were found to be significantly low, e.g. 4.7 Hz noise was observed for a theoretical time resolution of $\sim 112 \mu\text{s}$. This noise performance is encouraging, especially as the noise was predominantly from the surface rather than the method and could be further improved with improvement in the quality of surface.

4.7 Conclusion

FFD method allowed real-time resonant frequency shift measurements with a sub-millisecond time resolution and low noise. Quantitative validation of resonant frequency and dissipation shifts were successfully carried out with frequency sweep (FS) method using biotin-streptavidin and methanol-DI water experiments. The resonant frequency shift estimated from FFD method while driving close to baseline resonance was found within 1% (SD, 2.47%) and 1% (SD, 0.63%) of that obtained from FS method for biotin-streptavidin and methanol-water experiments respectively. Relative dissipation remains almost unchanged for biotin-streptavidin binding experiments. The small disagreements in the frequency shift estimated from the two methods were due to inaccuracies in calibration, which can be improved by better choice of the Device Under Test as described in Section 4.3.6. However, the accuracy of the current calibration procedure in measuring the known impedances, as evidenced in Table A.1 is reasonably up to the mark (\sim within $\pm 5\%$ error with respect to theoretical estimation). The capability of distinguishing time features down to $112 \mu\text{s}$ has been shown which agrees well with theoretical estimates. At this acquisition rate the Allan deviation noise for the baseline was measured as 4.8 Hz, which includes noise from the thiol-functionalised surface. The noise can be potentially improved through more stable functionalisation.

Chapter 5

Application of fixed frequency drive for detection of gram negative bacterial infection biomarker

5.1 Introduction

One of the objectives of the current research is to explore FFD for detection of a range of biomolecules with different molecular size and interaction affinity. The previous chapter demonstrated streptavidin (60 kDa) detection using biotin as the receptor. The biotin-streptavidin interaction is one of the most well-known receptor-antigen interaction with a dissociation constant of 10^{-15} M [155]. In this chapter, the FFD method has been employed for detection of a class of acylated homoserine lactone (AHL) biomolecules, comprising a molecular weight of 199.2 Da which is more than 2 orders of magnitude lower in comparison to streptavidin. AHL is an important biomarker for gram negative bacterial infection [156]. Therefore, feasibility of biomarker detection opens up a wide range of important clinical applications. The microfluidic chamber has been used in conjunction with the FFD method in order to assure controlled use of sample for clinical necessity. Moreover, molecular imprinted polymer (MIP) has been used for detection of AHL. The experimentally measured dissociation constant for MIP-AHL interaction obtained from Leicester Biotechnology Group using SPR technique is $\sim 10^{-10}$ M. QCM based detection of AHL using MIP as a receptor has been less studied in the literature. Hence, MIP based detection of AHL using FFD method is novel. An improvement in minimum detectable AHL concentration than existing literature using QCM has been demonstrated in this chapter.

5.1.1 Definition of biomarker

Mortality and morbidity numbers for infectious and non-communicable diseases are still very high [157–159]. Based on the pressing need for rapid and timely diagnosis of such diseases, healthcare initiatives have given special attention towards increasing access and inventions in treatment facilities [160]. However, a reliable and appropriate treatment for a patient needs an early definitive diagnosis. In recent times, scientific progress has paved the pathway for the discovery of substances or characteristics, termed as biomarkers, which *“are used as indicators of normal biological processes, pathogenic processes and pharmacological responses to any therapeutic intervention in order to assess the risk or presence of a particular disease”* [89]. Biomarkers used for disease diagnostics involve microRNA

expression profiles, circulating DNA and tumour cells, proteins, proteomic pattern, lipids, metabolites, imaging methods and electrical signals [89]. Certain disease specific biomarkers are found in easily accessible human body fluids, including blood, urine, serum, plasma and saliva, which make biomarker-based diagnosis potentially feasible at a wide scale. Blood is a very accessible sample and routinely used in clinical practice. However, detection of any biomarker from whole blood may not be convenient because of low concentrations. For example, conventional C-reactive protein (CRP) [161] is an inflammatory biomarker present in human blood. Prostate specific antigen (PSA), found in human serum, is considered as an important biomarker for prostate cancer diagnosis [162]. Clusterin is one of the biomarkers for Alzheimer's diagnosis that is present in human plasma [163]. Acylated homoserine lactone (AHL) serves as a significant biomarker for diagnosis of gram negative bacterial infections.

5.1.2 Importance of Acylated Homoserine Lactones

Human health deterioration due to bacterial infections [164–166] has become a global concern. A reliable and rapid diagnostic platform followed with suitable treatment and prognosis is therefore essential in order to combat bacterial infections. A number of biosensing techniques [167] have been developed in recent times for rapid and sensitive detection of bacteria. However, although the detection of bacteria confirms the presence of bacteria, it does not confirm whether it is a contamination, colonisation, or infection. Bacterial infection is a synthesis of evidence of bacteria and inflammation or systemic dysfunction and hence, more than one diagnostic approach is often needed for its confirmation [168].

Diagnosis of bacterial infection starts with a thorough clinical evaluation based on patient case history and small tests, such as chest radiography and lumbar puncture, depending on case definitions [168]. Results of clinical diagnostics is further cross-checked through another stage of examination comprising bedside investigations such as urine dipstick test and wet prep microscopy or laboratory based investigations including C-reactive protein (CRP) and procalcitonin tests, white blood cell and neutrophil counts, bacterial culture based test and nucleic acid amplification test (NAAT) [168]. Novel laboratory based diagnostic methods based on nanotechnology and mass spectrometry have immensely improved bacterial infection diagnosis in terms of reduced turnaround time [168]. Despite the advances in the diagnostic approaches, it is often challenging to distinguish between viral and bacterial infections, such as in case of febrile patients [169–171]. Such an uncertainty drives the clinicians to prescribe undesirable drugs such as antibiotics which can be

detrimental to the patient, healthcare system and society in the context of contemporary burgeoning problem of development of antibiotic resistance [172]. Hence, there is a need for a new method to deal with bacterial infections without promoting antibiotic resistance.

Specific phenotypes aid in growth and production of bacteria in different environment. Bacterial cells including gram positive and gram negative microbes communicate among each other employing certain chemical molecules as signals or auto inducers, whose concentration holds a direct correlation with the density of the bacteria pertaining to a particular environment. Such a phenomenon is known as “quorum sensing” (QS) [173]. Quorum sensing mediated phenotypic activities include virulence factor expression [174], toxin production [175] and biofilm formation [176]. Acylated Homoserine lactones (AHLs) are the most common chemical signaling molecules synthesized by gram-negative bacteria. A typical AHL molecule consists of a homoserine lactone ring and a lateral alkyl chain differing in length, saturation and oxidation state [177]. AHLs are capable of controlling the bacterial virulence genes and reducing the immune response in the host body, thereby facilitating bacterial infections. Virulence factor expression is introduced when a cut off concentration of AHLs is attained which gives an indication that the bacterial community is sufficiently large to develop infection in the host body [178]. Exact threshold concentration of AHLs required for initiation of different bacterial infections is still unclear in the existing literature and thus calls up for further investigations. However, AHLs have been successfully quantified in infectious human biological samples [173,179–182]. *N*-hexanoyl-L-homoserine lactone (C6-HSL) mediated QS in opportunistic human pathogen, such as *Serratia marcescens* – a gram negative bacteria, [183] has been found to be involved in nosocomial infections including respiratory tract, urinary tract and wound infections [184], to name a few. AHLs including *N*-butyryl-L-homoserine lactone (C4-HSL), *N*-hexanoyl-L-homoserine lactone (C6-HSL), *N*-octanoyl-L-homoserine lactone (C8-HSL), *N*-dodecanoyl-L-homoserine lactone (C12-HSL) and *N*-tetradecanoyl-L-homoserine lactone (C14-HSL) [185] have been identified in saliva and stools of patients suffering from bacteria aided gastrointestinal disorders such as inflammatory bowel disease at nanomolar levels. *N*-(3-oxododecanoyl-L-homoserine lactone (3-oxo-C12-HSL) has been found at nanomolar concentrations in *Pseudomonas aeruginosa* affected lungs and sputum tissues of cystic fibrosis patients [186]. Hence, AHLs can serve as potential biomarkers for gram negative bacteria related infections and disorders.

5.1.3 Conventional AHL detection techniques

Conventional detection methods for AHLs comprise thin layer chromatography (TLC) [174,176,187–191], polymerase chain reaction (PCR) [175,180,191–196], colorimetry [180], bioluminescence [197] and fluorescence-based techniques [194]. AHL detection is usually preceded by extraction of the same from genetically engineered bacterial reporter strains. However, such extractions are time prohibitive and labour intensive in nature. Conventional detection methods also need expertise of trained medical personnel and the sensitivity of the methods depends largely on the type of reporter strains used for analysis. On the contrary, detection techniques, such as High Performance Liquid Chromatography (HPLC) [198], Liquid Chromatography coupled with Mass Spectrometry (LC-MS) [181], High Performance Liquid Chromatography coupled with mass spectrometry (HPLC-MS) [199], Liquid Chromatography coupled with tandem Mass Spectrometry (LC-MS/MS) [200], Gas Chromatography coupled with Mass Spectrometry (GC-MS) [201], Matrix Assisted Laser Desorption Ionisation Mass Spectrometry (MALDI-MS) [202], Nuclear Magnetic Resonance Spectroscopy (NMR) [203] and Fourier Transform Infrared Spectroscopy (FTIR) [204] have also been attempted for detection of AHLs from cell free supernatants of gram negative bacterial cultures. Although, these detection techniques have achieved remarkable sensitivities in terms of AHL quantification (Table 5.1), they often require sample pre-treatment and/or molecular derivatization steps as pre-requisites for the analysis. Further, high costs are associated with massive instrumentation and assay performance for such techniques. Enzyme-linked immunosorbent assay (ELISA) [205], a traditional biochemical detection tool has also been tried for detection of different class of AHLs. ELISA is a relatively faster analytical technique compared with the above-mentioned methods in terms of time elapsed for intermediate sample processing steps, but it involves labelling of the target molecule (i.e. AHL with an enzyme), and is therefore not preferred for biosensing purposes. Hence, there is a need for a complimentary label free biosensing tools such as SPR, EIS and QCM that would reduce the cost and time for sample preparation. Label free AHL detection results can be verified with those obtained using conventional techniques in a routine clinical protocol.

Methods for AHL detection	Type of AHL molecule	Minimum Concentration Detected
Matrix Assisted Laser Desorption Ionisation Mass Spectrometry [202]	3-oxo-C12-HSL	0.9 nM
Enzyme linked immunosorbent assay [205]	3-oxo-C12-HSL	215 nM
High Performance Liquid Chromatography coupled with mass spectrometry [206]	C6-HSL	15 nM
Liquid Chromatography coupled with tandem Mass Spectrometry [173]	C6-HSL	2.5 nM
Thin layer chromatography [207]	C6-HSL	75 nM
Surface plasmon resonance [205]	3-oxo-C10-HSL	189 nM

Table 5.1. Comparison of sensitivities for some of the AHL detection techniques

5.1.4 Label-free AHL detection techniques

Label-free receptor-based biosensing methods with minimal sample processing steps have also been explored in order to overcome some of the limitations of conventional techniques related to AHL detection. Label-free receptor-based biosensors transduce the phenomenon of binding of the receptor or the bio-recognition element such as antibodies [208], aptamers [196] and molecular imprinted polymers (MIP) [209], to name but a few and the analyte or the target molecule into an electrical signal using various transduction techniques including optical, acoustic, thermal, electrochemical and magnetic. Optical biosensors, including surface plasmon resonance (SPR) [205], and electrochemical biosensors including differential pulse voltammetry (DPV) [178] and cyclic voltammetry (CV) [209] have achieved sensitivities comparable with the conventional methods in the context of AHL detection. However, such methods possess certain drawbacks as well. SPR faces numerous challenges when it comes to miniaturisation. There is a necessity of electroactive analyte for electrochemical biosensing techniques [28]. Hence, there is an unmet need to come up with simple, portable and inexpensive label-free biosensing techniques for AHL detection. Acoustic resonators including cantilevers [210], SAW [211] and QCM [212], to name a few have the potential for miniaturisation. QCM is one of the widely used acoustic resonators. They are entirely electronic and can be suitably integrated into portable detection platforms and therefore serve as the potential biosensing technique for AHL detection.

5.1.5 QCM based AHL detection: A way forward

Real-time detection of C6-HSL was performed using a 27 MHz QCR [183], in which, β -Cyclic oligosaccharide cyclodextrins (β -CD) was used as the receptor for C6-HSL. The change in resonant frequency due to interaction between β -CD immobilised 27 MHz QCM and the aqueous solution of C6-HSL was measured using the frequency sweep [125] method. Similarly, the frequency sweep method was also used for detection of acetyl-homoserine lactone and carboxybenzyl-homoserine lactone employing 8 MHz QCR and functional polymer receptors, based on 5-phenol-dipyrromethane and 5-phenyl-dipyrromethane [209]. However, the factors involving numerical fitting and expensive instrumentation restrict the application of frequency sweep method as a potential QCM tool for AHL detection. Hence, there is need for simple and low cost sensing technique, based on QCM. Simplicity and low cost satisfy the needs for online monitoring and affordable sensor respectively. Simplicity of transduction method also allows greater degree of multiplexability.

However, another deficiency of existing QCM sensors is limit of detection and the transducer is only one part of it. A suitable receptor is another key element which plays a vital role with regards to sensitivity.

5.1.6 Problem statement

The main objective of this research is to employ a simple tool based on quantification of QCR resonant frequency shift for detection of biomolecules with low molecular weight such as C6-HSL (~199.2 Da). Hence, the FFD method is explored for detection of C6-HSL biomolecule followed by validation with conventional frequency sweep method. The above validation will help in establishing FFD as a standalone method in QCM field for detection of small biomolecules.

5.1.7 Methodology

A 14.3 MHz QCM sensor based on the fixed frequency drive (FFD) technique as described in Chapter 3 of this thesis has been utilised for rapid and label-free detection of AHL using C6-HSL as a model QS molecule. Molecular imprinted polymers (MIPs) [213] have been selected as receptors for C6-HSL for the first time. MIPs are synthetic materials derived from acrylic or methacrylic monomers which are polymerised in the presence of specific target molecules termed as templates and have the capability of rebinding specifically to the target molecule. Special types of MIPs termed as Nano-MIPs were synthesized using a solid phase molecular imprinting technique [214] which depends on covalent immobilisation of the template molecule ((S)-(-)- α -Amino- γ -butyrolactone hydrobromide) on the surface of nano sized glass beads followed by polymerisation and a subsequent affinity separation step involving washing of the beads for removal of poor binders and unproductive polymers respectively. Polymerisation was conducted under the exposure of UV light and in presence of methacrylic acid monomers, cross linker including ethylene glycol dimethacrylate (EGDMA) and trimethylolpropane trimethacrylate (TRIM) and organic solvent including acetonitrile. The binding of C6-HSL to Nano-MIP immobilised 14.3 MHz QCR was measured using estimation of resonant frequency shift. The resonant frequency shifts were quantified for different C6-HSL concentrations, ranging from 1-50 μ M.

5.2 Experimental Hardware

5.2.1 Instrumentation

The network analyser described in Section 4.2.1 has been used for experiments involving C6-HSL detection.

5.2.2 Sensor Assembly

The sensor assembly (Figure 5.1) consisted of three main parts namely microfluidic cartridge, 14.3 MHz quartz crystal resonator (QCR) and printed circuit board (PCB). The details of QCR and PCB can be found in Section 4.2.2. The design and fabrication of the microfluidic cartridge was carried out by the group of Prof Wouter Wijngaart of Micro and Nanosystems laboratory, KTH Royal Institute of Technology (Stockholm, Sweden), as part of a EU project Norosensor, of which Loughborough University was a member (PI: Dr Sourav Ghosh) [215]. The microfluidic cartridge was fabricated using precision milling of acrylic substrates. The cartridge had peripheral fluidic inlet and outlet ports which are connected to a syringe pump via tubings. The sensor was assembled in a similar manner as described in Section 4.2.2. A sample chamber of 13 μL volume was formed when the microfluidic cartridge was clamped above the QCR and PCB. A quality factor of approximately 1900 was obtained when the assembled QCR was filled with liquid solution, which is expected for a 14.3 MHz QCR in liquid, thus indicating negligible damping by the O-ring.

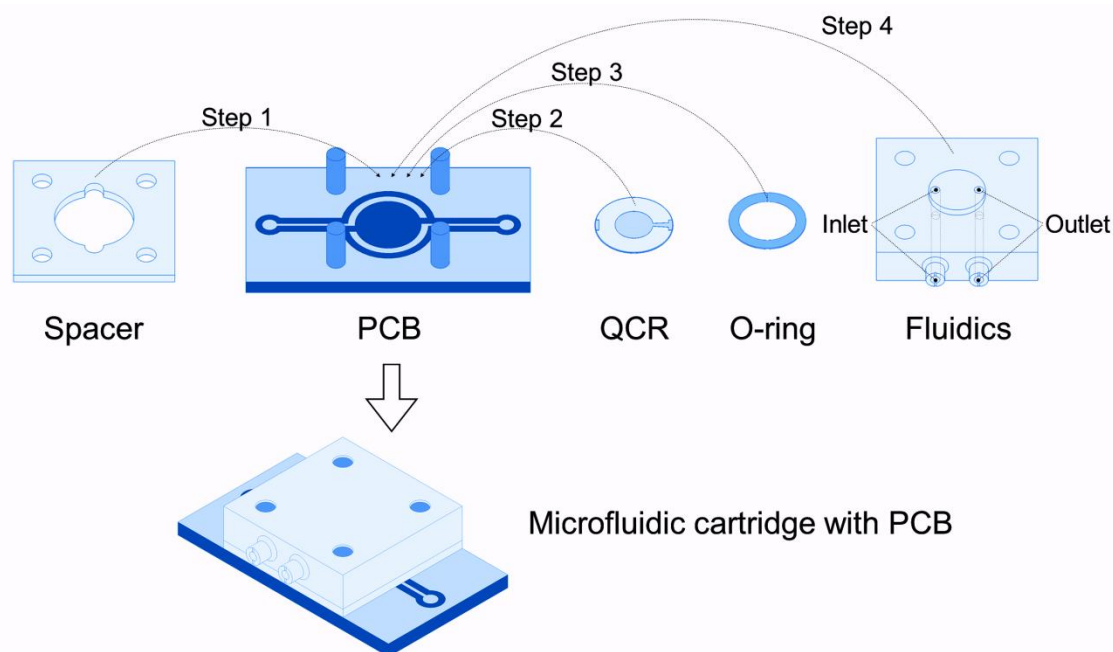


Figure 5.1. Schematic of an assembled QCM sensor used for AHL detection [215]

5.3 Materials and Excitation methods

The reagents needed for C6-HSL detection were borrowed from the Leicester Biotechnology Group of Department of Chemistry, University of Leicester (PI: Prof Sergey A Piletsky). The experimental steps involving immobilisation of anti-C6-HSL nano-MIP on 14.3 MHz QCRs were performed in collaboration with the Leicester Biotechnology Group.

5.3.1 Reagents

Methacrylic acid (MAA), ethylene glycol dimethacrylate (EGDMA), phosphate buffered saline (PBS), pentaerythritol-tetrakis-(3-mercaptopropionate) (CTA), 3-aminopropyltrimethyloxysilane (APTMS), trimethylolpropane trimethacrylate (TRIM), dodecanedioic acid, (S)-(-)- α -Amino- γ -butyrolactone hydrobromide, sodium carbonate (Na_2CO_3), sodium chloride (NaCl), N-hydroxysuccinimide (NHS), Cystamine, methanol, acetone, toluene and isopropanol were purchased from Sigma Aldrich, UK. PBS is composed of 8.1 mM Na_2HPO_4 , 1.1 mM KH_2PO_4 , 1 mM MgCl_2 , 2.7 mM KCl, and 138 mM NaCl with a pH of 7.4. Deionised (DI) water was obtained from Ultrapure Milli-Q water (Millipore, UK). 1-ethyl-3-(3-dimethylaminopropyl)-carbodiimide hydrochloride (EDC), Sodium hydroxide (NaOH), Dimethylformamide (DMF), ethanol and dry acetonitrile (ACN) were purchased from Fisher Scientific (UK). The MES buffer (2-[morpholino] ethanesulfonic

acid) was obtained from Thermo Scientific (UK). N-hexanoyl-L-Homoserine lactone (C6-HSL) was obtained from Cambridge bioscience. N, N'-diethyldithiocarbamic acid benzyl ester (Iniferter) was obtained from TCI Europe (Belgium). Glass beads (Spherglass® 2429) with diameters varying from 53 -106 μm were purchased from Blagden Chemicals, UK.

5.3.2 Protocol for preparation of glass beads

The glass beads were prepared by a collaborator named Mr. Omar Sheej Ahmad from the Leicester Biotechnology Group of the Department of Chemistry, University of Leicester [215]. Preparation of glass beads involves the following steps. Glass beads were first shaken with ceramic beads ($\sim 70\text{-}110\ \mu\text{m}$) on 45 μm sieves for three to four hours using a Vibratory Sieve Shaker AS 200 basic (Retsch, UK) in order to abrade the surface coating and expose a fresh surface. After recovery from the sieve, the surface of the beads was activated by boiling with 2 M NaOH for 15 min, followed by rinsing with deionised (DI) water and acetone, and then drying at 80 $^{\circ}\text{C}$. The dry beads were incubated overnight in 2 % v/v APTMS/toluene solution to introduce surface amino groups.

5.3.3 Protocol for preparation of anti-C6-HSL glass beads

Anti-C6-HSL glass beads were borrowed from the Leicester Biotechnology Group of the Department of Chemistry, University of Leicester [215]. The EDC/NHS chemistry was used to crosslink carboxylic groups with primary amines. Briefly, in order to get an activation buffer ($\sim 100\ \text{mL}$), (2.172 g, 11.12 mmol) of MES was mixed with (2.922 g, 49.99 mmol) of NaCl in distilled water and its pH is adjusted to 6.0 by adding few drops of NaOH [1 or 2 M]. An activation mixture was then prepared in a 50 mL volumetric flask by adding (0.125g, 5.43 mmol) of dodecanedioic acid to 20 mL of activation buffer. After that, (2.0 g, 0.01 mmol) EDC and (0.420g, 3.65 mmol) NHS were dissolved into 10 mL of fresh activation buffer and then the resulting solution was added to the dodecanedioic acid solution and mixed by Vortex Shaker. The glass beads, functionalised with APTMS were incubated for 20 minutes in the prepared solution. After that, the beads were washed with 50% DMF in water, activation buffer and acetone. The template ((S)-(-)- α -Amino- γ -butyrolactone hydrobromide) immobilisation on the surface of the beads was performed by incubating the glass beads functionalised with the activated dodecanedioic acid, in an aqueous solution ($\sim 50\ \text{mL}$) containing (0.07908 g, 4.43 mmol) of the template and (0.046g, 4.344 mmol) of sodium carbonate. The immobilisation was carried out for 2 hours. The beads were washed with

ultrapure water. Finally, the glass beads were dried under vacuum and stored in the fridge until used for the next time.

5.3.4 Protocol for polymerisation and anti- C6-HSL MIP nanoparticles synthesis

The polymerisation and anti-C6-HSL Nano-MIPs synthesis steps were performed at Leicester by Omar Sheej Ahmad from the Leicester Biotechnology Group of the Department of Chemistry, University of Leicester [215]. The polymerisation mixture was prepared in a 20 mL vial by mixing (0.3g, 0.61 mmol) CTA, (1.255g, 5.2 mmol) Iniferter, (4.8 g, 55.78 mmol) MAA as the backbone monomer, (5.4 g, 27.2 mmol) EGDMA, (5.4 g, 15.95 mmol) TRIM acting as cross-linkers and (17.55g, 247.5 mmol) of ACN respectively. The solution was mixed well and filtered through a 0.45 μm Teflon filter (to remove any insoluble compound) into a new vial covered with aluminium foil. The derivatised glass beads were incubated in a beaker sealed with a lid. The beaker was then placed for 10 minutes in a vacuum oven to remove the oxygen. The polymerisation mixture was added to the beaker, irradiated, and sandwiched between two UV light sources (Philips model HB/171/A, each fitted with 4x15 W lamps) for 1.50 minutes. The anti-AHL glass beads and polymerisation mixture were poured into a polyethylene solid phase extraction cartridge fitted with a frit (20 μm porosity), in order to separate glass beads (with the nanoparticles attached) from the other components. Two different washing steps were performed. Firstly, eight equivalents of cold ACN (0°C) were used to remove unreacted polymer and low affinity particles. This was followed by five washes with hot ACN (60-65°C) to elute high affinity nanoparticles. The final total volume of the high affinity anti-C₆-HSL Nano-MIPs was about 100 ml. The Nano-MIPs were kept refrigerated in acetonitrile solvent.

5.3.5 Protocol for immobilisation of QCR with anti- C6-HSL MIP nanoparticles

Nano-MIPs based on methacrylic acid (MAA) monomer have been chosen as the receptor for acoustic sensor due to strong binding interactions of MAA with AHLs including C4-HSL, C6-HSL and 3-oxo-C6-HSL [216–218]. The protocol for immobilisation of QCR with anti-C6-HSL MIP nanoparticles were taken from Leicester Biotechnology Group of Department of Chemistry, University of Leicester [215]. A cleaned QCR was incubated overnight in an ethanolic solution of cystamine with a concentration of 0.2 mg/ml. Cleaning was carried out as the per protocol mentioned in Section 4.3.2. The anti- C6-HSL Nano-MIP solution was

transferred from the acetonitrile to DI water by using centrifugal filter units. The QCR after overnight incubation with cystamine was washed many times in ethanol. The activated anti-C6-HSL Nano-MIP solution was prepared by adding EDC alone to the anti-C6-HSL Nano-MIP solution. The activation with EDC was used more than one time with new MIPs. Cystamine functionalised QCR was incubated for 20 minutes in activated anti-C6-HSL Nano-MIP solution.

5.3.6 Protocol for preparation of baseline

Functionalised QCR was dried using nitrogen gas after activation in anti-C6-HSL Nano-MIP solution. The functionalised QCR was placed in between an acrylic made microfluidic cartridge to allow controlled injection of sample, and a Printed Circuit Board (PCB) to facilitate the electrical connection. The actuation and electrical sensing of functionalised QCR were carried out employing a network analyser as described in Section 4.2.1. 1 mL of DI water was then injected (at 100 $\mu\text{L}/\text{min}$) over a functionalized QCR followed with subsequent injection (at 40 $\mu\text{L}/\text{min}$) of phosphate-buffer-saline (PBS buffer) for 50 min for achieving a stable baseline.

5.3.7 Protocol for preparation of C6-HSL stock solution

5.9 mg of C6-HSL with a molecular weight of 199.2 Da was added in 3 ml PBS to prepare 0.1 M C6-HSL stock solutions.

5.3.8 Steps of excitation

Experiment involving detection of C6-HSL molecule at a particular concentration was carried out using anti-C6-HSL Nano-MIP immobilised AT-cut thickness-shear-mode QCRs comprising a fundamental frequency of 14.3 MHz. Baseline measurements were taken for 30 min by conducting frequency sweeps (0.1 sec, 0.52 V) and fixed frequency/ FFD scans (0.1 sec, 0.47 V) every 2 min in phosphate buffer saline (PBS). During baseline measurements, PBS was flowed (at 40 $\mu\text{L}/\text{min}$) over the functionalised QCR. C6-HSL solution in PBS was injected (at 40 $\mu\text{L}/\text{min}$) after baseline measurements into the microfluidic cartridge for 30 min in order to facilitate binding of C6-HSL with Nano-MIPs. During the binding phase, similar frequency sweeps and FFD scans as mentioned above were taken. Concentrations of C6-HSL varied from 1-50 μM . Estimation of resonance parameters from FS method was obtained through fitting of complex electrical impedance with BVD model (Figure 2.1). The resonant frequency (f_{PBS}), feed through capacitance (susceptance of B) and the characteristic impedance (Z_0) required for FFD method were

estimated just prior to baseline measurements from a set of three frequency sweeps during PBS injection over functionalised QCR. The functionalised QCR was driven at V_{PBS} for a fixed frequency scan following the frequency sweep as the accuracy of estimation of resonant frequency from FFD technique is higher when driven close to resonance. The resonant frequency from each FFD scan was estimated using an analytical expression (Eq. 3.9) involving the characteristic impedance (Z_0) and the calibrated reactance of the motional arm (X_m) of the QCR.

5.4 Quantification of C6-HSL

Successful detection of C6-HSL using QCM and MIP has been demonstrated in this section. It has been previously evidenced from inertial loading experiments that changes in relative dissipation were negligible (Section 4.3.6). Hence, detection of C6-HSL was performed on the basis of resonant frequency shift. Resonant frequency shift obtained from FFD technique due to binding of C6-HSL with anti-C6-HSL Nano-MIP immobilised QCR was validated with FS method. Estimation of resonant frequency shifts from FFD [148] and FS methods at every measurement point were in good agreement with each other during the baseline and C6-HSL binding phases for a particular concentration (Figure 5.2). FFD technique is therefore a simple QCM based transduction technique and yet agreeable with conventional FS technique as well. FS and FFD methods were capable of detecting 1 μM C6-HSL in spiked PBS solution in 10 and 20 min respectively (based on signal to noise ratio greater than 5). The time of detection is higher for FFD due to slightly higher baseline noise (1.33 Hz) in comparison to FS (0.84 Hz) and can be improved by driving a QCR at lower driving voltage than 0.476 V.

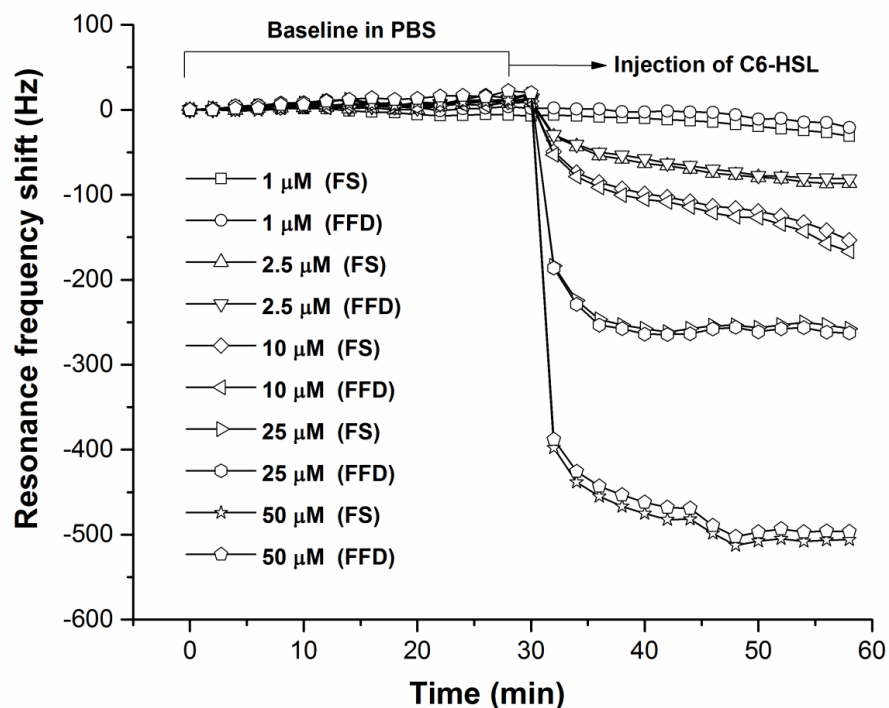


Figure 5.2. Resonant frequency shifts due to C6-HSL binding using frequency sweep (FS) and FFD methods for different concentrations with 2 min measurement interval.

The resonant frequency shifts estimated from FS and FFD methods after 30 min of C6-HSL injection for different concentrations also showed reasonable agreement (Figure 5.3).

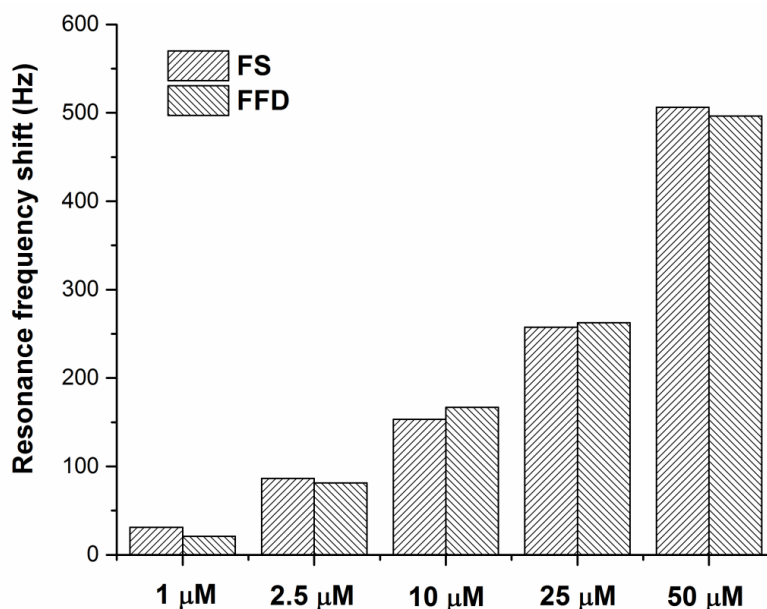


Figure 5.3. Resonant frequency shift 30 min after C6-HSL injection for different concentrations.

The agreement varied between -10.33 to +13.46 Hz over the range of C6-HSL concentrations explored (Figure 5.4). The slight variations were due to inaccurate calibration procedure and could be improved by using an appropriate DUT while performing the calibration (Section 4.3.6).

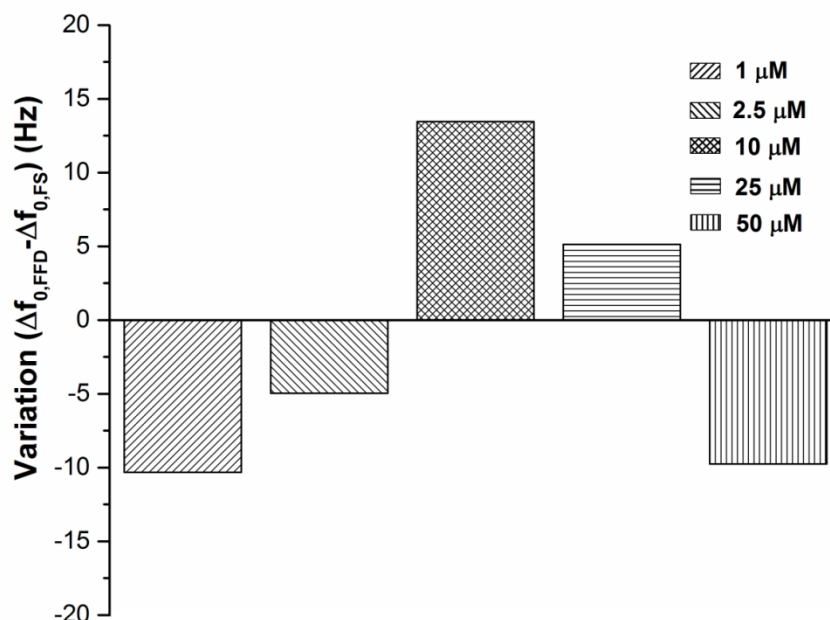


Figure 5.4. Variation in the resonant frequency shifts after 30 min for FFD (at different C6-HSL concentrations) with respect to frequency sweep (FS) method.

The average baseline noises estimated using Allan Deviation for FS and FFD methods were 1.48 Hz (SD, 0.63 Hz) and 1.83 Hz (SD, 0.46 Hz) respectively. Considering, the resonant frequency shift after 30 min of C6-HSL injection as the signal, the signal to noise ratios were calculated for all the tested C6-HSL concentrations employing FS (Figure 5.5) and FFD (Figure 5.6) methods. Analyte response curves for different concentrations are usually sigmoidal (S shaped) in nature [219]. A sigmoidal curve is composed of a linear, nonlinear and saturation regimes. AHL response curve for different tested concentrations reported in this work fell in the nonlinear regime. Hence, the graph depicting the variation of SNR with AHL concentration were fitted with a nonlinear function () for FS and FFD methods. Limit of detection (LOD) corresponding to a SNR of ~ 5 were estimated using the nonlinear fitting function for each of the methods. Calculated LODs for FS and FFD methods were approximately 180 and 193 nM respectively. The obtained LODs were comparable with the clinically relevant AHL concentration, which is typically in nM regime [185,186].

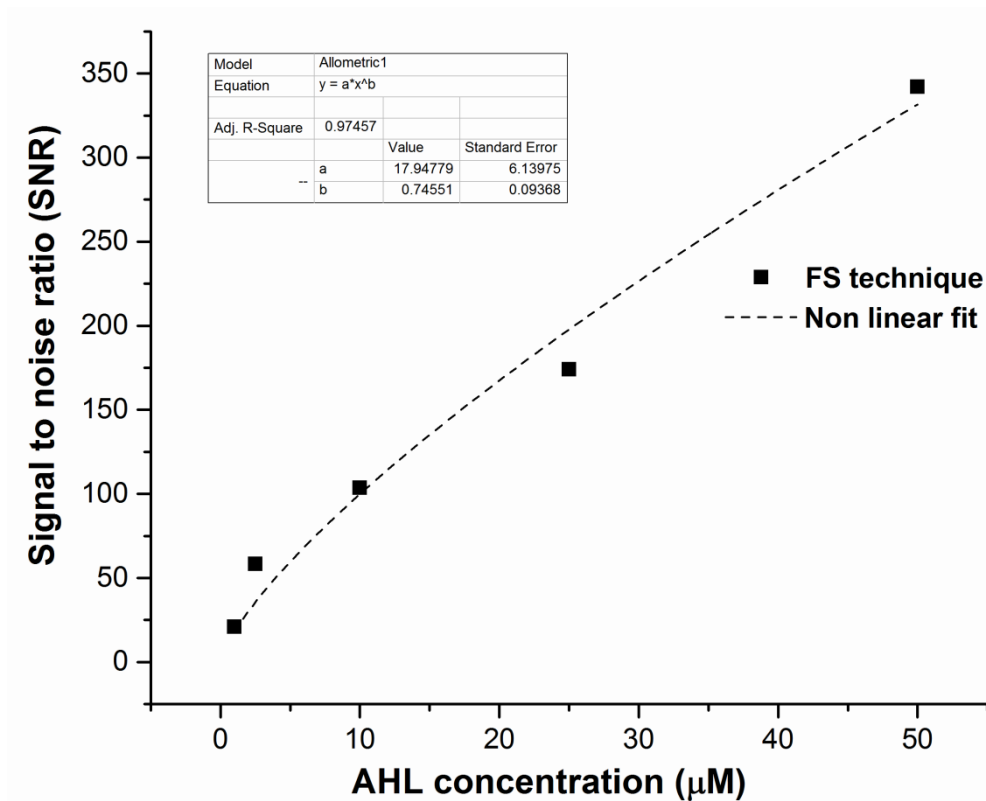


Figure 5.5. Variation of SNR at different C6-HSL concentrations for frequency sweep (FS) method.

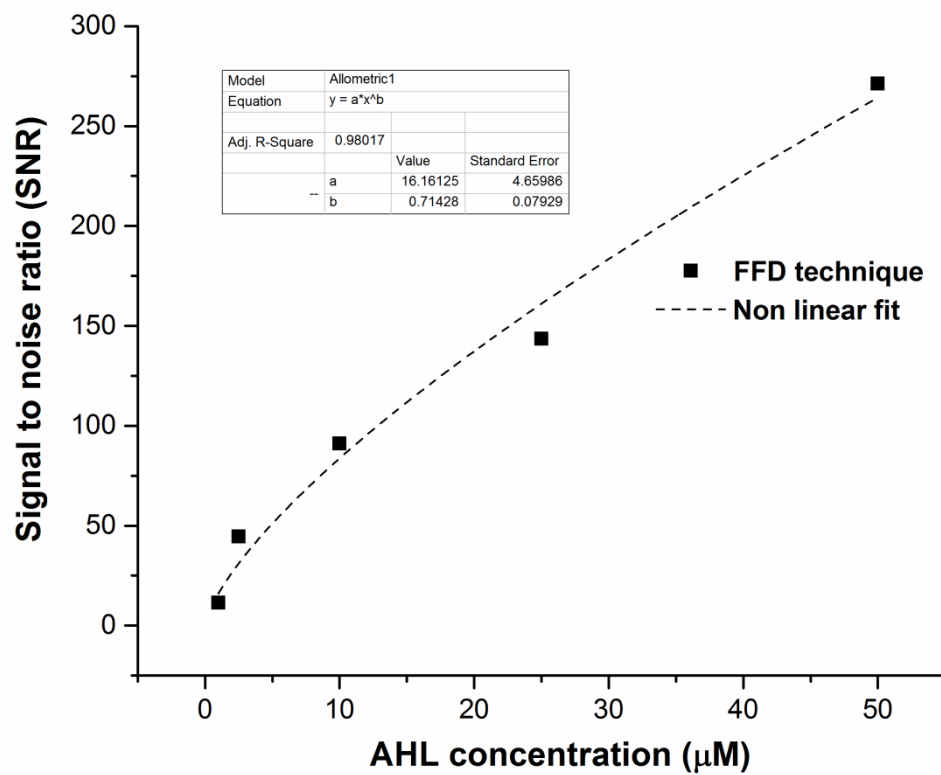


Figure 5.6. Variation of SNR at different C6-HSL concentrations for FFD method

5.5 Investigation of Specificity

Dopamine was chosen as the negative control for selectivity study as it has similar molecular weight (~153.18 Da) compared with C6-HSL (~199.2 Da). PBS was flowed (at 40 $\mu\text{L}/\text{min}$) over anti- C6-HSL Nano-MIP functionalised QCR for 30 min followed by subsequent injection of 50 μM Dopamine at the same flow rate. Similar measurements were taken during PBS and Dopamine injections as mentioned in Section 5.3.8. Another set of experiments with identical measurements were conducted where PBS was flowed (at 40 $\mu\text{L}/\text{min}$) continuously over the functionalised QCR for 60 min. The estimated resonant frequency shifts obtained with respect to the first measurement point after 60 min using FS technique for PBS, 50 μM C6-HSL and 50 μM dopamine injection experiments were 3.43, -506.2 and -15.7 Hz respectively (Figure 5.7). Negligible change in the conductance spectrum was observed between two frequency sweeps taken at an interval of 60 min during PBS injection. Figures 5.7 and 5.8 depict the stability of the baseline.

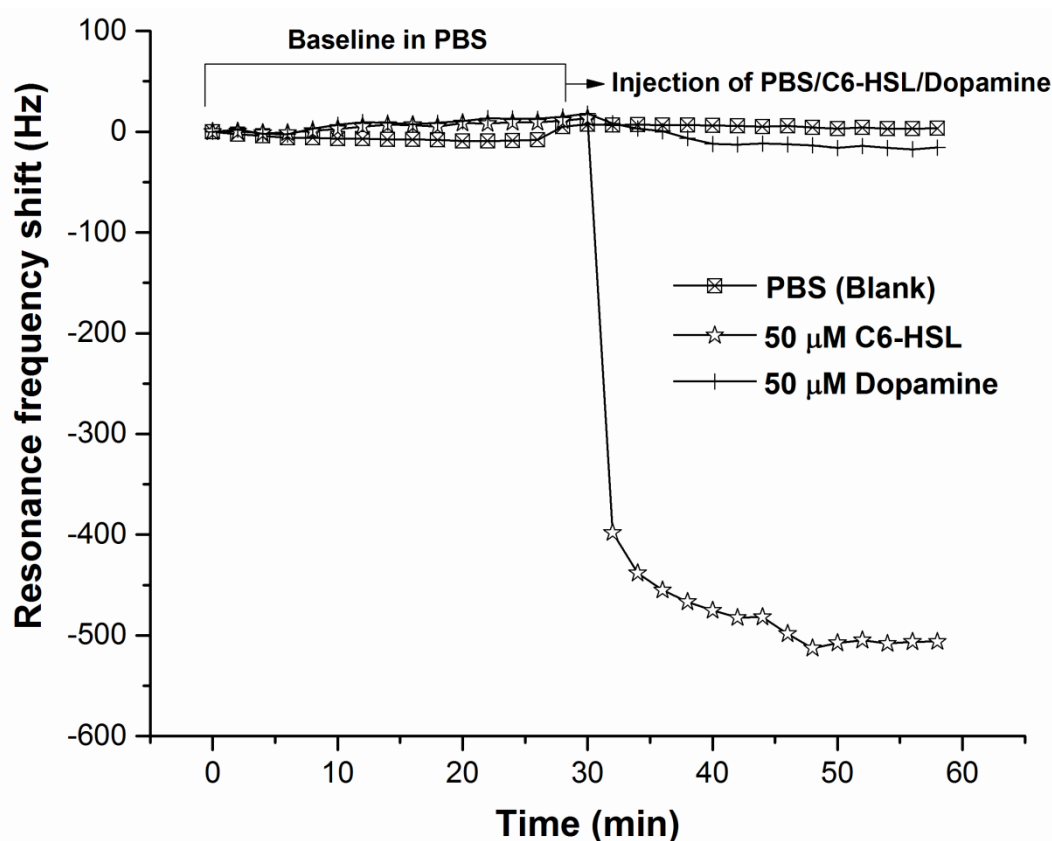


Figure 5.7. Resonant frequency shifts due to PBS injection and binding of C6-HSL and Dopamine using frequency sweep (FS) method with 2 min measurement interval.

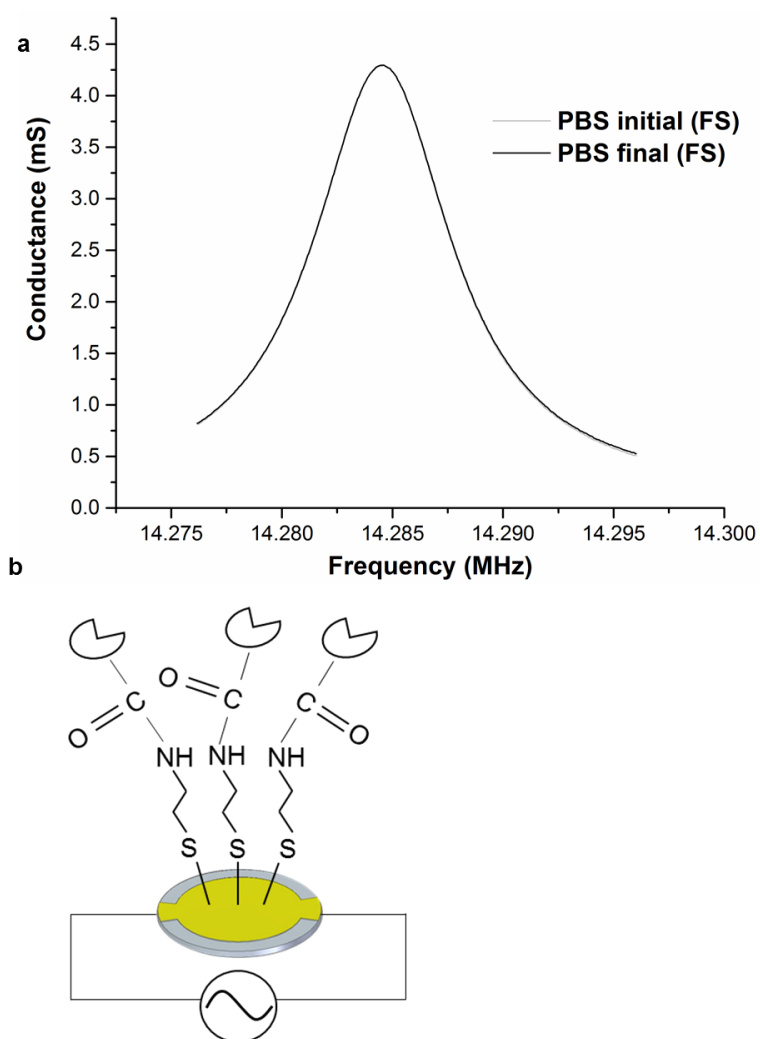


Figure 5.8. a. Negligible variation of conductance of anti-C6-HSL nano-MIP functionalised QCR after 60 min flow of PBS **b.** Anti-C6-HSL Nano-MIP immobilised QCR

Similarly, there was a negligible change in conductance spectrum between two frequency sweeps taken at an interval of 60 min during 50 μ M dopamine injection experiment in comparison to 50 μ M C6-HSL injection experiment (Figures 5.9 & 5.10).

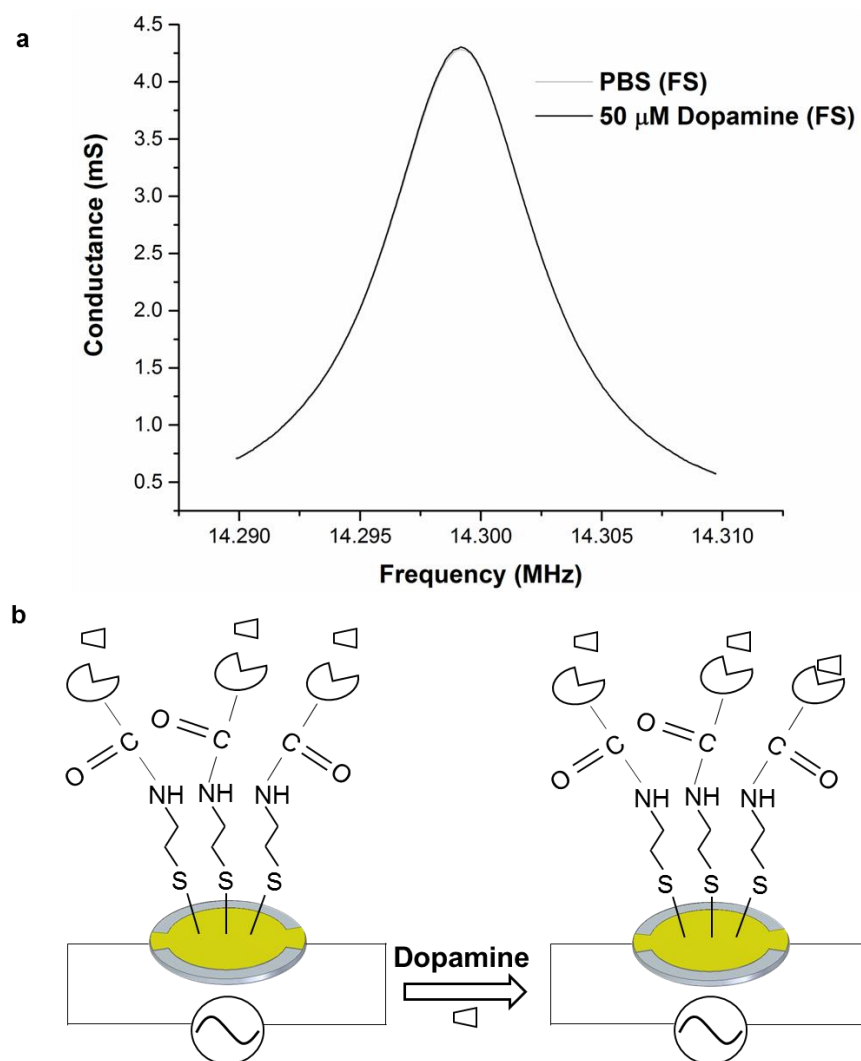


Figure 5.9. a. Negligible variation of conductance of anti-C6-HSL Nano-MIP functionalised QCR for two frequency sweeps in PBS and Dopamine with 60 min interval **b.** Non-specific binding of Dopamine to anti-C6-HSL nano MIP immobilised on a QCR.

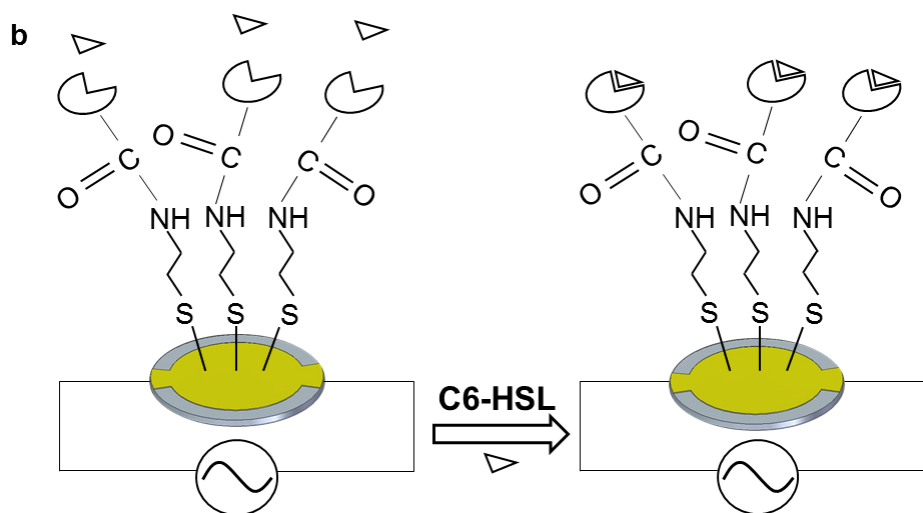
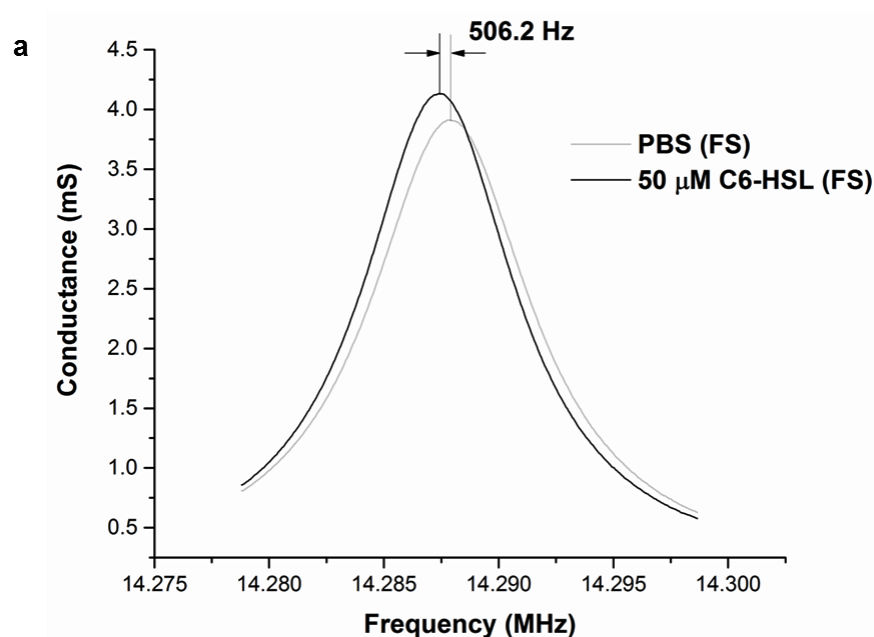


Figure 5.10. a. Variation of conductance of anti-C6-HSL nano MIP functionalised QCR for two frequency sweeps in PBS and C6-HSL respectively with 60 min interval **b.** Specific binding of C6-HSL to anti-C6-HSL Nano-MIP immobilised on a QCR.

Dopamine injection experiment employing FS and FFD methods showed satisfactory agreement with each other (Figure 5.11). Results obtained from 50 μ M dopamine injection were compared with that obtained from 50 μ M C6-HSL injection experiment.

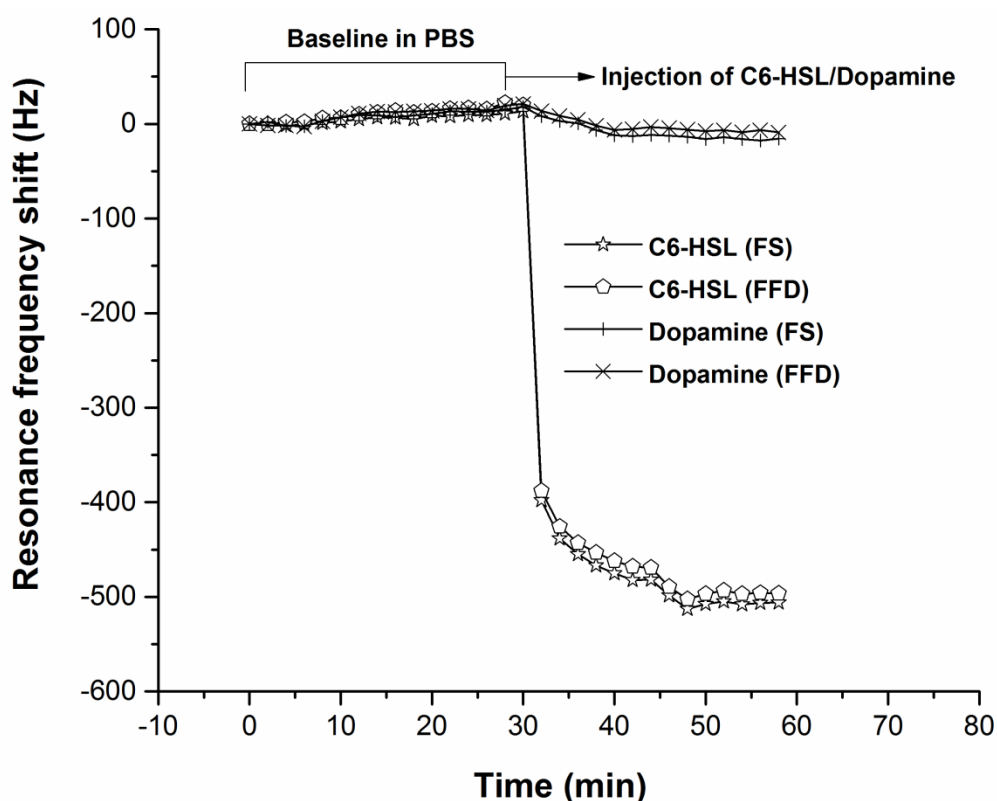


Figure 5.11. Resonant frequency shifts due to binding of 50 μ M C6-HSL and 50 mM Dopamine on functionalised QCRs using frequency sweep and FFD methods with 2 min measurement interval.

Resonant frequency shifts estimated using FS and FFD methods for 30 min interaction of anti- C6-HSL Nano-MIP and C6-HSL were approximately 32.2 and 56.1 times the resonant frequency shifts obtained from 30 min interaction of anti- C6-HSL nano MIP and Dopamine (Figure 5.12) obtained using FS and FFD methods respectively. Such results demonstrated the specificity of anti- C6-HSL Nano-MIPs.

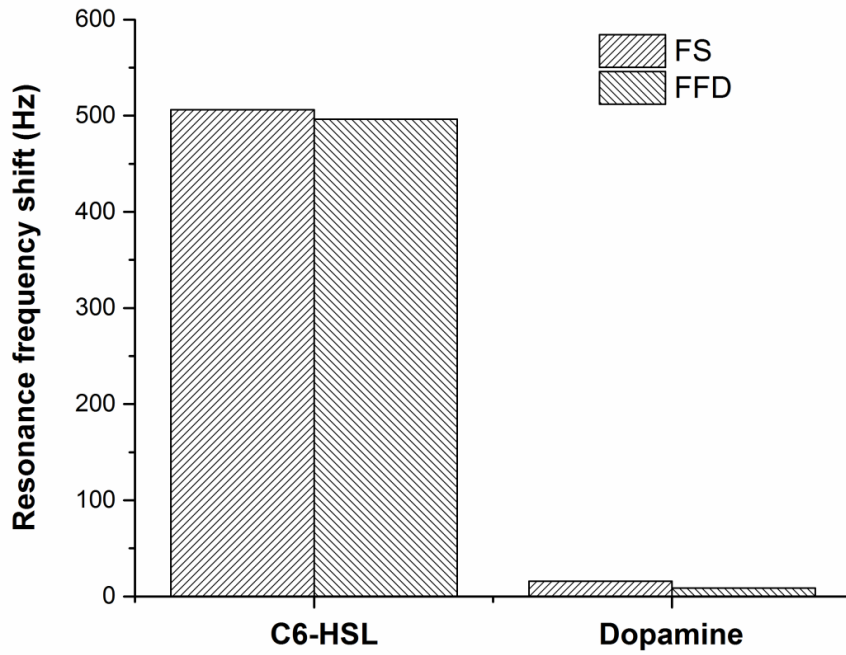


Figure 5.12. Resonant frequency shift 30 min after 50 μ M C6-HSL and Dopamine injections.

The variation in resonant frequency shift for FFD method with respect to FS method were approximately -9.76 and -6.86 Hz for C6-HSL and Dopamine injection experiments respectively (Figure 5.13). Such small variations can be corrected using accurate calibration procedure.

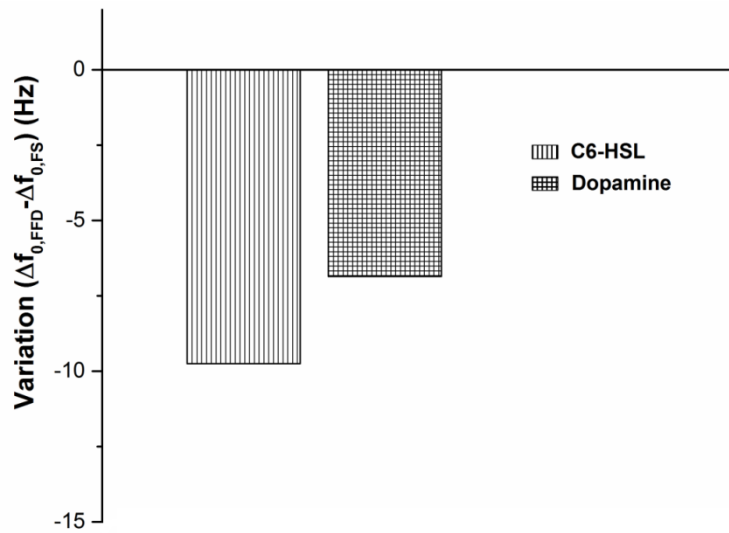


Figure 5.13. Variation in the resonant frequency shifts after 30 min for FFD (50 μ M C6-HSL and 50 μ M Dopamine) with respect to frequency sweep (FS) method.

5.6 Conclusion

A rapid and low cost online measurement of biomarkers is of high clinical need. Quartz crystal resonators have the potential to address this need as they are completely electronic and can be easily integrated into portable detection platforms. However, the clinically relevant concentrations for most biomarkers are low, particularly when early detection is needed. C6-HSL is a gram negative bacterial infection biomarker and induces the expression of pathogenic factors in gram negative bacteria after reaching a certain threshold concentration. As per the best knowledge of the author of this dissertation, 100 μM detection of C6-HSL has been reported using 27 MHz QCR and β -Cyclic oligosaccharide cyclodextrins receptor [183]. Fixed frequency drive (FFD) based detection of C6-HSL has been explored using a novel Nano-MIP as a receptor. FFD showed close agreement with FS (Figure 5.2). This demonstrated that the measurement of biomarker can be made using an instrument that is simple and low cost and usable at the point of care or in automated/online set-up. 1 μM of C6-HSL has been detected using FFD technique, which is approximately two orders of magnitude lower compared with the reported lowest C6-HSL detection using QCM [183]. A sample volume of 400 μL has been utilised for detection of 1 μM C6-HSL. A reciprocating flow [220] can be utilised to minimise the consumption of sample volume, which is a requirement for clinical sample. The specificity of the developed biosensor was also investigated by studying the interactions of 50 μM dopamine (negative control) and 50 μM C6-HSL (analyte) separately with anti- C6-HSL nano MIP immobilised QCRs and negligible response in terms of resonant frequency shift was obtained from dopamine experiment (-8.84 Hz) compared with C6-HSL experiment (-496.44 Hz) using FFD technique (Figure 5.12). The encouraging specificity is due to the higher affinity of the Nano-MIP.

Chapter 6

Application of fixed frequency drive for Human Immunoglobulin E detection

6.1 Introduction

This chapter focuses on the detection of an immunoprotein, i.e. (Human Immunoglobulin E), using FFD and an aptamer as the receptor. The findings from this chapter will help the understanding of the feasibility of FFD technique for detecting immunoprotein, which is approximately three orders of magnitude (~190 kDa) larger than an AHL molecule (~199.2 Da). Immunoglobulin E detection using oscillator circuit-based method and aptamer have been reported in QCM literature [131,221]. Herein, a simple technique based on QCM technology is presented for detection of Immunoglobulin E, which is easy to use and potentially favours portability and online integration.

6.1.1 Importance of Human Immunoglobulin E

The human immune system protects the body from different invaders including bacteria, viruses and microparasites, to name but a few [222]. Allergies, anaphylactic shock or mortality are caused by over-reaction of the immune system. Mammals consist of five classes of immunoglobulins namely IgA, IgD, IgE, IgG and IgM. Detection of immunoglobulin levels in human serum help in diagnosis of different types of hypersensitive reactions, such as immediate type, antibody dependent cytotoxic type, immune-complex disease type and delayed type. IgE concentration in human serum is related to immediate hypersensitivity [222]. Immunoglobulin E (IgE) is present in trace quantities in human serum [223] and has the ability to initiate some of the most powerful immune reactions including atopic dermatitis, allergic asthma and other immune deficiency related diseases [224]. People affected by allergy disorders constitute 20% of the global population [225]. The levels of serum total IgE are usually elevated for allergic patients in comparison to healthy individuals. According to previous studies, the threshold concentration of IgE in human serum for predicting allergies is 0.29 $\mu\text{g/mL}$ [226–228] which is equivalent to 1.53 nM assuming a molecular weight of 190 kDa [229]. Hence, a sensing platform based on quantification of hIgE will favour allergy diagnosis to a greater extent.

6.1.2 State-of-the art detection methods for human IgE

Conventional techniques including enzyme-linked immunosorbent assay (ELISA) [225], radioallergo sorbent test (RAST) [230], microarrays [231], polymerase chain reaction (PCR) [232], Matrix-Assisted Laser Desorption-Ionization Mass Spectroscopy (MALDI-MS) [233], flow cytometry [234], electrochemical luminescence [224] and rolling circle amplification [235] have provided unprecedented sensitivity and high throughput in case of human immunoglobulin E (hIgE) detection. However, intermediate sample amplification and processing steps involved with most of the above mentioned techniques are often very complex. Most of them demand a good laboratory infrastructure. Further, they are very time consuming and expensive diagnostic methods and also require expertise of trained medical personnel. Some of the methods also require labelling of hIgE analyte molecules with enzymes [225], fluorescent molecules [236], magnetic nano particles [237] or radioactive elements [231] which leads to occupancy of the binding sites and thus the affinity of the recognition element required for binding of the target molecule, i.e. hIgE is greatly influenced [223].

6.1.3 Label-free detection methods for human IgE

Label-free detection techniques with minimal sample preparation or processing steps including colorimetry [223], surface plasmon resonance (SPR) [228,238,239], electrochemical impedance spectroscopy (EIS) [240–245], differential pulse voltammetry (DPV) [246], field effect transistors (FET) [228,247–251] have also been tried for detection of hIgE. The above methods have shown promising results in terms of sensitive detection and quantification of hIgE molecules. However, most of these methods have disadvantages such as miniaturization hurdles, necessity for electroactive targets [28], to name but a few.

6.1.4 Potential of acoustic sensors for human IgE detection

Acoustic sensors such as quartz crystal microbalance (QCM) [131,221,229,238,252–255], film bulk acoustic resonator (FBAR) [256], surface acoustic wave (SAW) sensor [257,258] and flexural plate wave (FPW) sensor [222,259] have been explored for human IgE detection. They are entirely electronic and can be suitably integrated into portable detection platforms. Hence, they have particular merit in addressing the need for low cost POC sensors requiring low skills and infrastructure, thereby fulfilling the unmet need for rapid diagnostics of allergy. In recent times, QCM has gained worldwide attention as a sensitive,

specific and label-free tool for biomolecular detection among the class of acoustic sensors [1]. The detection principle of QCM states that relative resonant frequency shift measured employing different approaches such as oscillator circuits, impedance or ring down studies [85] relates to a relative increase in surface mass of an AT cut QCR [50]. Real-time quantification of hIgE based on oscillator circuits has been reported in the QCM literature [131,221,229,238,252–255]. Hitherto, 10, 20 and 25 MHz AT cut QCRs have been used for hIgE detection studies utilizing [252] oscillating circuits. From the author's best knowledge, there is no reported evidence of human IgE detection based on frequency sweep and ring down methods [85]. The minimum detectable hIgE concentration using 10 MHz oscillator circuit and biotinylated anti-hIgE aptamer as the receptor was 13.15 pM [131]. Aptamer has been chosen as the recognition element for hIgE due to its small size, low cost, robustness [260], in-vitro production and longer shelf life [221] in comparison to an antibody. The structure of an aptamer can also be easily modified [260]. A simple and label-free electronic method has been utilised for detection of hIgE using aptamer as the bio-recognition element.

Label-free methods for hIgE detection	Minimum Concentration Detected	Volume	Minimum Mass detected	Receptor used
FFD method (14.3 MHz QCR)	1.31 nM	30 μ L	7.5 ng	D17.4 biotinylated anti-human IgE aptamer
Surface plasmon resonance [228]	18.1 pM	70 μ L	240.8 pg	D17.4 biotinylated anti-human IgE aptamer
Colorimetric sensor [223]	0.2 nM	400 μ L	15.2 ng	Pseudoknot DNA oligonucleotide
Electrochemical Impedance spectroscopy [245]	0.1 nM	50 μ L	0.95 ng	Thiol modified DNA anti-IgE aptamer

Square wave voltammetry [241]	0.16 pM	5 μ L	0.152 pg	Anti-human IgE aptamer
Differential pulse voltammetry [240]	0.12 pM	10 μ L	0.23 pg	Thiol terminated anti-human IgE aptamer
Oscillator circuit (10 MHz QCR) [131]	13.15 pM	100 μ L	0.25 ng	Biotinylated anti-human IgE aptamer
Film bulk acoustic resonator (1.175 GHz) [256]	3.7 nM	200 μ L	141.4 ng	Mouse anti-human IgE antibody
Sezawa-mode surface acoustic wave sensor (200 MHz) [257]	3.7 nM	200 μ L	141.4 ng	Mouse anti-human IgE antibody
Flexural plate wave biosensor (21 MHz) [259]	0.46 nM	200 μ L	17.68 ng	Mouse anti-human IgE antibody

Table 6.1. Comparison of sensitivities between FFD and other label-free methods for hIgE detection

6.1.5 Problem statement of research

The main aim of this research is to apply a simple method of measurement of QCR resonant frequency shift for the detection of comparatively larger biomolecules than AHLs, such as Human IgE (~190 kDa). Hence, FFD technique is employed for detection of human IgE (hIgE) and the results are validated with frequency sweep technique.

6.1.6 Experimental methodology

Here in, a rapid and real-time detection of hIgE has been reported for the first time using FFD and FS techniques. Measuring of resonant frequency using FFD technique can be intermittent or continuous depending on user preferences. In this case, intermittent scans were taken for both FS and FFD techniques. Inertial loading experiments involving real-time interactions of hIgE at different concentrations and anti-hIgE aptamer immobilised 14.3 MHz QCRs were performed employing a custom-made network analyser. As soon as anti-hIgE aptamer immobilised QCR surface is loaded by hIgE analyte, there is a shift in QCR resonant frequency which is recorded by both FFD and FS methods.

6.2 Materials and Methods

6.2.1 Reagents

Acetone, isopropanol, ultra-pure 200-proof ethanol, phosphate buffered saline (PBS) and streptavidin were purchased from Sigma-Aldrich (UK). PBS contained 8.1 mM Na_2HPO_4 , 1.1 mM KH_2PO_4 , 1 mM MgCl_2 , 2.7 mM KCl, and 138 mM NaCl with a pH of 7.4. Deionised (DI) water for experiments was obtained from ultrapure water (Milli-Q Integral system, Millipore, USA). Human immunoglobulin-E (ab65866) and human immunoglobulin-G (ab91102) were procured from Abcam (Cambridge, UK). D17.4 biotinylated anti-hIgE aptamer with a base sequence of 5'-GGG GCA CGT TTA TCC GTC CCT CCT AGT GGC GTG CCC CTT TTT TTT TTT TTT TTT TTT T/3Bio/-3' was procured from Integrated DNA Technologies (IDT). Thiolated alkane solutions including HS-(CH₂)₁₁-EG6-Biotin and HS-(CH₂)₁₁-EG3-OCH₃ were purchased from ProChimia (Poland).

6.2.2 Protocol for immobilisation of D17.4 biotinylated anti-IgE aptamer on QCR and baseline preparation

D17.4 biotinylated anti-hIgE aptamer was chosen as the receptor for hIgE. The steps for immobilisation of QCR with D17.4 biotinylated anti-hIgE aptamer has been described below. The cleaned QCR was kept in 24-well plate and incubated in 250 μL of 1 mM ethanolic solution of a mixture of thiols comprising 10% biotin thiol (HS-(CH₂)₁₁-EG6-Biotin) and 90% methoxy thiol (HS-(CH₂)₁₁-EG3-OCH₃) by volume for approximately 18 hours in order to allow formation of self-assembled mono layer (SAM) of thiols over the QCR surface. Methoxy thiol was used as the blocking agent. Loosely bound thiol layer was removed by a series of ethanol and DI water washes after 18 hours. The QCR was dried using nitrogen gas and subsequently assembled following the sensor assembly steps. 1 mL of DI water

was injected over the SAM immobilized QCR (at 100 $\mu\text{L}/\text{min}$). PBS was then flowed over the SAM functionalised QCR (at 40 $\mu\text{L}/\text{min}$) for 40 minutes in order to achieve a stable baseline. 2.5 $\mu\text{g}/\text{mL}$ streptavidin solution was then injected (at 40 $\mu\text{L}/\text{min}$) for 15 min in order to allow binding of biotin from the SAM layer with streptavidin. 0.2 μM D17.4 biotinylated anti-hIgE aptamer solution in PBS was heated at 95°C for 5 min and then kept at room temperature for 20 min. The activated 0.2 μM biotinylated anti-IgE aptamer solution in PBS was injected (at 40 $\mu\text{L}/\text{min}$) after streptavidin injection for 20 min in order to prepare anti-hIgE aptamer immobilised QCR. PBS buffer was injected (at 40 $\mu\text{L}/\text{min}$) over anti-hIgE aptamer immobilised QCR (Figure 6.1) for nearly 50 min in order to establish a stable baseline.

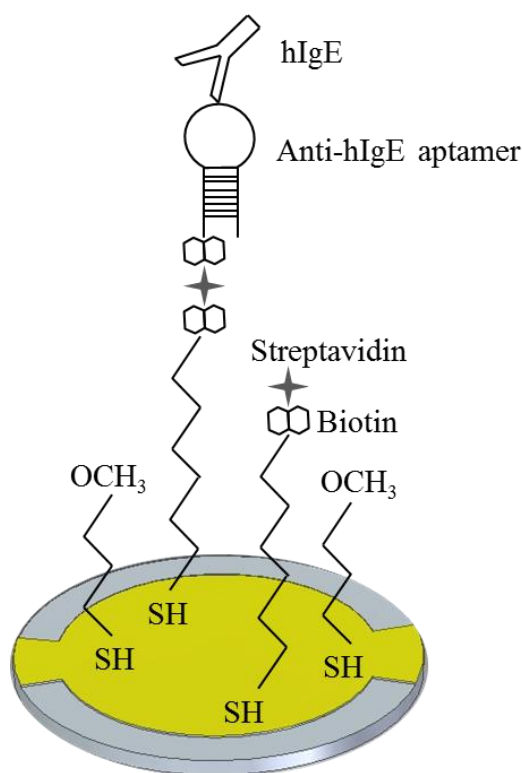


Figure 6.1. Specific binding of hIgE to D17.4 biotinylated anti-hIgE aptamer functionalised on a QCR.

6.2.3 Steps of excitation

AT-cut thickness-shear-mode 14.3 MHz QCRs were used for carrying out experiments involving detection of hIgE with varying concentrations. Subsequent frequency sweeps (10 sec, 0.1 V) and fixed frequency scans (10 sec, 0.1 V) were taken in PBS in order to establish

a baseline for 5 min. The measurement interval between two successive cycles of a combined scan comprising frequency sweep followed with a fixed frequency scan was 3 sec. PBS was injected (at 40 $\mu\text{L}/\text{min}$) over anti-hIgE aptamer immobilised QCR while the baseline measurements were taken. A solution of hIgE at a given concentration prepared from diluting 1mg/mL hIgE stock in PBS was introduced (at 40 $\mu\text{L}/\text{min}$) over the functionalised QCR following the baseline measurements for 30 min in order to aid binding of hIgE with anti-hIgE aptamer. Similar frequency sweeps and FFD scans as mentioned above were taken during hIgE injections as well. The concentration of hIgE varied from 1.31-10.53 nM. Resonant frequency from a particular frequency sweep was estimated from fitting of the experimentally obtained electrical admittance data using the BVD model (Figure 3.1). The essential parameters including resonant frequency (f_{PBS}), feed through capacitance and the characteristic shear wave impedance, were obtained before baseline measurements using a set of three frequency sweeps taken during PBS injection over functionalised QCR. Functionalised QCR was driven at f_{PBS} for all the fixed frequency scans taken during PBS and hIgE injections. The resonant frequency from each fixed frequency scan was evaluated using Eq. 3.9.

6.3 Quantification of Human Immunoglobulin E

The primary objective was to demonstrate the feasibility of FFD technique for hIgE detection using aptamer as a receptor. QCR resonant frequency shifts obtained from FS and FFD techniques were compared. A satisfactory agreement was observed during the baseline and hIgE binding phases for a given concentration (Figures 6.2 & 6.3) which showed the feasibility of further simplifying QCR quantification method. Further, use of aptamer as a receptor permits regeneration [261] of sensor surface. However, regeneration is not the motive of this research. FFD and FS techniques were capable of detecting 1.31 nM hIgE in 45 sec (based on $\text{SNR} > 5$) employing a sample volume of 30 μL , which corresponds to a mass of 7.5 ng.

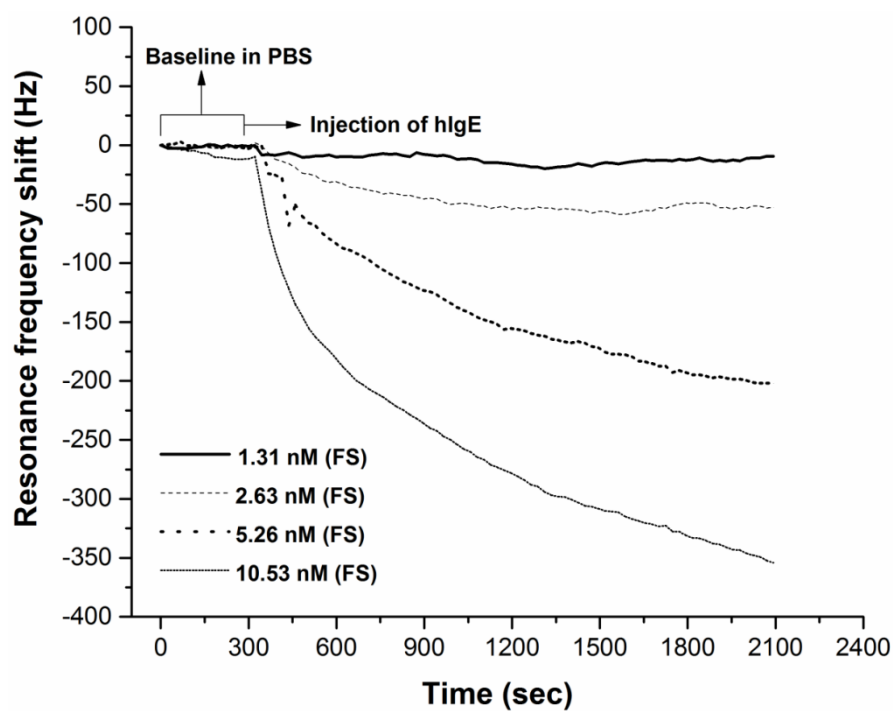


Figure 6.2. Resonant frequency shifts due to hlgE binding using FS method for different concentrations.

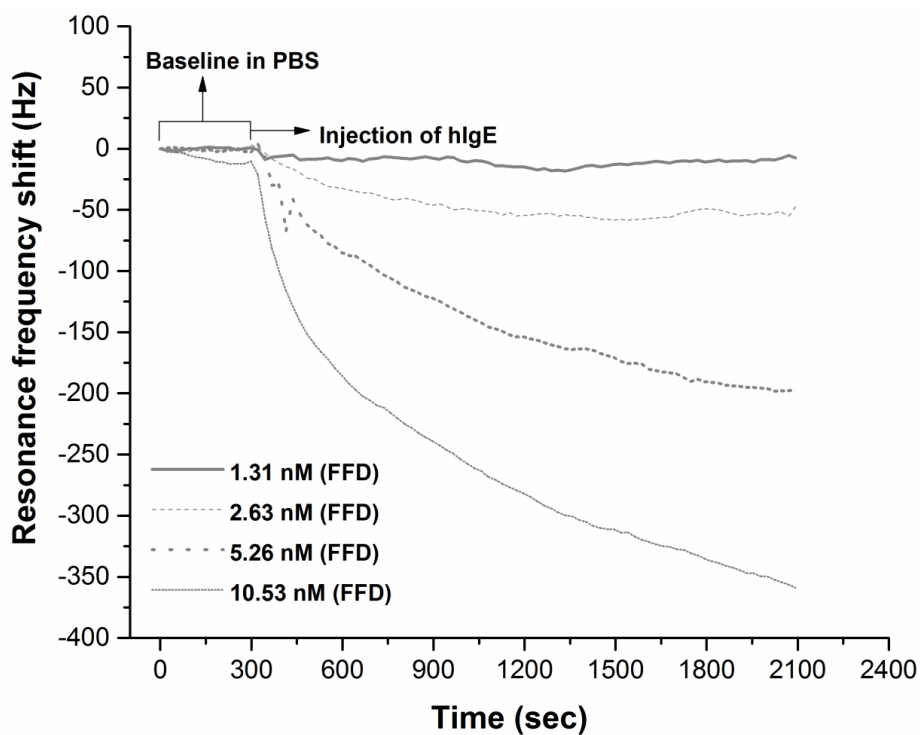


Figure 6.3. Resonant frequency shifts due to hlgE binding using FFD method for different concentrations.

The resonant frequency shifts obtained from FFD and FS methods after 30 min of hIgE injection for different concentrations were also in good agreement with each other (Figure 6.4).

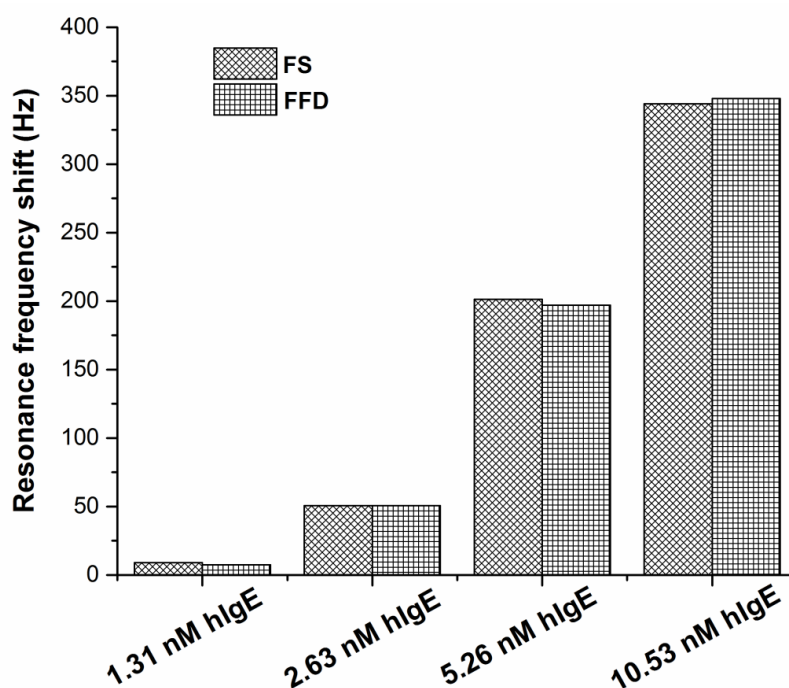


Figure 6.4. Resonant frequency shifts 30 min after hIgE injection for different concentrations.

The agreement between the two methods regarding estimated resonant frequency shifts after 30 min of hIgE injections for different concentrations varied between -4.21 and +3.94 Hz (Figure 6.5). Such differences are due to inaccuracies in calibration procedure. Discrepancies between FFD and FS estimates can be further improved through accurate calibration procedure as mentioned in Section 4.3.6.

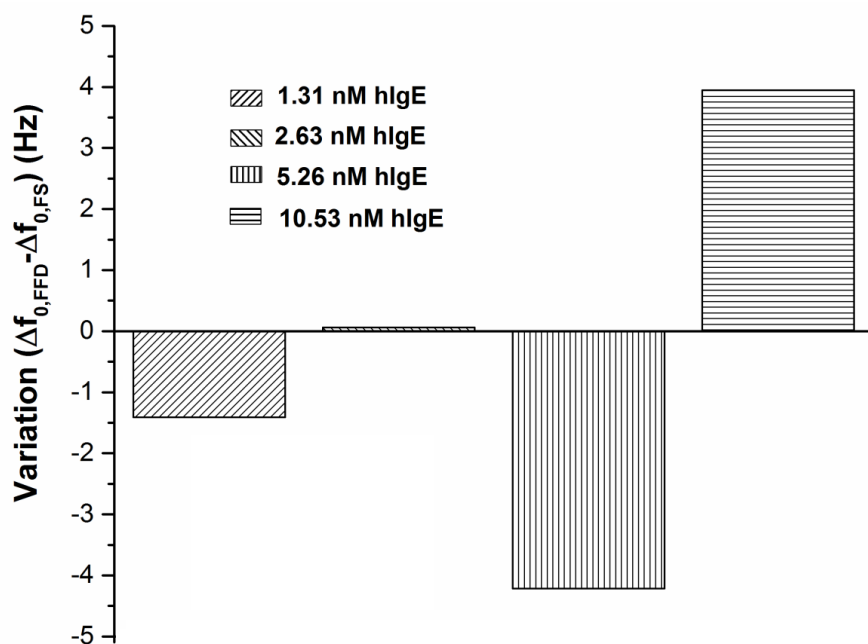


Figure 6.5. Variation in resonant frequency shifts after 30 min for FFD method (at different hlgE concentrations) method with respect to FS method.

The average baseline noises determined using Allan deviation for FS and FFD methods were 0.91 Hz (SD, 0.135 Hz) and 0.80 Hz (SD, 0.137 Hz) respectively. Similarly, variation of SNR for different hlgE concentrations were constructed for FS (Figure 6.6) and FFD (Figure 6.7) techniques as described in Section 5.4. The response of hlgE was fitted with a linear function () for FS and FFD techniques as it fell on the linear regime of sigmoidal curve. LODs were calculated based on a SNR value greater than for FS and FFD techniques. The obtained LODs from FS (0.96 nM) and FFD (1 nM) techniques were comparable with the critical concentration of IgE (1.53 nM) need for allergy diagnosis [226–228]. Although, the minimum detectable concentration achieved in this work (1.31 nM) is two orders of magnitude lower in comparison to the reported minimum detectable concentration (13.15 pM) using 10 MHz QCR, it can be improved by performing an optimisation of the appropriate aptamer and the buffer. Overall, a simple, fast, easy-to-use and robust biosensing technique (i.e. FFD) has been demonstrated for hlgE detection, which is potentially low cost as fabrication is scalable.

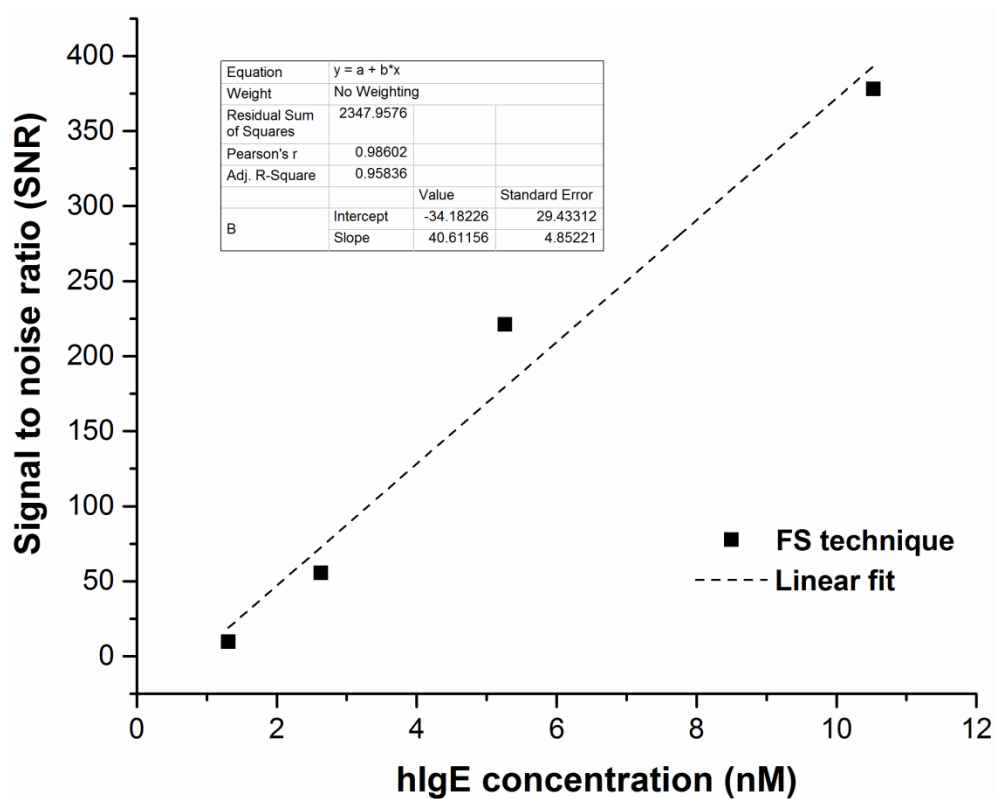


Figure 6.6. Variation of SNR at different hlgE concentrations for frequency sweep (FS) method

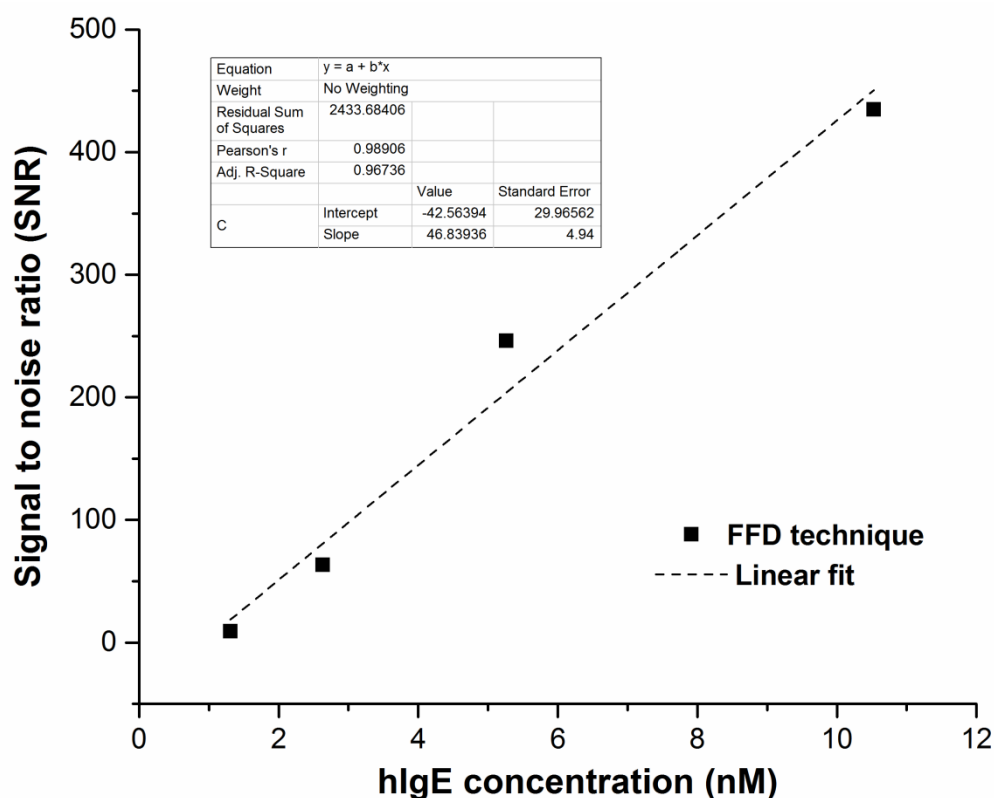


Figure 6.7. Variation of SNR at different hlgE concentrations for FFD method

6.4 Investigation of Specificity

Human Immunoglobulin G (hIgG) comprising a molecular weight of 150 kDa was selected as the negative control for non-specific adsorption study as it has a molecular weight similar to hlgE (190 kDa). PBS was injected (at 40 μ L/min) over anti-hlgE aptamer immobilised QCR for 5 min followed by immediate injection (at 40 μ L/min) of 10.53 nM hlgG solution for 30 min. Similar frequency sweeps and fixed frequency scans were taken during PBS and hlgG injections as mentioned in Section 6.2.3. Variation of resonant frequency shifts with time determined from FS and FFD methods for both baseline and non-specific adsorption phases were in good agreement with each other (Figures 6.8 & 6.9).

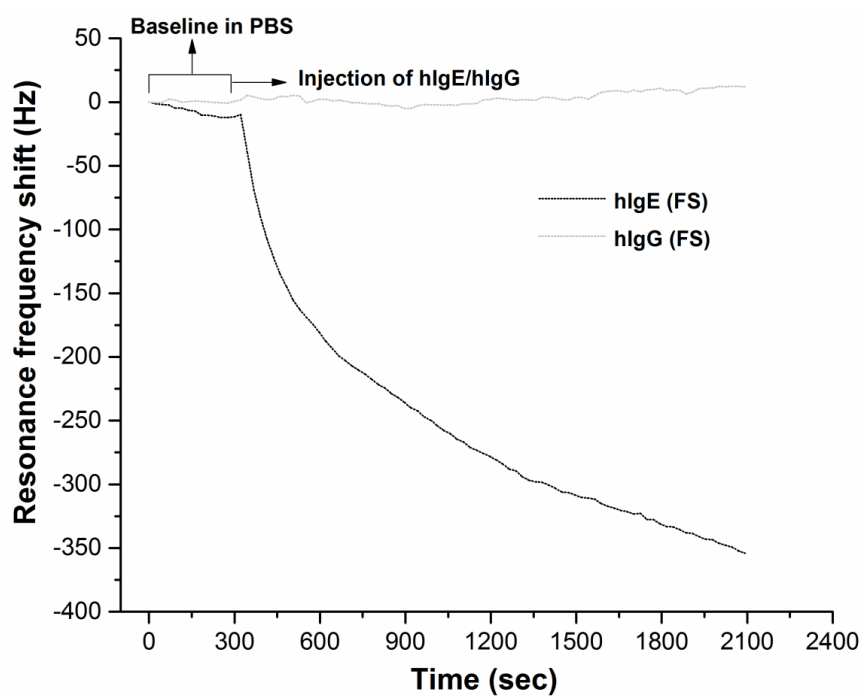


Figure 6.8. Resonant frequency shifts due to binding of 10.53 nM hIgE and 10.53 nM hIgG on functionalised QCRs using FS method

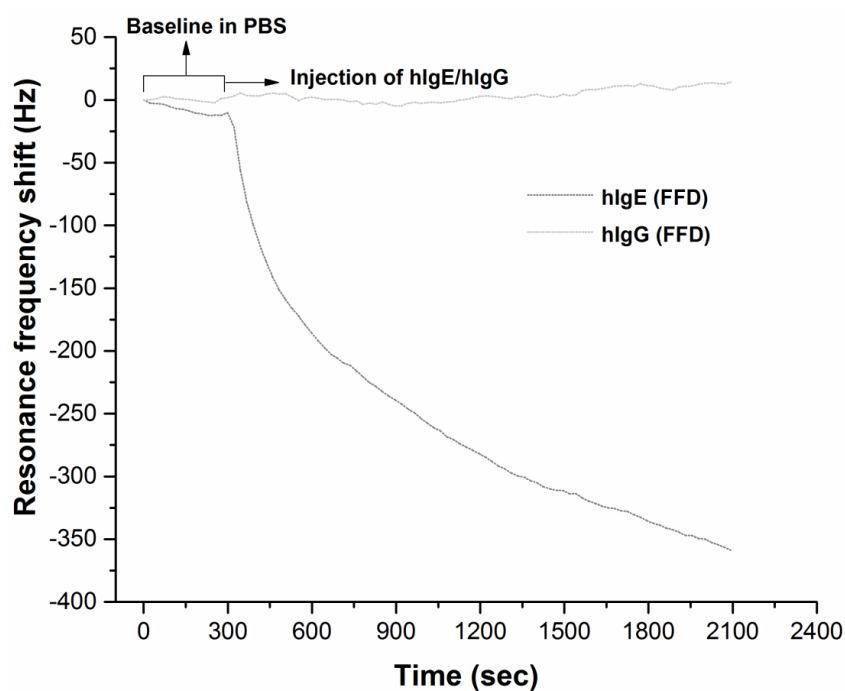


Figure 6.9. Resonant frequency shifts due to binding of 10.53 nM hIgE and 10.53 nM hIgG on functionalised QCRs using FFD method

Results obtained from non-specific adsorption experiment pertaining to 10.53 nM hIgG were compared with that obtained from specific adsorption experiment involving the same concentration of hIgE. Resonant frequency shifts estimated using FS and FFD techniques after 30 min of 10.53 nM injection of hIgE over anti-hIgE aptamer functionalised QCR were approximately 28.83 and 26.68 times the resonant frequency shifts obtained after 30 min of 10.53 nM injection of hIgG over anti-hIgE aptamer functionalised QCR using FS and FFD techniques respectively (Figure 6.10).

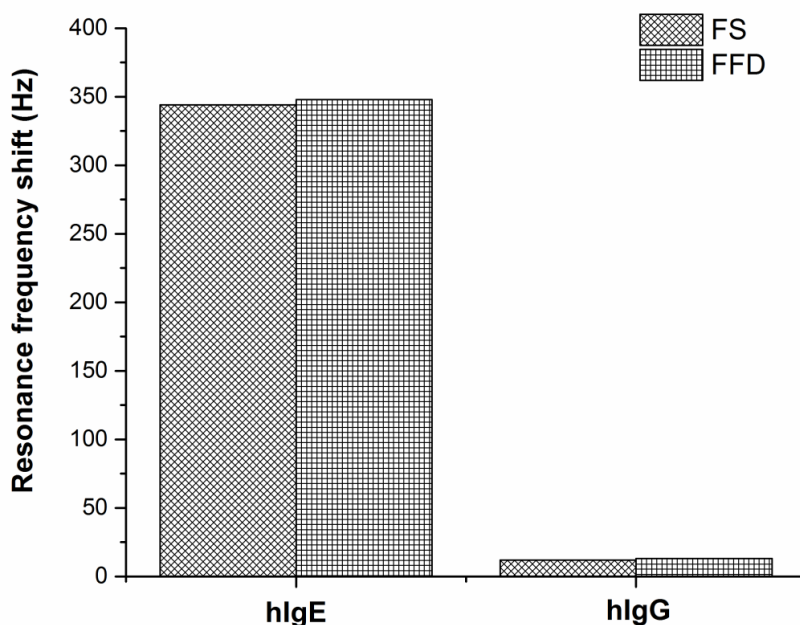


Figure 6.10. Resonant frequency shifts 30 min after 10.53 nM hIgE and hIgG injections

The variation in resonant frequency shifts with respect to FS method for specific and non-specific adsorption studies employing FFD method were approximately 3.94 and 1.10 Hz respectively (Figure 6.11). Use of D17.4 biotinylated anti-hIgE aptamer is believed to be primary reason for the specificity of the developed acoustic sensor.

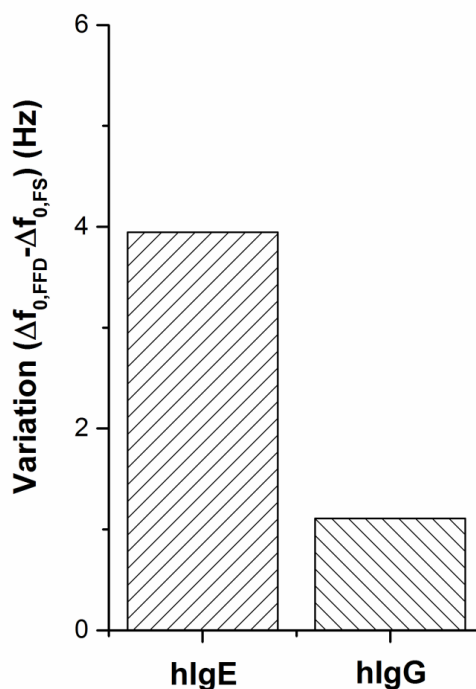


Figure 6.11. Variation in the resonant frequency shifts after 30 min from FFD method for 10.53 nM hlgE and 10.53 nM hlgG with respect to frequency sweep (FS) method.

6.5 Conclusion

Detection of immunoprotein levels in human serum favour diagnosis of hypersensitivity reactions. In particular, human immunoglobulin E (hlgE) serves as the potential biomarker for allergic diseases. Online measurement of hlgE using a fast and inexpensive sensing technique is therefore of utmost importance. Real-time measurement capability, portability and ease of use features of QCM therefore aid in hlgE detection. Herein, a simple QCM based technique termed as FFD technique has been demonstrated for hlgE detection. The agreement of the FFD with conventional frequency sweep (FS) method suggests that hlgE binding can be quantified with reasonable accuracy from each impedance data point. The minimum detectable hlgE concentration (1.31 nM) is comparable with the threshold concentration of hlgE needed for allergy diagnosis. The selectivity of the developed sensor was investigated employing FFD method by estimating the resonant frequency shift occurring from non-specific interaction of 10.53 nM hlgG solution in PBS with anti-hlgE aptamer immobilised QCR. Negligible resonant frequency shift (13.04 Hz) was obtained in comparison to the resonant frequency shift (347.96 Hz) obtained for specific interaction of 10.53 nM hlgE solution in PBS with anti-hlgE aptamer immobilised QCR. The higher affinity

of D17.4 biotinylated anti-hIgE aptamer contributed towards encouraging sensitivity and specificity of the developed IgE sensor.

Chapter 7

Conclusion and Future Work

7.1 Achievement of Objectives

This thesis was essentially triggered by the unmet need for simplicity, online measurement, multiplexability and high time resolution features in a biomolecular recognition tool. The introductory literature review therefore focused on mechanical resonators such as cantilevers [35], surface acoustic wave devices [45], quartz crystal microbalance [55] and film bulk acoustic resonator [262] which involve minimal intermediate sample preparation and washing procedures for investigation of biomolecular interactions. The possibility of miniaturisation and integration with electronics makes mechanical resonators a potential contender of a simplified biomolecular interaction tool. Quartz crystal microbalance has been used to illustrate a mechanical resonator in this thesis. QCM is commonly used to study real-time biomolecular interactions by measuring shifts in resonant frequency and dissipation of a quartz-crystal-resonator.

Commonly used resonant frequency and dissipation quantification methods associated with QCR such as admittance analysis [53] or QCM-D [141], which require repeated sweeps or ringing, are limited in time resolution (~1 second) due to the need for numerical fitting and averaging. This restricts the ability to study transient processes including gas-to-surface adsorption-desorption kinetics [145], protein-DNA interactions and protein folding [75], to name a few which mostly occur in a time scale ranging from sub-millisecond to few milliseconds. Further literature survey revealed a QCR quantification technique with improved time resolution. A 5 MHz QCR [83] was used for studying the shifts in resonant frequency and dissipation at multiple resonance modes with 10 ms time resolution through utilisation of single frequency measurements. However, single frequency measurement method can only be used to study specific transient processes which are strictly repetitive in nature. Such a method is also applicable over a narrow bandwidth.

Consideration of the challenges of state-of-the-art QCM techniques led to the development of a novel analytical method for measurement of QCR resonant frequency and dissipation by utilising a fixed frequency drive (FFD). FFD method terminates the need for fitting and measurement dead time unlike conventional methods and is applicable over a broad bandwidth. Quick needle touches were made on the self-assembled-monolayer-functionalised surface of a 14.3 MHz QCR in order to mimic a very fast dynamic process like

mass binding. Resonance frequency shifts associated with the transient processes of the touches were recorded with $\sim 112 \mu\text{s}$ resolution for the first time using continuous FFD technique. FFD measurements depicted 1 order of magnitude lower baseline noise (0.3 Hz) compared to continuous frequency sweep measurements (5.4 Hz) for a thiolated surface in phosphate buffered saline solution at a data acquisition rate of $\sim 66.5 \text{ ms}$.

FFD technique has been used for demonstration of label free detection of a small gram negative bacterial infection biomarker namely N-hexanoyl-L-Homoserine lactone ($\sim 199.2 \text{ Da}$), using molecular imprinted polymer nano particle as the receptor. A limit of detection of 180 nM has been obtained, which is comparable with the nanomolar threshold concentration necessary for initiation of infections in humans. The feasibility of FFD method has been shown for direct detection of large immunoprotein such as immunoglobulin E ($\sim 190 \text{ kDa}$) using aptamer as the receptor. A limit of detection of 1 nM has been achieved, which is commensurable with the critical concentration (1.53 nM) necessary for prediction of human allergies. An optimisation of bioassays can lead to improvement of LODs for both the biomolecules.

The agreements between FS and FFD techniques can be further improved with a more accurate calibration. This fixed frequency based simple method for determination of resonance frequency and dissipation of a mechanical resonator, with no need for averaging or fitting would potentially allow online integration and truly realtime measurements with low noise and also allow a significant greater multiplexability.

7.2 Comparison of FFD with state-of-the art techniques

Comparison of FFD technique with state-of-the art techniques based on simplicity, time resolution and future potentials for online integration and multiplexability have been discussed below.

1. FFD enables simpler estimation of resonant frequency, dissipation factor and motional branch parameters of a QCR

A resonance mode of an AT-cut quartz crystal resonator has been modelled using the Butterworth-Van Dyke (BVD) equivalent circuit. With the drive frequency and characteristic wave impedance known, the resonant frequency shift along a process can be quantified directly from the derived analytical expression using the measurements of motional reactance i.e. imaginary component of motional impedance recorded from a fixed frequency drive (**Eq. 3.19**). The dissipation factor can be quantified from the experimentally measured

motional resistance, i.e. the real component of motional impedance (**Eq. 3.20**). Accurate calibration and prior evaluation of shunt capacitance would result in true estimate of motional impedance. The drive frequency, which is fixed and set by the experimenter, is a known parameter and does not need to be located in the vicinity of QCR resonant frequency. The driving frequency can be located anywhere within ~ 2.8 resonance bandwidth of a 14.3 MHz QCR (**Figure 3.1**).

It has been shown that the characteristic wave impedance remains practically constant (**Figure 3.1**), and therefore the value measured using frequency sweep method at the beginning of a process on the surface, such as binding, can be used throughout the process. The characteristic wave impedance for a batch of QCRs at a given fundamental resonant frequency can also be provided by the QCR manufacturer. Hence, the FFD method allows real-time determination of resonant frequency and dissipation factor from each acquired impedance data point without the need for any fitting or averaging as in frequency sweep and ring down methods [85]. Oscillator circuits employing a frequency counter can easily estimate resonant frequency of a QCR devoid of any numerical fitting or analytical modelling. When the QCR oscillation amplitude is known, the dissipation factor can be estimated using an automatic gain control oscillator circuit [120]. The frequency sweep method can independently quantify QCR motional branch parameters including motional resistance, motional inductance and motional capacitance apart from resonant frequency and dissipation factor. Motional inductance and motional capacitance can be estimated from FFD, oscillator circuit and ring down methods provided that the QCR characteristic wave impedance magnitude is known to the user. Motional resistance can be directly measured using the FFD method whereas for oscillator circuit and ring down methods, use of a BVD model is essential for its estimation.

2. FFD provides high time resolution and low noise

Resonant frequency shifts can be read out using a continuous fixed frequency drive (FFD) at a time resolution or time per measurement that is practically limited either by the duration of transient processes on the QCR or the digital data acquisition time period of the instrument, whichever is dominant. For the commonly used 5 MHz QCR and the 14.3 MHz QCR used in this dissertation, the transient oscillation (, where Q is the quality factor and ω_0 is the fundamental angular resonant frequency in rad/s) durations are $\sim 215.3 \mu\text{s}$ and $\sim 44.5 \mu\text{s}$ respectively. The digital data acquisition rate for impedance for the measurement device used for the doctoral study is 30.518 kHz, i.e. a time period of $\sim 32.7 \mu\text{s}$. Hence, for 14.3

MHz QCRs, the time resolution of resonant frequency shift measurement using the fixed frequency drive (FFD) method presented in this thesis is governed by the transient processes. Quick needle touch experiments were carried out on a self-assembled-monolayer (SAM) functionalised 14.3 MHz QCR in phosphate buffered saline (PBS) solution and resonant frequency shift features with rise time front of $\sim 112 \mu\text{s}$ (rise time measured between transient levels 10% and 90% [154]) were distinguished using the fixed frequency drive (FFD) method (**Figure 4.15**).

Shifts in resonant frequency of a 5 MHz QCR were previously estimated with a time resolution of 10 ms by applying a phase shifted Lorentzian fit function on the deviation of electrical admittance data obtained from fixed frequency drive for a given time with respect to a reference state [83]. However, those fixed frequency measurements were only applicable for repetitive electrochemical processes involving square wave amperometry and cyclic voltammetry. A time resolution of 10 ms has been reported for frequency shift measurements using oscillator circuitry for a 10 MHz QCR [73]. Minimum time per measurement for oscillator circuits can be as low as 0.8 ms with use of reciprocal frequency counters [135]. The fastest resonant frequency readout obtained from a bench-top VNWA network analyser used in this dissertation was 0.8 s, although the time taken for a frequency sweep was ~ 66.5 ms. A highest time resolution of 5 ms has been provided by Q-Sense Company for resonant frequency measurement using ring down method [84] for a 5 MHz QCR. However, 5 ms time resolution is not enough to monitor biomolecular interactions [263,264] occurring in μs scale. Further, such a figure has not been substantiated by experimental data. Moreover, the analysis should be carried out with the same sensor as the noise from the sensor surface dominates. Hence, in this work, the comparison has been restricted with the available network analyser.

Estimation of Allan deviation baseline noises using the FFD method for a SAM-functionalised 14.3 MHz QCR for 30 data acquisition rates ranging from 32.7 to 41888481.2 μs have been explored in this dissertation (**Figure 4.14**). A study was also performed using FS method for the same SAM immobilised 14.3 MHz QCR for 3 data acquisition rates comparable to those used during fixed frequency measurements (**Table 4.1**). The baseline noise (0.3 Hz) measured using FFD by a custom built network analyser for a data acquisition rate of ~ 59.18 ms was found more than one order of magnitude lower than the noise (5.4 Hz) measured using FS by a commercial bench-top network analyser for a data acquisition rate of ~ 66.5 ms, which was the fastest rate setting on the bench-top analyser. The noise level

provided by Q-Sense for ring down studies for SAM immobilised surfaces was 2 Hz [54]. In general, the noise resolution [265] for an oscillator circuit using reciprocal counter is given by

$$\Delta f = \frac{1}{2\pi \Delta t} \quad (7.1)$$

where f is the QCR fundamental resonant frequency, Δt is the time resolution and f_c is the reciprocal counter frequency. Hence, 60 ms time resolution and 1 GHz reciprocal counter will provide a noise resolution of 0.24 Hz for 14.3 MHz QCR which is comparable with FFD method, although use of reciprocal counter increases the complexity of circuitry [135]. Allan deviation baseline noise has been estimated for anti-corrosion cataphoretic painting coated 5 MHz QCR in distilled water for data acquisition rates ranging from 1 sec to 2hrs 46 mins [133]. The noise varied from 0.021 to 0.84 Hz [133]. To the best knowledge of the author, studies relating baseline noises at different instrument data acquisition time periods for a given sensor surface are missing in the QCR literature for ring down method.

3. FFD has the future potential for on-line integration and multiplexability applications

In order to have a wide spread applicability; there is a need for a sensing technique that is suitable for large scale manufacturing. Hence, the solution is to incorporate the technique in integrated circuits or chips. The implementation of frequency sweep [73] and oscillator circuit [266] methods in printed circuit boards have already being explored for QCRs. An integrated circuit was also fabricated for estimation of QCR dissipation factor using ring down method [267]. However, exploration of integrated circuits for QCR resonant frequency estimation employing ring down method is missing in the literature. The estimation of QCR parameters using an analytical formula for the FFD method is simple and unique which gives it the strength to be applied on chip or multiplex with a much simpler circuit than other methods. With no need for a frequency synthesizer, a radio-frequency pulse generator or a fast analog-to-digital converter as in frequency sweep, ring down and oscillator circuit methods, FFD method potentially allows simple, inexpensive and low-power measurement of QCR resonant frequency and dissipation factor shifts, which can be implementable on printed circuit boards. The entire electronics excluding the QCR such as quartz driver circuit and data acquisition unit can also be implemented on a single silicon chip. Such a feature will enable online measurements in industrial processes [5,268,269] using QCRs.

Frequency sweep, ring down and oscillator circuit techniques have been explored for multiplexability applications [54,101,102,270–281]. In case of multiplexed detection, multiple QCR sensor surfaces are often fabricated on a single piece of quartz substrate. Such a sensor is termed as multi-channel monolithic QCM (MQCM). All QCRs can be driven in parallel by using separate driver circuits such as oscillators, pulse generators or frequency synthesizer for individual QCR and then synchronising the output from each of them by means of a central processing unit. This makes the integrated electronic circuit bulky in size, thereby making it difficult to be multiplexed. QCRs can also be driven in series mode with use of electronic switches which add complexity to the circuit. With no need for numerical fitting, the FFD method potentially favours a greater degree of multiplexing than the existing methods.

MQCMs are affected by acoustic and electrical couplings among adjacent QCRs, which need to be addressed for its effective operation. The acoustic wave generated in one QCR interferes with another after propagation through the quartz. Electrical coupling can arise due to the residual charges on QCRs [278] from multiple drives or from the electrical impedance of the solution flowing between the adjacent QCR fluidic channels [101]. Such interferences modulate the QCR responses, thereby generating erroneous results. Acoustic coupling in any method can be suppressed by various ways. Use of an inverted mesa quartz substrate [101] is one of the methods. Insertion of polydimethylsiloxane wall between adjacent QCR electrodes positioned on a single quartz [101] has also been tried for suppression of acoustic coupling. Maintaining a certain distance between the QCRs [280] also favours suppression of acoustic coupling. Spurious electric couplings in frequency sweep and FFD methods between the QCRs can be eliminated during data processing to a high degree from prior calibration; thereby relaxing requirements for design complexity, such as shielding. Calibration for frequency sweep method can be more cumbersome as the MQCM device needs to be calibrated at each and every frequency with a certain frequency span, whereas in FFD method, calibration at a single frequency such as bare QCR resonant frequency can suffice the requirement. For oscillator circuit and ring-down methods cancelling electric coupling apparently are immensely more problematic as there is no reported evidence of any defined calibration procedure in the existing literature, which limits the degree of multiplexability using these methods.

7.3 Future Investigations

Fixed frequency drive method has been validated in this dissertation with a quartz crystal resonator for biomolecular applications. But in principle, the method is applicable over a range of mechanical resonators. Also, FFD measurements depend on the accuracy of the calibration procedure. Although, it has been successfully used for direct detection of two classes of biomolecules with a range of molecular weight, the use of 14.3 MHz QCR in conjunction with FFD method does not appear to be sensitive in comparison to other conventional techniques for the explored biomolecules (**Tables 5.1 & 6.1**). Improvement of LOD through use of improved assay is extremely important. This involves use of appropriate receptors, quality surface functionalisation and use of appropriate buffer. Some important future studies which can be carried out based on these limitations have been discussed below.

7.3.1 Exploring detection of C6-HSL and hIgE in clinical samples

The initial feasibility studies of FFD technique have been carried out by detecting C6-HSL and hIgE in spiked PBS solution which is relatively simpler in nature. However, in reality, such biomarkers are usually found in complex samples such as serum [225], saliva [173], stools [173] and sputum [181] at lower concentrations along with several other molecules that are often larger and possess high concentrations. Hence, it is important to test the capability of FFD technique for detection of C6-HSL and hIgE in clinical specimen.

7.3.2 Exploring detection of other biomarkers

FFD technique has been successfully used for detection of two biomarkers namely N-hexanoyl-L-homoserine lactone (199.2 Da) and total human immunoglobulin E (190 kDa) in spiked PBS solution. Hence, it will be impressive to extend the concept of FFD for detection of other category of biomarkers namely cardiac disease biomarker such as C-reactive protein [282] (25.1 kDa), prostate cancer biomarker such as prostate specific antigen [282] (26 kDa) and Alzheimer's disease biomarker such as clusterin [163] (75 kDa) in spiked PBS solution for the initial feasibility studies. In the later stage, detection should be carried out in clinically relevant samples for each biomarker.

7.3.3 Exploring higher frequencies for sensitive detection

The theoretical absolute mass sensitivity for resonant frequency shift of a QCR is given by the following equation [62]:

where f_0 and ρ are the unperturbed fundamental resonant frequency, density, frequency constant and overtone number or resonance mode (1 for fundamental mode) of QCR. It is evident from Eq. 7.2 that the theoretical absolute mass sensitivity is directly proportional to the term f_0^3 as the other parameters are constant for any AT cut QCR.

Streptavidin detection experiment was carried out using FS and FFD methods by driving a 14.3 MHz QCR around its 3rd overtone, i.e. 42.9 MHz. Frequency sweeps (0.1 sec, 0.6 V) and FFD scans (0.1 sec, 0.6 V) around 42.9 MHz were taken every 1 min during injection of PBS (at 40 μ L/min) for 15 min. 42 nM streptavidin solution in PBS was then flowed (at 40 μ L/min) over SAM immobilised 14.3 MHz QCR surface (Section 4.3.3) for 15 min and similar FS and FFD measurements were also taken during injection of streptavidin. The average shift in resonant frequency from the baseline (measurements before streptavidin injection) due to streptavidin-biotin binding (Figure 7.1), calculated from the fixed frequency drive or FFD (-570.7 Hz) was within 2 % of that estimated from the frequency sweep method by fitting the experimentally recorded impedance employing the BVD model (-579.3 Hz). Baseline noise estimated from FS and FFD methods were 4.1 and 4.4 Hz respectively. Assuming (3rd overtone mode) and 14.3 MHz, the estimated maximum resonant frequency shift using Sauerbrey theory (Eq. 4.2) comes out to be -690 Hz. The measured resonant frequency shift values at 3rd overtone were found to be within -18% of the theoretical estimate for both FS and FFD methods.

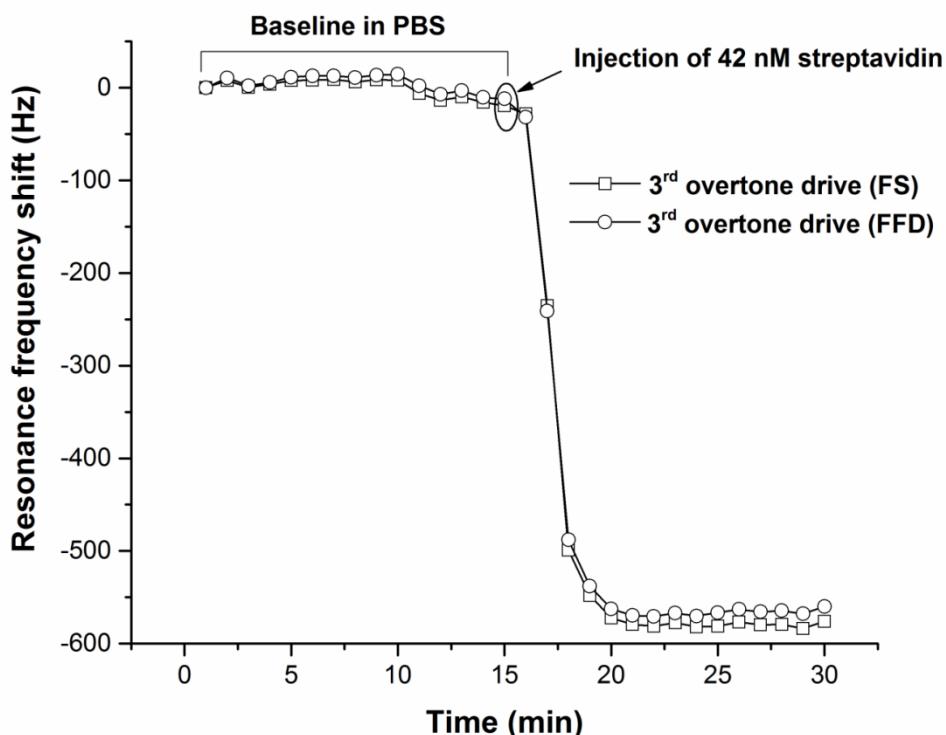


Figure 7.1. 3rd overtone resonant frequency shift due to streptavidin binding using frequency sweep and FFD methods with 1 min measurement interval.

50 MHz QCR also called mesa quartz crystal was also explored for streptavidin detection. 50 MHz QCR was cleaned using a different protocol which has been reported in Section A.11. Continuous frequency sweeps at 665 ms data acquisition rate employing SDR network analyser were taken every ~1.25 sec during 15 min flow of PBS followed with subsequent flow of 2.5 µg/mL streptavidin (at 40 µL/min) over biotin thiol immobilised 50 MHz QCR for another 15 min. The result obtained from 50 MHz QCR was compared with the streptavidin binding result for 14.3 MHz QCR. Resonant frequency shifts due to biotin-streptavidin interaction obtained for 50 MHz QCR was approximately -2080 Hz as compared with -140 Hz for 14.3 MHz QCR (Figure 7.2) for the same concentration of streptavidin (42 nM). Baseline noise estimated for 14.3 and 50 MHz QCRs were 1.5 and 3.5 Hz respectively. The measured resonant frequency shift value (-2080 Hz) using 50 MHz QCR was within -26% of the theoretical estimate (-2806 Hz) obtained using Sauerbrey equation (Eq. 4.2). Hence, exploration of higher order resonance modes of 14.3 MHz QCR or using a QCR with an unperturbed fundamental resonance greater than 14.3 MHz will be interesting in terms of sensitive detection of disease biomarkers.

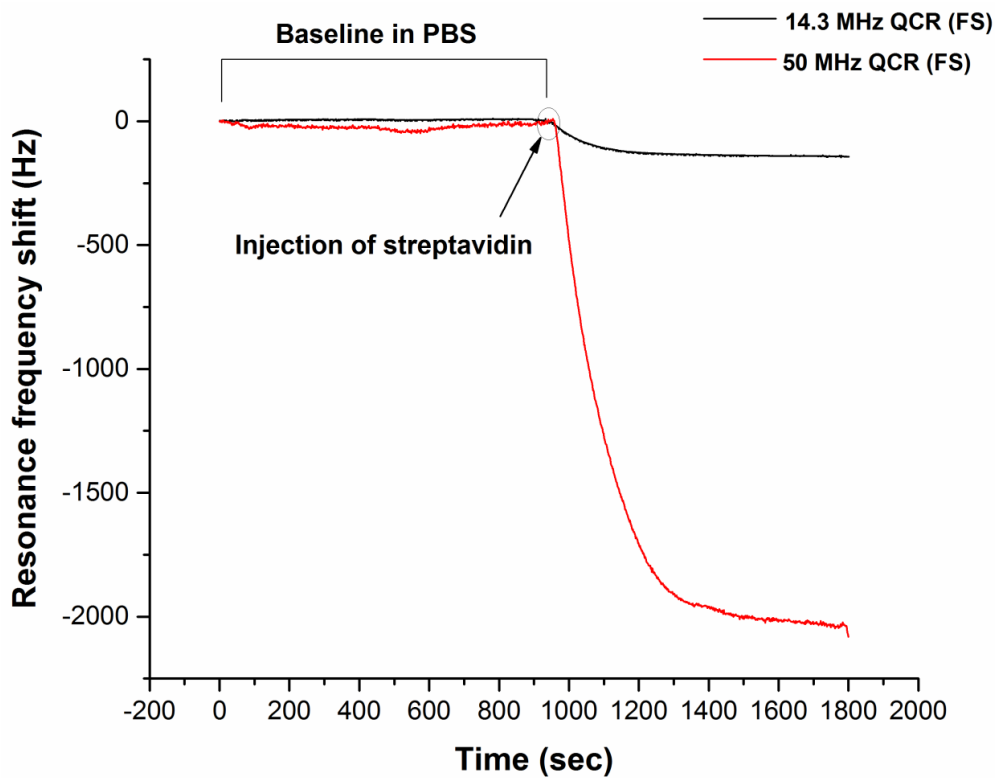


Figure 7.2. Variation of resonant frequency shift in continuous frequency sweep mode involving streptavidin binding experiments employing SDR network analyser for 14.3 and 50 MHz QCRs.

However, it is evident from Section A.9 that the quality factor reduces with the increase in fundamental resonant frequency of QCR and is enhanced at higher modes of vibration of a QCR. The minimum obtainable Allan deviation noise for a liquid loading of a QCR is given by the following [153]:

$$\dots\dots\dots (7.3)$$

where f_0 is the nominal frequency, η and ρ , absolute viscosity and density of the liquid. Hence, noise increases with increase in frequency and therefore, there is a limit to which higher frequencies can be explored for sensitive detection depending on the attainable experimental noise and quality factor.

7.3.4 Modification of calibration procedure

Accuracy of measurements depends on the calibration procedure. The calibration has been performed between two terminals of short, open and loaded electrical circuits (Figure 7.3).

Ideally, the calibration should be performed using the same circuits between the electrodes on a printed circuit board (PCB) with which a QCR attaches for enabling electrical connection (Figure 7.4). The ends of a resistor and a wire need to be soldered on the PCB for taking measurements from loaded and short circuits respectively in the proposed set up. Ideal calibration procedure aids in getting rid of parallel capacitance contribution appearing from PCB.

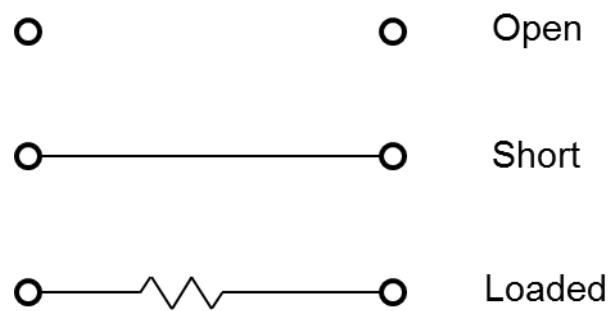


Figure 7.3. Calibration set up used for this dissertation

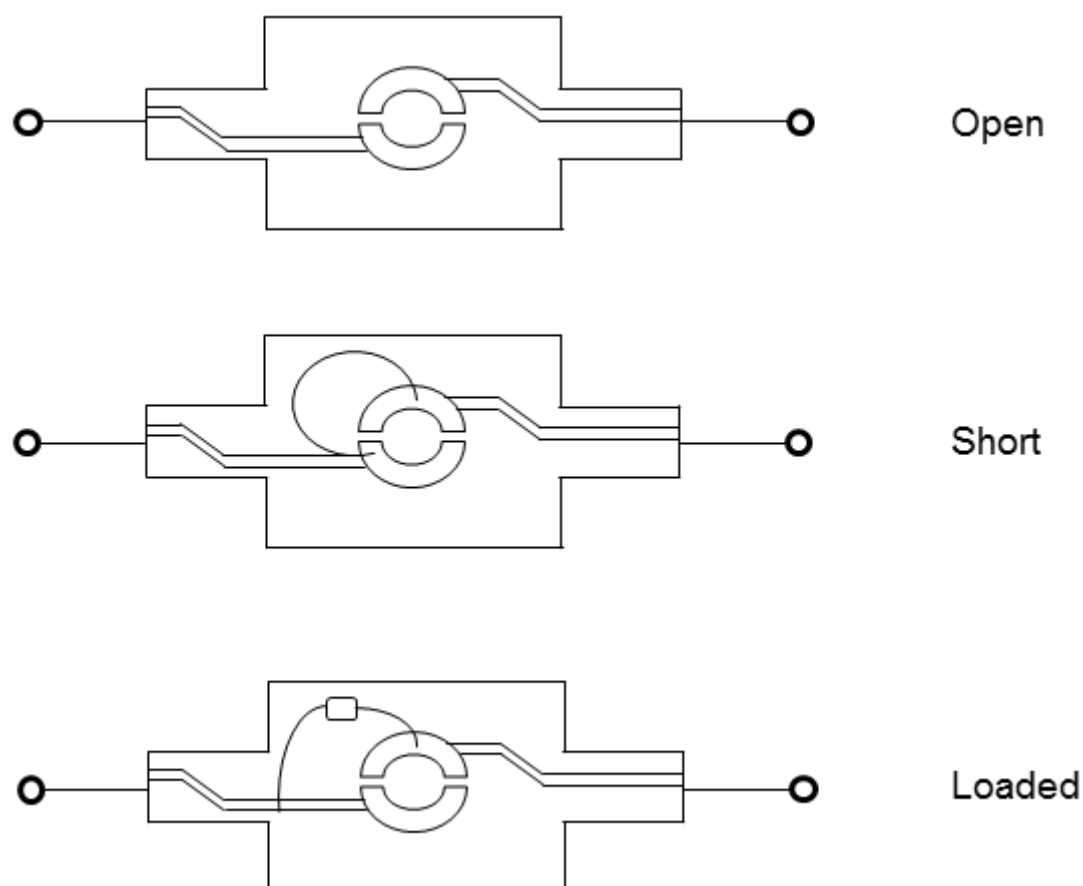


Figure 7.4. Modified calibration set up for accurate measurements

7.3.5 Exploring self-oscillating quartz crystal resonator

The QCR is driven at a fixed frequency using a frequency generator for all the FFD experiments reported in this dissertation. However, a single quartz crystal resonator in a self-oscillating mode such as an automatic gain control (AGC) oscillator circuit using encapsulated quartz can serve as a generator of fixed frequency drive for a sensor QCR, as well and provide temperature compensation (Figure 7.5). The oscillator and the sensor QCRs can be also in the same liquid for better compensation. There is no need for any frequency counter as impedance meter attached to the sensor QCR can be utilised for its passive interrogation of resonant frequency and dissipation using FFD method. Such a mode of operation will be useful for online integration and multiplexability applications.

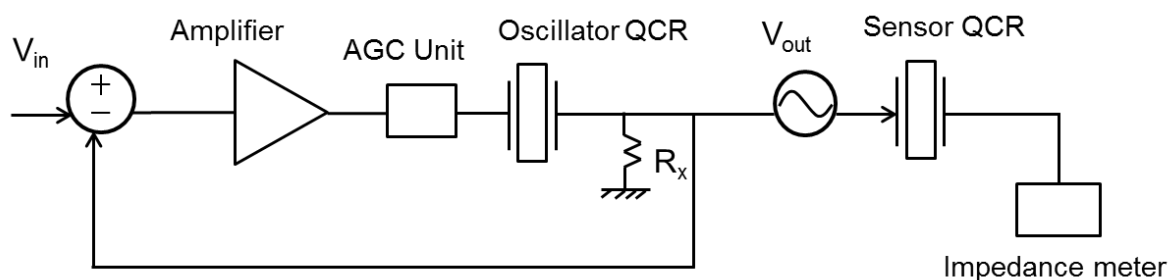


Figure 7.5. A simplified block diagram for a self-oscillation mode

7.3.6 Exploring applications apart from biomolecular measurements

The main focus of this dissertation has been on validation of fixed frequency drive technique for biomolecular measurements. But this can be applied over a range of other applications where acoustic sensors can be applied such as humidity sensing [283], adsorption studies of crude oil on different surfaces [284], health monitoring of equipment [285], viscosity studies of industrial oils [286], and studying the tribological characteristics of immersed alumina and stainless steel surfaces in charged aqueous suspensions [287], to name a few.

Appendix A

Supplementary Information

A.1 Calibration Theory

In reality, it is difficult to measure the voltage and the current between the terminals of an AT-cut QCR directly. Hence, true current and true voltage between the terminals of a QCR is obtained by the linear combination of the measured voltage and current at any two points inside the complex quartz network. Let, V_1 and V_2 are the voltages at any two arbitrary points inside the quartz network. Hence, true current and true voltage can be written as follows:

$$I = G_1 V_1 + G_2 V_2 \quad (A.1)$$

$$V = V_1 + V_2 \quad (A.2)$$

In Eqns. (A.1) and (A.2), constants G_1 and G_2 are dimensionless while constants V_1 and V_2 have the dimensions of conductance. The unknowns G_1 , G_2 , V_1 and V_2 can be evaluated from the following four conditions.

- True voltage at short circuit is zero.

$$V = 0 \quad (A.3)$$

V_1 and V_2 are the voltages measured at the two arbitrary points under short circuit condition.

- Let, V_0 be the open circuit voltage measured by cathode ray oscilloscope.

$$I = 0 \quad (A.4)$$

and are the voltages measured at the two arbitrary points under open circuit condition.

- True current at open circuit is zero.

(A.5)

and are the voltages measured at the two arbitrary points under short circuit condition.

- Let, be the impedance of the circuit under loaded condition.

(A.6)

and are the voltages measured at the two arbitrary points under loaded condition. The constants , , and obtained by solving simultaneously Eqns. (A.3), (A.4), (A.5) and (A.6) are as follows:

(A.7)

(A.8)

(A.9)

$$\frac{V_1}{V_2} = \frac{Z_1}{Z_2} \quad (A.10)$$

Using Eqns. (A.7), (A.8), (A.9) and (A.10), true voltage (), current () and the impedance () between the terminals of a QCR can be rewritten as follows:

$$V = \frac{V_1}{V_2} \cdot V_2 \quad (A.11)$$

$$I = \frac{V}{Z} \quad (A.12)$$

$$Z = \frac{V}{I} \quad (A.13)$$

and are the measured voltages at the two arbitrary points inside the complex network of the resonator.

Validation of the calibration theory has been carried out for known components (Table A.1).

Type of electrical circuit	Theoretically measured impedance ()	Calibrated impedance ()	% Error with respect to theory
180 resistor in series with 100 pF capacitor	211.63	215.076	1.6
200 resistor in series with 56 pF	281.96	284.352	0.8

capacitor			
-----------	--	--	--

Table A.1. Comparison of impedance magnitudes between theoretically and experimentally measured techniques

A.2 Explanation of Mathematica code for producing the calibration file (abcd.dat)

The following segment narrates the steps to obtain an abcd.dat file using Wolfram Mathematica.

startDir = "B:\\LboroCalibration"; : The following command allows the user to choose the starting directory where all the necessary files related to calibration are stored.

SetDirectory[SystemDialogInput["Directory",startDir, WindowTitle -> "Select a directory for to open calibration file OC, SC, LC, VC"]]

The abovementioned command allows the user to select a directory from his workspace for opening the calibration files. OC, SC, LC and VC represent the frequency scan files related to open circuit, short circuit, loaded circuit and diode measurements (voltage circuit) using ADT machine.

Output:

\\ws3.lboro.ac.uk\\MM-AlzheimersDiagnostics\\ArnabGuhaProject\\Arnab

Experimental Data\\LU2_20160606_calibration_14_3_MHz

{vCal, calRes} = {1.853⁻, 100.0} : The following command allows the user to enter the value of measured rms voltage obtained from oscilloscope and the resistance of the loaded circuit.

Output: {2.62054,100.0}

FilesinDir = FileNames["LU2_calibr*.fms", IgnoreCase -> True] : The following command lists all the calibration files with 'fms' extension from the required directory starting with the phrase 'LU2_calibr'.

Output:

```
{LU2_calibr_14_3_MHz_20160606_100_ohm_LC_0000.fms,  
LU2_calibr_14_3_MHz_20160606_100_ohm_LC_0001.fms,  
LU2_calibr_14_3_MHz_20160606_1_853_V_rms_VC_0000.fms,  
LU2_calibr_14_3_MHz_20160606_1_853_V_rms_VC_0001.fms,  
LU2_calibr_14_3_MHz_20160606_SC_0000.fms,  
LU2_calibr_14_3_MHz_20160606_SC_0001.fms,  
LU2_calibr_20161102_14_3_MHz_OC_0000.fms,  
LU2_calibr_20161102_14_3_MHz_OC_0001.fms}
```

DirFile = MatrixForm[Transpose[{Table[i, {i, 1, Length[FilesinDir]}], FilesinDir}],

TableAlignments -> Left] : The following command lists the calibration files in a tabular manner.

Output:

```
1 LU2_calibr_14_3_MHz_20160606_100_ohm_LC_0000.fms  
2 LU2_calibr_14_3_MHz_20160606_100_ohm_LC_0001.fms  
3 LU2_calibr_14_3_MHz_20160606_1_853_V_rms_VC_0000.fms  
4 LU2_calibr_14_3_MHz_20160606_1_853_V_rms_VC_0001.fms  
5 LU2_calibr_14_3_MHz_20160606_SC_0000.fms  
6 LU2_calibr_14_3_MHz_20160606_SC_0001.fms
```

7 LU2_calibr_20161102_14_3_MHz_OC_0000.fms

8 LU2_calibr_20161102_14_3_MHz_OC_0001.fms

namPatt = {"OC_", "SC_", "LC_", "VC_"} : The following command is used to assign the open circuit, short circuit, loaded circuit and voltage circuit calibration files.

Output:

{OC_, SC_, LC_, VC_}

```
{OCfile, SCfile, LCfile, VCfile} = Table[FilesinDir  
[Last[Position[StringCases[FilesinDir, namPatt[i]], namPatt[i]]][1]], {i,  
Length[namPatt]}]
```

The abovementioned command lists the name of the last file among each category namely open circuit, short circuit, loaded circuit and voltage circuit calibration files respectively.

Output:

LU2_calibr_20161102_14_3_MHz_OC_0001.fms,

LU2_calibr_14_3_MHz_20160606_SC_0001.fms,

LU2_calibr_14_3_MHz_20160606_100_ohm_LC_0001.fms,

LU2_calibr_14_3_MHz_20160606_1_853_V_rms_VC_0001.fms

fCalibr[a_, b_, c_, d_, M1_, M2_] = {{a, b}, {c, d}}.{M1, M2}

The abovementioned command defines the calibration equation.

Output:

{a M1 + b M2, c M1 + d M2}

fCalibrMx[calMatr_, M1_, M2_] := calMatr.{M1, M2}

The abovementioned command establishes relationship between calibration matrix and the arbitrary voltages obtained under different conditions.

```
{TrueCurrent[a_, b_, c_, d_, M1_, M2_], TrueVoltage[a_, b_, c_, d_, M1_, M2_]} =  
fCalibr[a, b, c, d, M1, M2]
```

The above command defines the calibration equation for true current and true voltage respectively.

Output:

```
{a M1 + b M2, c M1 + d M2}
```

```
Fabcd[M1oc_, M2oc_, M1sc_, M2sc_, M1Lc_, M2Lc_, M1vc_, M2vc_, RL_, vVcalib_] =  
{ { (M2oc (M1sc M2Lc - M1Lc M2sc) vVcalib) /  
  ( (M1oc M2Lc - M1Lc M2oc) (M1vc M2sc - M1sc M2vc) RL) ,  
  - (M1oc (M1sc M2Lc - M1Lc M2sc) vVcalib) /  
    ( (M1oc M2Lc - M1Lc M2oc) (M1vc M2sc - M1sc M2vc) RL) } ,  
  {  $\frac{M2sc \text{ vCal}}{M1vc M2sc - M1sc M2vc}$  ,  $\frac{M1sc \text{ vCal}}{-M1vc M2sc + M1sc M2vc}$  } };
```

The above command line assigns the mathematical expressions for a, b, c and d respectively.

```
extradrop = 40;
```

The above command assigns the maximum number of rows to be dropped off from the beginning of any frequency scan file.

```
headSize = 31;
```

The above command assigns the header size of any frequency scan file.

```
header = Take[Import[VCfile, "TSV"], headSize - 2];
```

The above command reduces the head size of VC file to 29.

```
Dimensions [Header]
```

The above command will display the current head size.

Output: {29}

```
hdList = MatrixForm[{Range[Length[header]], header}]
```

The above command will display the list of headers of VC file in matrix format.

Output:

```
( 1      {Frequency mode scan}
 2      {}
 3      {Scan time, 0.100012}
 4      {Amplitude, 0.1}
 5 {Central frequency, MHz, 14.3}
 6      {Span frequency, MHz, 0.2}
 7      {Decimation factor, 2}
 8      {}
 9      {DDS1 settings:}
10      {Function, 1}
11      {}
12      {DDS2 settings:}
13      {Function, 1}
14      {Amplitude, 1.}
15      {Gain1, 5.015}
16      {Gain2, 5.015}
17      {}
18      {DDS3 settings:}
19      {Function, 0}
20      {Amplitude, 1.}
21      {Gain1, 51.943}
22      {Gain2, 51.943}
23      {}
24      {DDS4 settings:}
25      {Function, 0}
26      {Amplitude, 1.}
27      {Gain1, 51.943}
28      {Gain2, 51.943}
29      {}
)
```

```

headerOC = Take[Import[OCfile, "TSV"], headSize];
CdOCd = Drop[Import[OCfile, "TSV"], headSize];
headerSC = Take[Import[SCfile, "TSV"], headSize];
CdSCd = Drop[Import[SCfile, "TSV"], headSize];
headerLC = Take[Import[LCfile, "TSV"], headSize];
CdLCd = Drop[Import[LCfile, "TSV"], headSize];
headerVC = Take[Import[VCfile, "TSV"], headSize];
CdVCd = Drop[Import[VCfile, "TSV"], headSize]; (*Data*)

```

The above command lines allow the user to import and drop off the head size from all category of fms files, i.e., OC, SC, LC and VC.

```

gains1F = {headerOC[[15, 2]], headerSC[[15, 2]], headerLC[[15, 2]], headerVC[[15, 2]]}

```

The above command will read and display 1F gain among the header portion of each file.

Output:

```

{5.015, 5.015, 5.015, 5.015}

```

```

gains3F = {headerOC[[21, 2]], headerSC[[21, 2]], headerLC[[21, 2]], headerVC[[21, 2]]}

```

The above command will read and display 3F gain among the header portion of each file.

Output:

```

{51.943, 51.943, 51.943, 51.943}

```

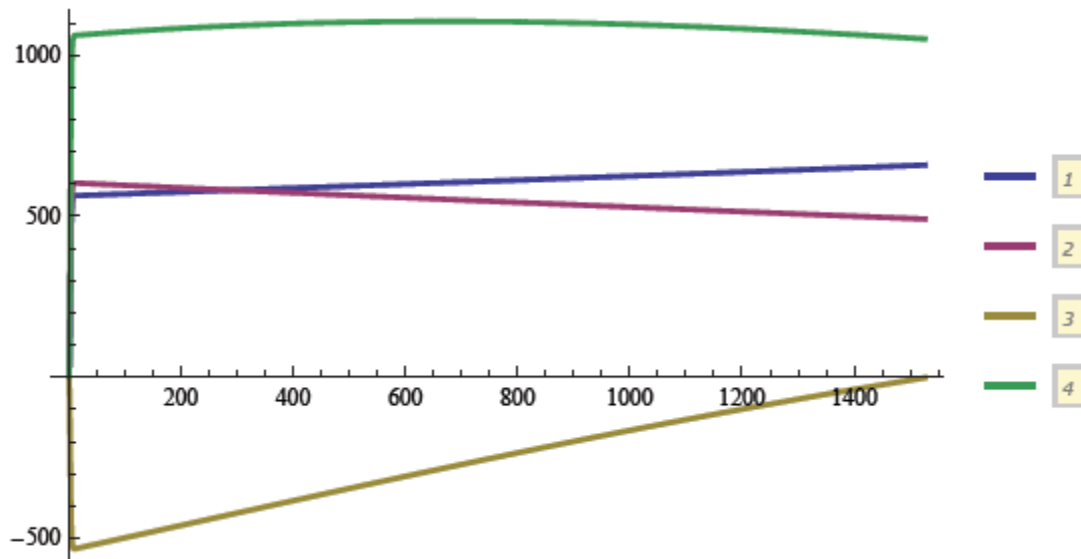
```

ListLinePlot[{CdOCdT[[1]], CdOCdT[[2]], CdSCdT[[1]], CdSCdT[[2]]},
  PlotStyle → Thick, PlotLegends → Automatic]

```

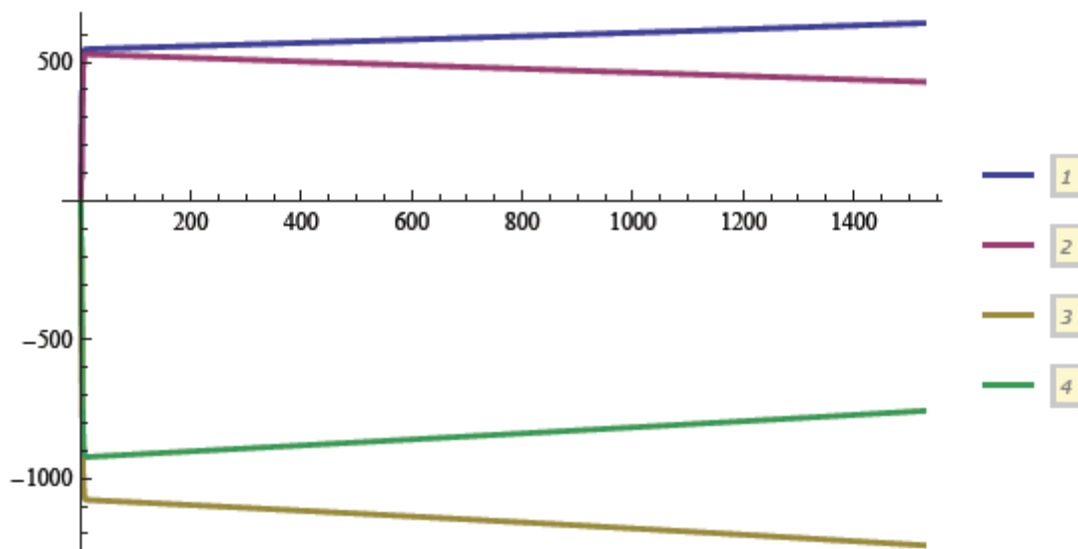
The above command transposes the column matrix to a row matrix for a particular file and plots it with the number of observations. For example, **CdOCd^T[[1]]** represents the transposed form of the first column of data for a fms scan file of an open circuit measurement.

Output:



```
ListLinePlot[{CdVCd[[1]], CdVCd[[2]], CdVCd[[3]], CdVCd[[4]]},
  PlotStyle -> Thick, PlotLegends -> Automatic]
```

Similarly, the above command will give the output displayed below:



```
datLength = Dimensions[CdOCd][[1]]
```

The above command will display the number of data points pertaining to 1st column of an open circuit fms file.

Output: **1526**

```
{headerOC[[3]], headerSC[[3]], headerLC[[3]], headerVC[[3]]}
```

The above command will display the third row of the headSize for each category of file.

Output:

```
{ {Scan time, 0.100012}, {Scan time, 0.100012},  
  {Scan time, 0.100012}, {Scan time, 0.100012} }
```

```
{Dimensions[CdOCd][1], Dimensions[CdSCd][1],  
  Dimensions[CdLCd][1], Dimensions[CdVCd][1]}
```

The above command allows the user to verify the number of data points pertaining to each file.

Output: **{ 1526, 1526, 1526, 1526 }**

```
sizeOK = (Dimensions[CdSCd][1] == datLength) &&  
  (Dimensions[CdLCd][1] == datLength) && (Dimensions[CdVCd][1] == datLength)
```

The above command verifies that whether the dimensions of a particular column in each fms file (SC, LC, VC etc) is same or not.

Output: **True**

```
inDex = Range[Length[CdOCd]] ;  
  
inDHead = Range[Length[headerOC]] ;
```

The above command allows the user to perform the indexing of the number of rows for the data and header related files for an open circuit measurement.

Length[headerOC] : The following command will display the length of the header file for an open circuit measurement file.

Output: **31**

datLength : The following command will display the length of the data points for each files.

Output: **1526**

$$\mathbf{midIdx} = \mathbf{Round}\left[\frac{\mathbf{datLength} + 0.5}{2}\right]$$

The above command finds the index number for the central data.

Output: **763**

```
{TimSc, CentF, SpanF, Decim, GainAll, AmplSc} = {headerOC[[3, 2]], headerOC[[5, 2]] 106,  
headerOC[[6, 2]] 106, headerOC[[7, 2]], headerOC[[15, 2]], headerOC[[4, 2]]};
```

The above command will provide information about scan time, central frequency, frequency span, decimation factor, 1F gain and amplitude from the header portion of the open circuit file.

Output:

```
({TimSc, CentF, SpanF, Decim, GainAll, AmplSc})
```

```
{0.100012, 1.43 × 107, 200 000., 2, 5.015, 0.1}
```

```
parF[head1F_] := {head1F[[3, 2]], head1F[[5, 2]] 106,  
head1F[[6, 2]] 106, head1F[[7, 2]], head1F[[15, 2]], head1F[[4, 2]]};
```

The above command assigns a vector for scan time, central frequency, frequency span, decimation factor, 1F gain and amplitude from the header portion each file.

```
param =
```

```
MatrixForm[{parF[headerOC], parF[headerSC], parF[headerLC], parF[headerVC]}]
```

The above command displays scan time, central frequency, frequency span, decimation factor, 1F gain and amplitude in a matrix format for each type of file.

Output:

$$\begin{pmatrix} 0.100012 & 1.43 \times 10^7 & 200\,000. & 2 & 5.015 & 0.1 \\ 0.100012 & 1.43 \times 10^7 & 200\,000. & 2 & 5.015 & 0.1 \\ 0.100012 & 1.43 \times 10^7 & 200\,000. & 2 & 5.015 & 0.1 \\ 0.100012 & 1.43 \times 10^7 & 200\,000. & 2 & 5.015 & 0.1 \end{pmatrix}$$

$$\text{nPointsEstim} = \text{Floor} \left[\frac{1.0 \times 10^9}{1024 \times 32 \text{ Decim}} \text{TimSc} \right]$$

The above command estimates the length of data points based on decimation factor and time scan.

Output: **1526**

nPointsEstim = datLength

The above command checks whether the estimated number of data points matches with that of the actual length of the data.

Output: **True**

```
cU1Aoc = (Transpose[CdOCd][1] + i Transpose[CdOCd][2]) / gains1F[1];
cU2Aoc = (Transpose[CdOCd][3] + i Transpose[CdOCd][4]) / gains1F[1];
cU1Asc = (Transpose[CdSCd][1] + i Transpose[CdSCd][2]) / gains1F[2];
cU2Asc = (Transpose[CdSCd][3] + i Transpose[CdSCd][4]) / gains1F[2];
cU1ALc = (Transpose[CdLCd][1] + i Transpose[CdLCd][2]) / gains1F[3];
cU2ALc = (Transpose[CdLCd][3] + i Transpose[CdLCd][4]) / gains1F[3];
cU1Avc = (Transpose[CdVCd][1] + i Transpose[CdVCd][2]) / gains1F[4];
cU2Avc = (Transpose[CdVCd][3] + i Transpose[CdVCd][4]) / gains1F[4];
```

The above command calculates the array of input voltages obtained from two channels pertaining to each type of circuit measurement. The above command also takes into account the real and imaginary components of the measured voltages for each kind of circuits.

```

cU1oc =
    (Transpose[CdOCd][[1, midIndx]] + i Transpose[CdOCd][[2, midIndx]]) / gains1F[[1]];
cU2oc = (Transpose[CdOCd][[3, midIndx]] + i Transpose[CdOCd][[4, midIndx]]) /
    gains1F[[1]];
cU1sc = (Transpose[CdSCd][[1, midIndx]] + i Transpose[CdSCd][[2, midIndx]]) /
    gains1F[[2]];
cU2sc = (Transpose[CdSCd][[3, midIndx]] + i Transpose[CdSCd][[4, midIndx]]) /
    gains1F[[2]];
cU1lc = (Transpose[CdLCd][[1, midIndx]] + i Transpose[CdLCd][[2, midIndx]]) /
    gains1F[[3]];
cU2lc = (Transpose[CdLCd][[3, midIndx]] + i Transpose[CdLCd][[4, midIndx]]) /
    gains1F[[3]];
cU1vc = (Transpose[CdVCd][[1, midIndx]] + i Transpose[CdVCd][[2, midIndx]]) /
    gains1F[[4]];
cU2vc = (Transpose[CdVCd][[3, midIndx]] + i Transpose[CdVCd][[4, midIndx]]) /
    gains1F[[4]];

```

The above command will provide information about the input voltages (OC, SC, LC and VC) for the central data point, i.e. for the central frequency.

cU1Avc[midIndx] - cU1vc

The above command allows the user to verify that whether the code for **cU1Avc** and **cU1vc** were written correctly or not.

Output:

```

0. + 0. i

{cU1oc, cU2oc, cU1sc, cU2sc, cU1lc, cU2lc, cU1vc, cU2vc}

```

The above command will display information about the input voltages (OC, SC, LC and VC) for the central data point, i.e. for the central frequency.

Output:

```

{121.528 + 108.751 i, -225.942 - 180.34 i, -49.5025 + 220.156 i,
 25.7908 - 213.047 i, -49.5025 + 220.156 i, 52.0799 + 128.89 i,
 -137.261 - 165.518 i, 117.808 + 95.3111 i, -230.262 - 167.984 i}

```

$$\{cC, dC\} = \left\{ \frac{cU2sc \ vCal}{cU1vc \ cU2sc - cU1sc \ cU2vc}, \frac{cU1sc \ vCal}{-cU1vc \ cU2sc + cU1sc \ cU2vc} \right\}$$

The above command will display the value of c and d based on the central data point.

Output:

```
{-0.0128377 + 0.0127698 i, -0.0147802 + 0.0120022 i}
```

```
voltMeasCal = FullSimplify[Chop[{cC, dC}.{cU1vc, cU2vc}]]
```

The above command will allow the user to recalculate the value of voltage obtained from oscilloscope measurements based on the value of c and d based on central data point.

Output:

2.69

```
abcdM = Fabcd[cU1oc, cU2oc, cU1sc, cU2sc, cU1Lc, cU2Lc, cU1vc, cU2vc, calRes, vCal]
```

The above command will display the value of a, b, c and d based on the central data point.

Output:

```
{{-0.000289635 - 0.000358546 i, -0.000151739 - 0.000211146 i},  
{-0.0128377 + 0.0127698 i, -0.0147802 + 0.0120022 i}}
```

```
voltMeasCal = FullSimplify[Chop[abcdM.{cU1Lc, cU2Lc}]]
```

The above command will display the value of true current and true voltage for a loaded circuit.

Output:

```
{0.0170084 - 0.00190652 i, 1.70084 - 0.190652 i}
```

```
Chop[ $\frac{\text{voltMeasCal}[[2]]}{\text{voltMeasCal}[[1]]}$ ]
```

The above command will allow the user to calculate the value of true impedance for the loaded circuit.

Output: **100**

cU1Lc : The following command will display the value of input voltage based on central data point for channel 1.

Output:

```
52.0799 + 128.89 i
```

```
singleFile = SystemDialogInput["FileSave", startDir, WindowTitle →  
    "Save a single frequency point calibrating file (a,b,c,d) file"]
```

The above command will allow the user to create an abcd.dat file pertaining to a single frequency point in the working directory.

Output:

```
B:\LboroCalibration\abcd_single_1f
```

```
ValueQ[singleFile]
```

The above command verifies that whether a single file has been created or not.

Output: **True**

```
If[ValueQ[singleFile], Export[singleFile,  
    {{Re[abcdM[[1, 1]], Im[abcdM[[1, 1]]], {Re[abcdM[[1, 2]], Im[abcdM[[1, 2]]},  
    {Re[abcdM[[2, 1]], Im[abcdM[[2, 1]]], {Re[abcdM[[2, 2]], Im[abcdM[[2, 2]]}}},  
    "TSV"] , Print["abcd file name not given"]]
```

The above command will export the value of a, b, c and d based on central frequency point to the single file created.

Output:

```
B:\LboroCalibration\abcd_single_1f
```

```
singleFile = .
```

The code for obtaining an abcd.dat file for central frequency point finishes here.

```
abcdMA = Table[Fabcd[cU1Aoc[[i]], cU2Aoc[[i]], cU1Asc[[i]], cU2Asc[[i]], cU1ALc[[i]],  
    cU2ALc[[i]], cU1Avc[[i]], cU2Avc[[i]], calRes, vCal], {i, 1, datLength}];
```

The above command will tabulate the complex values of a, b, c and d pertaining to each data point and will store that in array.

```
abcdMA[midIdx] = abcdM
```

The above command verifies that whether the value of a, b, c and d obtained previously for a single frequency point matches with the value of a, b, c and d obtained from the middle index of a set of data from the tabulated array.

Output: **True**

```
Dimensions[abcdMA]
```

The above command will display the dimensions of the tabulated array of a, b, c, d values.

Output: {1526, 2, 2 }

```
frMy = Table
$$\left[ \text{CentF} - \frac{\text{SpanF}}{2} + \frac{(i - 1)}{\text{datLength} - 1} \text{SpanF}, \{i, 1, \text{datLength}\} \right];$$

```

The above command will produce an array of frequency based on the data length.

```
abcdMAtoF =  
Table[{frMy[[i]], Re[abcdMA[[i, 1, 1]]], Im[abcdMA[[i, 1, 1]]], Re[abcdMA[[i, 1, 2]]],  
Im[abcdMA[[i, 1, 2]]], Re[abcdMA[[i, 2, 1]]], Im[abcdMA[[i, 2, 1]]],  
Re[abcdMA[[i, 2, 2]]], Im[abcdMA[[i, 2, 2]]]}, {i, 1, datLength}];
```

The above command will tabulate the frequency and complex values of a, b, c and d pertaining to each data point in an array format.

```
Dimensions[abcdMAtoF]
```

The above command will display the dimension of the array comprising of frequency and complex values of a, b, c and d.

Output: { 1526, 9 }

```
abcdMAtoF[midIdx]
```

The above command will display the value of frequency along with complex values of a, b, c and d of the middle index of the array **abcdMAtoF[[midIdx]]**.

Output:

```
{1.42999×107, -0.000289635, -0.000358546, -0.000151739,  
-0.000211146, -0.0128377, 0.0127698, -0.0147802, 0.0120022}
```

```
arrayFile = SystemDialogInput["FileSave", startDir,  
WindowTitle → "Save an array of frequency calibrating (a,b,c,d) file"]
```

The above command will allow the user to create an abcd.dat file pertaining to multiple frequency points in the working directory.

Output:

```
B:\LboroCalibration\abcd_array_1f
```

```
If[ValueQ[arrayFile], Export[arrayFile, abcdMAtOF, "TSV"],  
Print["abcd file name not given"]]
```

The above command will export the values of a, b, c and d based on multiple frequency points to a single file.

Output:

```
B:\LboroCalibration\abcd_array_1f
```

```
arrayFile = .
```

The code for obtaining an abcd.dat file for multiple frequency points finishes here.

A.3 Resonant frequency shift calculation using Sauerbrey theory

The thickness, t of an AT cut QCR in terms of wavelength can be written as follows:

$$t = \frac{\lambda}{2n} \quad (A.14)$$

where λ is the wavelength of the bulk acoustic wave and n is the overtone number. For the fundamental mode of vibration n is equal to 1. The overtone number n is always an odd integer for AT cut QCRs.

Using Eq. A.14, the unperturbed resonant frequency for the n order resonant mode, f_n is given by:

$$\dots\dots\dots \frac{v}{\lambda} = f \quad (A.15)$$

where v is the velocity of the bulk acoustic wave through quartz and f is the frequency constant for an AT cut quartz crystal. Hence, the unperturbed fundamental resonant frequency of a QCR can be written as follows:

$$\dots\dots\dots f = \frac{v}{\lambda} \quad (A.16)$$

$$\dots\dots\dots \lambda = \frac{v}{f} \quad (A.17)$$

Differentiating Eq. A.15 with respect to f , we get:

$$\dots\dots\dots \frac{d}{df} \left(\frac{v}{\lambda} \right) = 1 \quad (A.18)$$

$$\text{Or, } \dots\dots\dots \frac{d}{df} \left(\frac{v}{\lambda} \right) = 1 \quad (A.19)$$

The thickness, t of a quartz crystal can also be written as follows:

$$\dots\dots\dots t = \frac{A}{\rho} \quad (A.20)$$

where, ρ is the density of the quartz and A is the effective area of the QCR.

Differentiating Eq. A.20 with respect to f , we get:

$$\dots\dots\dots \frac{d}{df} \left(\frac{A}{\rho} \right) = 0 \quad (A.21)$$

$$\text{Or, } \dots\dots\dots \frac{d}{df} \left(\frac{A}{\rho} \right) = 0 \quad (A.22)$$

Using Eqs. (A.19) and (A.22), we get the following Sauerbrey's equation [50]:

$$\dots\dots\dots \frac{d}{df} \left(\frac{A}{\rho} \right) = 0 \quad (A.23)$$

Using Eq. A.15, we can write as follows:

$$\dots\dots\dots \frac{d}{df} \left(\frac{v}{\lambda} \right) = 1 \quad (A.24)$$

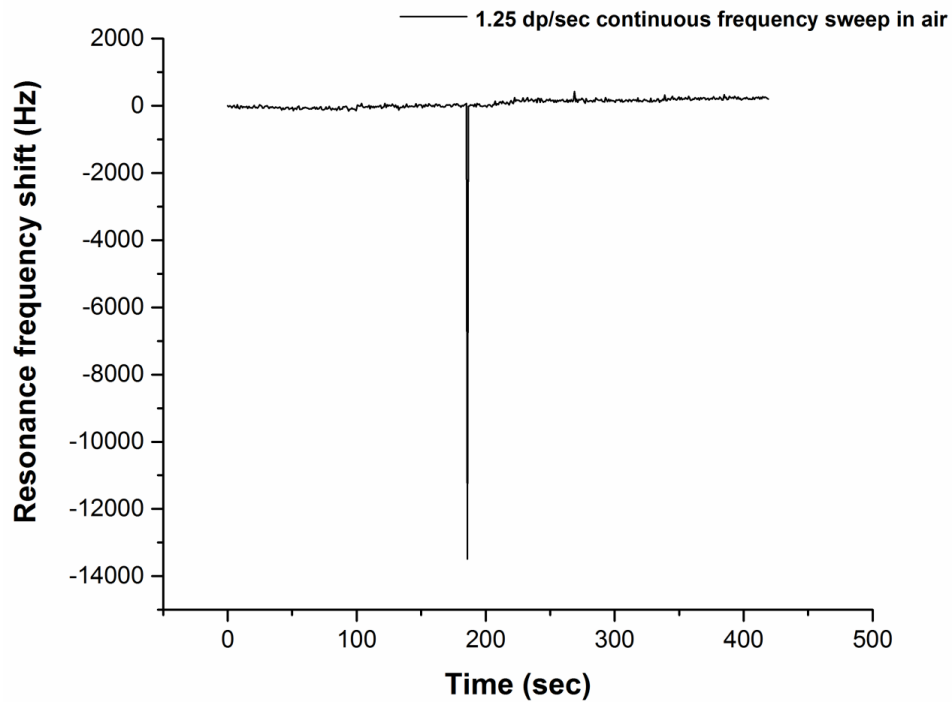


Figure A.1. Variation of resonant frequency shift with time for continuous frequency sweep in air at 1.25 Hz sampling rate employing SDR network analyzer

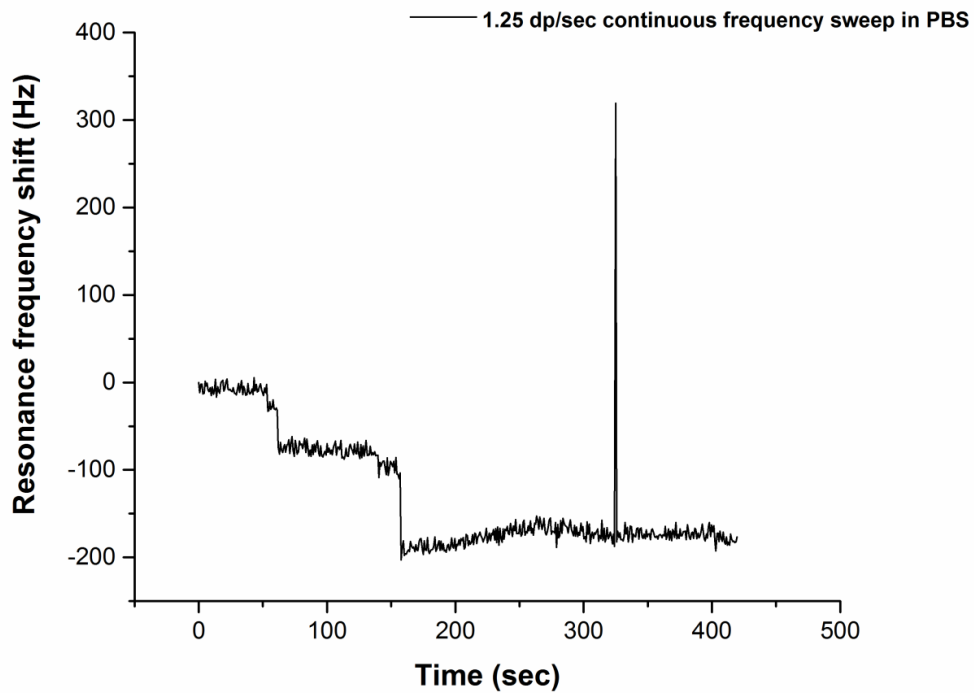


Figure A.2. Variation of resonant frequency shift with time for continuous frequency sweep in PBS at 1.25 Hz sampling rate employing SDR network analyzer

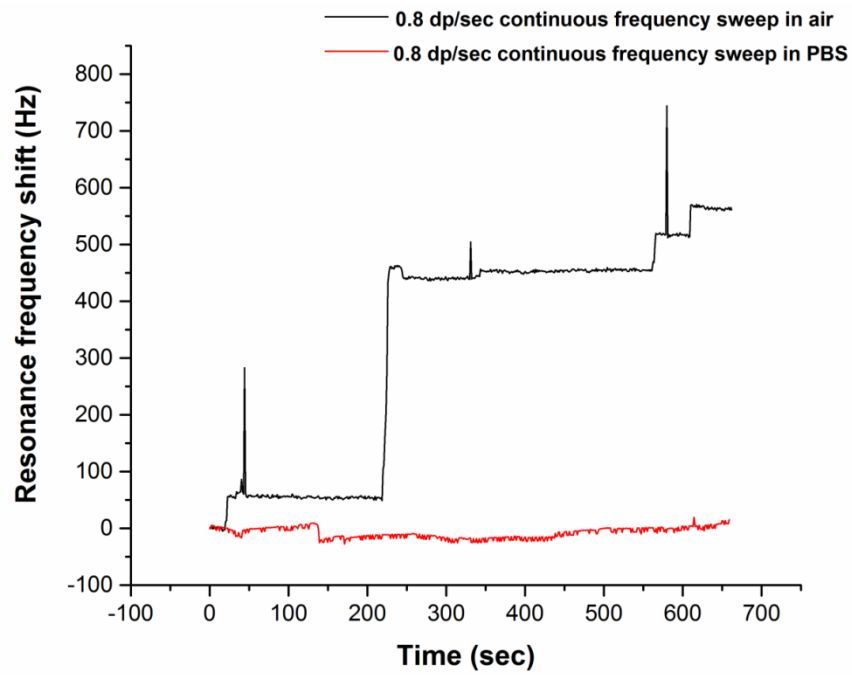


Figure A.3. Variation of resonant frequency with time for continuous frequency sweep in air and PBS at 0.8 Hz sampling rate employing SDR network analyzer

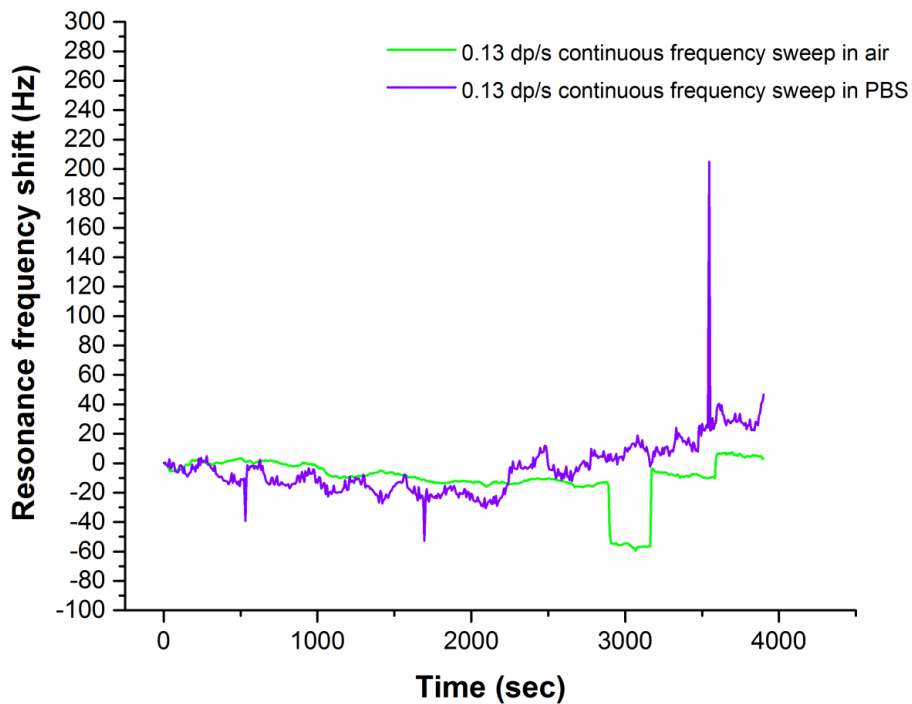


Figure A.4. Variation of resonant frequency with time for continuous frequency sweep in air and PBS at 0.13 Hz sampling rate employing SDR network analyzer

The resonant frequency of the thiol functionalized QCR was estimated before application of continuous fixed frequency drives and the QCR was connected to a custom made network analyzer (Section 4.2.1). The QCR underwent subsequent fixed frequency scans around resonance for 2147, 268, 34, 20, 10 and 5 seconds in air corresponding to data acquisition rates of 1, 7, 60, 477, 3816 and 30518 Hz respectively. The QCR was also touched for numerous occasions for less than a second during each of the continuous FFDs. After that, PBS buffer was deposited on top of the QCR using a micro pipette in such a way that there is no void space above the crystal surface. For most of the cases, rise in resonant frequency is observed in air and PBS medium, thereby indicating dominance of elastic loading over inertial loading. For 1 Hz sampling rate in air, decrease in resonant frequency was observed till 1000 secs and beyond that, a gradual increase in resonant frequency was observed. Similar phenomenon was observed for a FFD taken in PBS at the same sampling rate around ~ 1600 sec. Such observations indicated that elastic loading was dominant during the later part of the fixed frequency scan (Figure A.5). Frequent sharp rise in resonance frequencies were observed both in air and PBS for other sampling rates including 7, 60, 477, 3816 and 30518 Hz, thereby giving indication of elastic loading (Figures A.6 & A.7).

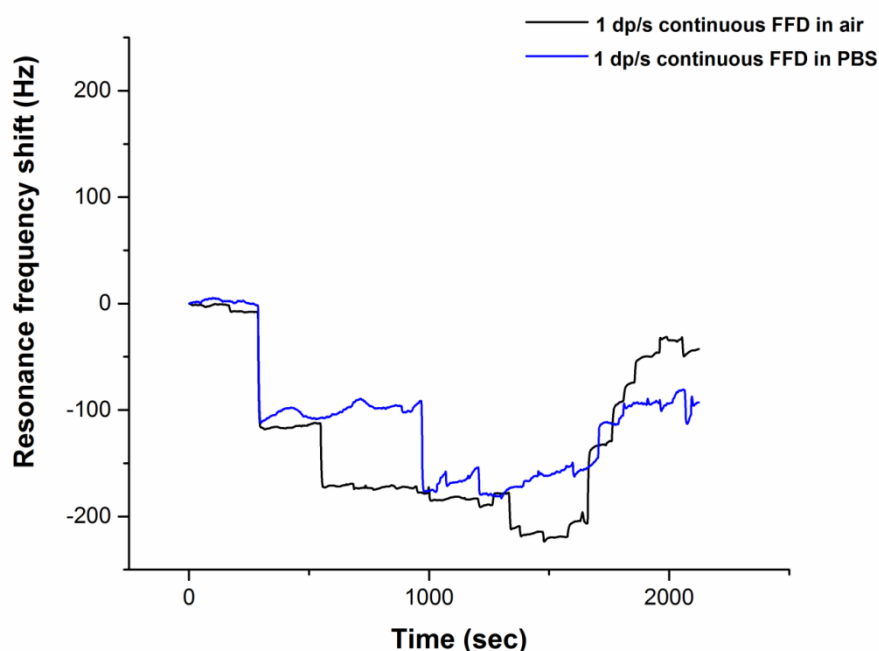


Figure A.5. Variation of resonant frequency with time for continuous FFD in air and PBS at 1 Hz sampling rate using customized network analyzer

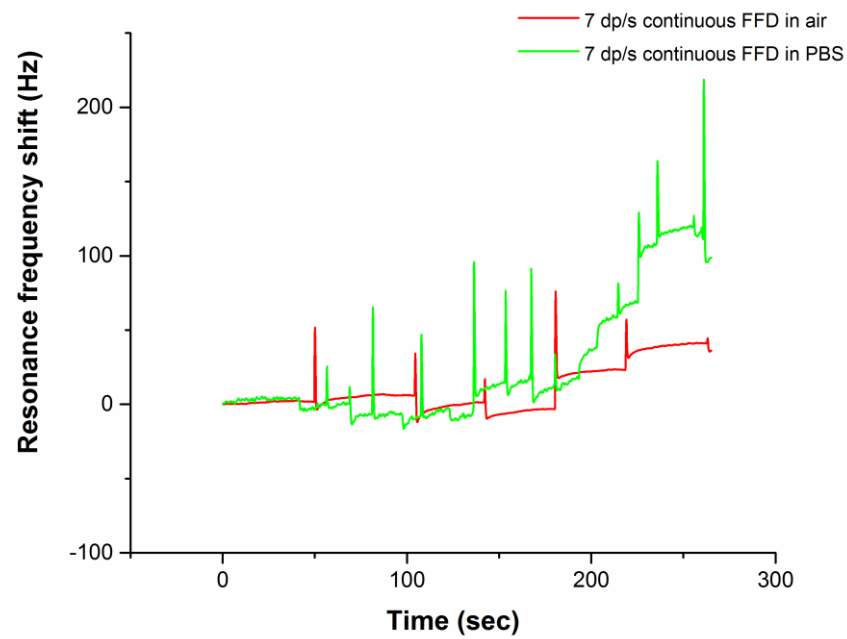


Figure A.6. Variation of resonant frequency with time for continuous FFD in air and PBS at 7 Hz sampling rate using customized network analyzer

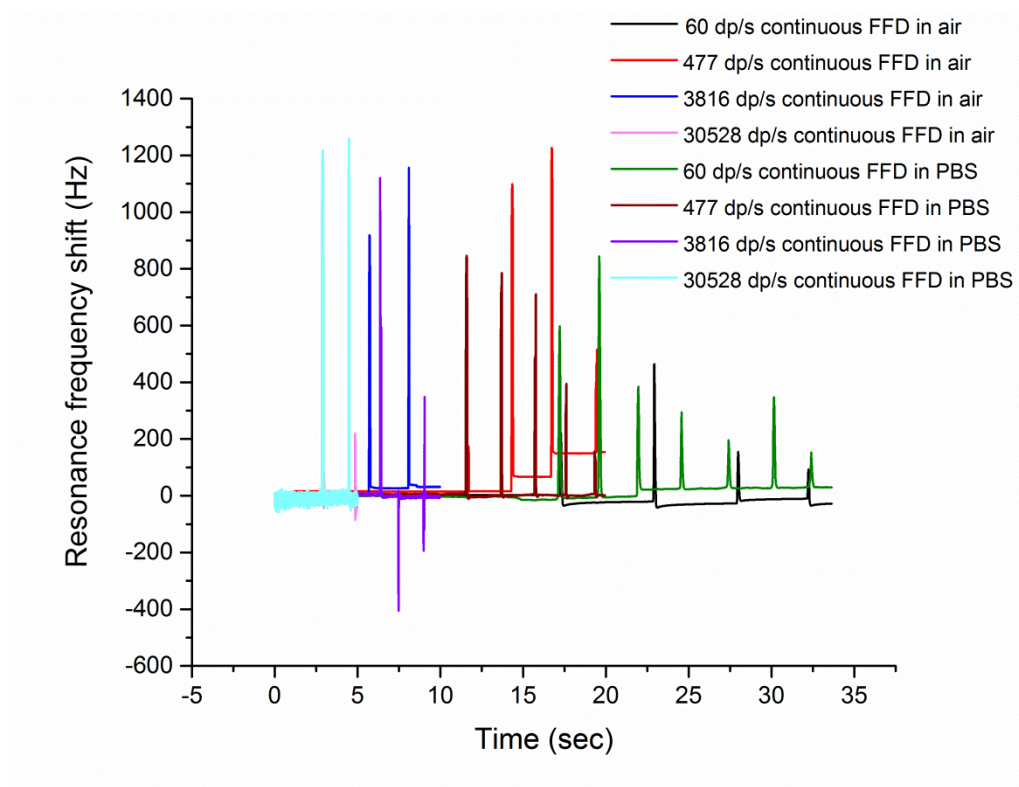


Figure A.7. Variation of resonant frequency with time for continuous FFD in air and PBS at 60, 477, 3816 and 30528 Hz sampling rates using customized network analyzer

A.5 Continuous mode FFD and FS experiments for streptavidin detection

14.3 MHz QCRs were cleaned and functionalized with self-assembled mono layer of thiols in the same way as reported during intermittent mode experiments (Sections 4.3.2 & 4.3.3). Continuous frequency sweeps at different sampling rates (0.13, 0.8 and 1.25 Hz) and fixed frequency drive (FFD) around PBS resonant frequency at a data acquisition rate of 7 Hz were performed separately using VNWA-3E and custom made network analyzers respectively for 30 min. 2 μL of streptavidin was spiked in PBS buffer after 15 minutes of PBS flow in order to achieve a final concentration of 2.5 $\mu\text{g/mL}$. Resonant frequency shifts obtained from continuous frequency sweeps for sampling rates of 0.13, 0.8 and 1.25 Hz were -135, -142 and -89 Hz respectively. -170 Hz was observed in case of continuous FFD (Figure A.8). Continuous frequency sweep data corresponding to a sampling rate of 1.25 Hz was extremely noisy. The change in relative dissipation (Figure A.9) on account of streptavidin binding were negligible for continuous mode experiments

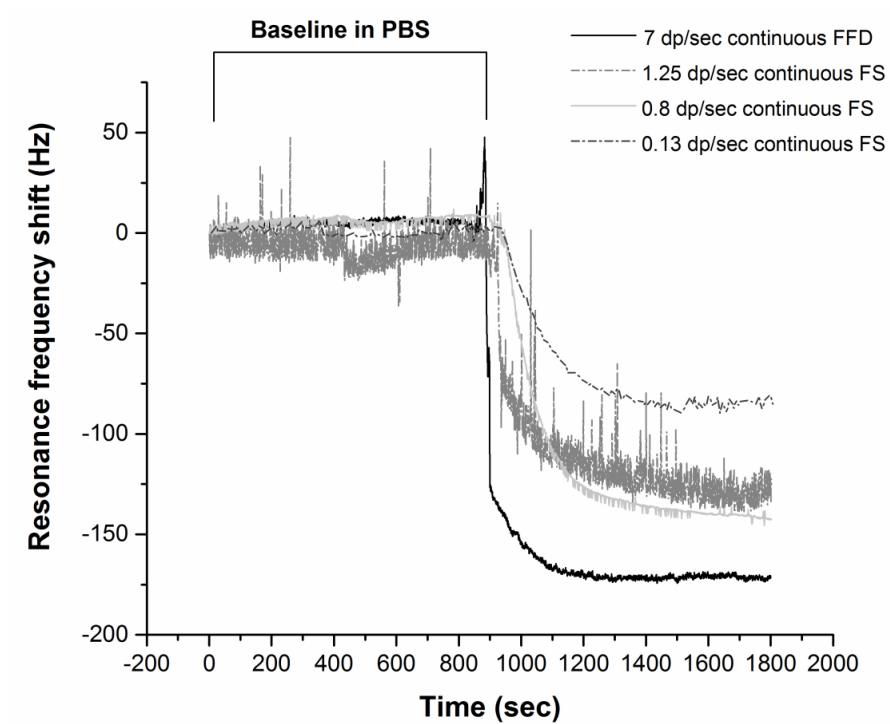


Figure A.8. Variation of resonant frequency shift with time pertaining to streptavidin binding experiments for continuous FFD and FS methods

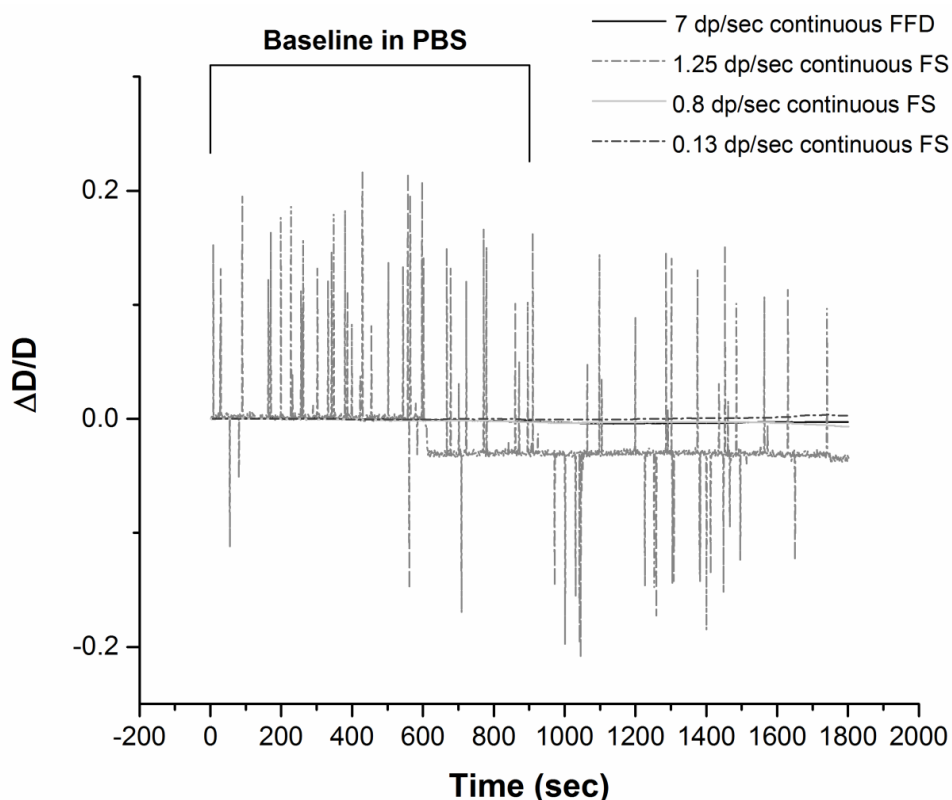


Figure A.9. Variation of relative dissipation with time pertaining to streptavidin binding experiments for continuous FFD and FS methods

A.6 Continuous mode FFD experiments involving hlgE detection

14.3 MHz QCRs were immobilised with biotinylated anti-hlgE aptamer as per the protocol mentioned in Section 6.2.2. PBS buffer was flowed over anti-hlgE aptamer immobilised QCR (at 40 $\mu\text{L}/\text{min}$) for 50 min. After that, fixed frequency drive at 0.5 V driving voltage was taken for 60 minutes duration. Natural hlgE was spiked in PBS buffer after 30 minutes of buffer flow in order to achieve the desired final concentrations. Negative control experiments were carried out separately by flowing PBS buffer and 21.06 nM hlgG over the biotinylated anti-hlgE aptamer surface. Continuous FFD was operated at a data acquisition rate of 7 Hz. Maximum resonant frequency shift obtained from 30 minutes of injection of 2.63, 5.26, 10.53 and 21.06 nM hlgE were nearly -50, -101, -168 and -316 Hz (Figure A.10) respectively. There was hardly any change in relative dissipation due to binding of hlgE with anti-hlgE aptamer (Figure A.11) from the continuous FFD experiments.

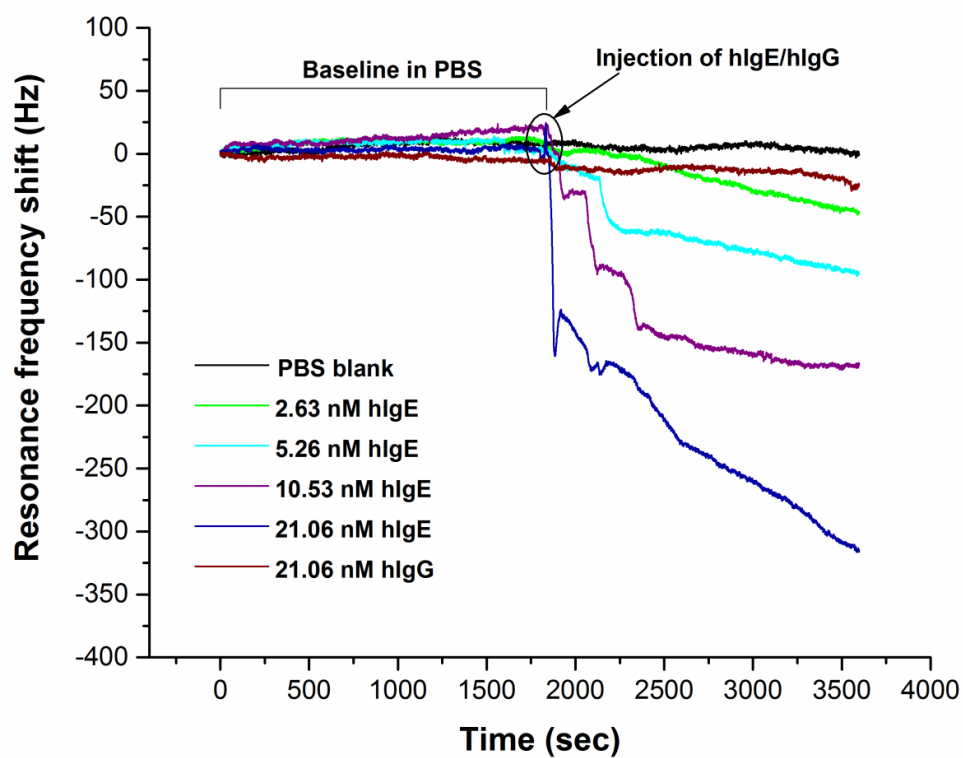


Figure A.10. Resonant frequency shifts involving hlgE binding using continuous FFD

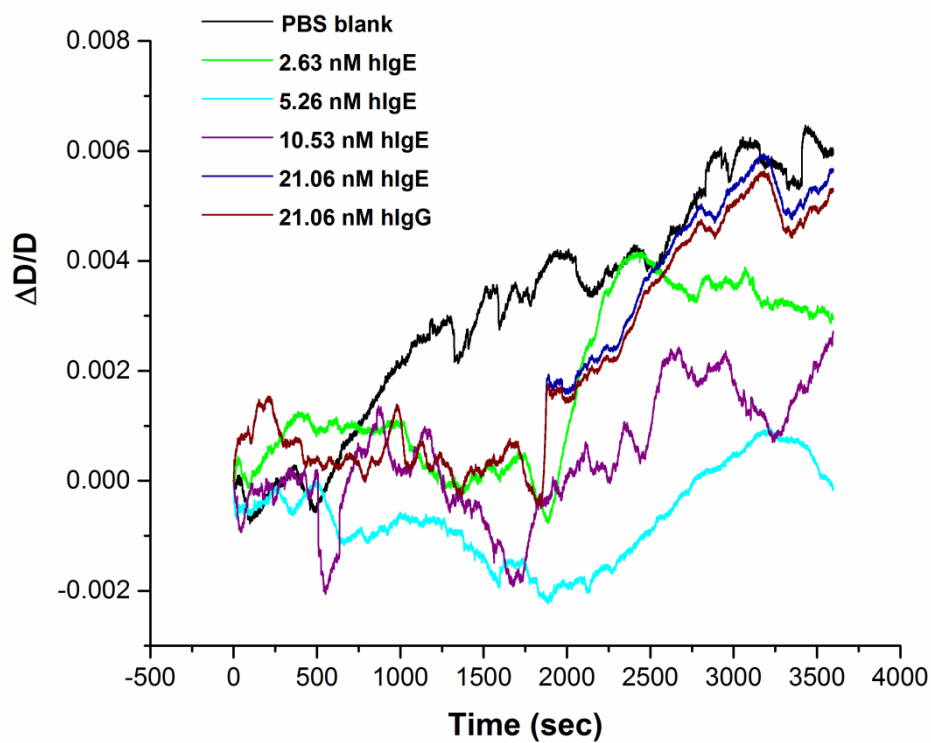


Figure A.11. Relative dissipation shifts involving hIgE binding using continuous FFD

A.7 Continuous FFD and FS experiments for C6-HSL detection

14.3 MHz QCRs were immobilised with anti-C6-HSL nano MIPs using the protocol mentioned in Section 5.3.5. PBS buffer was injected over immobilised QCR (at 40 $\mu\text{L}/\text{min}$) for 50 min. Fixed frequency drive (FFD) at 0.5 V driving voltage was then taken for 60 min duration. Required volume of C6-HSL was spiked in PBS buffer after 30 minutes of PBS flow in order to achieve the desired final concentration. Continuous FFD was operated at a data acquisition rate of 7 Hz. Maximum resonant frequency shift obtained from 30 minutes of injection of 2.5 and 25 μM C6-HSL were nearly -19.8 and -410 Hz (Figure A.12) respectively. Similar experiment involving continuous frequency sweeps at 0.8 Hz sampling rate were conducted for 25 μM C6-HSL using SDR network analyser. A resonant frequency shift of -46.6 Hz was obtained from continuous frequency sweep experiment (Figure A.13).

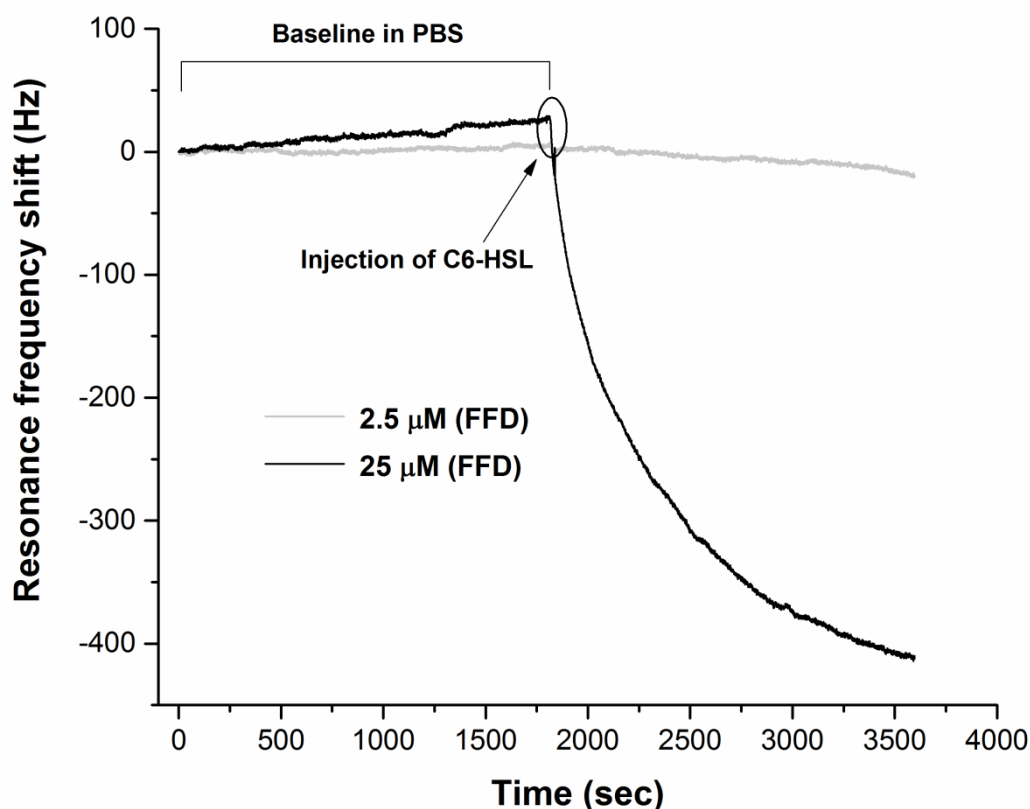


Figure A.12. Resonant frequency shifts involving C6-HSL binding using continuous FFD

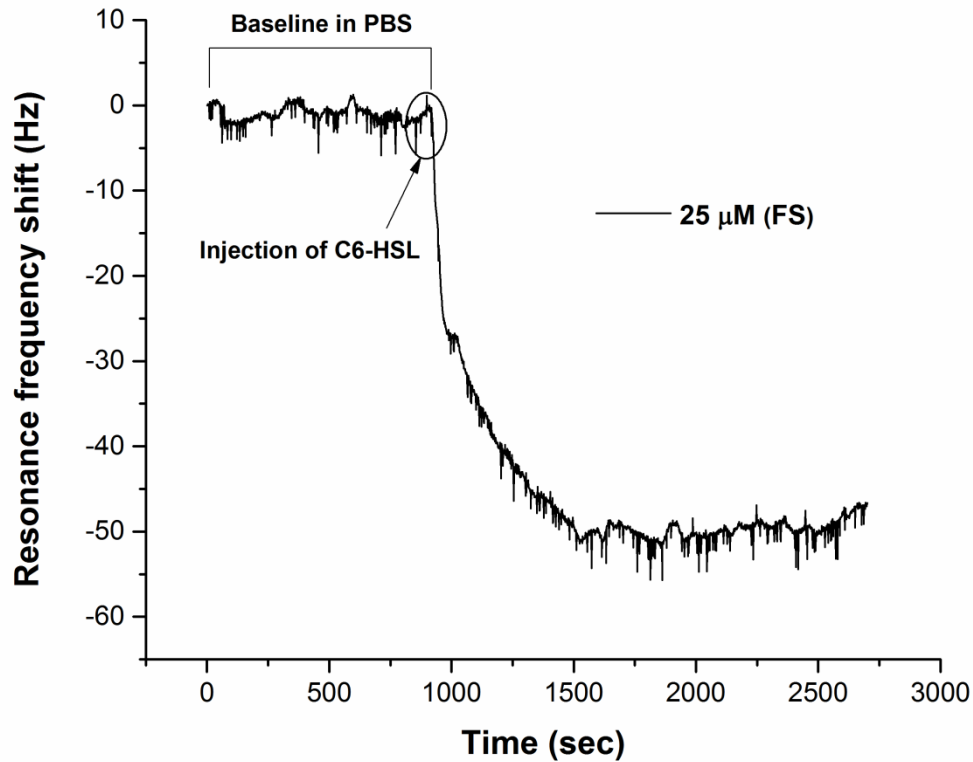


Figure A.13. Resonant frequency shifts involving C6-HSL binding using continuous FS

A.8 Cleaning protocol of mesa QCR

Cleaning of high fundamental frequency QCR (50 MHz) includes the following steps:

- 1) QCR is rinsed with milliQ water.
- 2) QCR is rinsed with ethanol.
- 3) QCR is dried with nitrogen gas after rinsing with ethanol.
- 4) QCR is cleaned using argon plasma for 45 seconds.
- 5) QCR is rinsed with milliQ water.
- 6) QCR is rinsed with ethanol.
- 7) QCR is dried with nitrogen gas after rinsing with ethanol.

A.9 Derivation of quality factor and half resonance bandwidth for liquid loading of a QCR surface

The governing equation for shear motion of the liquid film in contact with a vibrating quartz crystal in terms of displacement from the QCR surface and time is given by

$$\dots\dots\dots \text{---} \text{---} \text{---} \quad (A.26)$$

where η and ρ are the absolute viscosity and density of the liquid and \vec{v}_c is the centre of mass velocity of the liquid. The trial solution for centre of mass velocity \vec{v}_c is given by the following expression.

$$\vec{v}_c = \frac{\eta}{\rho} \frac{\partial^2 \zeta}{\partial x^2} \quad (A.27)$$

where ω_n is the unperturbed angular resonant frequency of a QCR at its n^{th} mode of vibration.

Using Eq. A.26 and Eq. A.27 and solving for ζ , we get

$$\zeta = \frac{\eta}{\rho} \frac{\partial^2 \zeta}{\partial x^2} \quad (A.28)$$

Using Eq. A.27 and Eq. A.28, the real part of ζ can be written as follows.

$$\zeta = \frac{\eta}{\rho} \frac{\partial^2 \zeta}{\partial x^2} \quad (A.29)$$

where δ is the penetration depth of the bulk acoustic wave.

Force acting per unit area F on the liquid at the QCR surface is given by the following expression.

$$F = \frac{\eta}{\rho} \frac{\partial^2 \zeta}{\partial x^2} \quad (A.30)$$

Average power P due to liquid motion at the surface of a QCR is written as follows

$$P = \frac{\eta}{\rho} \frac{\partial^2 \zeta}{\partial x^2} \quad (A.31)$$

Energy dissipated from the surface during one cycle of oscillation is given by

$$E = \frac{\eta}{\rho} \frac{\partial^2 \zeta}{\partial x^2} \quad (A.32)$$

where ω_0 is the unperturbed QCR resonant frequency at n^{th} mode of vibration and ω_1 is the fundamental resonant frequency of a QCR. The thickness of the quartz can be written as follows

$$h = \frac{v_s}{\omega_1} \quad (A.33)$$

where v_s is the speed of the shear wave through the quartz substrate and G and ρ are the shear modulus and density of the quartz. Considering the velocity profile of the acoustic wave as $v = \frac{a}{2} \sin \frac{\omega t}{2}$ and Eq. A.33, the total energy stored by the quartz per unit area is given by

$$U = \frac{1}{2} \rho \int_0^h v^2 dz = \frac{1}{4} \rho \frac{a^2}{\omega^2} \omega^2 \sin^2 \frac{\omega t}{2} \quad (A.34)$$

Using Eq. A.32 and E. A.34, the quality factor for liquid loading of one surface of a QCR at its n^{th} mode of vibration is therefore given by

$$Q = \frac{\omega_0}{\Delta \omega} = \frac{\omega_0}{\omega_0 - \omega_1} \quad (A.35)$$

The expression of half resonance bandwidth for a liquid loading using Eq. A.35 can be expressed as follows.

$$\Delta \omega = \omega_0 - \omega_1 \quad (A.36)$$

The table below depicts the theoretical values of quality factor and half resonance bandwidth for different QCRs. The parameters of the quartz and DI water have been taken from Section 4.4.4 for calculation of quality factor and half resonance bandwidth.

QCR and its mode of vibration	Quality factor in DI water	Half resonance bandwidth (kHz) in DI water
5 MHz (fundamental)	3700.43	0.68
14.3 MHz (fundamental)	2188.11	3.27
42.9 MHz (3 rd overtone of 14.3 MHz QCR)	3789.92	5.66
19.5 MHz (fundamental)	1873.79	5.2
136.5 MHz (7 th overtone mode of 19.5 MHz)	4957.58	13.76

Table A.2. Theoretical quality factor and half resonance bandwidth for different QCRs and its mode of vibration

A.10 Location of spurious modes for 14.3 MHz QCR under liquid loading

Conductance of 5 different 14.3 MHz QCRs were calculated under DI water loading from frequency sweeps performed at fundamental and 3rd overtone modes. Frequency sweeps were taken for a span of 4MHz in order to locate the spurious modes at the above mentioned modes of vibration. The distance of the peak of the resonance mode from the peak of the nearest satellite mode has been tabulated below.

Peak to peak distance (kHz) for DI water loading		
14.3 MHz QCR	Fundamental mode	3 rd overtone mode
QCR-1	79.62	45.69
QCR-2	79.78	43.69
QCR-3	79.05	45.61
QCR-4	76.57	44.97
QCR-5	80.82	47.16

Table A.3. Location of satellite modes for fundamental and 3rd overtone modes of vibration for a 14.3 MHz QCR

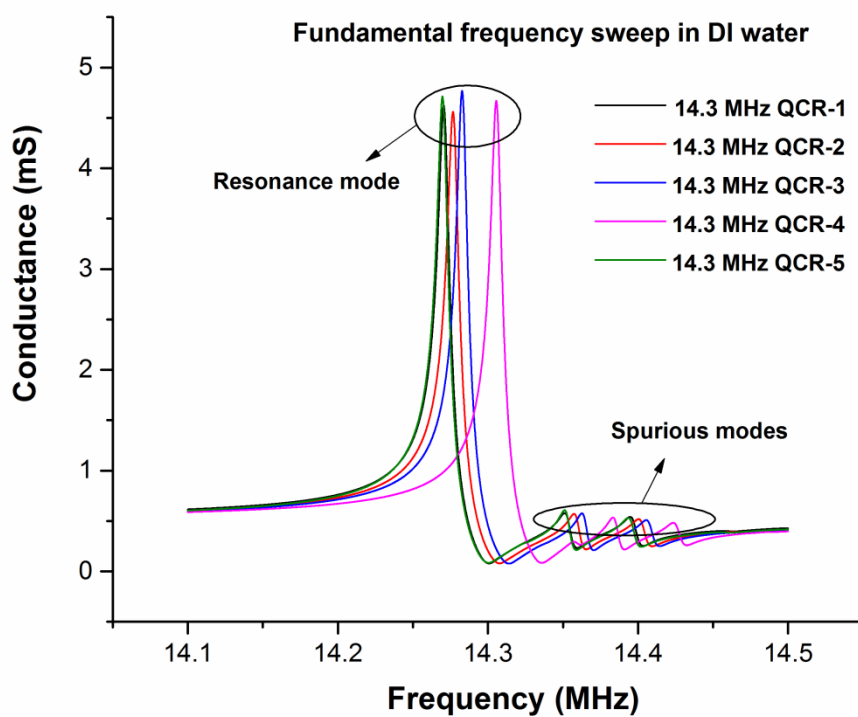


Figure A.14. Variation of conductance with frequency during a frequency sweep taken at a fundamental mode of 14.3 MHz QCRs

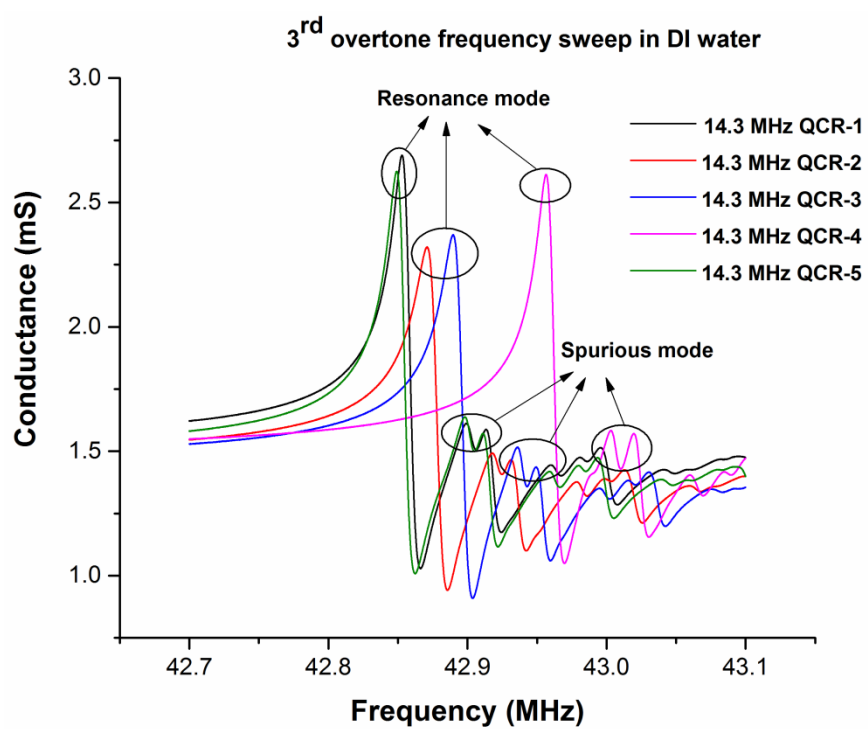


Figure A.15. Variation of conductance with frequency during a frequency sweep taken at a 3rd overtone mode mode of 14.3 MHz QCRs

Appendix B

List of Publications

Most of the work presented in this dissertation has been submitted for publications in the following journals and conferences.

B.1 Journal Papers

1. A. Guha, N. Sandström, V. P. Ostanin, W. V. D Wijngaart, D. Klenerman, S. K. Ghosh, "Simple and ultrafast resonant frequency and dissipation shift measurements using a fixed frequency drive," *Sensors and Actuators B: Chemical*, 2018 (Accepted for publication).
2. A. Guha, O. S. Ahmad, N. Sandström, V. P. Ostanin, W. V. D Wijngaart, D. Klenerman, S. K. Ghosh, "Real-time and label-free acoustic detection of quorum sensing signaling molecules using a fixed frequency drive" *Analytical Chemistry*, 2018 (Under co-author review).
3. A. Guha, N. Sandström, V. P. Ostanin, W. V. D Wijngaart, D. Klenerman, S. K. Ghosh, "Application of fixed frequency drive method for rapid and direct detection of human IgE" *Sensors*, 2018 (Under co-author review).

B.2 Conference Proceedings

1. A. Guha, N. Sandström, V. P. Ostanin, W. V. D Wijngaart, D. Klenerman, S. K. Ghosh, "Measurement of resonant frequency of a quartz crystal oscillator with immensely improved time resolution using a fixed frequency drive", *19th International Conference on Biosensors and Bioelectronics*, 21-22 August 2017, London, UK (Oral presentation).
2. A. Guha, N. Sandström, V. P. Ostanin, W. V. D Wijngaart, D. Klenerman, S. K. Ghosh, "Measurement of protein binding with vastly improved time resolution using a quartz crystal microbalance driven at a fixed frequency", *5th International Conference on Biosensing Technology*, 7-10 May 2017, Riva Del Garda, Italy (Poster presentation).

References

- [1] C.I. Cheng, Y.-P. Chang, Y.-H. Chu, Biomolecular interactions and tools for their recognition: focus on the quartz crystal microbalance and its diverse surface chemistries and applications, *Chem. Soc. Rev.* 41 (2012) 1947. doi:10.1039/c1cs15168a.
- [2] A. Szabo, L. Stolz, R. Granzow, Surface plasmon resonance and its use in biomolecular interaction analysis (BIA), *Curr. Opin. Struct. Biol.* 5 (1995) 699–705. doi:10.1016/0959-440X(95)80064-6.
- [3] B. Zimmermann, C. Hahnefeld, F.W. Herberg, B. Zimmermann, Applications of biomolecular interaction analysis in drug development, *Targets*. 1 (2002) 66–73. www.drugdiscoverytoday.com.
- [4] Y. Zhou, L. Liu, Y. Hao, M. Xu, Detection of A β Monomers and Oligomers: Early Diagnosis of Alzheimer's Disease, *Chem. - An Asian J.* 11 (2016) 805–817. doi:10.1002/asia.201501355.
- [5] P.R. Kraus, F.L. Cooper, D.H. Emmons, S. Ferguson, R.D. McClain, J.J. Spates, Use of quartz crystal microbalance sensors for monitoring fouling and viscoelastic phenomena in industrial process applications, *Slcon 2001 - Proc. 1st ISA/IEEE Sensors Ind. Conf.* (2001) 241–245. doi:10.1109/SFICON.2001.968537.
- [6] S. Scarano, S. Mariani, M. Minunni, Label free Affinity sensing: application to food analysis, *Acta Imeko*. 5 (2016) 36–44. www.imeko.org.
- [7] C. Justino, A. Duarte, T. Rocha-Santos, Recent Progress in Biosensors for Environmental Monitoring: A Review, *Sensors*. 17 (2017) 2918. doi:10.3390/s17122918.
- [8] P.A. Serra, *Biosensors for Health, Environment and Biosecurity*, InTech, 2011. doi:10.5772/928.
- [9] Relative sizes of biological materials, (n.d.). <http://ib.bioninja.com.au/standard-level/topic-1-cell-biology/11-introduction-to-cells/cell-scale.html> (accessed September 14, 2018).
- [10] M. Liu, J.K. Nicholson, J.A. Parkinson, J.C. Lindon, Measurement of Biomolecular Diffusion Coefficients in Blood Plasma Using Two-Dimensional ^1H - ^1H Diffusion-Edited Total-Correlation NMR Spectroscopy, *Anal. Chem.* 69 (1997) 1504–1509. doi:10.1021/ac9612133.
- [11] J.R. Helliwell, A. Brink, S. Kaenket, V.L. Starkey, S.W.M. Tanley, X-ray diffraction in temporally and spatially resolved biomolecular science, *Faraday Discuss.* 177 (2015) 429–441. doi:10.1039/c4fd00166d.
- [12] M. Citartan, S.C.B. Gopinath, J. Tominaga, Y. Chen, T.H. Tang, Use of UV-vis-NIR spectroscopy to monitor label-free interaction between molecular recognition elements and erythropoietin on a gold-coated polycarbonate platform, *Talanta*. 126 (2014) 103–109. doi:10.1016/j.talanta.2014.03.043.
- [13] M. Dimura, T.O. Peulen, C.A. Hanke, A. Prakash, H. Gohlke, C.A. Seidel, Quantitative FRET studies and integrative modeling unravel the structure and dynamics of biomolecular systems, *Curr. Opin. Struct. Biol.* 40 (2016) 163–185. doi:10.1016/j.sbi.2016.11.012.

- [14] M.D. Hall, A. Yasgar, T. Peryea, J.C. Braisted, A. Jadhav, A. Simeonov, N.P. Coussens, Fluorescence polarization assays in high-throughput screening and drug discovery: A review, *Methods Appl. Fluoresc.* 4 (2016). doi:10.1088/2050-6120/4/2/022001.
- [15] W. Xia, T. Yang, G. Shankar, I.M. Smith, Y. Shen, D.M. Walsh, D.J. Selkoe, A specific enzyme-linked immunosorbent assay for measuring beta-amyloid protein oligomers in human plasma and brain tissue of patients with Alzheimer disease, *Arch Neurol.* 66 (2009) 190–199. doi:10.1001/archneurol.2008.565.
- [16] I.J. Colton, J.D. Carbeck, J. Rao, G.M. Whitesides, Affinity capillary electrophoresis: A physical-organic tool for studying interactions in biomolecular recognition, *Electrophoresis.* 19 (1998) 367–382. doi:10.1002/elps.1150190303.
- [17] P. Torreri, M. Ceccarini, P. Macioce, T.C. Petrucci, Biomolecular interactions by Surface Plasmon Resonance technology., *Ann. Ist. Super. Sanita.* 41 (2005) 437–41. doi:10.1021/ja061521a.
- [18] M. Kabiri, L.D. Unsworth, Application of isothermal titration calorimetry for characterizing thermodynamic parameters of biomolecular interactions: Peptide self-assembly and protein adsorption case studies, *Biomacromolecules.* 15 (2014) 3463–3473. doi:10.1021/bm5004515.
- [19] H. Huang, Z. Liu, X. Yang, Application of electrochemical impedance spectroscopy for monitoring allergen-antibody reactions using gold nanoparticle-based biomolecular immobilization method, *Anal. Biochem.* 356 (2006) 208–214. doi:10.1016/j.ab.2006.05.021.
- [20] O.H. Willemsen, M.M.E. Snel, A. Cambi, J. Greve, B.G. De Grooth, C.G. Figdor, Biomolecular Interactions Measured by Atomic Force Microscopy, *Biophys. J.* 79 (2000) 3267–3281. doi:10.1016/S0006-3495(00)76559-3.
- [21] G. Tosolini, F. Perez-Murano, J. Bausells, L.G. Villanueva, Self sensing cantilevers for the measurement of (biomolecular) forces, *Proc. 8th Spanish Conf. Electron Devices, CDE'2011.* (2011). doi:10.1109/SCED.2011.5744171.
- [22] V. Blondeau-Patissier, W. Boireau, B. Cavallier, G. Lengaigne, W. Daniau, G. Martin, S. Ballandras, Integrated love wave device dedicated to biomolecular interactions measurements in aqueous media, *Sensors.* 7 (2007) 1992–2003. doi:10.3390/s7091992.
- [23] M.C. Dixon, Quartz crystal microbalance with dissipation monitoring: Enabling real-time characterization of biological materials and their interactions, *J. Biomol. Tech.* 19 (2008) 151–158.
- [24] J. Juan Colás, Dual-Mode Electro-photonic Silicon Biosensors, 2017. doi:10.1007/978-3-319-60501-2.
- [25] M. Nirschl, F. Reuter, J. Vörös, Review of transducer principles for label-free biomolecular interaction analysis, *Biosensors.* 1 (2011) 70–92. doi:10.3390/bios1030070.
- [26] H. Sharma, R. Mutharasan, Review of biosensors for foodborne pathogens and toxins, *Sensors Actuators, B Chem.* 183 (2013) 535–549. doi:10.1016/j.snb.2013.03.137.
- [27] A.C. Mongra, A. Kaur, R.K. Bansal, Review Study On Electrochemical-Based

- Biosensors, *Int. J. Eng. Res. Appl.* 2 (2012) 743–749.
- [28] S.K. Ghosh, Anharmonic Acoustic Technique for Detection of Surface-bound Particles, University of Cambridge, 2011. <http://www.dspace.cam.ac.uk/handle/1810/243858>.
 - [29] Y. Yang, Quantitative characterization of biomolecular assemblies and interactions using atomic force microscopy, *Methods*. 29 (2003) 175–187. doi:10.1016/S1046-2023(02)00308-0.
 - [30] N. Jalili, K. Laxminarayana, A review of atomic force microscopy imaging systems: Application to molecular metrology and biological sciences, *Mechatronics*. 14 (2004) 907–945. doi:10.1016/j.mechatronics.2004.04.005.
 - [31] T. Ando, T. Uchihashi, S. Scheuring, Filming biomolecular processes by high-speed atomic force microscopy, *Chem. Rev.* 114 (2014) 3120–3188. doi:10.1021/cr4003837.
 - [32] S. Gupta, K. Ramesh, S. Ahmed, V. Kakkar, Lab-on-chip technology: A review on design trends and future scope in biomedical applications, *Int. J. Bio-Science Bio-Technology*. 8 (2016) 311–322. doi:10.14257/ijbsbt.2016.8.5.28.
 - [33] R. Abdolvand, B. Bahreyni, J.E.Y. Lee, F. Nabki, Micromachined resonators: A review, *Micromachines*. 7 (2016). doi:10.3390/mi7090160.
 - [34] E. Hafner, Crystal Resonators, *IEEE Trans. Sonics Ultrason.* 21 (1974) 220–237.
 - [35] B.N. Johnson, R. Mutharasan, Biosensing using dynamic-mode cantilever sensors: A review, *Biosens. Bioelectron.* 32 (2012) 1–18. doi:10.1016/j.bios.2011.10.054.
 - [36] A. Guha, N. Sandström, V.P. Ostanin, W. van der Wijngaart, D. Klenerman, S.K. Ghosh, Simple and ultrafast resonance frequency and dissipation shift measurements using a fixed frequency drive.pdf, *Sensors Actuators B Chem.* 281 (2019) 960–970.
 - [37] D. Erickson, S. Mandal, A.H.J. Yang, B. Cordovez, Nanobiosensors: Optofluidic, electrical and mechanical approaches to biomolecular detection at the nanoscale, *Microfluid. Nanofluidics*. 4 (2008) 33–52. doi:10.1007/s10404-007-0198-8.
 - [38] G. Stan, S.D. Solares, Frequency, amplitude, and phase measurements in contact resonance atomic force microscopies, *Beilstein J. Nanotechnol.* 5 (2014) 278–288. doi:10.3762/bjnano.5.30.
 - [39] R. Fogel, J. Limson, A.A. Seshia, Acoustic biosensors, *Essays Biochem.* 60 (2016) 101–110. doi:10.1042/EBC20150011.
 - [40] M. Alvarez, K. Zinoviev, M. Moreno, L.M. Lechuga, Cantilever biosensors, *Opt. Biosens.* (2008) 419–452. doi:10.1016/B978-044453125-4.50012-7.
 - [41] S. Xu, Electromechanical biosensors for pathogen detection, *Microchim. Acta*. 178 (2012) 245–260. doi:10.1007/s00604-012-0831-4.
 - [42] A.A. Vives, Piezoelectric transducers and applications, *Piezoelectric Transducers Appl.* (2008) 1–532. doi:10.1007/978-3-540-77508-9.
 - [43] J.G. Rodríguez-Madrid, G.F. Iriarte, O.A. Williams, F. Calle, High precision pressure sensors based on SAW devices in the GHz range, *Sensors Actuators, A Phys.* 189 (2013) 364–369. doi:10.1016/j.sna.2012.09.012.
 - [44] K. Kustanovich, V. Yantchev, V. Kirejev, G.D.M. Jeffries, T. Lobovkina, A. Jesorka, A high-performance lab-on-a-chip liquid sensor employing surface acoustic wave

- resonance, *J. Micromechanics Microengineering*. 27 (2017). doi:10.1088/1361-6439/aa8f21.
- [45] T.M.A. Gronewold, Surface acoustic wave sensors in the bioanalytical field: Recent trends and challenges, *Anal. Chim. Acta*. 603 (2007) 119–128. doi:10.1016/j.aca.2007.09.056.
 - [46] S. Jayasvasti, D. Isarakorn, S. Nundrakwang, Comparative study of QCM analyzers based on pierce oscillator and electromechanical impedance techniques, *BMEiCON 2016 - 9th Biomed. Eng. Int. Conf.* (2017). doi:10.1109/BMEiCON.2016.7859608.
 - [47] R.L. Bunde, E.J. Jarvi, J.J. Rosentreter, Piezoelectric quartz crystal biosensors, *Talanta*. 46 (1998) 1223–1236. doi:10.1016/S0039-9140(97)00392-5.
 - [48] M. Thompson, A.L. Kiplingt, W.C. Duncan-Hewitt, L. V. Rajakovic, B.A. Cavic-Vlasak, Thickness-shear-mode Acoustic Wave, *Analyst*. 116 (1991) 881–890.
 - [49] M. Rodahl, F. Hook, B. Kasemo, QCM operation in liquids: An explanation of measured variations in frequency and Q factor with liquid conductivity, *Doktorsavhandlingar Vid Chalmers Tek. Hogs.* 68 (1997) 2219–2227. doi:10.1021/ac951203m.
 - [50] G. Sauerbrey, Verwendung von Schwingquarzen zur Wägung dünner Schichten und zur Mikrowägung, *Zeitschrift Für Phys.* 155 (1959) 206–222. doi:10.1007/BF01337937.
 - [51] K. Keiji Kanazawa, J.G. Gordon, The oscillation frequency of a quartz resonator in contact with liquid, *Anal. Chim. Acta*. 175 (1985) 99–105. doi:10.1016/S0003-2670(00)82721-X.
 - [52] X. Wang, J.S. Ellis, E.L. Lyle, P. Sundaram, M. Thompson, Conformational chemistry of surface-attached calmodulin detected by acoustic shear wave propagation, *Mol. Biosyst.* 2 (2006) 184–192. doi:10.1039/b600186f.
 - [53] H. Furusawa, M. Komatsu, Y. Okahata, In Situ Monitoring of conformational changes of and peptide bindings to calmodulin on a 27 MHz quartz-crystal microbalance, *Anal. Chem.* 81 (2009) 1841–1847. doi:10.1021/ac8022229.
 - [54] M.E. Yakovleva, G.R. Safina, B. Danielsson, A study of glycoprotein-lectin interactions using quartz crystal microbalance, *Anal. Chim. Acta*. 668 (2010) 80–85. doi:10.1016/j.aca.2009.12.004.
 - [55] Y. Wu, H. Ma, D. Gu, J. He, A quartz crystal microbalance as a tool for biomolecular interaction studies, *RSC Adv.* 5 (2015) 64520–64525. doi:10.1039/c5ra05549k.
 - [56] C. Kößlinger, S. Drost, F. Aberl, H. Wolf, S. Koch, P. Woias, A quartz crystal biosensor for measurement in liquids, *Biosens. Bioelectron.* 7 (1992) 397–404. doi:10.1016/0956-5663(92)85038-C.
 - [57] B. Beckera, M.A. Cooper, A survey of the 2006-2009 quartz crystal microbalance biosensor literature, *J. Mol. Recognit.* 24 (2011) 754–787. doi:10.1002/jmr.1117.
 - [58] R.E. Speight, M.A. Cooper, A Survey of the 2010 Quartz Crystal Microbalance Literature, *J. Mol. Recognit.* 25 (2012) 451–473. doi:10.1002/jmr.2209.
 - [59] F. Höök, B. Kasemo, T. Nylander, C. Fant, K. Sott, H. Elwing, Variations in coupled water, viscoelastic properties, and film thickness of a Mefp-1 protein film during

- adsorption and cross-linking: A quartz crystal microbalance with dissipation monitoring, ellipsometry, and surface plasmon resonance study, *Anal. Chem.* 73 (2001) 5796–5804. doi:10.1021/ac0106501.
- [60] D. Johannsmann, Viscoelastic, mechanical, and dielectric measurements on complex samples with the quartz crystal microbalance, *Phys. Chem. Chem. Phys.* 10 (2008) 4516. doi:10.1039/b803960g.
- [61] A. Lin, Y.J. Li, L. Wang, S.J. Chen, M.E. Gross, E.S. Kim, Label-free detection of prostate-specific antigen with FBAR-based sensor with oriented antibody immobilization, *IEEE Int. Ultrason. Symp. IUS.* (2011) 797–800. doi:10.1109/ULTSYM.2011.0195.
- [62] J. V Garcia, Y. Jimenez, C. March, A. Montoya, A. Arnau, QCM technology in biosensors, *Biosens. - Emerg. Mater. Appl.* (2011) 153–178. doi:10.5772/17991.
- [63] X. Zhao, G.M. Ashley, L. Garcia-Gancedo, H. Jin, J. Luo, A.J. Flewitt, J.R. Lu, Protein functionalized ZnO thin film bulk acoustic resonator as an odorant biosensor, *Sensors Actuators, B Chem.* 163 (2012) 242–246. doi:10.1016/j.snb.2012.01.046.
- [64] T. Yoetz-Kopelman, Y. Ram, A. Freeman, Y. Shacham-Diamand, Faradaic impedance spectroscopy for detection of small molecules binding using the avidin-biotin model, *Electrochim. Acta.* 173 (2015) 630–635. doi:10.1016/j.electacta.2015.05.114.
- [65] I. Tothill, Z. Altintas, Molecular biosensors: promising new tools for early detection of cancer, *Nanobiosensors Dis. Diagnosis. Volume 4* (2015) 1. doi:10.2147/NDD.S56772.
- [66] G. Selvolini, G. Marrazza, MIP-based sensors: Promising new tools for cancer biomarker determination, *Sensors (Switzerland).* 17 (2017). doi:10.3390/s17040718.
- [67] S. Patel, R. Nanda, S. Sahoo, E. Mohapatra, Review Article Biosensors in Health Care : The Milestones Achieved in Their Development towards Lab-on-Chip-Analysis, 2016 (2016). doi:10.1155/2016/3130469.
- [68] P. Prakrankamanant, Quartz crystal microbalance biosensors: Prospects for point-of-care diagnostics, *J. Med. Assoc. Thail.* 97 (2014).
- [69] J.A. Spriet, Online Monitoring of Fermentation Processes, *Ferment. Process.* 2 (1981) 115–121.
- [70] J.G. Lee, Y. Jang, L. Fortunato, S. Jeong, S. Lee, T.O. Leiknes, N. Ghaffour, An advanced online monitoring approach to study the scaling behavior in direct contact membrane distillation, *J. Memb. Sci.* 546 (2018) 50–60. doi:10.1016/j.memsci.2017.10.009.
- [71] J.C. Encarnação, T. Schulte, A. Achour, H. Björkelund, K. Andersson, Detecting ligand interactions in real time on living bacterial cells, *Appl. Microbiol. Biotechnol.* 102 (2018) 4193–4201. doi:10.1007/s00253-018-8919-3.
- [72] A.F. Coskun, A.E. Cetin, B.C. Galarreta, D.A. Alvarez, H. Altug, A. Ozcan, Lensfree optofluidic plasmonic sensor for real-time and label-free monitoring of molecular binding events over a wide field-of-view, *Sci. Rep.* 4 (2014) 1–7. doi:10.1038/srep06789.

- [73] J. Schröder, R. Borngräber, F. Eichelbaum, P. Hauptmann, Advanced interface electronics and methods for QCM, *Sensors Actuators, A Phys.* 97–98 (2002) 543–547. doi:10.1016/S0924-4247(02)00036-5.
- [74] O.M. Uy, R.P. Cain, B.G. Carkhuff, R.T. Cusick, B.E. Wood, Miniature quartz crystal microbalance for spacecraft and missile applications, *Johns Hopkins APL Tech. Dig. (Applied Phys. Lab.* 20 (1999) 199–213.
- [75] J.M. Beechem, decay data obtained on the millisecond time scale: Application to protein:DNA interactions and protein folding reactions Joseph M. Beechem Vanderbilt University, Dept. of Molecular Physiology and Biophysics, 1640 (1992) 676–680.
- [76] A. Rojnuckarin, S. Kim, S. Subramaniam, Brownian dynamics simulations of protein folding: Access to milliseconds time scale and beyond, *Proc Natl Acad Sci U S A.* 95 (1998) 4288–4292. doi:10.1073/pnas.95.8.4288.
- [77] V.S. Pande, I. Baker, J. Chapman, S.P. Elmer, S. Khaliq, S.M. Larson, Y.M. Rhee, M.R. Shirts, C.D. Snow, E.J. Sorin, B. Zagrovic, Atomistic protein folding simulations on the submillisecond time scale using worldwide distributed computing, *Biopolymers.* 68 (2003) 91–109. doi:10.1002/bip.10219.
- [78] J.-P. Vilardaga, M. Bünemann, C. Krasel, M. Castro, M.J. Lohse, Measurement of the millisecond activation switch of G protein-coupled receptors in living cells., *Nat. Biotechnol.* 21 (2003) 807–812. doi:10.1038/nbt838.
- [79] A. Kharlamova, J.C. Demuth, S.A. McLuckey, Vapor treatment of electrospray droplets: Evidence for the folding of initially denatured proteins on the sub-millisecond time-scale, *J. Am. Soc. Mass Spectrom.* 23 (2012) 88–101. doi:10.1007/s13361-011-0258-x.
- [80] T. Uzawa, T. Kimura, K. Ishimori, I. Morishima, T. Matsui, M. Ikeda-Saito, S. Takahashi, S. Akiyama, T. Fujisawa, Time-resolved small-angle X-ray scattering investigation of the folding dynamics of heme oxygenase: Implication of the scaling relationship for the submillisecond intermediates of protein folding, *J. Mol. Biol.* 357 (2006) 997–1008. doi:10.1016/j.jmb.2005.12.089.
- [81] M. Edvardsson, M. Rodahl, B. Kasemo, F. Höök, A dual-frequency QCM-D setup operating at elevated oscillation amplitudes, *Anal. Chem.* 77 (2005) 4918–4926. doi:10.1021/ac050116j.
- [82] K.A. Marx, Quartz crystal microbalance: A useful tool for studying thin polymer films and complex biomolecular systems at the solution-surface interface, *Biomacromolecules.* 4 (2003) 1099–1120. doi:10.1021/bm020116i.
- [83] J. Petri, S. Hochstädt, T. Nentwig, A. Pausch, A. Langhoff, D. Johannsmann, A Fast Electrochemical Quartz Crystal Microbalance, which Acquires Frequency and Bandwidth on Multiple Overtones, *Electroanalysis.* (2016) 1–9. doi:10.1002/elan.201600580.
- [84] Q-Sense E1 Tracking changes at the surface, (n.d.). http://www.biolinscientific.com/zafepress.php?url=%2Fpdf%2FQ-Sense%2FProducts%2FE1%2FQS_P_E1_brochure.pdf (accessed July 31, 2017).
- [85] D. Johannsmann, *The Quartz Crystal Microbalance in Soft Matter Research: Fundamentals and Modeling*, 2014. doi:10.1007/978-3-319-07836-6.

- [86] H. Anderson, I. Katardjiev Prof. (Uppsala University, Disciplinary Domain of Science and Technology, Technology, Department of Engineering Sciences, Solid State Electronics), B. Ingemarsson Dr. (Attana AB), Development of Electroacoustic Sensors for Biomolecular Interaction Analysis, 2009. <http://uu.diva-portal.org/smash/record.jsf?pid=diva2:228419>.
- [87] M.M. Pedroso, A.M. Watanabe, M.C. Roque-Barreira, P.R. Bueno, R.C. Faria, Quartz Crystal Microbalance monitoring the real-time binding of lectin with carbohydrate with high and low molecular mass, *Microchem. J.* 89 (2008) 153–158. doi:10.1016/j.microc.2008.02.001.
- [88] P.J. Molino, M.J. Higgins, P.C. Innis, R.M.I. Kapsa, G.G. Wallace, Fibronectin and bovine serum albumin adsorption and conformational dynamics on inherently conducting polymers: A QCM-D study, *Langmuir*. 28 (2012) 8433–8445. doi:10.1021/la300692y.
- [89] S.T. Sanjay, G. Fu, M. Dou, F. Xu, R. Liu, H. Qi, X. Li, Biomarker detection for disease diagnosis using cost-effective microfluidic platforms, *Analyst*. 140 (2015) 7062–7081. doi:10.1039/C5AN00780A.
- [90] M. Swierczewska, G. Liu, S. Lee, X. Chen, High-sensitivity nanosensors for biomarker detection, *Chem. Soc. Rev.* 41 (2012) 2641–2655. doi:10.1039/C1CS15238F.
- [91] M. Mascini, S. Tombelli, Biosensors for biomarkers in medical diagnostics, *Biomarkers*. 13 (2008) 637–657. doi:10.1080/13547500802645905.
- [92] H. Hampel, R. Frank, K. Broich, S.J. Teipel, R.G. Katz, J. Hardy, K. Herholz, A.L.W. Bokde, F. Jessen, Y.C. Hoessler, W.R. Sanhai, H. Zetterberg, J. Woodcock, K. Blennow, Biomarkers for alzheimer's disease: Academic, industry and regulatory perspectives, *Nat. Rev. Drug Discov.* 9 (2010) 560–574. doi:10.1038/nrd3115.
- [93] K. Blennow, H. Zetterberg, Cerebrospinal fluid biomarkers for Alzheimer's disease., *J. Alzheimers. Dis.* 18 (2009) 413–417. doi:10.3233/JAD-2009-1177.
- [94] P.J. Tighe, R.R. Ryder, I. Todd, L.C. Fairclough, ELISA in the multiplex era: Potentials and pitfalls, *Proteomics - Clin. Appl.* 9 (2015) 406–422. doi:10.1002/prca.201400130.
- [95] Abcam, Multiplex immunoassay techniques: a review of current methods, (2018). <https://www.abcam.com/kits/multiplex-immunoassay-techniques-review-of-methods-western-blot-elisa-microarray-and-luminex> (accessed August 2, 2018).
- [96] B. Wu, L.C. Chen, Y. Huang, Y. Zhang, Y. Kang, D.H. Kim, Multiplexed Biomolecular Detection Based on Single Nanoparticles Immobilized on Pneumatically Controlled Microfluidic Chip, *Plasmonics*. 9 (2014) 801–807. doi:10.1007/s11468-013-9661-4.
- [97] J.P. Pursey, Y. Chen, E. Stulz, M.K. Park, P. Kongsuphol, Microfluidic electrochemical multiplex detection of bladder cancer DNA markers, *Sensors Actuators, B Chem.* 251 (2017) 34–39. doi:10.1016/j.snb.2017.05.006.
- [98] N. Liu, X. Li, X. Ma, G. Ou, Z. Gao, Rapid and multiple detections of staphylococcal enterotoxins by two-dimensional molecularly imprinted film-coated QCM sensor, *Sensors Actuators, B Chem.* 191 (2014) 326–331. doi:10.1016/j.snb.2013.09.086.
- [99] S. Johnson, T.F. Krauss, Label-free affinity biosensor arrays: novel technology for molecular diagnostics, *Expert Rev. Med. Devices*. 14 (2017) 177–179. doi:10.1080/17434440.2017.1283982.

- [100] D. Grieshaber, R. MacKenzie, J. Vörös, E. Reimhult, *Electrochemical Biosensors - Sensor Principles and Architectures*, *Sensors*. 8 (2008) 1400–1458. doi:10.3390/s8031400.
- [101] K. Jaruwongrungrunsee, U. Waiwijit, A. Wisitsoraat, M. Sangworasil, C. Pintavirooj, A. Tuantranont, Real-time multianalyte biosensors based on interference-free multichannel monolithic quartz crystal microbalance, *Biosens. Bioelectron.* 67 (2015) 576–581. doi:10.1016/j.bios.2014.09.047.
- [102] X. Jin, Y. Huang, A. Mason, X. Zeng, Multichannel Monolithic Quartz Crystal Microbalance Gas Sensor Array, *Anal. Chem.* 81 (2009) 595–603. doi:10.1021/ac8018697.
- [103] Y. Yan, Z. Zeng, C. Chen, H. Jiang, Z.Y. Chang, D.M. Karabacak, M.A.P. Pertijs, An energy-efficient reconfigurable readout circuit for resonant sensors based on ring-down measurement, *Proc. IEEE Sensors*. 2014–Decem (2014) 221–224. doi:10.1109/ICSENS.2014.6984973.
- [104] A.-S. Rollier, M. Faucher, B. Legrand, D. Collard, L. Buchaillot, Electrostatic actuators operating in liquid environment: Suppression of pull-in instability and dynamic response, *arXiv Prepr. arXiv0711.3321*. (2007).
- [105] P.L.T.M. Frederix, M.R. Gullo, T. Akiyama, A. Tonin, N.F. De Rooij, U. Staufer, A. Engel, Assessment of insulated conductive cantilevers for biology and electrochemistry, *Nanotechnology*. 16 (2005) 997–1005. doi:10.1088/0957-4484/16/8/001.
- [106] D.A. Buttry, Applications of the Quartz Crystal Microbalance to Electrochemistry, *Electroanal. Chem. - A Ser. Adv.* 17 (1991) 1–86.
- [107] M.R. Deakin, D.A. Buttry, Electrochemical Applications of the Quartz Crystal Microbalance, *Anal. Chem.* 61 (1989) 1147 A-1154 A. doi:10.1021/ac00195a001.
- [108] N. Balke, S. Jesse, B. Carmichael, S. V Kalinin, A.N. Morozovska, L. Qing, S. Jesse, S. V Kalinin, S. Jesse, A.P. Baddorf, S. V Kalinin, R. Wagner, J.P. Killgore, R.C. Tung, N. Balke, S. Jesse, P. Yu, B. Carmichael, Quantification of surface displacements and electromechanical phenomena via dynamic atomic force microscopy, *Nanotechnology*. 27 (2016) 1–12.
- [109] C. Koblinger, E. Uttenthaler, S. Drost, F. Aberl, H. Wolf, G. Brink, A. Stanglmaier, E. Sackmann, Comparison of the QCM and the SPR method for surface studies and immunological applications, *Sensors Actuators B. Chem.* 24 (1995) 107–112. doi:10.1016/0925-4005(95)85023-6.
- [110] A.J. Slavin, Stabilization of sample temperature in a surface-science vacuum chamber to 0.03 K and quartz-crystal microbalance frequency to 0.06 Hz over 0.5 h, *Rev. Sci. Instrum.* 81 (2010) 0–5. doi:10.1063/1.3488368.
- [111] C. Ricciardi, G. Canavese, R. Castagna, I. Ferrante, A. Ricci, S.L. Marasso, L. Napione, F. Bussolino, Integration of microfluidic and cantilever technology for biosensing application in liquid environment, *Biosens. Bioelectron.* 26 (2010) 1565–1570. doi:10.1016/j.bios.2010.07.114.
- [112] S.J. Martin, V.E. Granstaff, G.C. Frye, Characterization of a Quartz Crystal Microbalance with Simultaneous Mass and Liquid Loading, *Anal. Chem.* 2281 (1991) 2272–2281. doi:10.1021/ac00020a015.

- [113] V.M. Mecea, From Quartz Crystal Microbalance to Fundamental Principles of Mass Measurements, *Anal. Lett.* 38 (2005) 753–767. doi:10.1081/AL-200056171.
- [114] A. Alassi, M. Benammar, D. Brett, Quartz crystal microbalance electronic interfacing systems: A review, *Sensors (Switzerland)*. 17 (2017) 1–41. doi:10.3390/s17122799.
- [115] F. Eichelbaum, R. Borngräber, J. Schröder, R. Lucklum, P. Hauptmann, J. Schro, R. Borngra, Interface circuits for quartz-crystal-microbalance sensors, *Rev. Sci. Instrum.* 70 (1999) 2537–2545. doi:10.1063/1.1149788.
- [116] J. Zhang, X.D. Su, S.J. O’Shea, Antibody/antigen affinity behavior in liquid environment with electrical impedance analysis of quartz crystal microbalances, *Biophys. Chem.* 99 (2002) 31–41. doi:10.1016/S0301-4622(02)00109-6.
- [117] A.J. Valimaa, J.T. Santos, C.F. Ockeloen-Korppi, M.A. Sillanpaa, Electrode configuration and electrical dissipation of mechanical energy in quartz crystal resonators, *J. Micromechanics Microengineering*. 28 (2018). doi:10.1088/1361-6439/aac781.
- [118] M. Ferrari, V. Ferrari, An oscillator circuit for dual-harmonic tracking of frequency and resistance in quartz resonator sensors, *Meas. Sci. Technol.* 20 (2009). doi:10.1088/0957-0233/20/12/124005.
- [119] R. Borngräber, J. Schröder, R. Lucklum, P. Hauptmann, Is an oscillator-based measurement adequate in a liquid environment?, *IEEE Trans. Ultrason. Ferroelectr. Freq. Control*. 49 (2002) 1254–1259. doi:10.1109/TUFFC.2002.1041542.
- [120] C. Chagnard, P. Gilbert, A.N. Watkins, T. Beeler, D.W. Paul, An electronic oscillator with automatic gain control: EQCM applications, *Sensors Actuators, B Chem.* 32 (1996) 129–136. doi:10.1016/0925-4005(96)80121-3.
- [121] E.A. Vittoz, M.G.R. Degrauwe, S. Bitz, High-Performance Crystal Oscillator Circuits: Theory and Application., *IEEE J. Solid-State Circuits*. 23 (1987) 774–783. doi:10.1109/4.318.
- [122] I.D. Avramov, A 0-phase circuit for QCM-based measurements in highly viscous liquid environments, *IEEE Sens. J.* 5 (2005) 425–432. doi:10.1109/JSEN.2004.841450.
- [123] A. Arnau, Y. Montagut, J. V García, Y. Jiménez, A different point of view on the sensitivity of quartz crystal microbalance sensors, *Meas. Sci. Technol.* 20 (2009) 124004. doi:10.1088/0957-0233/20/12/124004.
- [124] F. Wudy, M. Multerer, C. Stock, G. Schmeer, H.J. Gores, Rapid impedance scanning QCM for electrochemical applications based on miniaturized hardware and high-performance curve fitting, *Electrochim. Acta*. 53 (2008) 6568–6574. doi:10.1016/j.electacta.2008.04.079.
- [125] Z. Farka, D. Kovář, P. Skládál, Rapid detection of microorganisms based on active and passive modes of QCM, *Sensors (Switzerland)*. 15 (2015) 79–92. doi:10.3390/s150100079.
- [126] G. Liu, Z. Dong, D. Li, Y. Wang, Impedance measurement of quartz crystal based on network analysis method, (2010) 79972N. doi:10.1117/12.888541.
- [127] M. Rodahl, B. Kasemo, Frequency and dissipation-factor responses to localized liquid deposits on a QCM electrode, *Sensors Actuators B Chem.* 37 (1996) 111–116.

doi:10.1016/S0925-4005(97)80077-9.

- [128] G. Ohlsson, C. Langhammer, I. Zorić, B. Kasemo, A nanocell for quartz crystal microbalance and quartz crystal microbalance with dissipation-monitoring sensing, *Rev. Sci. Instrum.* 80 (2009). doi:10.1063/1.3202207.
- [129] F. Höök, M. Rodahl, C. Keller, K. Glasmastar, C. Fredriksson, P. Dahqvist, B. Kasemo, The dissipative QCM-D technique: interfacial phenomena and sensor applications for proteins, biomembranes, living cells and polymers, *Time*. 2 (1999) 966–972. doi:10.1109/FREQ.1999.841467.
- [130] J. Karim, A.H.M.Z. Alam, A.N. Nordin, Mems-Based Oscillators : a Review, *IIUM Eng. J.* 15 (2014) 1–15.
- [131] C. Yao, Y. Qi, Y. Zhao, Y. Xiang, Q. Chen, W. Fu, Aptamer-based piezoelectric quartz crystal microbalance biosensor array for the quantification of IgE, *Biosens. Bioelectron.* 24 (2009) 2499–2503. doi:10.1016/j.bios.2008.12.036.
- [132] D. Johannsmann, L.O. Heim, A simple equation predicting the amplitude of motion of quartz crystal resonators, *J. Appl. Phys.* 100 (2006). doi:10.1063/1.2359138.
- [133] L. Rodriguez-Pardo, J. Cao-Paz, A. Fariña, A. Covelo, X.R. Nóvoa, C. Pérez, Quartz crystal oscillator sensor for qcm monitoring of water absorption in anticorrosion cataphoretic paintings, 2009 IEEE Int. Freq. Control Symp. Jt. with 22nd Eur. Freq. Time Forum. (2009) 1038–1042. doi:10.1109/FREQ.2009.5168352.
- [134] M.A. Syahbana, D.J.H.D. Santjojo, S.P. Sakti, High-resolution multiple channel frequency counter using spartan-3E FPGA, *Proceeding - 2016 Int. Semin. Sensors, Instrumentation, Meas. Metrol. ISSIMM 2016.* (2017) 111–114. doi:10.1109/ISSIMM.2016.7803734.
- [135] A. Krzywaźnia, J. Ociepa, J. Pękała, Microcomputer system of parallel measuring structure for period/frequency monitoring, *Meas. Sci. Technol.* 7 (1996) 1179–1181. doi:10.1088/0957-0233/7/8/014.
- [136] G.N.M. Ferreira, A.-C. da-Silva, B. Tomé, Acoustic wave biosensors: physical models and biological applications of quartz crystal microbalance., *Trends Biotechnol.* 27 (2009) 689–697. doi:10.1016/j.tibtech.2009.09.003.
- [137] X.L. Su, Y. Li, A QCM immunosensor for Salmonella detection with simultaneous measurements of resonant frequency and motional resistance, *Biosens. Bioelectron.* 21 (2005) 840–848. doi:10.1016/j.bios.2005.01.021.
- [138] J.L. Casteleiro-Roca, J.L. Calvo-Rolle, M.C. Meizoso-Lopez, A. Piñón-Pazos, B.A. Rodríguez-Gómez, New approach for the QCM sensors characterization, *Sensors Actuators, A Phys.* 207 (2014) 1–9. doi:10.1016/j.sna.2013.12.002.
- [139] Crystal Resonator Chemistry Measurement System, (n.d.). https://www.sii.co.jp/jp/segg/files/2013/04/file_PRODUCT_MASTER_1692_GRAPHIC_04.pdf (accessed November 23, 2017).
- [140] A. Arnau, A Review of Interface Electronic Systems for AT-cut Quartz Crystal Microbalance Applications in Liquids, *Sensors*. 8 (2008) 370–411. doi:10.3390/s8010370.
- [141] Y. Zhang, B. Du, X. Chen, H. Ma, Convergence of dissipation and impedance

- analysis of quartz crystal microbalance studies, *Anal. Chem.* 81 (2009) 642–648. doi:10.1021/ac8019762.
- [142] C.. F. Beards, *Structural Vibration : Analysis and Damping*, Arnold, London, 1996.
 - [143] A.F. Hill, K.J. Barnham, S.P. Bottomley, *Protein Folding , Misfolding , n.d.*
 - [144] P. Sedlak, J. Majzner, J. Šikula, K. Hajek, Noise Measurement Setup for Quartz Crystal Microbalance, *Radioengineering.* 21 (2012) 207–212. http://radioeng.cz/fulltexts/2012/12_01_0207_0212.pdf.
 - [145] K.D. Rendulic, A. Winkler, Adsorption and desorption dynamics as seen through molecular beam techniques, *Surf. Sci.* 299–300 (1994) 261–276. doi:10.1016/0039-6028(94)90659-9.
 - [146] W. Shockley, D.J. Koneval, Trapped-Energy Modes in Quartz Filter Crystals, *J. Acoust. Soc. Am.* 41 (1967) 981–993.
 - [147] M.K. Mustafa, A. Nabok, D. Parkinson, I.E. Tothill, F. Salam, A. Tsargorodskaya, Detection of beta amyloid peptide (1–16) and amyloid precursor protein (APP770) using spectroscopic ellipsometry and QCM techniques: A step forward towards Alzheimers disease diagnostics-amyloid peptide (1-16) and amyloid precursor protein (APP770) using , *Biosens. Bioelectron.* 26 (2010) 1332–1336. doi:10.1016/j.bios.2010.07.042.
 - [148] A. Guha, N. Sandström, V.P. Ostanin, W. van der Wijngaart, D. Klenerman, S.K. Ghosh, Simple and ultrafast resonance frequency shift measurements using a fixed frequency drive, *Sensors Actuators B Chem.* (n.d.).
 - [149] W. Shu, E.D. Laue, A.A. Seshia, Investigation of biotin-streptavidin binding interactions using microcantilever sensors, *Biosens. Bioelectron.* 22 (2007) 2003–2009. doi:10.1016/j.bios.2006.08.047.
 - [150] M.K. young Park, Biotin-streptavidin binding interactions of dielectric filled silicon bulk acoustic resonators for smart label-free biochemical sensor applications, *Sensors (Basel).* 14 (2014) 4585–4598. doi:10.3390/s140304585.
 - [151] M.A. Lombardi, *Fundamentals of Time and Frequency*, in: *Mechatronics Handb.*, CRC Press LLC, 2002. doi:10.1201/9781420037241.ch10.
 - [152] J.R. Vig, E.S. Ferre-Pikal, (IEEE Standard 1139-1999) *IEEE Standard Definitions of Physical Quantities for Fundamental Frequency and Time Metrology - Random Instabilities*, 1999. doi:10.1109/IEEESTD.1999.90575.
 - [153] L. Rodríguez-Pardo, J.F. Rodríguez, C. Gabrielli, H. Perrot, R. Brendel, Sensitivity, noise, and Resolution in QCM sensors in liquid media, *IEEE Sens. J.* 5 (2005) 1251–1256. doi:10.1109/JSEN.2005.859257.
 - [154] E.M. Cherry, D.E. Hooper, *Amplifying Devices and Low-Pass Amplifier Design*, John Wiley & Sons, Inc., New York-London-Sydney, 1968.
 - [155] Y. Gao, L. Zhang, W. Huo, Y. Gao, S. Shi, Determination of Affinity and Kinetic Constants of the Biotin-Streptavidin Complex Using Microfluidic GMR Biosensors, *IEEE Trans. Magn.* 51 (2015) 12–15. doi:10.1109/TMAG.2015.2443125.
 - [156] V.C. Kalia, Quorum sensing inhibitors: An overview, *Biotechnol. Adv.* 31 (2013) 224–245. doi:10.1016/j.biotechadv.2012.10.004.

- [157] I.E. Tothill, Biosensors for cancer markers diagnosis, *Semin. Cell Dev. Biol.* 20 (2009) 55–62. doi:10.1016/j.semcdb.2009.01.015.
- [158] WHO, World Malaria Report, 2016. doi:10.4135/9781452276151.n221.
- [159] A. Qureshi, Y. Gurbuz, J.H. Niazi, Biosensors for cardiac biomarkers detection: A review, *Sensors Actuators, B Chem.* 171–172 (2012) 62–76. doi:10.1016/j.snb.2012.05.077.
- [160] M.T. Novak, C.N. Kotanen, S. Carrara, A. Guiseppi-Elie, F.G. Moussy, Diagnostic tools and technologies for infectious and non-communicable diseases in low-and-middle-income countries, *Health Technol. (Berl)*. 3 (2013) 271–281. doi:10.1007/s12553-013-0060-9.
- [161] J.D. McBride, M.A. Cooper, A high sensitivity assay for the inflammatory marker C-Reactive protein employing acoustic biosensing., *J. Nanobiotechnology.* 6 (2008) 5. doi:10.1186/1477-3155-6-5.
- [162] T. Fortin, A. Salvador, J.P. Charrier, C. Lenz, X. Lacoux, A. Morla, G. Choquet-Kastylevsky, J. Lemoine, Clinical quantitation of prostate-specific antigen biomarker in the low nanogram/milliliter range by conventional bore liquid chromatography-tandem mass spectrometry (multiple reaction monitoring) coupling and correlation with ELISA tests., *Mol. Cell. Proteomics.* 8 (2009) 1006–15. doi:10.1074/mcp.M800238-MCP200.
- [163] W. Jongbloed, M.A.C. Herrebout, M.A. Blankenstein, R. Veerhuis, Quantification of clusterin in paired cerebrospinal fluid and plasma samples., *Ann. Clin. Biochem.* 51 (2014) 557–67. doi:10.1177/0004563213503456.
- [164] R.A. Weinstein, R. Gaynes, J.R. Edwards, Overview of Nosocomial Infections Caused by Gram-Negative Bacilli, *Clin. Infect. Dis.* 41 (2005) 848–854. doi:10.1086/432803.
- [165] N. Woodford, D.M. Livermore, Infections caused by Gram-positive bacteria: a review of the global challenge, *J. Infect.* 59 (2009) S4–S16. doi:10.1016/S0163-4453(09)60003-7.
- [166] V. Ki, C. Rotstein, Bacterial skin and soft tissue infections in adults: A review of their epidemiology, pathogenesis, diagnosis, treatment and site of care., *Can. J. Infect. Dis. Med. Microbiol. = J. Can. Des Mal. Infect. La Microbiol. Médicale.* 19 (2008) 173–84. <http://www.ncbi.nlm.nih.gov/pubmed/19352449%5Cnhttp://www.pubmedcentral.nih.gov/articlerender.fcgi?artid=PMC2605859>.
- [167] S. Tokonami, T. Iida, Review: Novel sensing strategies for bacterial detection based on active and passive methods driven by external field, *Anal. Chim. Acta.* 988 (2017) 1–16. doi:10.1016/j.aca.2017.07.034.
- [168] T.H. Boyles, S. Wasserman, Diagnosis of bacterial infection, *South African Med. J.* 105 (2015) 419–421. doi:10.7196/SAMJ.9647.
- [169] K.J. Downes, S.S. Shah, Biomarkers in infectious diseases, *J. Pediatric Infect. Dis. Soc.* 1 (2012) 343–346. doi:10.1093/jpids/pis099.
- [170] T. Yusa, K. Tateda, A. Ohara, S. Miyazaki, New possible biomarkers for diagnosis of infections and diagnostic distinction between bacterial and viral infections in children, *J. Infect. Chemother.* 23 (2017) 96–100. doi:10.1016/j.jiac.2016.11.002.
- [171] E. Eden, I. Srugo, T. Gottlieb, R. Navon, O. Boico, A. Cohen, E. Bamberger, A. Klein,

- K. Oved, Diagnostic accuracy of a TRAIL, IP-10 and CRP combination for discriminating bacterial and viral etiologies at the Emergency Department, *J. Infect.* 73 (2016) 177–180. doi:10.1016/j.jinf.2016.05.002.
- [172] C.L. Ventola, The antibiotic resistance crisis: part 1: causes and threats., *P T A Peer-Reviewed J. Formul. Manag.* 40 (2015) 277–83. doi:Article.
- [173] A. Kumari, P. Pasini, S. Daunert, Detection of bacterial quorum sensing N-acyl homoserine lactones in clinical samples, *Anal. Bioanal. Chem.* 391 (2008) 1619–1627. doi:10.1007/s00216-008-2002-3.
- [174] Q. Yang, Y. Han, X.H. Zhang, Detection of quorum sensing signal molecules in the family Vibrionaceae, *J. Appl. Microbiol.* 110 (2011) 1438–1448. doi:10.1111/j.1365-2672.2011.04998.x.
- [175] Q. Yang, Y. Han, N.T.N. Tinh, N.T. Hien, P. Bossier, Detection of Quorum Sensing Signal Molecules in *Edwardsiella ictaluri* Ei-151, *Indian J. Microbiol.* 52 (2012) 581–586. doi:10.1007/s12088-012-0312-9.
- [176] L. Ravn, A.B. Christensen, S. Molin, M. Givskov, L. Gram, Methods for detecting acylated homoserine lactones produced by Gram-negative bacteria and their application in studies of AHL-production kinetics, *J. Microbiol. Methods.* 44 (2001) 239–251. doi:10.1016/S0167-7012(01)00217-2.
- [177] E. Baldrich, F.X. Muñoz, C. García-Aljaro, Electrochemical detection of quorum sensing signaling molecules by dual signal confirmation at microelectrode arrays, *Anal. Chem.* 83 (2011) 2097–2103. doi:10.1021/ac1028243.
- [178] H. Jiang, D. Jiang, J. Shao, X. Sun, Magnetic molecularly imprinted polymer nanoparticles based electrochemical sensor for the measurement of Gram-negative bacterial quorum signaling molecules (N-acyl-homoserine-lactones), *Biosens. Bioelectron.* 75 (2016) 411–419. doi:10.1016/j.bios.2015.07.045.
- [179] K. Lakshmana Gowda, J. John, M.A.M. Marie, G. Sangeetha, S.R. Bindurani, Isolation and characterization of quorum-sensing signalling molecules in *Pseudomonas aeruginosa* isolates recovered from nosocomial infections, *Apmis.* 121 (2013) 886–889. doi:10.1111/apm.12047.
- [180] W.F. Yin, K. Purmal, S. Chin, X.Y. Chan, C.L. Koh, C.K. Sam, K.G. Chan, N-Acyl homoserine lactone production by *Klebsiella pneumonia* isolated from human tongue surface, *Sensors.* 12 (2012) 3472–3483. doi:10.3390/s120303472.
- [181] B. Middleton, H.C. Rodgers, M. CÃ¡mara, A.J. Knox, P. Williams, A. Hardman, M. Cámara, Direct detection of N -acylhomoserine lactones in cystic fibrosis sputum, *FEMS Microbiol. Lett.* 207 (2002) 1–7. doi:10.1111/j.1574-6968.2002.tb11019.x.
- [182] H.J. Cheng, R. Ee, Y.M. Cheong, W.S. Tan, W.F. Yin, K.G. Chan, Detection of quorum sensing activity in the multidrug-resistant clinical isolate *pseudomonas aeruginosa* strain GB11, *Sensors (Switzerland).* 14 (2014) 12511–12522. doi:10.3390/s140712511.
- [183] C. Okano, M. Arai, E. Nasuno, K. Iimura, T. Morohoshi, T. Ikeda, N. Kato, Cyclodextrin Interaction with N -Hexanoyl Homoserine Lactone as Quorum Sensing Signal Produced in Gram-Negative Bacteria, *Trans. Mat. Res. Soc. Japan.* 37 (2012) 315–318.

- [184] A. Annapoorani, A.K.K.A. Jabbar, S.K.S. Musthafa, S.K. Pandian, A.V. Ravi, Inhibition of Quorum Sensing Mediated Virulence Factors Production in Urinary Pathogen *Serratia marcescens* PS1 by Marine Sponges, *Indian J. Microbiol.* 52 (2012) 160–166. doi:10.1007/s12088-012-0272-0.
- [185] A. Kumari, P. Pasini, S.K. Deo, D. Flomenhoft, H. Shashidhar, S. Daunert, Biosensing systems for the detection of bacterial quorum signaling molecules, *Anal. Chem.* 78 (2006) 7603–7609. doi:10.1021/ac061421n.
- [186] M. Cooley, S.R. Chhabra, P. Williams, N-Acylhomoserine Lactone-Mediated Quorum Sensing: A Twist in the Tail and a Blow for Host Immunity, *Chem. Biol.* 15 (2008) 1141–1147. doi:10.1016/j.chembiol.2008.10.010.
- [187] P.D. Shaw, G. Ping, S.L. Daly, C. Cha, J.E. Cronan, K.L. Rinehart, S.K. Farrand, Detecting and characterizing N-acyl-homoserine lactone signal molecules by thin-layer chromatography, *Proc. Natl. Acad. Sci.* 94 (1997) 6036–6041. doi:10.1073/pnas.94.12.6036.
- [188] R. Kumar, S. Chhibber, V. Gupta, K. Harjai, Screening and profiling of quorum sensing signal molecules in *Pseudomonas aeruginosa* isolates from catheterized urinary tract infection patients, *Indian J Med Res.* 134 (2011) 208–213. doi:IndianJMedRes_2011_134_2_208_84751 [pii].
- [189] C. García-Aljaro, L. Eberl, K. Riedel, A.R. Blanch, C. Garcia-Aljaro, Detection of quorum-sensing-related molecules in *Vibrio scophthalmi*., *BMC Microbiol.* 8 (2008) 138. doi:10.1186/1471-2180-8-138.
- [190] X. Li, Y. Han, Q. Yang, X.H. Zhang, Detection of quorum sensing signal molecules and mutation of *luxS* gene in *Vibrio ichthyenteri*, *Res. Microbiol.* 161 (2010) 51–57. doi:10.1016/j.resmic.2009.10.004.
- [191] C. García-Aljaro, G.J. Vargas-Cespedes, A.R. Blanch, Detection of acylated homoserine lactones produced by *Vibrio* spp. and related species isolated from water and aquatic organisms, *J. Appl. Microbiol.* 112 (2012) 383–389. doi:10.1111/j.1365-2672.2011.05199.x.
- [192] Y.T. Horng, S.C. Deng, M. Daykin, P.C. Soo, J.R. Wei, K.T. Luh, S.W. Ho, S. Swift, H.C. Lai, P. Williams, The LuxR family protein SpnR functions as a negative regulator of N-acylhomoserine lactone-dependent quorum sensing in *Serratia marcescens*, *Mol. Microbiol.* 45 (2002) 1655–1671. doi:10.1046/j.1365-2958.2002.03117.x.
- [193] L.N.H. Lactones, I. Llamas, N. Keshavan, J.E. Gonza, Use of *Sinorhizobium meliloti* as an Indicator for Specific Detection of, *Society.* 70 (2004) 3715–3723. doi:10.1128/AEM.70.6.3715.
- [194] J.B.O. Andersen, A. Heydorn, M. Hentzer, L.E.O. Eberl, O. Geisenberger, R.E.N. Molin, M. Givskov, B.B.A.K. Christensen, gfp -Based N -Acyl Homoserine-Lactone Sensor Systems for Detection of Bacterial Communication, *Appl. Environ. Microbiol.* 67 (2001) 575–585. doi:10.1128/AEM.67.2.575.
- [195] K. Tang, Y. Zhang, M. Yu, X. Shi, T. Coenye, P. Bossier, X.H. Zhang, Evaluation of a new high-throughput method for identifying quorum quenching bacteria, *Sci. Rep.* 3 (2013) 1–9. doi:10.1038/srep02935.
- [196] Z.G. Zhao, Y.M. Yu, B.Y. Xu, S.S. Yan, J.F. Xu, F. Liu, G.M. Li, Y.L. Ding, S.Q. Wu, Screening and anti-virulent study of N-acyl homoserine lactones DNA aptamers

- against *Pseudomonas aeruginosa* quorum sensing, *Biotechnol. Bioprocess Eng.* 18 (2013) 406–412. doi:10.1007/s12257-012-0556-6.
- [197] M.B. Miller, B.L. Bassler, Ensing in, *Annu. Rev. Microbiol.* 55 (2001) 165–99. doi:10.1146/annurev.micro.55.1.165.
- [198] S. Poonguzhali, M. Madhaiyan, T. Sa, Production of acyl-homoserine lactone quorum-sensing signals is wide-spread in gram-negative *Methylobacterium*, *J. Microbiol. Biotechnol.* 17 (2007) 226–233.
- [199] J. Liu, K. Fu, Y. Wang, C. Wu, F. Li, L. Shi, Y. Ge, L. Zhou, Detection of Diverse N-Acyl-Homoserine Lactones in *Vibrio alginolyticus* and Regulation of Biofilm Formation by N-(3-Oxodecanoyl) Homoserine Lactone In vitro, *Front. Microbiol.* 8 (2017) 1–15. doi:10.3389/fmicb.2017.01097.
- [200] C.A. Ortori, J.F. Dubern, S.R. Chhabra, M. Cámara, K. Hardie, P. Williams, D.A. Barrett, Simultaneous quantitative profiling of N-acyl-L-homoserine lactone and 2-alkyl-4(1H)-quinolone families of quorum-sensing signaling molecules using LC-MS/MS, *Anal. Bioanal. Chem.* 399 (2011) 839–850. doi:10.1007/s00216-010-4341-0.
- [201] T.R.I. Cataldi, G. Bianco, L. Palazzo, V. Quaranta, Occurrence of N-acyl-L-homoserine lactones in extracts of some Gram-negative bacteria evaluated by gas chromatography-mass spectrometry, *Anal. Biochem.* 361 (2007) 226–235. doi:10.1016/j.ab.2006.11.037.
- [202] Y.W. Kim, C. Sung, S. Lee, K.J. Kim, Y.H. Yang, B.G. Kim, Y.K. Lee, H.W. Ryu, Y.G. Kim, MALDI-MS-based quantitative analysis for ketone containing homoserine lactones in *pseudomonas aeruginosa*, *Anal. Chem.* 87 (2015) 858–863. doi:10.1021/ac5039362.
- [203] J.S. Kumar, S. Umesha, K.S. Prasad, P. Niranjana, Detection of Quorum Sensing Molecules and Biofilm Formation in *Ralstonia solanacearum*, *Curr. Microbiol.* 72 (2016) 297–305. doi:10.1007/s00284-015-0953-0.
- [204] R. Taghadosi, M.R. Shakibaie, S. Masoumi, Biochemical detection of N-Acyl homoserine lactone (AHL) from biofilm-forming uropathogenic *Escherichia coli* (UPEC) isolated from urinary tract infection (UTI) samples, *Reports Biochem. Mol. Biol.* 3 (2015).
- [205] K. Wöllner, X. Chen, E. Kremmer, P.M. Krämer, Comparative surface plasmon resonance and enzyme-linked immunosorbent assay characterisation of a monoclonal antibody with N-acyl homoserine lactones, *Anal. Chim. Acta.* 683 (2010) 113–118. doi:10.1016/j.aca.2010.10.015.
- [206] F. Nievas, P. Bogino, F. Sorroche, W. Giordano, Detection, characterization, and biological effect of quorum-sensing signaling molecules in Peanut-nodulating bradyrhizobia, *Sensors.* 12 (2012) 2851–2873. doi:10.3390/s120302851.
- [207] U.M. Pinto, E. de Souza Viana, M.L. Martins, M.C.D. Vanetti, Detection of acylated homoserine lactones in gram-negative proteolytic psychrotrophic bacteria isolated from cooled raw milk, *Food Control.* 18 (2007) 1322–1327. doi:10.1016/j.foodcont.2006.09.005.
- [208] S. Palliyil, C. Downham, I. Broadbent, K. Charlton, A.J. Porter, High-Sensitivity Monoclonal Antibodies Specific for Homoserine Lactones Protect Mice from Lethal *Pseudomonas aeruginosa* Infections, *Appl. Environ. Microbiol.* 80 (2014) 462–469.

doi:10.1128/AEM.02912-13.

- [209] S. Susmel, C. Comuzzi, Selectivity and Efficiency of Conductive Molecularly Imprinted Polymer (c-MIP) Based on 5-Phenyl-Dipyrromethane and 5-Phenol-Dipyrromethane for Quorum Sensing Precursors Detection, *Chemosensors*. 5 (2017) 5. doi:10.3390/chemosensors5010005.
- [210] L.G. Carrascosa, M. Moreno, M. ??lvarez, L.M. Lechuga, Nanomechanical biosensors: A new sensing tool, *TrAC - Trends Anal. Chem.* 25 (2006) 196–206. doi:10.1016/j.trac.2005.09.006.
- [211] D. Hauden, Miniaturized Bulk and Surface Acoustic Wave Quartz Oscillators Used as Sensors, *IEEE Trans. Ultrason. Ferroelectr. Freq. Control*. 34 (1987) 253–258. doi:10.1109/T-UFFC.1987.26939.
- [212] M. Michalzik, R. Wilke, S. Büttgenbach, Miniaturized QCM-based flow system for immunosensor application in liquid, *Sensors Actuators, B Chem.* 111–112 (2005) 410–415. doi:10.1016/j.snb.2005.03.048.
- [213] L.E.I. Ye, K. Mosbach, The Technique of Molecular Imprinting – Principle, State of the Art, and Future Aspect, *J. Incl. Phenom. and Macrocyclic Chem.* 41 (2001) 107–113. doi:10.1023/A:1014498404292.
- [214] F. Canfarotta, A. Poma, A. Guerreiro, S. Piletsky, Solid-phase synthesis of molecularly imprinted nanoparticles, *Nat. Protoc.* 11 (2016) 443–455. doi:10.1038/nprot.2016.030.
- [215] A. Guha, O.S. Ahmad, A. Guerreiro, N. Sandström, V.P. Ostanin, W. van der Wijngaart, D. Klenerman, S.A. Piletsky, S.K. Ghosh, Label free acoustic detection of gram negative bacterial infection biomarker using a fixed frequency drive, 2018. doi:10.15713/ins.mmj.3.
- [216] E. V. Piletska, G. Stavroulakis, K. Karim, M.J. Whitcombe, I. Chianella, A. Sharma, K.E. Eboigbodin, G.K. Robinson, S.A. Piletsky, Attenuation of vibrio fischeri quorum sensing using rationally designed polymers, *Biomacromolecules*. 11 (2010) 975–980. doi:10.1021/bm901451j.
- [217] E. V. Piletska, G. Stavroulakis, L.D. Larcombe, M.J. Whitcombe, A. Sharma, S. Primrose, G.K. Robinson, S.A. Piletsky, Passive control of quorum sensing: Prevention of pseudomonas aeruginosa biofilm formation by imprinted polymers, *Biomacromolecules*. 12 (2011) 1067–1071. doi:10.1021/bm101410q.
- [218] E.M. dos S. Cavaleiro, Development of Polymeric Materials to Inhibit Bacterial Quorum Sensing, Cranfield University & University of Aveiro, 2014. doi:10.1017/CBO9781107415324.004.
- [219] A. DeLean, P.J. Munson, D. Rodbard, Simultaneous analysis of families of sigmoidal curves: application to bioassay, radioligand assay, and physiological dose-response curves., *Am. J. Physiol. Metab.* 235 (1978) E97. doi:10.1152/ajpendo.1978.235.2.E97.
- [220] R.-J. Yang, C.-C. Chang, J.-K. Chen, Y.-J. Pan, Membrane Actuation for Micropumps, in: *Encycl. Microfluid. Nanofluidics*, Springer, Boston, 2008: pp. 1078–1082. <https://www.grc.nasa.gov/www/k-12/airplane/machrole.html#>.
- [221] M. Liss, B. Petersen, H. Wolf, E. Prohaska, An aptamer-based quartz crystal protein biosensor, *Anal. Chem.* 74 (2002) 4488–4495. doi:10.1021/ac011294p.

- [222] I.Y. Huang, M.C. Lee, Development of a FPW allergy biosensor for human IgE detection by MEMS and cystamine-based SAM technologies, *Sensors Actuators, B Chem.* 132 (2008) 340–348. doi:10.1016/j.snb.2008.01.048.
- [223] C.-C. Chang, C.-Y. Chen, X. Zhao, T.-H. Wu, S.-C. Wei, C.-W. Lin, Label-free colorimetric aptasensor for IgE using DNA pseudoknot probe., *Analyst.* 139 (2014) 3347–51. doi:10.1039/c4an00253a.
- [224] Y.M. Liu, J.J. Yang, J.T. Cao, J.J. Zhang, Y.H. Chen, S.W. Ren, An electrochemiluminescence aptasensor based on CdSe/ZnS functionalized MoS₂ and enzymatic biocatalytic precipitation for sensitive detection of immunoglobulin e, *Sensors Actuators, B Chem.* 232 (2016) 538–544. doi:10.1016/j.snb.2016.03.165.
- [225] G. Proczek, A.-L. Gassner, J.-M. Busnel, H.H. Girault, Total serum IgE quantification by microfluidic ELISA using magnetic beads, *Anal. Bioanal. Chem.* 402 (2012) 2645–2653. doi:10.1007/s00216-011-5495-0.
- [226] L.B. Buravkova, M.P. Rykova, Y.G. Gertsik, E.N. Antropova, Effects of space flights on human allergic status (IgE-mediated sensitivity), *Acta Astronaut.* 60 (2007) 254–258. doi:10.1016/j.actaastro.2006.08.006.
- [227] D.R. Jackola, M.N. Blumenthal, A. Rosenberg, Evidence for two independent distributions of serum immunoglobulin e in atopic families: Cognate and non-cognate IgE, *Hum. Immunol.* 65 (2004) 20–30. doi:10.1016/j.humimm.2003.10.012.
- [228] Y.H. Kim, J.P. Kim, S.J. Han, S.J. Sim, Aptamer biosensor for lable-free detection of human immunoglobulin E based on surface plasmon resonance, *Sensors Actuators, B Chem.* 139 (2009) 471–475. doi:10.1016/j.snb.2009.03.013.
- [229] C. Yao, T. Zhu, Y. Qi, Y. Zhao, H. Xia, W. Fu, Development of a quartz crystal microbalance biosensor with aptamers as bio-recognition element, *Sensors.* 10 (2010) 5859–5871. doi:10.3390/s100605859.
- [230] J.J. Garcia, M. Blanca, F. Moreno, J.M. Vega, C. Mayorga, J. Fernandez, C. Juarez, A. Romano, E. De Ramon, Determination of IgE antibodies to the benzylpenicilloyl determinant: A comparison of the sensitivity and specificity of three radio allergeo sorbent test methods, *J. Clin. Lab. Anal.* 11 (1997) 251–257. doi:10.1002/(SICI)1098-2825(1997)11:5<251::AID-JCLA3>3.0.CO;2-A.
- [231] K. Stadtherr, H. Wolf, P. Lindner, An aptamer-based protein biochip, *Anal. Chem.* 77 (2005) 3437–3443. doi:10.1021/ac0483421.
- [232] S. Rahmatpour, A.H. Khan, R. Nasiri Kalmarzi, M. Rajabibazl, G. Tavoosidana, E. Motevaseli, N. Zarghami, E. Sadroddiny, Application of immuno-PCR assay for the detection of serum IgE specific to Bermuda allergen, *Mol. Cell. Probes.* 32 (2017) 1–4. doi:10.1016/j.mcp.2016.10.002.
- [233] J.R. Cole, L.W.D. Jr, E.J. Morgan, L.B. MCGOWN, Affinity Capture and Detection of Immunoglobulin E in Human Serum using an Aptamer-Modified Surface in Matrix Assisted Laser Desorption/Ionization Mass Spectrometry, *Anal Chem.* 79 (2007) 273–279. doi:10.1021/ac061256b.Affinity.
- [234] D. Pomponi, M.L. Bernardi, M. Liso, P. Palazzo, L. Tuppo, C. Rifaiani, M. Santoro, A. Labrada, M.A. Ciardiello, A. Mari, E. Scala, Allergen micro-bead array for IgE detection: A feasibility study using allergenic molecules tested on a flexible multiplex flow cytometric immunoassay, *PLoS One.* 7 (2012) 1–16.

doi:10.1371/journal.pone.0035697.

- [235] B. Schweitzer, S. Wiltshire, J. Lambert, S. O'Malley, K. Kukanskis, Z. Zhu, S.F. Kingsmore, P.M. Lizardi, D.C. Ward, Immunoassays with rolling circle DNA amplification: a versatile platform for ultrasensitive antigen detection., *Proc. Natl. Acad. Sci. U. S. A.* 97 (2000) 10113–9. doi:10.1073/pnas.170237197.
- [236] J.L. He, Z.S. Wu, S.B. Zhang, G.L. Shen, R.Q. Yu, Novel fluorescence enhancement IgE assay using a DNA aptamer, *Analyst.* 134 (2009) 1003–1007. doi:10.1039/b812450g.
- [237] B. Teste, F. Malloggi, J.-M. Siaugue, A. Varenne, F. Kanoufi, S. Descroix, Microchip integrating magnetic nanoparticles for allergy diagnosis, *Lab Chip.* 11 (2011) 4207–4213. doi:10.1039/C1LC20809H.
- [238] X. Su, J. Zhang, Comparison of surface plasmon resonance spectroscopy and quartz crystal microbalance for human IgE quantification, *Sensors Actuators, B Chem.* 100 (2004) 309–314. doi:10.1016/j.snb.2004.01.020.
- [239] S. Kim, J. Lee, S.J. Lee, H.J. Lee, Ultra-sensitive detection of IgE using biofunctionalized nanoparticle-enhanced SPR, *Talanta.* 81 (2010) 1755–1759. doi:10.1016/j.talanta.2010.03.036.
- [240] K.-J. Huang, Y.-J. Liu, J.-T. Cao, H.-B. Wang, An aptamer electrochemical assay for sensitive detection of immunoglobulin E based on tungsten disulfide-graphene composites and gold nanoparticles, *RSC Adv.* 4 (2014) 36742–36748. doi:10.1039/c4ra06133k.
- [241] C.Y. Lee, K.Y. Wu, H.L. Su, H.Y. Hung, Y.Z. Hsieh, Sensitive label-free electrochemical analysis of human IgE using an aptasensor with cDNA amplification, *Biosens. Bioelectron.* 39 (2013) 133–138. doi:10.1016/j.bios.2012.07.009.
- [242] Y.F. Liu, J.J. Tsai, Y.T. Chin, E.C. Liao, C.C. Wu, G.J. Wang, Detection of allergies using a silver nanoparticle modified nanostructured biosensor, *Sensors Actuators, B Chem.* 171–172 (2012) 1095–1100. doi:10.1016/j.snb.2012.06.039.
- [243] D.T. Tran, V. Vermeeren, L. Grieten, S. Wenmackers, P. Wagner, J. Pollet, K.P.F. Janssen, L. Michiels, J. Lammertyn, Nanocrystalline diamond impedimetric aptasensor for the label-free detection of human IgE, *Biosens. Bioelectron.* 26 (2011) 2987–2993. doi:10.1016/j.bios.2010.11.053.
- [244] A. Salimi, S. Khezrian, R. Hallaj, A. Vaziry, Highly sensitive electrochemical aptasensor for immunoglobulin e detection based on sandwich assay using enzyme-linked aptamer, *Anal. Biochem.* 466 (2014) 89–97. doi:10.1016/j.ab.2014.08.019.
- [245] D. Xu, D. Xu, X. Yu, Z. Liu, W. He, Z. Ma, Label-free electrochemical detection for aptamer-based array electrodes, *Anal. Chem.* 77 (2005) 5107–5113. doi:10.1021/ac050192m.
- [246] S. Khezrian, A. Salimi, H. Teymourian, R. Hallaj, Label-free electrochemical IgE aptasensor based on covalent attachment of aptamer onto multiwalled carbon nanotubes/ionic liquid/chitosan nanocomposite modified electrode, *Biosens. Bioelectron.* 43 (2013) 218–225. doi:10.1016/j.bios.2012.12.006.
- [247] X. Luo, I. Lee, J. Huang, M. Yun, X.T. Cui, Ultrasensitive protein detection using an aptamer-functionalized single polyaniline nanowire., *Chem. Commun. (Camb).* 47

- (2011) 6368–70. doi:10.1039/c1cc11353d.
- [248] Y. Ohno, K. Maehashi, K. Matsumoto, Label-free biosensors based on aptamer-modified graphene field-effect transistors, *J. Am. Chem. Soc.* 132 (2010) 18012–18013. doi:10.1021/ja108127r.
 - [249] K. Maehashi, T. Katsura, K. Kerman, Y. Takamura, K. Matsumoto, E. Tamiya, Label-free protein biosensor based on aptamer-modified carbon nanotube field-effect transistors, *Anal. Chem.* 79 (2007) 782–787. doi:10.1021/ac060830g.
 - [250] M. Hasegawa, Y. Hirayama, Y. Ohno, K. Maehashi, K. Matsumoto, Characterization of reduced graphene oxide field-effect transistor and its application to biosensor, *Jpn. J. Appl. Phys.* 53 (2014). doi:10.7567/JJAP.53.05FD05.
 - [251] K. Maehashi, K. Matsumoto, Y. Takamura, Aptamer-Based Label-Free Immunosensors Using Carbon Nanotube Field-Effect Transistors, *Electroanalysis*. 21 (2009) 1285–1290. doi:10.1002/elan.200804552.
 - [252] X. Su, F. Chew, S.F.Y. Li, Self-assembled monolayer-based piezoelectric crystal immunosensor for the quantification of total human immunoglobulin E, *Anal. Biochem.* 273 (1999) 66–72.
 - [253] U. Schaible, M. Liss, E. Prohaska, J. Decker, K. Stadtherr, H. Wolf, Affinity measurements of biological molecules by a quartz crystal microbalance (QCM) biosensor., *Methods Mol. Med.* 94 (2004) 321–330. doi:10.1385/1592596797.
 - [254] C. Yao, Q. Chen, M. Chen, B. Zhang, Y. Luo, Q. Huang, J. Huang, W. Fu, A Novel Piezoelectric Quartz Micro-Array Immunosensor for Detection of ImmunoglobulinE, *J. Nanosci. Nanotechnol.* 6 (2006) 7. doi:http://dx.doi.org/wwwproxy0.library.unsw.edu.au/10.1166/jnn.2006.605.
 - [255] X. Su, F. Tim Chew, S.F.Y. Li, Piezoelectric quartz crystal based label-free analysis for allergy disease, *Biosens. Bioelectron.* 15 (2000) 629–639. doi:10.1016/S0956-5663(00)00112-3.
 - [256] Y.-C. Chen, W.-C. Shih, W.-T. Chang, C.-H. Yang, K.-S. Kao, C.-C. Cheng, Biosensor for human IgE detection using shear-mode FBAR devices, *Nanoscale Res. Lett.* 10 (2015) 69. doi:10.1186/s11671-015-0736-3.
 - [257] Y.-C. Chen, W.-T. Chang, C.-C. Cheng, J.-Y. Shen, K.-S. Kao, Development of human IgE biosensor using Sezawa-mode SAW devices, *Curr. Appl. Phys.* 14 (2014) 608–613. doi:10.1016/j.cap.2014.02.012.
 - [258] H.J. Lee, S.O. Jung, J.Y. Shim, Surface acoustic wave immunosensor for diagnosing allergy disease and method for diagnosing allergy disease using the same, 09150484.5, 2009. doi:10.1371/journal.pone.0010853.
 - [259] I. Huang, M. Lee, Y. Chang, Development of a Novel Flexural Plate Wave Biosensor for Immunoglobulin-E Detection by Using SAM and MEMS Technologies, (2006) 70–73.
 - [260] K.J. Feng, C.H. Sun, J.H. Jiang, R.Q. Yu, An Aptamer-Based Competitive Fluorescence Quenching Assay for Ige, *Anal. Lett.* 44 (2011) 1301–1309. doi:10.1080/00032719.2010.511747.

- [261] J.A. Goode, J.V.H. Rushworth, P.A. Millner, Biosensor Regeneration: A Review of Common Techniques and Outcomes, *Langmuir*. 31 (2015) 6267–6276. doi:10.1021/la503533g.
- [262] L. García-Gancedo, W.I. Milne, J.K. Luo, a. J. Flewitt, Sensors based on SAW and FBAR technologies, *Spie*. 8793 (2013) 879308. doi:10.1117/12.2022205.
- [263] N. Plattner, F. Noe, Protein conformational plasticity and complex ligand-binding kinetics explored by atomistic simulations and Markov models, *Nat. Commun*. 6 (2015). doi:10.1038/ncomms8653.
- [264] M.A. Morando, G. Saladino, N. D’Amelio, E. Pucheta-Martinez, S. Lovera, M. Lelli, B. López-Méndez, M. Marenchino, R. Campos-Olivas, F.L. Gervasio, Conformational Selection and Induced Fit Mechanisms in the Binding of an Anticancer Drug to the c-Src Kinase, *Sci. Rep*. 6 (2016) 1–9. doi:10.1038/srep24439.
- [265] P. Horowitz, W. Hill, *The Art Of Electronics*, Press Syndicate of the University of Cambridge, Cambridge, n.d.
- [266] S. Beißner, J.W. Thies, C. Bechthold, P. Kuhn, B. Thürmann, S. Dübel, A. Dietzel, Low-cost, in-liquid measuring system using a novel compact oscillation circuit and quartz-crystal microbalances (QCMs) as a versatile biosensor platform, *J. Sensors Sens. Syst*. 6 (2017) 341–350. doi:10.5194/jsss-6-341-2017.
- [267] C. Mista, M. Zalazar, A. Pealva, M. Martina, J.M. Reta, Open Source Quartz Crystal Microbalance with dissipation monitoring, *J. Phys. Conf. Ser*. 705 (2016). doi:10.1088/1742-6596/705/1/012008.
- [268] B. Kim, T. Yamamoto, Y. Kim, In-Line Measurement of Water Contents in Ethanol Using a Zeolite-Coated Quartz Crystal Microbalance, *Sensors*. 15 (2015) 27273–27282. doi:10.3390/s151027273.
- [269] N. Turner, M. Bloxham, S.A. Piletsky, M.J. Whitcombe, I. Chianella, The use of Quartz Crystal Microbalance as an analytical tool to monitor particles/surface and particle/particle interactions in dry ambient and pressurized conditions: a study using common inhaler components, *R. Soc. Chem*. (2013) 1–3. doi:10.1039/x0xx00000x.
- [270] S. Saha, M. Raje, C.R. Suri, Sandwich microgravimetric immunoassay: Sensitive and specific detection of low molecular weight analytes using piezoelectric quartz crystal, *Biotechnol. Lett*. 24 (2002) 711–716. doi:10.1023/A:1015238201367.
- [271] A. Jbari, L. Bellarbi, N. Zine, C.A. Mills, J. Samitier, A. Errachid, Multiplexed frequency spectrum analyzer instrumentation for the characterization of multiple QCM-based biosensors, 2007 Int. Conf. Sens. Technol. Appl. SENSORCOMM 2007, *Proc.* (2007) 436–440. doi:10.1109/SENSORCOMM.2007.4394960.
- [272] H. Ogi, H. Nagai, Y. Fukunishi, T. Yanagida, M. Hirao, M. Nishiyama, Multichannel wireless-electrodeless quartz-crystal microbalance immunosensor, *Anal. Chem*. 82 (2010) 3957–3962. doi:10.1021/ac100527r.
- [273] W. Tao, P. Lin, Y. Ai, H. Wang, S. Ke, X. Zeng, Multichannel quartz crystal microbalance array: Fabrication, evaluation, application in biomarker detection, *Anal. Biochem*. 494 (2016) 85–92. doi:10.1016/j.ab.2015.11.001.
- [274] Y.-Y. Chen, L.-C. Huang, T.-T. Wu, J.-H. Sun, Isolation of bulk acoustic waves in a sensor array with phononic crystals, 2011 IEEE Int. Ultrason. Symp. (2011) 2487–

2490. doi:10.1109/ULTSYM.2011.0618.

- [275] H.H. Lu, Y.K. Rao, T.Z. Wu, Y.M. Tzeng, Direct characterization and quantification of volatile organic compounds by piezoelectric module chips sensor, *Sensors Actuators, B Chem.* 137 (2009) 741–746. doi:10.1016/j.snb.2009.01.060.
- [276] D. Croux, A. Weustenraed, P. Pobedinskas, F. Horemans, H. Diliën, K. Haenen, T. Cleij, P. Wagner, R. Thoelen, W. De Ceuninck, Development of multichannel quartz crystal microbalances for MIP-based biosensing, *Phys. Status Solidi Appl. Mater. Sci.* 209 (2012) 892–899. doi:10.1002/pssa.201100715.
- [277] C. Garcia-Hernandez, C. Medina-Plaza, C. Garcia-Cabazon, F. Martin-Pedrosa, I. Del Valle, J.A. de Saja, M.L. Rodríguez-Méndez, An electrochemical quartz crystal microbalance multisensor system based on phthalocyanine nanostructured films: Discrimination of musts, *Sensors (Switzerland)*. 15 (2015) 29233–29249. doi:10.3390/s151129233.
- [278] G.S. Huang, M. Te Wang, M.Y. Hong, A versatile QCM matrix system for online and high-throughput bio-sensing, *Analyst*. 131 (2006) 382–387. doi:10.1039/b515722f.
- [279] C.A. Mills, K.T.C. Chai, M.J. Milgrew, A. Glidle, J.M. Cooper, D.R.S. Cumming, A multiplexed impedance analyzer for characterizing polymer-coated QCM sensor arrays, *IEEE Sens. J.* 6 (2006) 996–1001. doi:10.1109/JSEN.2006.877936.
- [280] H. Shen, T. Zhou, J. Hu, A high-throughput QCM chip configuration for the study of living cells and cell-drug interactions, *Anal. Bioanal. Chem.* 409 (2017) 6463–6473. doi:10.1007/s00216-017-0591-4.
- [281] A. Tuantranont, A. Wisitsora-at, P. Sritongkham, K. Jaruwongrungrsee, A review of monolithic multichannel quartz crystal microbalance: A review, *Anal. Chim. Acta.* 687 (2011) 114–128. doi:10.1016/j.aca.2010.12.022.
- [282] B. Leca-Bouvier, B. Leca-Bouvier, L.J. Blum, L.J. Blum, Biosensors for protein detection: A review, *Anal. Lett.* 38 (2005) 1491–1517. doi:10.1081/AL-200065780.
- [283] F. Pascal-Delannoy, B. Sorli, A. Boyer, Quartz Crystal Microbalance (QCM) used as humidity sensor, *Sensors Actuators, A Phys.* 84 (2000) 285–291. doi:10.1016/S0924-4247(00)00391-5.
- [284] A. Abudu, L. Goual, Adsorption of Crude Oil on Surfaces Using Quartz Crystal Microbalance with Dissipation (QCM-D) under Flow Conditions [†], *Energy & Fuels*. 23 (2009) 1237–1248. doi:10.1021/ef800616x.
- [285] L. Swathy, L. Abraham, Analysis of vibration and acoustic sensors for machine health monitoring and its wireless implementation for low cost space applications, 2014 First Int. Conf. Comput. Syst. Commun. (2014) 80–85. doi:10.1109/COMPSC.2014.7032625.
- [286] D.C. Ash, M.J. Joyce, C. Barnes, C.J. Booth, A.C. Jefferies, Viscosity measurement of industrial oils using the droplet quartz crystal microbalance, *Meas. Sci. Technol.* 14 (2003) 1955–1962. doi:10.1088/0957-0233/14/11/013.
- [287] C.K. Curtis, A. Marek, A.I. Smirnov, J. Krim, A comparative study of the nanoscale and macroscale tribological attributes of alumina and stainless steel surfaces immersed in aqueous suspensions of positively or negatively charged nanodiamonds, *Beilstein J. Nanotechnol.* 8 (2017) 2045–2059. doi:10.3762/bjnano.8.205.

